Core-shell cobalt iron oxide nanoparticles for the electrocatalysis of the oxygen evolution reaction

Lisa Royer

UNIVERSITÉ DE STRASBOURG

ÉCOLE DOCTORALE des Sciences Chimiques (ED222)

Institut de Chimie et Procédés pour l'Energie, l'Environnement et la Santé (ICPEES-UMR 7515) et Institut de Physique et Chimie des Matériaux de Strasbourg (IPCMS-UMR 7504)

THÈSE présentée par :

Lisa ROYER

Soutenue le : **8 novembre 2022**

Pour obtenir le grade de : **Docteur de l'université de Strasbourg**

Discipline/ Spécialité: Chimie physique

Nanoparticules cœur-coquille d'oxyde de fer et de cobalt pour l'électrocatalyse de la réaction de dégagement de l'oxygène

THÈSE dirigée par :

Mme SAVINOVA Elena	Professeur, ICPEES, Université de Strasbourg
M. BONNEFONT Antoine	Professeur, LEPMI, Université de Grenoble-Alpes
M. PICHON Benoît	Professeur, IPCMS, Université de Strasbourg

RAPPORTEURS :

Mme CHANEAC Corinne	Professeur, LCMCP, Sorbonne Université
M. FRIEDRICH K. Andreas	Professeur, German Aerospace Center (DE)

AUTRES MEMBRES DU JURY :

Mme DUBAU Laetitia	Directeur de recherches, LEPMI, Université de Grenoble-Alpes
M. GALLET Jean-Jacques	Maitre de conférences, LCPMR, Sorbonne Université
M. MAROUN Fouad	Directeur de recherches, Ecole polytechnique, LPMC

Remerciements

Ces trois années de thèse ont été une expérience intense qui m'a permis de mieux comprendre le monde de la recherche et de l'enseignement dans un milieu très enrichissant. Ce manuscrit et les articles qui en découlent sont le résultat de collaborations avec de multiples acteurs avec lesquels j'ai eu la chance de pouvoir travailler et que je tiens à remercier.

Comment commencer sans remercier les personnes sans qui rien de cela n'aurait été possible ? Mes directeurs de thèse Elena Savinova, Benoît Pichon et Antoine Bonnefont qui m'ont fait confiance dans la réalisation de ce projet. Merci Antoine pour toutes les explications que tu as su me donner sur l'impédance et la simulation des données obtenues mais aussi pour toutes nos journées/nuits au synchrotron toujours dans la bonne humeur et pour toutes nos discussions très intéressantes sur le métier d'enseignant chercheur. Bonne chance pour ton nouveau poste de professeur à Grenoble ! Merci également à Benoît de m'avoir transmis ses connaissances sur les nanoparticules et leur synthèse et d'avoir toujours encouragé mon autonomie et mon esprit critique. Et enfin merci à Elena qui a toujours été disponible pour une réunion imprévue dès qu'un soucis se présentait et qui a su me pousser et m'encourager quand les expériences ne fonctionnaient pas sans que l'on ne comprenne pourquoi. Ce fut une chance et un grand plaisir d'avoir travaillé avec vous pendant 3 ans, j'ai beaucoup appris à vos côtés.

Au cours de ma thèse j'ai eu l'opportunité de réaliser des expériences en partenariat avec les synchrotrons ESRF à Grenoble, SOLEIL à Paris et BESSY à Berlin, ces expériences n'auraient jamais été possibles sans l'expertise des personnes qui y travaillent et qui m'ont transmis leurs connaissances et aidé dans l'analyse des résultats : Viktoriia Saveleva pour les mesures de K edge en recuit, Jean Jacques Gallet et Fabrice Bournel pour m'avoir accompagnée lors des runs à SOLEIL et pour leur aide dans l'analyse des premières données et enfin Juan Velasco Velez qui a pris le temps de m'apprendre sa méthode graphène qui m'a permis d'observer les changements du L edge du fer et du cobalt sur la ligne ISISS de BESSY.

Je souhaiterais également remercier Simon Hettler ainsi que Raul Arenal pour les images STEM-HAADF et EELS et pour le temps qu'ils ont consacré à faire les mesures et à analyser les résultats. Nos réunions ont été productives et ces images d'une importance cruciale pour prouver l'existence de la structure cœur-coquille de mes nanoparticules ainsi que leur comportement en oxydation et réduction. L'imagerie de ces nanoparticules est particulièrement difficile, et pour cela je suis très reconnaissante à Thierry Dintzer qui a su produire (sans (trop) râler) des images plus que correctes de

nanoparticules qui n'auraient jamais dû être imagées. J'ai beaucoup apprécié nos nombreuses séances de MEB et nos discussions aussi variées qu'intéressantes lors de ces occasions. Merci à Cédric Leuvrey qui a de temps en temps remplacé Thierry au MEB et qui a patiemment cross-polishé les (très) nombreux échantillons que je lui ai donnés afin d'en observer la tranche. Les images TEM ont été obtenues par de nombreuses personnes : Kevin Sartori, Barbara Freis, Damien Mertz, Théo Lucante et Yuvna Ramnarain ; merci pour le temps que vous avez consacré à l'imagerie de mes échantillons. Big up à Yuvna qui à chaque fois que l'on avait un problème sur le TEM était toujours disponible pour nous aider.

D'autres caractérisations ont été nécessaires sur mes nanoparticules et leurs précurseurs et pour cela je tiens à remercier Didier Burger pour les ATG, Marc Lenertz et Christophe Lefevre pour la DRX et pour leurs conseils sur l'utilisation du logiciel fullprof (aka mon pire cauchemar). Merci également à Céline Kiefer qui m'a montré comment utiliser l'infra-rouge et la DLS et m'a donné des conseils sur la synthèse des nanoparticules.

Pendant ces trois ans j'ai eu l'opportunité de donner des TDs et d'encadrer les élèves de l'ECPM, cela m'a énormément apporté et n'a pas toujours été facile surtout durant le confinement ou nous avons dû réadapter tous les formats des TDs pour les faire en ligne. Je tiens donc à remercier tous les professeurs qui m'ont fait confiance dans l'encadrement de leurs TDs : Elena Savinova, Sergey Pronkin, Sylvie Bégin, Patrick Filizian, Nathalie Viart et Michel Bouquey.

Durant mon doctorat, j'ai eu le plaisir d'encadrer des stagiaires, le travail de deux d'entre elles a été très important et a mené à la publication d'un article. Pour cela je souhaiterais remercier Maud Zilbermann et Julie Guehl (et merci aussi pour les gâteaux !).

La bonne humeur étant essentielle pour la bonne réalisation d'un doctorat cela va sans dire que je remercie tous mes collègues de l'IPCMS et de l'ICPEES d'avoir sur m'intégrer et d'avoir toujours été là pour moi. Merci à mes collègues de l'ICPEES Benjamin, Alejandra, Taylan, Tristan, Mathias, Viktoriia et Evgeniia pour nos sorties et pour les parties de tarot les midis, à Sergey et François pour ces sessions de HIIT (si j'arrive à faire des pompes c'est grâce à vous), à Gwenaëlle et Sergey pour l'aide qu'ils m'ont apporté sur les expériences électrochimiques, à Alain qui m'a toujours aidé à réparer mon vélo ou ma voiture, à Julien et Agnès qui m'ont aidé à naviguer dans les méandres des papiers à remplir et enfin à Sylviane qui a su réparer mes erreurs sur les missions/commandes sans jamais s'énerver (bonne retraite à toi à la fin du mois !). Merci également à mes collègues de l'IPCMS de m'avoir accueilli durant la première année de mon doctorat : Barbara qui a souvent paniqué avec moi lorsque l'on devait donner un TD le lendemain, Wissal et Yuvna qui se sont toujours portées volontaires pour garder mon chat quand je devais partir en déplacement, Antonio et Varun qui m'ont (très) souvent invitée à

manger des repas plus fantastiques les uns que les autres. Merci à Guillaume, Joëlle, Pier, Alexandre, Fred, Yihui, Joana, Théo, Juan, Angie, Marlène et Laurianne pour la bonne ambiance qui régnait dans le labo et enfin à l'ADDEPT pour les activités qui ont été organisées (barbecue, tournoi de pétanque, soirée jeux de société).

Enfin merci à toutes les personnes qui m'ont soutenue sans nécessairement comprendre ce que je faisais. Mes amis Mathieu, Julie, Camille, Gauthier, Etienne, Gabriel, Morgane, Javid, Eléa, Romain et Antoine qui ont toujours su me changer les idées et que j'espère revoir très bientôt. Ma famille : mes parents qui m'ont tout appris, sans votre éducation je ne pense pas que je serais allée aussi loin dans les études, mon frère et ma sœur qui ont fait l'effort de s'intéresser à tout ce que je faisais, bon courage à vous pour votre dernière année d'études.

En tout dernier lieu je souhaite remercier mon compagnon Andrea qui a été présent à chaque moment de cette thèse. Merci d'apprendre le français, d'avoir fait les trajets pour venir me voir depuis les Pays-Bas et pour toutes tes petites attentions. J'ai hâte de te rejoindre et d'adopter un chien avec toi pour tenir compagnie à Krokmou. J'espère que d'ici un an et demi on puisse tous les deux nous appeler docteurs. Grazie mille per tutto!

Table of contents

List of abbreviations

AEM: anion exchange membrane

AEMFC: anion exchange membrane fuel cell

AEY: Auger electron yield

BE: binding energy

BET: Brunauer, Emmett and Teller

CCP: cubic closed packed

CE: counter electrode

CV: cyclic voltammogram

DLS: Dynamic light scattering

ECSA: electrochemical active surface area

EDX: Energy dispersive X-ray spectroscopy

EELS: Electron energy loss spectroscopy

EXAFS: Extended X-ray absorption fine structure

FT-IR: Fourier Transform Infra-red spectroscopy

FY: fluorescence yield

HER: hydrogen evolution reaction

HR-TEM: high resolution transmission electron microscopy

IEC: ion exchange capacity

KE: kinetic energy

NAP XPS: near ambient pressure X-ray photoelectron spectroscopy

NEXAFS: Near edge absorption fine structure, also known as XANES

NFs: nanofibers

NPs: nanoparticles

OER: oxygen evolution reaction

Oh sites: octahedral sites

ORR: oxygen reduction reaction

PEM: Proton exchange membrane

RDS: rate-determining step

RE: reference electrode

RHE: Reversible hydrogen electrode

SEM: scanning electron microscopy

Td sites: tetrahedral sites

TEY: total electron yield

TEM: transmission electron microscopy

TGA: thermogravimetric analysis

WE: working electrode

XAS: X-ray absorption spectroscopy

XPS: X-ray photoelectron spectroscopy

XRD: X-ray diffraction

General Introduction

Our expansive life conditions and living standards generate a tremendous rise in energy consumption which results in the inevitable fossil fuel resources depletion. This depletion combined with the need to limit greenhouse gas emissions led the world to diversify its sources of energy. The development of new renewable energies has then become a challenge as they could help in reducing the dependence on fossil energies but also decrease the amount of greenhouse gas emissions.

Due to the intermittent character of renewable energy production from sun and wind, the excess of energy production has to be stored to use at a later time. A promising way to store efficiently electric energy as chemical energy consists in converting it to dihydrogen (H_2). Indeed, hydrogen has a very high energy density (120 kJ/g) compared to gasoline (45.8 kJ/g) so this molecule is considered as a fuel and energy carrier for many applications. It can be produced thanks to water electrolysis by applying a voltage to an electrochemical cell consisting of two electrodes immersed in an electrolyte

and separated by a membrane, O_2 is generated at the anode (oxygen evolution reaction: OER) while H_2 is generated at the cathode (hydrogen evolution reaction: HER). Consequently, hydrogen production via water electrolysis performed with the excess energy produced by solar or wind energies would be an environmentally friendly way to generate it, store it and then use it as a fuel for various applications. Water electrolysis is consequently regarded as a promising way to produce "green" hydrogen. This reaction can be performed either in acidic or in alkaline media, using either a proton-exchange membrane, or an anion-exchange membrane, or a liquid alkaline electrolyte.

The important potential needed for this reaction to occur still hinders the development of water electrolysis for hydrogen production. Indeed, for this reaction to occur a minimum thermodynamic potential of 1.23V *vs.* RHE (Real Hydrogen Electrode) has to be applied but the real potential is usually much higher than this value. Indeed, out of the two anodic and cathodic half-reactions, the OER at the anode has the most sluggish kinetics and, as a consequence, an overpotential has to be applied in addition to the 1.23 V to increase the kinetics of the reaction. In order to decrease this overpotential as much as possible, catalysts are used and extensive research has been performed on iridium and ruthenium oxides (in acidic and alkaline media). Non-noble transition metal oxides (TMOs)-based catalysts (in alkaline media) have also been extensively studied for the OER as they present the advantage to be more abundant and cost-effective than iridium or ruthenium-based anode materials. However, some TM such as cobalt or nickel are becoming quite rare and are classified as critical materials by the European union so their use has also to be limited.

Numerous publications report on the activities and behavior of TMO-based catalysts during the OER. Among them, cobalt or nickel-based catalysts are among the most promising active electrocatalysts. However, many difficulties and questions are encountered when designing these catalysts, evaluating their activities and understanding the OER mechanism:

- Some catalysts are not conductive and are supported by/or mixed with carbon, which degrades during the OER due to the carbon oxidation reaction, and is consequently not suitable for industrial applications.
- The catalyst loading seems to play a role in the activity measurements (even in the presence of some types of carbon), likely due to a contact resistance between catalytic particles, and its evaluation is not straightforward.
- If the catalyst presents a heterogeneous structure and chemical composition, then determining the active sites and active structures is an issue.
- The catalysts are degrading or evolving under the OER conditions and consequently linking their structure and composition to their activity is not straightforward.

- The OER mechanism (via anion redox or cation redox) and active sites are not well-understood and often involve some structural transformations (reversible or irreversible) of the catalyst.
- The electrolyte nature and concentration seem to play a role in the activity but the phenomena leading to these changes are not well understood.
- During the OER on porous catalytic layers, the pores are clogged by O_2 evolution which makes the active sites unavailable and decreases the activity as the surface of the catalyst has to be maximized for a good efficiency.

To resolve these issues the use of *in situ* and *operando* techniques on an ideally well-defined catalyst is needed. To design such a catalyst, several criteria have to be met:

- ✓ Conductivity: to limit the ohmic losses in the catalytic layer
- ✓ Stability: to avoid rapid degradation of the catalyst during the OER
- ✓ Large specific surface: to use low amounts of a catalyst
- ✓ Activity: to be efficient for the OER

Our strategy consisted in the development of a catalyst that meets all of the above criteria and we have chosen to design core-shell cobalt iron oxide nanoparticles (NPs). Core-shell structures are of high interest because only the shell (usually composed of rare and expensive materials) has to be electrochemically active, hence the core volume can be composed of earth-abundant and cost-effective materials. These Fe_3O_4@$CoFe_2O_4$ NPs then limit the cobalt utilization by using a conductive Fe_3O_4 core and an electrochemically active $CoFe_2O_4$ shell. Moreover, the iron oxide core may influence the catalyst behavior thanks to synergistic structural or electronic effects. An advantage of the Fe_3O_4@$CoFe_2O_4$ nanostructures is that both the core and the shell material present a similar cell parameter, thus the shell can grow epitaxially on top of the core, so that the structure is crystalline. Also, even though the reasons behind this improvement are not clear yet, the presence of iron within cobalt- or nickel-based catalysts has been reported to improve the OER activity. Therefore, the presence of iron as a co-catalyst could be beneficial.

The NPs are synthesized via two consecutive reactions of thermal decomposition of metal complexes in a high boiling temperature solvent in the presence of a surfactant. The thermal decomposition method allows the synthesis of NPs with well-defined size, size distribution, chemical composition, and shape. Hence, an ideally well-defined catalyst can be designed.

In this thesis, we aim at developing an 'ideal' catalyst to evaluate its catalytic properties and link them to the chemical structure but also to understand *operando* the phenomena happening at the surface of the catalyst during the OER. For this purpose, we synthesized four different types of core-

shell cobalt iron oxide NPs, characterized them electrochemically, and then used X-ray absorption spectroscopy to investigate the oxide structure and the oxidation states of metal cations during the OER. Chapter 1 will be devoted to the OER reaction principles, the different catalysts that have been reported active in alkaline media, their *operando* transformations, and the synthesis principles and advantages of core-shell NPs by thermal decomposition of metal salts. Then, chapter 2 will present the materials and methods used in this work for the core-shell NPs syntheses, physical, electrochemical and *operando* characterizations. Following this, chapter 3 will present the catalyst used in this work: the core-shell NPs and their characterizations by various methods to be sure that they correspond to a well-defined catalyst. In chapter 4, the influence of the electrode loading on the activity will be investigated thanks to the impedance spectroscopy. The experimental data will be modeled via various electronic circuits. Once the loading influence has been understood and the activity has been determined, chapter 5 will focus on the activity comparison of the different types of the synthesized NPs, and on the study of the impact of the core size on the overall activity. Finally, chapter 6 will investigate *operando* the transformations occurring on the catalyst during the OER and study the evolution of the oxidation state of metal cations, unraveling some synergetic effects between iron and cobalt during the reaction.

Chapter 1: State of the art

1) *Context*

The rapid improvement of living standards and the following increase in energy consumption and depletion of fossil fuel resources combined with the need to limit greenhouse gas emissions led the world to diversify its sources of energy. The development of new renewable energies has become urgent as the energy crisis and environmental pollution are becoming more and more serious. Indeed, they could help in reducing the dependence on fossil energies but also decrease the amount of greenhouse gas emissions.

However, renewable energy production is not constant over time as the wind for the windmills or the sun for the solar panels are intermittent phenomena. Consequently, depending on the importance of the energy demand, the energy produced has to be stored or needs to be completed by another energy source. Stocking the produced energy to use later thanks to energy storage techniques is a possibility to avoid interruption in the energy supply However, even though researchers are working on solutions for the energy storage, most of the solutions still involve some waste generation, energy losses, or limited storage possibilities[1].

Electrolysis is a technique in which an electric current is used to drive a chemical reaction that wouldn't occur otherwise. It takes a compound and breaks it apart; this reaction is not spontaneous and electrical energy needs to be given to the system for it to occur. Different type of electrolysis reactions exists and are used in industrial processes for the production of dihydrogen, aluminum, or chlorine for example.

Hydrogen has been considered a clean and highly interesting energy source to use in fuel cells that will convert H_2 chemical energy into electrical energy. This reaction produces water as a product and doesn't produce greenhouse gas[2]. In addition, hydrogen is an interesting way to store energy as unlike the sun or the wind it can be stored in compressed gas or liquid form and then be directly available for the electricity production. Indeed, the option to use an electrical current to create hydrogen is raising the interest of many scientists because hydrogen has a very high energy density: 120 kJ/g. Compared to gasoline which presents an energy density of 45.8 kJ/g, 1kg of hydrogen then contains as much energy as about 3 kg of gazoline[3]. This molecule is considered a fuel and energy carrier for many applications[4,5].

However, even if hydrogen is a highly interesting molecule for the energy storage, its production nowadays mainly originates from natural gas reforming processes where methane and water react to form carbon monoxide, carbon dioxide, and dihydrogen. Even though the carbon

dioxide can be captured and reused for biomass applications this process is neither clean nor renewable. Consequently, hydrogen production via water electrolysis performed with the excess energy produced by solar or wind energies would be an environmentally friendly way to generate it, store it, and then use it as a fuel for various applications. Additionally, water splitting creates very pure hydrogen, which avoids purification processes and water is an abundant resource on earth. Water electrolysis is consequently regarded as a promising way to produce "green" hydrogen[3]. However, the important potential needed for this reaction to occur still hinders the development of water electrolysis for hydrogen production.

2) *Water electrolysis and OER mechanism*

Water electrolysis (Equation 1) is of particular interest in this study because of its simple and abundant reactant (water) and its non-toxic and interesting products (dioxygen and dihydrogen).

$$2H_2O_{(liq)} \rightarrow O_{2(g)} + 2H_{2(g)}$$

Equation 1: water electrolysis process

This process takes place in an electrochemical cell composed of two electrodes (anode and cathode) immersed in an electrolyte that are connected to an external power supply (Figure 1). The drive of the process is the potential difference between the anode and the cathode. During this process, water is reduced at the cathode in the hydrogen evolution reaction (HER), producing hydrogen and oxidized at the anode in the oxygen evolution reaction (OER), producing oxygen. This process can occur in alkaline or acidic media at low temperatures with liquid water or at high ones with the water vapor[6].

The lowest (thermodynamic) potentials at which the oxygen evolution reaction (OER) and the hydrogen evolution reaction (HER) can occur are 1.23V vs RHE and 0 V vs RHE respectively. However, the real potentials one needs to apply for these reactions to occur are higher because of the sluggish kinetics at the electrodes, highlighting the need for catalysts for these reactions. The difference between the actual potential required to reach a certain current density (j) and the theoretical potential is called the overpotential (η). A catalyst is considered better than another if its overpotential is smaller for a given current density. The challenge is then to develop catalysts that will present low overpotentials for both the OER and the HER.

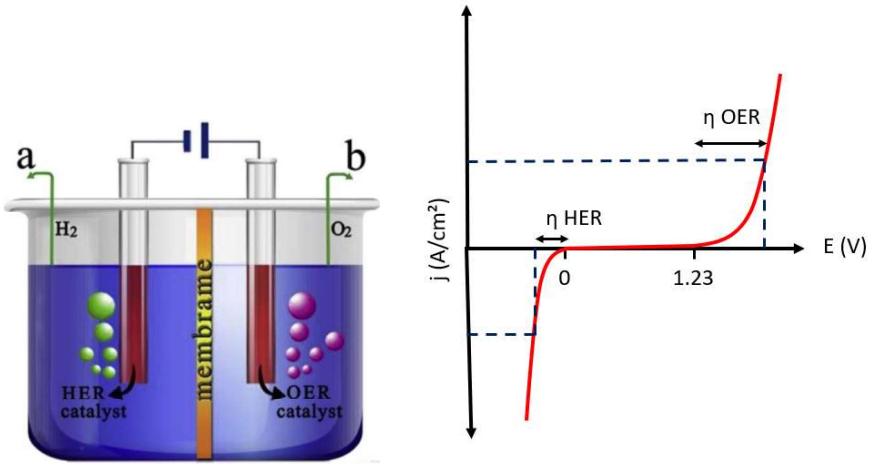

Figure 1: Left: water electrolysis cell. HER, hydrogen evolution reaction; OER, oxygen evolution reaction, taken from[7]. Right: current potential curves. OER is the anodic part and HER the cathodic one.

To avoid gas crossover, a semi-permeable ion exchange membrane separates the two sides of the cell. In acidic media this membrane is a proton exchange membrane (PEM), one of the more common materials used in the industry for PEM is Nafion®, a fluorinated polymer bearing sulfonic functional groups. PEM electrolyzer presents a compact system design, fast response, and high voltage efficiency, which makes it an ideal candidate for the development of this technology at a larger scale[6]. Usually, catalysts used in acidic media are platinum at the cathode and iridium or ruthenium at the anode[8]. As these materials are scarce and expensive, their replacement by earth-abundant cost-effective materials would be interesting.

An alternative to PEM that is rising interests at the moment is the use of anion exchange membranes (AEM)[9]. These membranes would let the OH^- ions cross the membrane while being impermeable to the O_2 and H_2 generated during water splitting. The development of these membranes has been a real challenge for a long time. First, the struggle was to find the groups and functions that needed to be in the membrane in order to obtain a stable membrane with high ionic conductivity. Nowadays, AEMs usually present quaternary ammonium groups bound to a polymer backbone[10]. Thanks to extended research on polymer membranes, some satisfying solutions to create a performant AEM have been found[11,12]. The advantage of this technology is that as the local media is alkaline, cost-effective transition metal oxide (TMO) based materials that are usually stable at high pH can be used to replace iridium or ruthenium used at the anode for the PEM technology. It is a promising solution for future developments of water splitting[13].

As presented above the OER is the bottleneck for water electrolysis development due to its sluggish kinetics: it involves a four-electron process. Also, even though the reaction mechanism is not very well understood yet, adsorbed and intermediate species are formed during this reaction which makes this half reaction difficult to realize. HER in alkaline media on the other hand presents less sluggish kinetics even though it still requires a catalyst to increase the rate of this reaction, and the HER kinetics is known to be slower in alkaline compared to acid media.

$$HER: 2H_2O_{(liq)} + 2e^- \rightarrow H_{2\,(g)} + 2OH^- \qquad E° = 0\ V\ vs\ RHE$$

$$OER: 4OH^- \rightarrow 2H_2O + O_2 + 4e^- \qquad E° = 1.23\ V\ vs\ RHE$$

Equation 2: Hydrogen evolution reaction and oxygen evolution reaction in alkaline media

Consequently, even though the HER in alkaline media has also attracted much intention, research also highly focused on the development of OER catalysts. However, the mechanism of the OER is still being debated in the literature: two main OER mechanism scheme for metal oxides in alkaline medium have been proposed in the literature (Figure 2). M refers to the metal cation and active center, all the reaction mechanisms are beginning by the same first elementary reactions:

1) Adsorption of OH^- on M
2) M-O formation thanks to the reaction with another OH^- from the electrolyte.

The overpotential of the OER is related to the kinetics constraints of the slowest elementary reaction (the rate determining step). These steps are then followed by other intermediate steps. For the first proposed mechanism (plain black cycle of Figure 2), the next two steps are the following:[14]

3) MOOH intermediate is formed by a nucleophilic attack on the M-O intermediary
4) O_2 is released and the active center goes back to its initial state

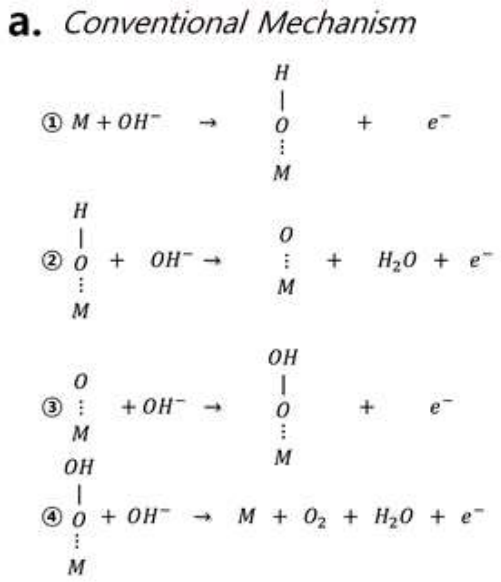

Figure 2: General OER mechanism taken from[54] M is the metal center

In the second pathway (dashed line of Figure 2), the mechanism is a little different and there is only one other step[16]: after the formation of M-O intermediate, two M-O neighbor species associate to directly generate O_2 and then both active centers go back to their initial state. Following chapters will show that this view of the OER is oversimplified. Notably, it does not consider either redox transitions on the surface and/or in subsurface of the oxide catalyst (which may be localized on the transition metal cation or oxygen anion) or involvement of lattice oxygen in the OER.

A computational way to describe the catalytic activity of OER catalysts has been described by Man *et al.*[17]. This method is based on the difference between the energies of M-OH formation (1st step) and M-OOH formation (3rd step) which corresponds to the rate-determining step. The activity of an OER catalyst can then be determined by DFT calculations. Using the above-mentioned criteria, Man *et al.* correlated the overpotential of various compounds within a volcano plot in Figure 3. According to

the Sabatier principle: a good catalyst should bind neither too strongly nor too weakly to the intermediates in order for the reaction to happen. Consequently, good catalysts are at the top of the volcano. Among transition metals compounds with cobalt, iron, nickel or manganese seem to be good candidates as catalysts for the OER.

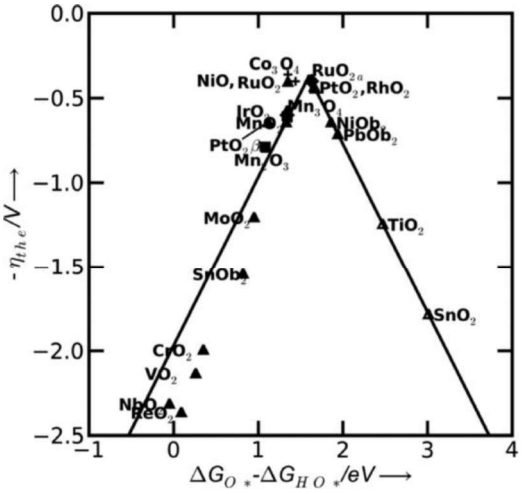

Figure 3: Theoretical overpotential for oxygen evolution vs. the difference between the standard free energy of two subsequent intermediates taken from [17]

However, even though Volcano's plots are a great indicator of the potential activity of a catalyst, they are not able to describe it fully and the ideal catalyst cannot be found only thanks to these simulations. Consequently, numerous publications have been devoted to the investigation of TMO based catalyst in alkaline media for the OER. These compounds and how their activities for the OER can be determined will be presented in the next parts.

3) Catalysts for alkaline water electrolysis

In this part, the determination of the activity and the catalytic properties of a catalyst will be presented as well as various types of TMO based catalysts, their reported activities and Tafel slopes.

a) Catalyst properties and characterizations

As stated above, water splitting can only occur above a minimum potential of 1.23 V vs RHE at room temperature. However, because of energy and ohmic losses, in a real system one needs to apply an additional potential to this minimum voltage: the overpotential (η). The minimization of this overpotential is of great importance for the future of this technology and can be achieved using efficient electrocatalysts[13].

A catalyst is a substance that accelerates a chemical reaction without being consumed during the reaction. During the reaction, bonds are broken and rebuilt and catalysts help in making this process easier by lowering the activation energy of the reaction (energy barrier which has to be overcome for the reaction to occur). Considering water splitting, this catalyst has to meet different criteria:

- It has to be stable in the media in which the reaction is taking place.
- It has to be active for the considered reaction.
- It has to present a high specific surface to use smaller quantities.
- It has to be conductive to limit the ohmic drop within the catalytic layer.

AEM able to operate in an alkaline media allow the use of electrocatalysts such as earth-abundant TMOs that are usually stable at high pH. In order to determine the efficiency of a catalyst, various parameters can be considered:

- The current generated by the reaction at a given potential per unit surface area (surface activity) or per unit mass (mass activity) of catalyst (Figure 4).

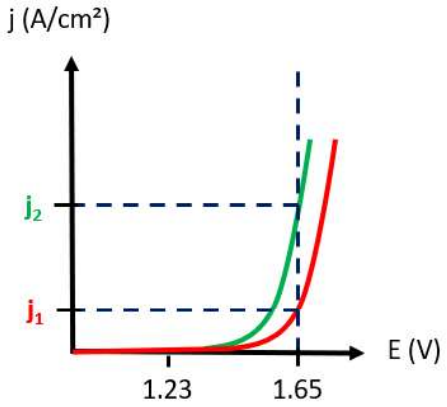

Figure 4: Linear sweep voltammetry curves obtained for two different catalysts. The green curve corresponds to a more active catalyst.

In the literature, the activity is often given by dividing the current obtained for a given potential by the geometric surface of the electrode and not the catalyst real surface. If this is done for the same catalyst loading and with a catalyst that has a similar electrochemical active surface area (ECSA) or Brunauer, Emmett Teller (BET) surface this is not an issue but it becomes one if one wants to compare the activity results of different publications. To compare these results and obtain the surface activity or mass activity of a catalyst, its real surface or mass is needed[18]. Instead of measuring the current density reached at a given potential to compare the activities of various catalysts, many publications indicate the potential needed to reach a given current density (often 10 mA/cm²).[19]

- The Tafel slope (Equation 3) that derives from the Butler Volmer equation is another factor that needs to be considered when determining the activity of a catalyst. Indeed, the Tafel slope can give some insights in the rate determining step of the reaction as well as the reaction mechanism[20].

$$\eta = a + b\,log(j)$$

$$for\ a\ single\ electron\ transfer\ step\ and\ large\ anodic\ overpotentials:$$

$$a = -\frac{ln\,10\,RT}{(1-\alpha)F}log(j_0) \qquad and \qquad b = \frac{ln10RT}{(1-\alpha)F}$$

Equation 3: Tafel equation

Here, j is the current density; η the overpotential (η= $E_{applied}$ -1.23 V), R the perfect gas constant, F the Faraday constant, α the electron transfer coefficient and j_0 is the exchange current density (the absolute value of the anodic and cathodic current density flowing across the interface under equilibrium). Note that for multi-electron transfer electrode reactions the expression for the Tafel slope becomes more complex.

Tafel slopes are obtained from the cyclic voltammetry or linear sweep voltammetry curves in the OER region: when the current variation as a function of the applied potential becomes exponential (Figure 4).

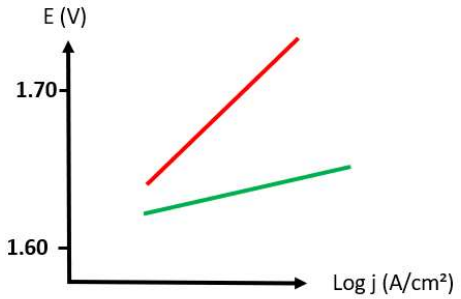

Figure 5: Tafel slopes of 2 different catalysts.

The slope of these curves characterizes by how much the potential needs to be increased to obtain a 10-fold increase of the current. As for a given variation of the applied potential a small Tafel slope will involve a bigger change in current than a more important Tafel slope, a good catalyst will present a low Tafel slope.

However, the Tafel slope alone is not enough to fully characterize a catalyst. Indeed, different catalysts can have the same Tafel slope and they can have different exchange current densities for a given value of the potential. Thus, to fully characterize the catalyst it is necessary to give the Tafel slope and the current density measured at a given potential.

- The stability of the catalyst is also an important parameter for future applications, it can be evaluated by repeating cycles many times or by applying the same potential for a long time. If the activity of the catalyst and the Tafel slope of the compound don't vary on the long term then the catalyst is considered as stable.

To sum up, good OER catalysts have to present a high activity for a given potential, a low Tafel slope, high surface area, as well as to be stable and conductive[21]. Another issue is the wettability of the electrodes: indeed, when the gases are generated at the surface of the electrodes, bubbles are created. This deteriorates the activity because as long as the bubble is not big enough to leave the electrode then it leads to an increasing ohmic resistivity as the electron transfer at the surface is blocked[22]. This situation is also an issue because it leads to very high local current densities flowing through the electrode. This can affect the catalyst stability, consequently, a hydrophilic catalyst is better for the OER. Catalyst also has to be safe for the health and cheap enough to foresee a large-scale production in the future.

b) Impedance spectroscopy characterizations

One important factor to consider to measure accurately the activity of a catalyst is to verify if all the surface of the said catalyst is involved in the reaction. Indeed, if the catalyst layer is too thick or the material not conductive enough it is possible that only a fraction of the particles will be involved in the reaction due to an ionic and electronic resistance within the layers of the material. One way to evaluate this resistance is to perform measurements by means of the electrochemical impedance spectroscopy.

Impedance is evaluated by applying an AC potential to an electrochemical cell and then by measuring the current flowing through the cell. With this technique, one can measure the conductivity of the catalytic layer (that will be different from the intrinsic conductivity of the material due to interparticle resistance). It has an imaginary and a real component, one can plot the imaginary part as a function of the real one and obtain the Nyquist plot (Figure 6).

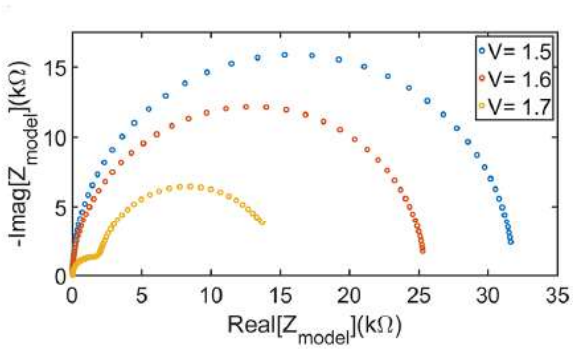

Figure 6: Nyquist plot taken from ref[23]

With these Nyquist plots, it is possible to determine the solution resistance, the charge transfer resistance, the ionic and electronic resistance as well as the capacitance of the material.

In conductive materials the only correction that needs to be done is the one of the ohmic drop caused by the solution resistance. However, more recently, less conductive materials that are more common on earth and consequently cheaper have been explored such as oxides for the OER for example[24]. It has been a bottleneck to understand better the electronic conductivity and kinetics of charge transfer during the OER. Very often the catalytic material is mixed with carbon to form an ink that is then deposited on the electrode. The addition of carbon makes the catalytic layer conductive and increases its apparent activity by involving all of the catalyst in the reaction[25]. However, at the potentials at which the OER occurs, carbon materials are unstable and are prone to oxidation. Hence, addition of carbon can be used to determine the activity of the material but it won't be possible to use

it at an industrial scale. Consequently, a more in-depth analysis for electrocatalytic reactions utilizing poorly conducting materials is needed to adequately evaluate and understand their properties.

Dong Young Chung and al [45] worked on the HER reaction with a molybdenum disulfide catalyst and analyzed how the conductivity of the material affected its electrocatalytic performances. They demonstrated that the conductivity of the catalyst is really important and that if too many layers of not too conductive nanoparticles are deposited on an electrode then it would modify the measured activity of the catalyst.

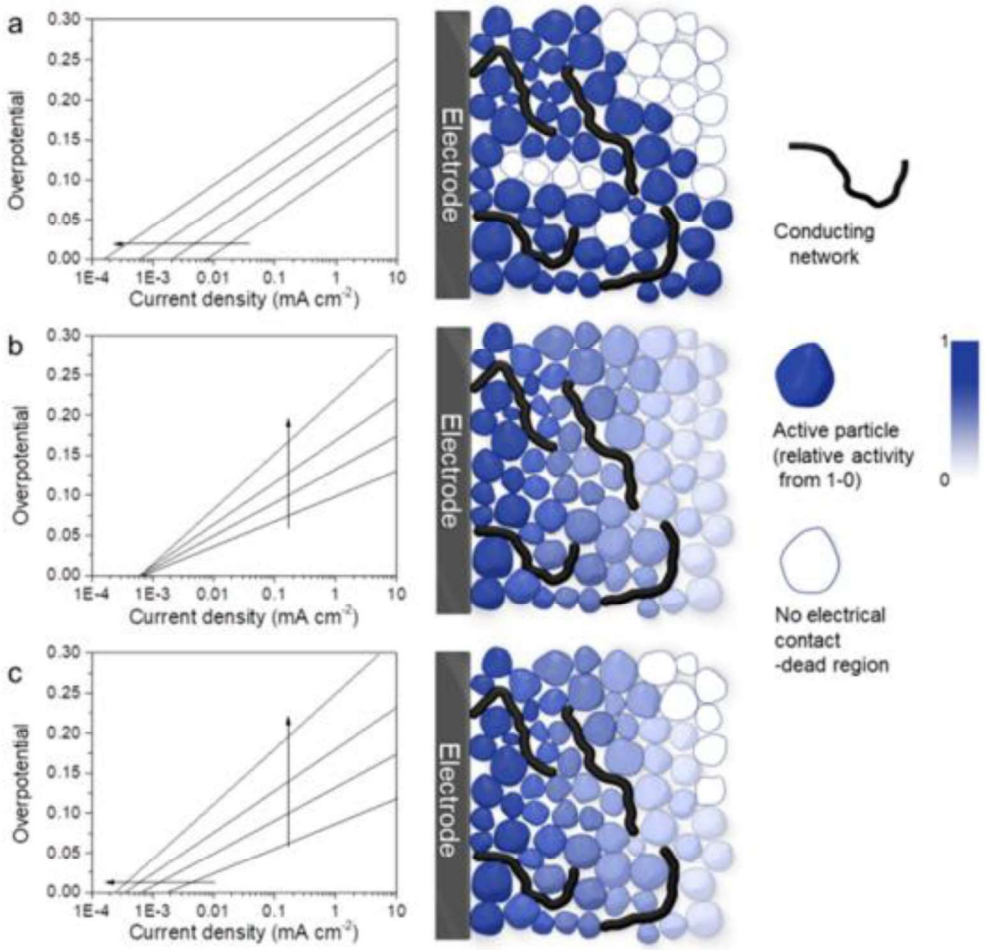

Figure 7: Schematic representation of the catalytic layer resistivity on the Tafel plots (left) and cartoons showing conducting pathways through the catalytic layer (right). Top: formation of dead zones, middle: progressive increase in film resistance, and bottom: combined effects (bottom). Taken from ref[26]

In order to measure the resistance of the catalyst, electrochemical impedance spectroscopy is a commonly used characterization technique but its interpretation is not always straightforward due to the effect of charge transport and polarization but also to the fact that all the above-mentioned phenomena can be modified according to the position of the particle in the catalyst layer (Figure 7).

Consequently, the apparent (measured) activity will be modified. In that case, one has to consider a distributed impedance within a porous catalyst. The phenomena has been studied on polymers[27] but can also be applied to oxide materials.

As a first approximation one can consider that the electrical charge crosses the electrode materials and the electrolyte and that only the resistance to charge transfer of the whole layer is considered. This is the Randles model whose equivalent electric circuit is presented in Figure 8. It is well adapted when the catalyst layer deposited on the electrode is very conductive or when all the particles of the catalyst are available to participate to the reaction. The Randles model is one of most common ones: it includes a solution resistance: R_s; a double layer capacitor: C; and a charge transfer resistance R_{tr}. It is also a starting point for other more complex models.

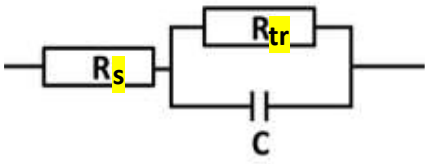

Figure 8: Randles model for impedance measurements

However, when the catalyst layer becomes too thick and that the material is not conductive enough to assure a good charge transfer across the layer, one can consider a distributed repartition of the charge transfer according to the region of the catalyst. To model the impedance, the catalyst can then be separated into different layers. This is the transmission line model[28]. The electric circuit that represents this model is presented in Figure 9. It has been developed first for polymer films but it can also be a good model for catalysts that are porous or that present a certain resistivity toward ionic transport.

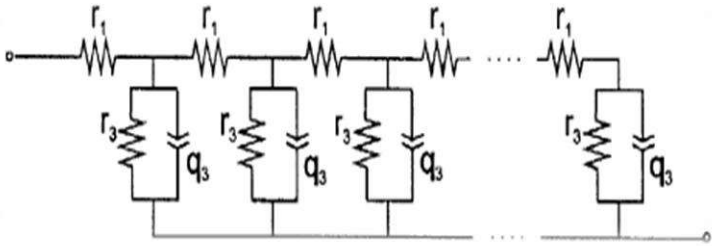

Figure 9: Transmission line model for impedance measurements taken from.[29]

On this circuit the r_1 is the ionic and electronic resistance within the layers of the catalyst, r_3 is the charge transfer resistance and q_3 is the capacitance within the layer.

c) Catalysts for the OER in alkaline media

Numerous publications investigated different types of electrocatalyst in alkaline media and some of them have shown great performances[30]. Among them are materials such as: noble metal-based catalysts, earth abundant transition metal oxides such as spinels or perovskites, metal oxyhydroxides, etc… This work will focus on the development made on transition metal based electrocatalysts for alkaline water electrolysis.

The type of materials that seems interesting is the layered structure type family. This is a type of materials that has been used since the 1970s in alkaline batteries. These structures are composed of different type of materials. It consists of metal hydroxide $M(OH)_2$ layers (M being a transition metal), which under the OER conditions transform into metal oxyhydroxide MOOH layers[31]. These materials have shown great activity for the OER, they are usually cobalt or nickel-based compounds because of their well-known activity for the OER. $Ni(OH)_2$/NiOOH system has shown really good activity, a systematic study performed by Subbaraman *et al* on this type of structures has shown that the OER activity decreases in the following order: Ni>Co>Fe>Mn[32].

Perovskite materials also seem to be of great interest for the OER. Their general formula is ABX_3 (X is usually an oxygen atom) and they have been studied as a promising bifunctional catalyst for the OER and for the oxygen reduction reaction (ORR)[33]. In this crystalline structure A and B are two different cations which sizes are very different (A is larger). The type of cations in the structure, their charge and their coordination can be tuned. Consequently, one can generate some distortions in the structure by doping with various insertion atoms, changing the properties of these materials.[31] Another option to improve their activity for the OER is to generate oxygen vacancies[34]. They can be generated by treating the sample at high temperature and low pressure of oxygen for example or by doping by foreign atoms.[35] Mixed perovskites with both rare earth (La or Ba) and transition metal such as Ni, Co or Mn have shown promising results for the OER.[36] However, they present the issue of containing rare earth compounds which quantities on earth are limited and which demand is growing worldwide.

Last but not least, a material that is rising more and more interest for the OER is the spinel structure (Figure 10). This compound of general formula AB_2O_4 in which oxygen atoms are arranged in a cubic closed packed (CCP) lattice and the metal cations A and B are in the octahedral and tetrahedral sites, seems to be of particular interest. There are two types of spinel structures. One is called normal spinel with the atom A^{2+} in the tetrahedral (Td) sites and B^{3+} in the octahedral ones (Oh), the other is called the inverse spinel where A^{2+} is occupying half the octahedral sites and $B^{2+/3+}$ is occupying both the tetrahedral and the octahedral sites.

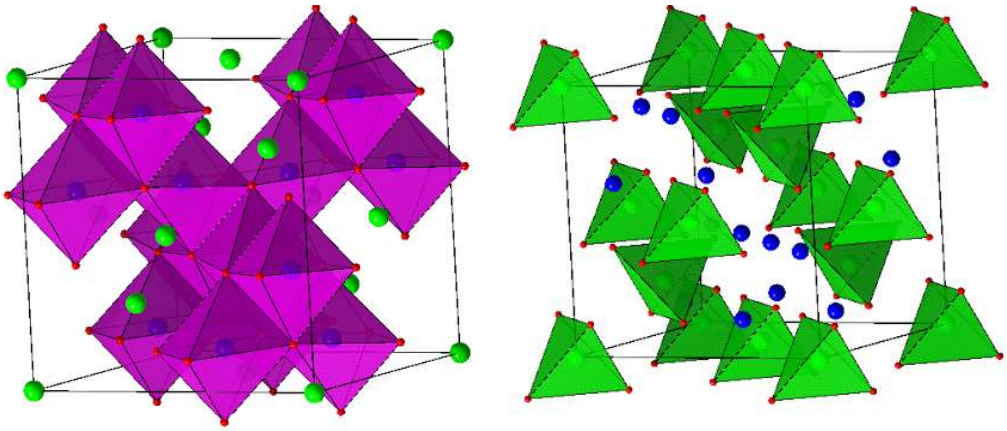

Figure 10: AB_2O_4 spinel structure and its representation. Blue spheres: atom A in the octahedral sites, green spheres: atom B in the tetrahedral sites, red spheres: oxygen atom, taken from.[37]

This family is of great interest because spinels are showing both octahedral (Oh) and tetrahedral (Td) coordination for the cations inside the structure. As a result, the d electronic level is split into two different sub-levels (Td: t_2 and e; Oh: t_{2g} and e_g)[38]. There are more than 100 different compounds in the spinel family so it offers a very wide choice of potential OER catalysts. Moreover, spinels are usually stable in alkaline solutions even under high anodic potential, thus they can generally withstand OER conditions[31].

Some groups have recently shown that spinels were submitted to a structural transformation to produce a metal oxyhydroxide layer at the surface of the catalyst[39–43] when a high potential required for the OER to occur is applied. The formation of this layer could explain their high activity for the OER. However, the reversibility of the formation of this layer is being debated in the literature and it will be discussed later in this chapter. Oxygen vacancies and defects can also be introduced in spinel structures to modify the physical and electrochemical properties of the material.

However, this field of spinel OER catalysts requires deeper investigation. For the same materials different values of the OER activity can be found in the literature: for example, for cobalt spinel (Co_3O_4) different activity values of 9.6[44]; 52[45]; 78[46] or 240 A/g_{oxide}[25] at 1.65V *vs* RHE have been documented. These important variations can be explained by the fact that the activity depends on multiple factors such as the surface state and defects of the catalyst as well as the conduction of the catalyst layer, the electrolyte concentration or the presence of a conductive material such as carbon in the catalyst to improve its conductivity will also play an important role. Systematic studies are necessary to characterize accurately the activity of a catalyst. The influence of various factors on the activity will be discussed in the next paragraphs.

- ***Influence of the type of electrolyte and its concentration on the activity:***

To understand the effect of the electrolyte concentration and the effect of the counter ion (K^+, Na^+, Li^+ etc) Duan *et al.*[47] recently studied the impact of the composition of the electrolyte on cobalt and iron based catalysts. On a CoOOH catalyst (Figure 11) they observed that higher concentrations of KOH electrolyte were increasing the OER activity of a material. This increase in activity at higher electrolyte concentrations was also observed by Huang *et al.*[48] on cobalt-zinc oxyhydroxide catalysts as well as by Zhou *et al*.[49] on zinc cobalt iron spinel oxides. It was explained by the authors by the change in the activation entropy and an increase of the number of active sites and probably a faster charge transfer.

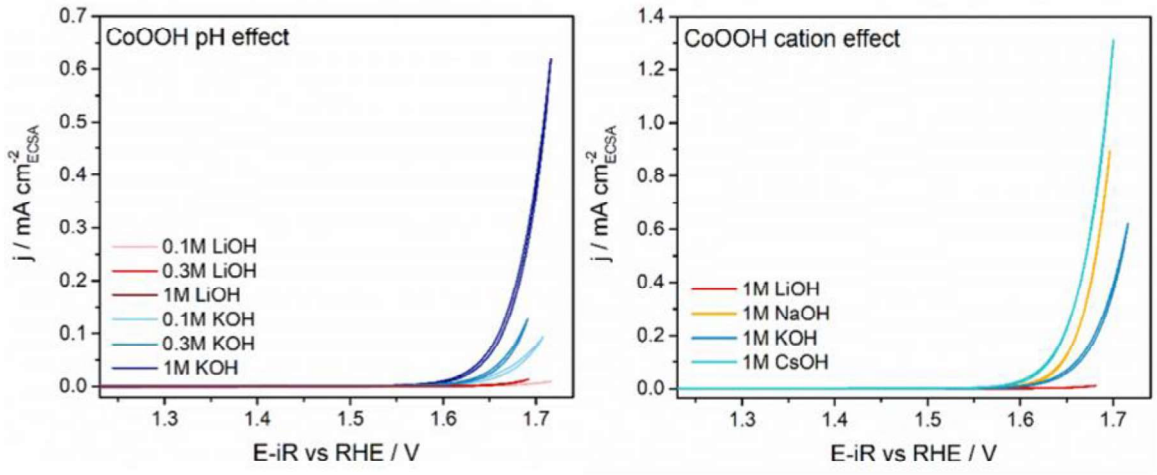

Figure 11: Effect of the concentration and the nature of the electrolyte on the activity of a CoOOH catalyst taken from.[47]

It is interesting to note that Duan *et al.* also saw an impact of the counter ion nature (Figure 11): for the same electrolyte concentration, they used Li^+, Na^+, K^+, and Cs^+ and observed that for this catalyst the activity highly varied according to the nature of the electrolyte. For LiOH almost no activity was observed when for CsOH the activity was the highest. Between KOH and CsOH electrolyte they observed a 3-fold increase of the activity. This effect was also observed by Garcia *et al.*[50] on NiOOH catalyst with CsOH electrolyte presenting the best activity for the OER. This effect suggests that bigger cations are better for the OER, this is probably related to the interaction of the cation with the active oxygen species within the three-dimensional oxide structure. It should however be noted that cation effect has also been observed for metal electrodes and may thus be related to the cation-dependent water structure at the interface.

Giordano *et al.*[51] also studied the pH influence of oxide based catalysts for the OER and concluded on the importance of measuring the voltammetric curves with respect to the RHE as it is a pH-

dependent reference that guarantees separation of kinetic and thermodynamic effects on the overpotential and ensures a fair comparison at different pHs. They also stated that for systems containing transition metal oxides (they can sustain charge buildup with a change in the TM oxidation state) the decoupling of proton and electron transfers during the OER reaction is possible. It has been suggested by M. Koper[52] that the pH dependence of the OER activity indicates the presence of non-concerted proton–electron transfer steps during the OER. Grimaud *et al.* [53] studied perovskite compounds for the OER and, by increasing the pH, they obtained higher OER activities. They concluded that non-concerted proton–electron transfer steps are coupled to the activation of lattice oxygen redox reactions on their catalyst.

Kim et al.[54] also studied the OER on perovskite catalysts and arrived at the conclusion that both the lattice oxygen evolution and the conventional OER on the oxide surface occur simultaneously, the former dominating at high pH.

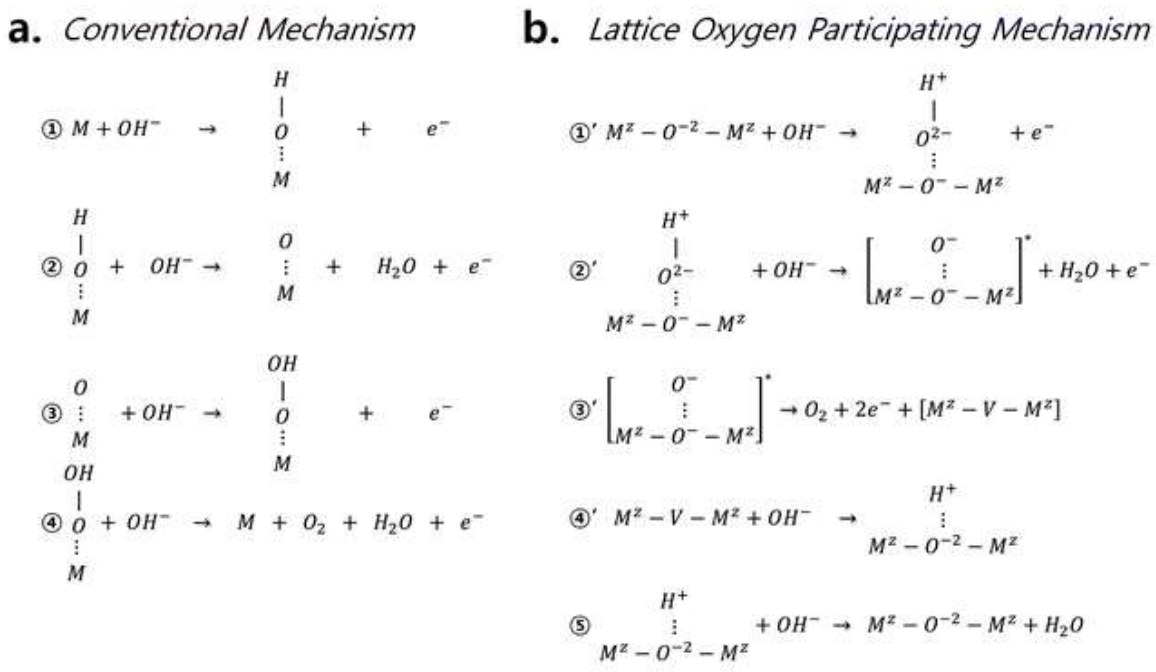

Figure 12: Two types of OER mechanisms proposed by Kim et al.[54] on perovskite catalysts. Here M stands for the transition metal cation and V for the vacancy.

Consequently, the electrolyte nature and concentration can play an important role on the determination of the activity as well as shed some light on the reaction mechanism (involving the oxygen atom from the oxide lattice or not).

- ***Ligand effect on the determination of the activity:***

Another factor that can influence the catalytic activity is the ligand surrounding the NPs. Indeed, in order to avoid their aggregation, particles are often synthesized in the presence of surfactants. Li *et al*.[55] suggested that the presence of a surfactant such as oleic acid or oleylamine is detrimental for electrocatalytic reactions. They studied platinum particles dispersed in carbon for the Oxygen reduction reaction (ORR) and removed the ligand surrounding them using different techniques such as thermal treatment (5 h at 185 °C), chemical washing (in acetic acid at 75 °C for 10 h, addition of ethanol and centrifugation), and UV-Ozone (UV irradiation for 30 min). These various techniques increased the specific surface area of the particles and their specific activity (Figure 13). They obtained a more than 3-fold increase between the untreated sample and the sample on which they removed the surfactant thanks to a thermal treatment. On iridium particles the same trend has been observed for the OER[56] in acidic media. The surfactant was partially removed from the surface of the particles and an increase in the activity was observed. Consequently, the ligand removal from the particles surface is an important parameter to consider when evaluating the activity of a catalyst whenever the catalyst synthesis involves surfactants.

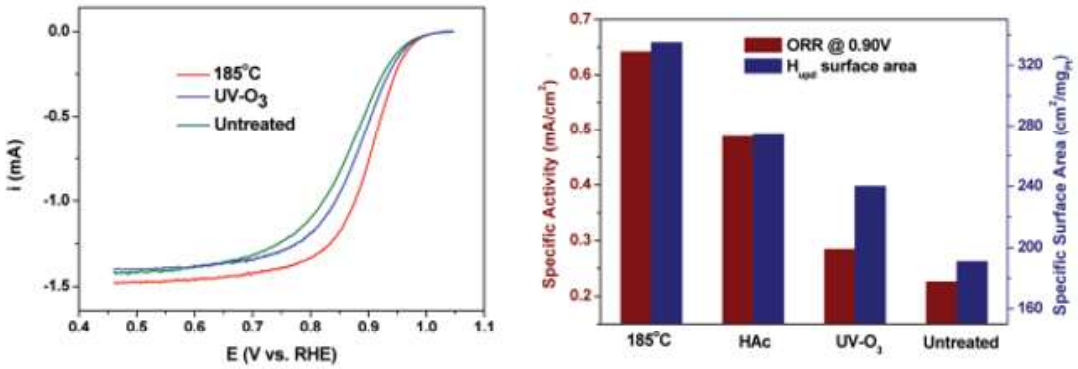

Figure 13: Rotating disc voltammograms of Pt/C drop-cast on a GC electrode (loading 20 µg.cm^{-2} $_{disk}$) in 0.1 M perchloric acid O_2-saturated electrolyte at 20 °C acquired at the scan rate 20 mVs^{-1} and rotation speed 1600 rpm. The specific ORR activity was determined at 0.90 V. This figure illustrates the impact of ligand removal on platinum particles taken from[55]

- ***Carbon and loading effect on the determination of the activity***:

The presence of carbon is also an important parameter to consider when evaluating the activity as for example, Kéranguéven *et al* measured the OER activity of a Co_3O_4 catalyst and obtained an activity that was highly increased in the presence of pyrolytic carbon of the Sibunit family (green) compared to a carbon-free cobalt spinel (black)[25].

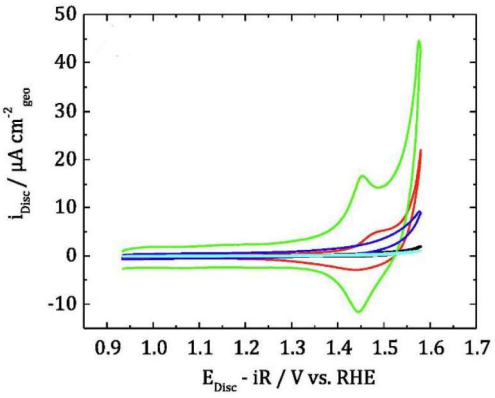

Figure 14: RRDE voltammograms of Co_3O_4 (black), 16Co_3O_4ISACSibunit152 (green), 16Co_3O_4ISACBDD (red), Sibunit152 (blue) and BDD (cyan) at 1600 rpm and 10 mV s^{-1} in N_2 saturated 1 mol L^{-1} NaOH. The loadings are 15 µg cm^{-2} for Co_3O_4AC, 93.7 µg cm^{-2} (15 µg cm^{-2} oxide loading) for 16Co_3O_4ISACSibunit152 and 16Co_3O_4ISACBDD and 91 µg cm^{-2} for pristine BDD and Sibunit152. This graph has been taken from ref [25].

Consequently, the presence of carbon enhances the activity by improving electrical connectivity of the catalyst particles and increasing the overall electrical conductivity to the catalyst (and thus increasing the extent of the catalyst utilization). However, its presence is also an issue as carbon does oxidize within the potential range of the OER, so it is useful to determine the OER activity of a material but its quick degradation under OER potential highlights the need for the development of carbon-free catalysts.

Another factor that could influence the activity of a catalyst is its loading. Indeed, if too important loadings of non-conductive or poorly conductive catalysts are deposited on the electrode then not all of the catalyst particles will be involved in the reaction, on that matter, the use of lower loadings can then be an option. Haase *et al.*[57] indeed found especially high activity values of their $CoO_x(OH)_y$ catalysts (5000 to 14 000 A/g_{cobalt}). These values were obtained for low loadings compared to the literature (0.25 to 2 µg/cm² in their study instead of conventionally used 100-300 µg/cm²).

Considering all the above-mentioned parameters that can influence the electrochemical activity of a catalyst, a non-exhaustive list of some catalyst's OER activities per unit mass at 1.65 V *vs* RHE and Tafel slopes from the literature is presented in Table 1. The loading, the electrolyte concentration and the presence of carbon (and if so which type) has been indicated. This table only focuses on the activity per unit mass as the catalyst loading on the electrode is often given but only a few publications are measuring the actual surface area (ECSA or BET) of the catalysts and consequently even if their results are comparable within the same paper, they cannot always be compared to the specific activity documented in other publications.

Table 1: OER activities at 1.65V vs RHE per unit mass and Tafel slopes of various TMO catalysts. Measurements were performed at room temperature.

Catalyst	Mass activity (A/g)	Tafel slope (mV/decade)	Catalyst loading (μg/cm²)	Type of carbon (if any)	Electrolyte and its concentration	Reference
$Co(OH)_2$	125*	59	204	Graphene	0.1 M KOH	[58]
CoFe layered double hydroxide	185*	43				
$CoFe_2O_4$ NFs	16	82	429	No carbon	0.1 M KOH	[59]
$CoFe_2O_4$ NPs	2	223				
$CuFe_2O_4$ NFs	0.3	93				
Fe_2O_3 NFs	0.2	148				
$NiFe_2O_4$ NFs	3.4	98				
$CoCr_2O_4$	23.4	177	204	No carbon	0.1 M KOH	[45]
Co_2TiO_4	2.1	83				
$MgCo_2O_4$	120	70				
Co_3O_4	51.6*	61				
Co_3O_4	9.6	83	210	No carbon	0.1 M KOH	[44]
$Co(OH)_2$	12	63				
Fe_3O_4	21	96	960	No carbon	1 M KOH	[46]
Co_3O_4	78	72				
$CoFe_2O_4$	182	58				
Co_3O_4@CoO@Co	56	92	127	No carbon	0.1 M KOH	[60]
Fe_3O_4@CoO	77A/g_{oxide} 154 A/g_{cobalt}*	89	300 (catalyst)	Vulcan XC-72	0.1 M KOH	[61]
Au@Co_3O_4	312A/g_{oxide} 500A/g_{cobalt}*	60	200 (catalyst+carbon) 64 (catalyst) 40 (Co_3O_4)	Vulcan XC-72	0.1 M KOH	[62]
Au@$CoFeO_x$	16 200A/g_{TM}*	58	56 (TM)	Vulcan XC-72	1 M KOH	[63]
Au@$NiCo_2S_4$	50 000 A/g_{oxide}*	44.5	200	Carbon black	1 M KOH	[64]
Fe_3O_4	15 A/g_{oxide}	105	100	No carbon	1 M KOH	[65]
$Co_{0.25}Fe_{2.75}O_4$	50 A/g_{oxide} 600 A/g_{cobalt}	80				
$Co_{0.5}Fe_{2.5}O_4$	90 A/g_{oxide} 540 A/g_{cobalt}	45				
$Co_{0.75}Fe_{2.25}O_4$	170 A/g_{oxide} 680 A/g_{cobalt}	46				
$CoFe_2O_4$	170 A/g_{oxide} 510 A/g_{cobalt}	45				
$Co_{1.25}Fe_{1.75}O_4$	220 A/g_{oxide} 528 A/g_{cobalt}	48				
$Co_{1.5}Fe_{1.5}O_4$	310 A/g_{oxide} 620 A/g_{cobalt}	46				
$Co_{1.75}Fe_{1.25}O_4$	350 A/g_{oxide} 600 A/g_{cobalt}	50				

Co_2FeO_4	450 A/g_{oxide} 675 A/g_{cobalt}	50				
$Co_{2.25}Fe_{0.75}O_4$	500 A/g_{oxide} 666 A/g_{cobalt}	52				
$Co_{2.5}Fe_{0.5}O_4$	430 A/g_{oxide} 516 A/g_{cobalt}	47				
$Co_{2.75}Fe_{0.25}O_4$	300 A/g_{oxide} 327 A/g_{cobalt}	56				
Co_3O_4	150 A/g_{oxide}	61				
Co_3O_4	123*A/g_{oxide}	61.2	300	No carbon	1 M NaOH	[25]
Co_3O_4	240*A/g_{oxide}	80	15	Sibunit		
Co_3O_4	152*A/g_{oxide}	65	15	BDD		
$CoO_x(OH)_y$ 9nm	5000* A/g_{cobalt}	37	2.98	No carbon	0.1 M KOH	[57]
$CoO_x(OH)_y$ 6nm	5000* A/g_{cobalt}	39	0.82			
$CoO_x(OH)_y$ 4nm	11 000* A/g_{cobalt}	43	0.82			
$CoO_x(OH)_y$ 1nm	14 000* A/g_{cobalt}	43	0.25			

*NFs: nanofibers. * Estimated by extrapolation to 1.65 V vs. RHE using the Tafel slope provided in the reference*

Various approaches have been proposed in order to enhance the OER activity of the catalysts, notably varying the composition, the particle size, the defect concentration (notably by introducing oxygen vacancies), or, recently, forming core-shell structures.[60,62–64,66] Indeed, good catalysts are often scarce and expensive materials (iridium, ruthenium, or to a lesser extent cobalt or nickel). Catalysis being primarily a surface phenomenon (even if the OER mechanism may involve lattice oxygen, the reaction occurs in the near-surface region), it is possible to limit the quantity of the active component by using core-shell structures with the catalytic component present only in the shell. This motivated studies of core-shell iridium and ruthenium nanostructures in view of an application for PEM electrolysis.[67,68] It was argued that Au substrates could enhance the OER activity of TMOs due to an electronic effect that favors the transformation of the TM in a 4+ oxidation state.[69,70] For example, very high OER activity was documented for Co_3O_4 and CoOOH films deposited on an Au(111) substrate.[43] Similarly, high activities were observed on core-shell NPs comprised of a gold core and a TMO shell in alkaline electrolytes, sometimes reaching 10 000 A/g_{TM} at 1.65 V vs. RHE. While they demonstrated outstanding OER activities[62–64], industrial utilization of such catalysts does not seem to be practical as gold is a scarce and expensive metal. Moreover, it should be noted that the activity reported for the gold core-shell NPs were documented for carbon-containing electrodes even though the utilization of conductive core-catalytic shell NPs could potentially allow avoiding carbon addition to the catalytic layers.

TMO catalysts developed for AEM electrolysis are usually cobalt and nickel based. In the meantime, global cobalt demand has recently experienced unprecedented growth so that it has been

recently classified as critical material by the European Union so the limitation is imperative for long term applications of cobalt-based catalysts.[71] Although the exact role of Fe is still debated, several publications have demonstrated that presence of Fe cations in TM (Co, Ni) oxide phases results in synergetic effects which enhance the OER[72,73]. Indeed, one of the hypotheses is that the iron can give electron to the surrounding atoms which will modify the filling of their orbitals and will facilitate their oxidation/reduction compared to the other metal cations. Suntivich et al. studied different perovskite properties for the OER and unraveled that a filling of the e_g orbital close to the unity was responsible for better activities towards the OER[74]. Dionigi *et al.*[75] concluded on NiFe and CoFe layered double hydroxide that the electronic structure of the iron sites was flexible and that their synergy with the nearest-neighbor M sites (M = metal cation) through forming O-bridged Fe-O-M reaction centers was stabilizing the OER intermediates. This synergy with the surrounding atoms explains lower overpotentials observed for iron-based materials. On spinel materials the same effect has been observed by Saddeler *et al.*[65] They studied the impact of the cobalt vs iron content in $Co_xFe_{3-x}O_4$ catalysts and evidenced that the proportion of iron in the structure played an important role in the catalytic activity. For example, Co_2FeO_4 showed a higher activity than pure cobalt spinel (Co_3O_4). The presence of iron consequently helps in the enhancement of the OER activity and among the spinel family, one type of material that is interesting to study because it contains iron is the ferrites.

The general formula of ferrites is MFe_2O_4 (with M a transition metal such as cobalt, nickel, copper…) they are usually inverse spinels. This is a family that has been extensively studied in the literature. However, the activity results obtained in the literature show significant scatter: for example, Li *et al.* evidenced that $CoFe_2O_4$ ferrite under the form of nanofibers (NFs) is the most active among $CoFe_2O_4$, $NiFe_2O_4$ and $CuFe_2O_4$[59] while Silva *et al.*[76] concluded that $CuFe_2O_4$ is the most active of all the above-mentioned ferrites.

As it can be seen in Table 1, the activity values reported on the literature significantly differ from one publication to another. This can be explained by (i) the fact that the currents were not always corrected from the ohmic losses, (ii) by the insufficient conductivity of the catalyst resulting in an incomplete utilization of the active sites on the material, (iii) some measurements performed in the presence, the other – in the absence of carbon, (iv) utilization of different types of electrolytes and pH, the presence of structural defects, etc.... The observed differences highlight the need for the development of a systematic method to investigate catalytic properties and activities of electrocatalysts.

Finally, the synthesis of carbon-free, noble metal-free and gold-free catalysts is an important challenge for the development of cost-effective OER catalysts. Iron oxide Fe_3O_4 seems to be a good

candidate to replace gold in the core of the NPs as it might help to enhance the OER activity due to a synergetic effect between iron and its surrounding atoms.

4) OER catalysts under operating conditions

In this part, the techniques used to study *operando* and *in situ* the transformations occurring during the OER in this work will first be presented. Then a non-exhaustive presentation of the observations made in the literature under operating conditions on cobalt and iron-based catalysts will be detailed.

a) XPS and NEXAFS to study the catalysts transformations

Among the many techniques (TEM, FT-IR, XRD, Raman spectroscopy…) used to study operando the transformations of the catalysts during the OER, XPS and NEXAFS are two techniques used in this work to characterize and study operando the OER. Their principles will be detailed in this part.

X-ray photoelectron spectroscopy (XPS) is a well-known technique that allows to determine the composition of the near-surface layer of a material (from 1 to 10 nm depending on the kinetic energy of photoelectrons). This technique consists of the collection and analysis of photoelectrons emitted from the sample when excited by photons. It provides both qualitative and quantitative information on the oxidation state of the elements, the presence of different type of species or the formation of alloys[77].

The sample is irradiated by photons presenting an energy $h\nu$ and interacts with the electrons present in the atoms of the sample. Consequently, photoelectrons are emitted. They have a well-defined kinetic energy (KE) that depends on how strongly they were linked to the atom: the binding energy (BE) and on the work function of the spectrometer φ (typically about 4.5eV). The equation for the calculation of these energies is the following[78]:

$$KE = h\nu - BE - \varphi$$

Equation 4: Relation between binding and kinetic energy in XPS.

With the XPS technique, when acquired under the appropriate conditions one can get a complete elemental analysis of the surface and near-surface region. Moreover, the technique is also quantitative: the intensity of a given peak is proportional to the fraction of the atom from which it derives.

Additionally, some information about the chemical and oxidation states can be obtained thanks to the observation of a shift in the BE of the element[78]. It is possible to perform XPS measurements in the presence of a gas (NAP XPS) such as H_2O, O_2, H_2 etc… to observe how the material will evolve under operando conditions.

If in XPS the electrons are fully ejected from the atom, some other techniques exploiting the fact that the electron is excited to another energy level also exist: this is the case for all the X-ray absorption (XAS) techniques. They measure the X-ray absorption coefficient of a sample as a function of the X-ray photon energy below and above the absorption edge of a certain element. According to the energy range of the source, XAS can be divided into soft (1 keV), tender (1-5 keV) and hard (5 keV) X-ray[79]. The spectrum is usually divided in two different regions. The Near Edge Absorption Fine Structure: NEXAFS (or XANES) from a few eV below the absorption edge to approximately 50 eV above the edge, and the extended X-ray absorption fine-structure (EXAFS) from approximately 50 eV edge to as much as 1000 eV[80] above the edge. The comparison of these techniques is given in Figure 15 and Figure 16.

NEXAFS and particularly the soft X-ray absorption is surface-sensitive. It exhibits strong and distinctive features in the energy region just below and up to about 50 eV above the absorption edge[81]. A NEXAFS spectrum reflects the dependence of the photo absorption cross section on the photon energy for values from just below the ionization threshold up to around 50 eV above it. It can provide information about the local structure; oxidation states of the atoms and their environment, notably it is possible to determine if the atom is present in an octahedral (Oh) or in a tetrahedral (Td) site.

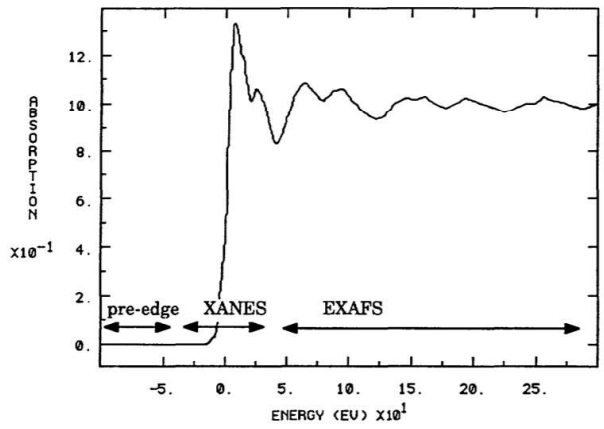

Figure 15: Description of the XANES (or NEXAFS) and EXAFS regions taken from.[82]

For the XAS techniques, the core electrons are excited to an unoccupied energy level above the Fermi level. When this happens, holes are being formed in the core level of the atom and this generates the emission of photons that can be detected in the fluorescence yield (FY)[83], secondary electrons are

also emitted as a consequence of these holes being created: they are measured in the total electron yield (TEY). If among these electrons only the Auger electrons are selected, we obtain the Auger electron yield (AEY). In the FY mode the mean free path of the photon is of the same order of magnitude as the incident photon, the technique is then quite sensitive to the "bulk" and less to the surface. Meanwhile the TEY and AEY techniques are more surface sensitive as the photons are less attenuated than the electrons. The AEY mode is even more surface sensitive than the TEY mode as only the elastically scattered Auger electrons are collected with this technique but the signal is noisier than in the TEY mode. The depth of the analysis depends on the material, but in average for AEY the estimated depth is about 2-3 nm when for the TEY mode, it is rather between 4 and 10 nm[84]. In Figure 16 a summary of all the above-mentioned techniques is shown.

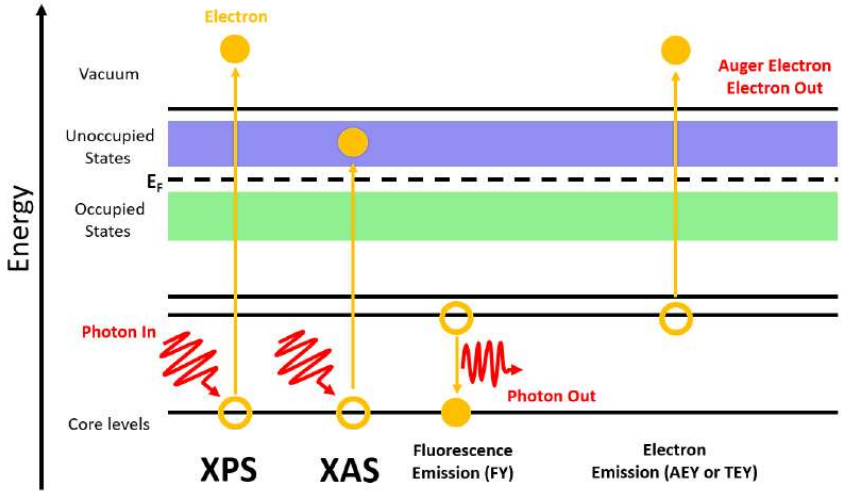

Figure 16: Scheme of electron and photon emissions occurring during XPS and XAS taken from ref[85].

The XPS and the XAS are the two techniques that will be used in this work to get a better understanding of the catalyst transformations during the OER. In the next parts, a state of the art of the understanding of the transformations occurring on cobalt based catalysts during the OER will be developed.

b) In situ and operando measurements to understand the OER mechanism

The complex processes taking place during the OER and the need for a deeper understanding of the reaction mechanism have motivated the use of powerful tools such as Raman spectroscopy, Infra-red (IR) spectroscopy, near ambient pressure X-ray photoelectron (NAP-XPS), Near-edge X-ray absorption fine structure spectroscopies (NEXAFS), transmission electron microscopy (TEM) or X-ray diffraction (XRD) to study this reaction. In the following paragraphs, the main conclusions on the transformations observed for various cobalt-based catalyst during the OER will be developed.

Cobalt spinel Co_3O_4

First, a material that was extensively studied and that generated lots of publications is cobalt spinel: Co_3O_4 (Co (II) and Co(III)). For this catalyst, the consensus seems to be that Co_3O_4 undergoes a surface transformation in CoOOH which reversibility and role is debated in the literature.

First, Yeo *et al.*[70] studied the OER on a Co_3O_4 catalyst by Raman spectroscopy and observed the attenuation of the vibrational peak characteristic of Co_3O_4 as well as the growth of a peak attributed to CoOOH formation in the potential range of the OER. This formation was correlated to the OER activity. Using NAP-XPS, Favaro *et al.*[86] also confirmed this.

Thanks to operando TEM experiments, Ortiz Pena *et al.*[41] studied Co_3O_4 NPs in the OER potential range and observed an irreversible amorphization on the NPs surface that they attributed to the transformation of spinel NPs in a CoO_xH_y phase. Bergmann *et al.*[87] studied the structure and the oxidation state of nanocrystalline Co_3O_4 thin films during the OER using *in situ* X-ray diffraction and 'quasi-*in situ*' absorption spectroscopy (samples were freeze-quenched under potential control) and on the cobalt K edge it was observed (Figure 17 A) that in the potential interval of the OER the Co(II) ions were oxidized into octahedrally (Oh) coordinated, di-μ-O(H)-bridged Co(III/IV) species. This oxidation resulted in a reversible formation of a sub-nanometer thick amorphous $CoO_x(OH)_y$ shell. Such reversibility was also observed by Reikovski *et al.*[43], they applied operando surface X-ray diffraction to study structurally well-defined epitaxial cobalt oxide thin Co_3O_4(111) film electrodeposited on Au(111). However, they observed fast and fully reversible Co_3O_4(111)/CoOOH(001) transformation at potentials 300 mV negative of the 'onset' of the OER, and thus concluded that the observed structural transformation was not OER-driven. By comparing the OER activity of Co_3O_4(111) and CoOOH(001) epitaxial crystalline films the authors argued against di-μ-oxo bridged Co cations being responsible for the OER activity of Co oxides.

Wiegmann *et al.* [42] also investigated the formation of this layer and its thickness. They found out that it could be several nanometers thick. They also observed that the thicker the catalytic layer was becoming, the higher the activity was, implying the implication of more than a topmost layer of the catalyst in the OER reaction (Figure 17 B). In another publication, Bergmann *et al.*[88] proposed the existence of 2 types of sites for the OER mechanism: a 'fast' one and a 'slow' one where the cobalt is bonded differently with the adjacent oxygen atom (Figure 17 C). The cobalt atoms close to the surface are considered more reducible and consequently more active for the OER. In this article they claim that the OER is intimately coupled to the formal Co^{3+}/Co^{4+} redox transition leading to protonatable μ_2-O sites as well as oxidized $Co^{+3+\delta}$ ions bound to terminal $O^{-(2-\delta)}$ ligands.

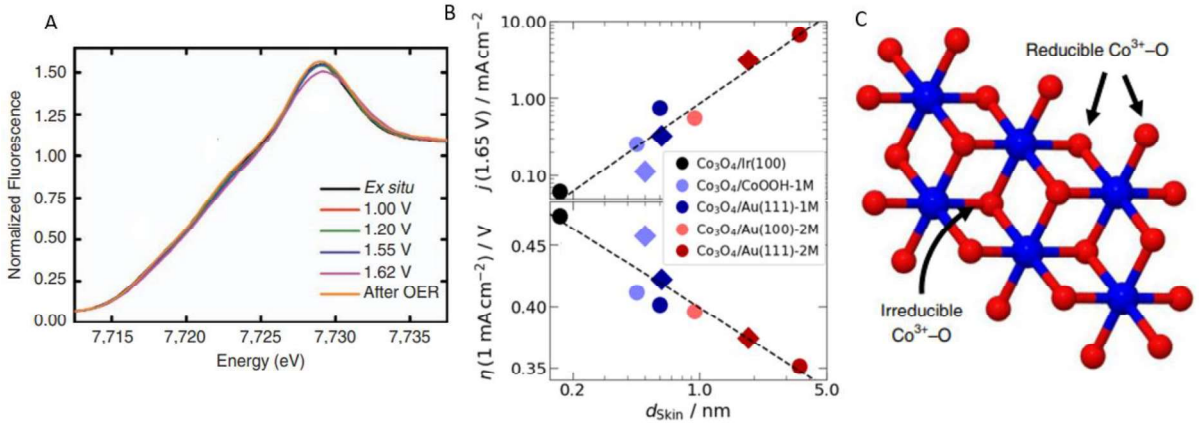

Figure 17: A) Co-K edge measured for different potentials on a freeze quenched Co_3O_4 thin film taken from[87]. B) Catalytic activity at 1.65 V vs RHE and overpotential needed to reach 1 mA.cm$^{-2}_{ECSA}$ as a function of the thickness of the CoO_xOH_y layer B) formed at the surface of a Co_3O_4 thin film catalyst, taken from.[42] C) Structural model of a layered $CoO_x(OH)_y$ and the different sites on which the OER can occur, taken from.[88]

<u>CoO_x H_y particles</u>:

The OER has also been studied operando on materials such as $Co(OH)_2$ particles by Mefford *et al.*[89]. CVs presented in Figure 18 showed two pairs of anodic/cathodic peaks at 1.1 V and at 1.5 V. On Co_3O_4 similar peaks were observed around these potentials[25,43].

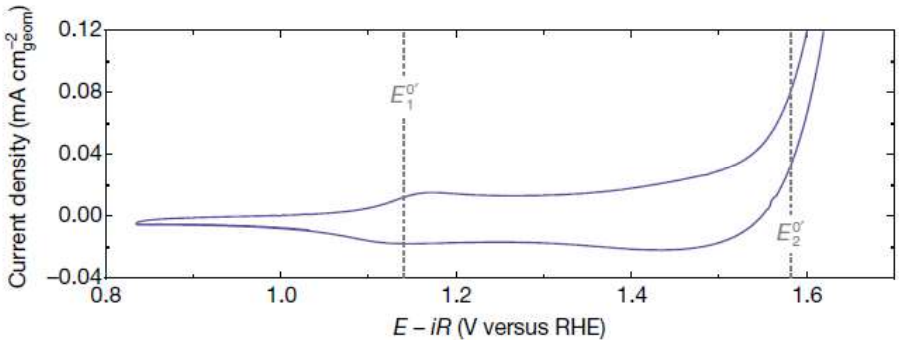

Figure 18: Cyclic voltammetry curves obtained on $Co(OH)_2$ in 0.1 M KOH with 10 mV/s scan rate, taken from.[89]

This CV curve was then correlated with Soft X-ray scanning transmission X-ray microscopy (STXM) spectra measurements they performed on the cobalt under an applied potential, as shown in Figure 19. These curves evidenced the oxidation of cobalt from Co (II) to Co (III) in the OER potential interval.

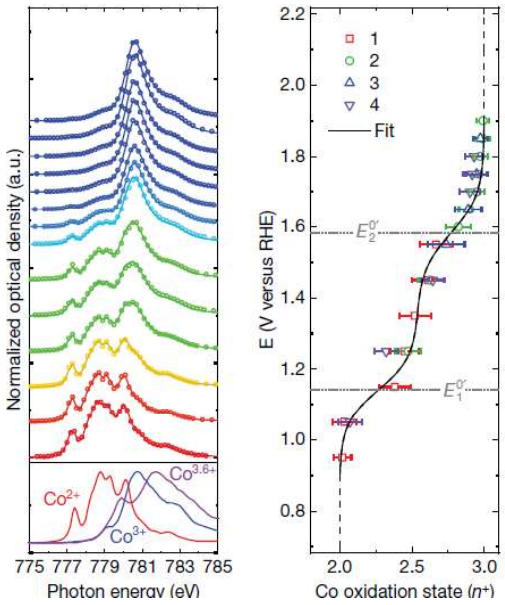

Figure 19:Voltage-dependent particle-averaged Co L_3-edge STXM-XAS spectra. Reference spectra are included for the as synthesized β-Co(OH)2 (Co^{2+}), $LiCoO_2$ (Co^{3+}) and $Sr_6Co_5O_{15}$ ($Co^{3.6+}$) taken from.[89]

Under the OER conditions, the cobalt is first exhibiting a $Co^{2.5+}$ oxidation state above 1.1 V and then above 1.5 V it fully transforms into Co (III).

Enman *et al.*[90] on the other hand studied CoO_xH_y thanks to NEXAFS K-edge spectra of cobalt and demonstrated that Co(III) is, on average, further oxidized during the OER. Consequently, they proposed Co (IV) as the OER intermediate.

<u>$CoO_x(OH)_y$ catalysts:</u>

Haase *et al.*[57] recently studied the impact of the particle size of a $CoO_x(OH)_y$ catalyst on the OER activity (Figure 20 A) and transformations during the OER (Figure 20 B and C). They concluded that small NPs (1-2 nm) were presenting higher specific activities than larger ones (5-9 nm), hinting at a size dependence of the OER. It is worth noting that their results were obtained for low loadings compared to what is usually seen in the literature and that their catalyst was not mixed with carbon.

While confirming the increase of the average cobalt oxidation state from 2+ to 3+δ, the authors arrived to the conclusion that during the OER an electron 'hole' resides on oxygen ions rather than on Co cations leading to the formation of electron-deficient 'oxyl' rather than Co (IV) species (similar to what has been previously proposed for IrOx-catalyzed OER[91,92].

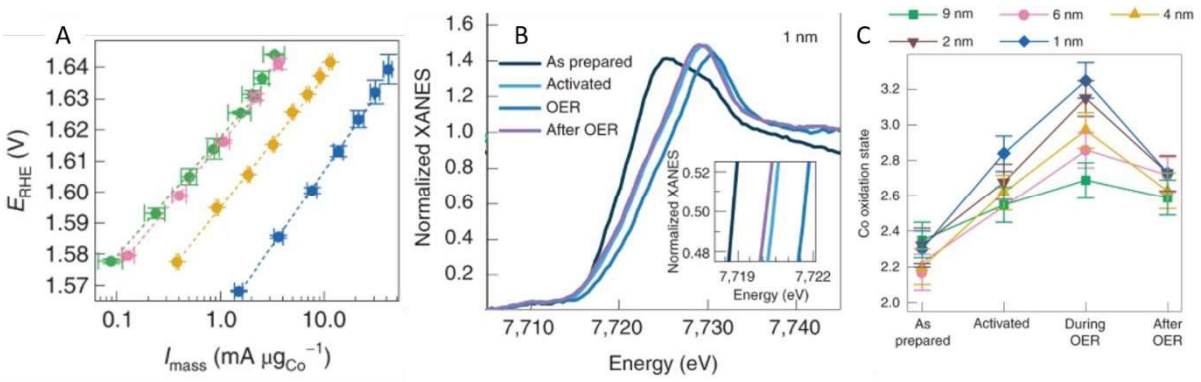

Figure 20: A) Tafel slopes for the OER on $CoO_x(OH)_y$ NPs. B) NEXAFS Co-K edge of the 1 nm diameter NPs. C) Cobalt average oxidation state before, during and after the OER. The diameters of the NPs are 9 nm (green), 6 nm (pink), 4 nm (yellow), 2 nm (brown) and 1 nm (blue).

Cobalt iron catalysts:

As it was shown that iron participated in the enhancement of the OER activity, its role was also studied operando thanks to XAS techniques on various CoFe oxides[93]. Smith *et al.*[94] remarked that the presence of iron yielded an anodic shift and a decreased Tafel slope of the catalyst up to a composition-independent voltage : $E_{transition}$=1.53V associated to the emergence of a Co (III/IV) oxidation process (Figure 21 A and B). They proposed a branching catalytic mechanism (Figure 21 C) in which the iron activates a disproportionation of the di-µ-oxo bridged Co(III)-Co(II) intermediates. Thanks to the oxidation of di-µ-oxo bridged Fe–Co sites, a secondary reaction site is then activated at voltages above $E_{transition}$.

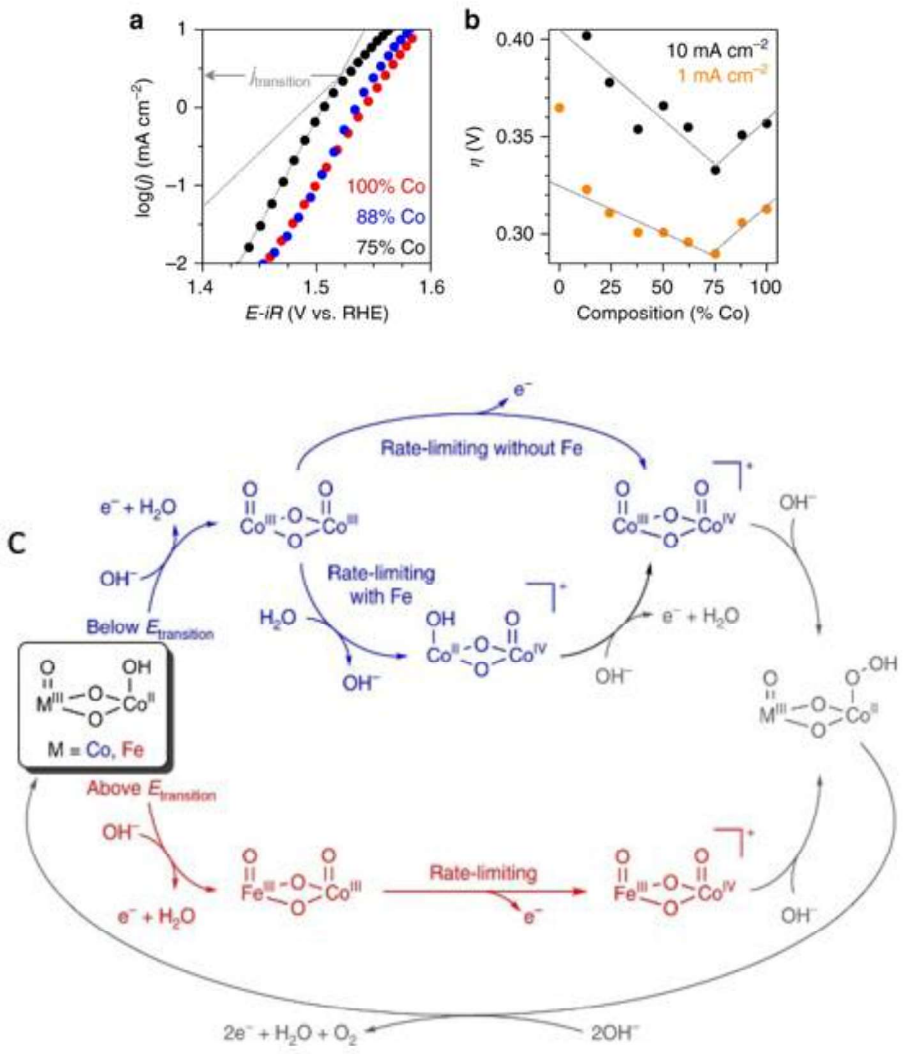

Figure 21: A) Tafel plots for the OER measured on the thin $CoFeO_x$ films in 1 M KOH. The change in the slope is indicated by the thin black lines. B) Overall electrocatalytic OER performance as a function of the film composition. C) Mechanism proposed by Smith et al.[94] for the OER on an $CoFeO_x$ catalyst.

In any case, in this study the cobalt is reaching a Co (IV) oxidation state in this mechanism and the iron stays in a Fe (III) oxidation state. However, Fe oxidation to higher oxidation degrees than Fe (III) was suggested by Enman *et al.*[90], on $Co(Fe)O_xH_y$ catalysts. They confirmed that iron is playing a key role in the OER mechanism and demonstrated thanks to the study of the Fe K- edge and Co K-edge spectra that on a Co/Fe catalyst Fe (III) was further oxidized while the cobalt was not (Figure 22). They are suggesting two different pathways for the reaction to occur: (1) The OER mechanism proceeds through the cobalt site but does not involve Co (IV). (2) The reaction mechanism involves Fe (>III). The authors privilege the second interpretation.

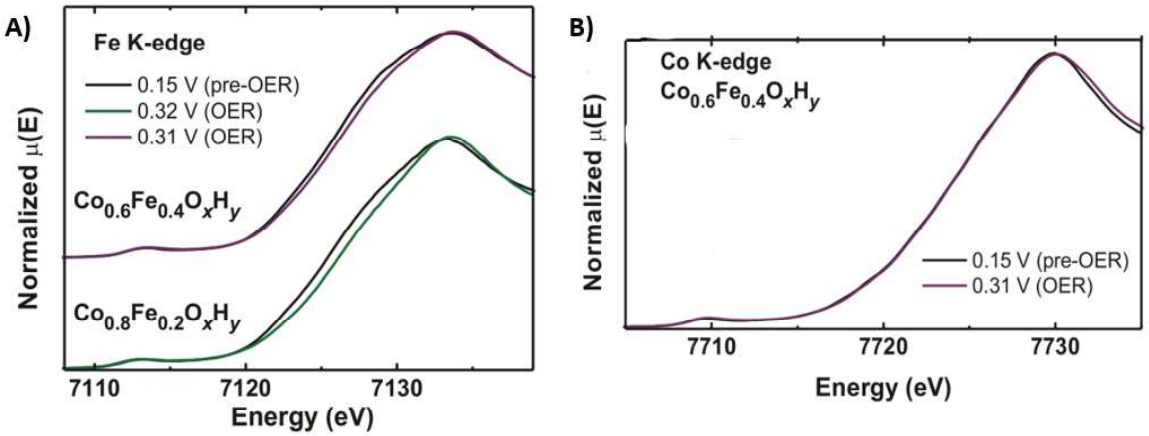

Figure 22: Fe K-edge (A) and Co K-edge (B) evolution during the OER taken from.[90]

Calvillo *et al.*[95] also studied the Fe K-edge and the Co K-edge to scrutinize the chemical and structure change of a Co-Fe spinel powder. They demonstrated that the samples suffered irreversible oxidation under the OER conditions leading to the formation of a layer consisting of Co_3O_4, CoOOH and Fe_2O_3. They also stated that it was the Co (II) cations in tetrahedral (Td) sites which were experiencing these changes. Indeed, $CoFe_2O_4$ in which the cobalt is in the octahedral sites was stable under the working conditions, presenting only a slight oxidation of the surface, while Co_2FeO_4 which presents more cobalt in the Td sites suffered important modifications (Figure 23).

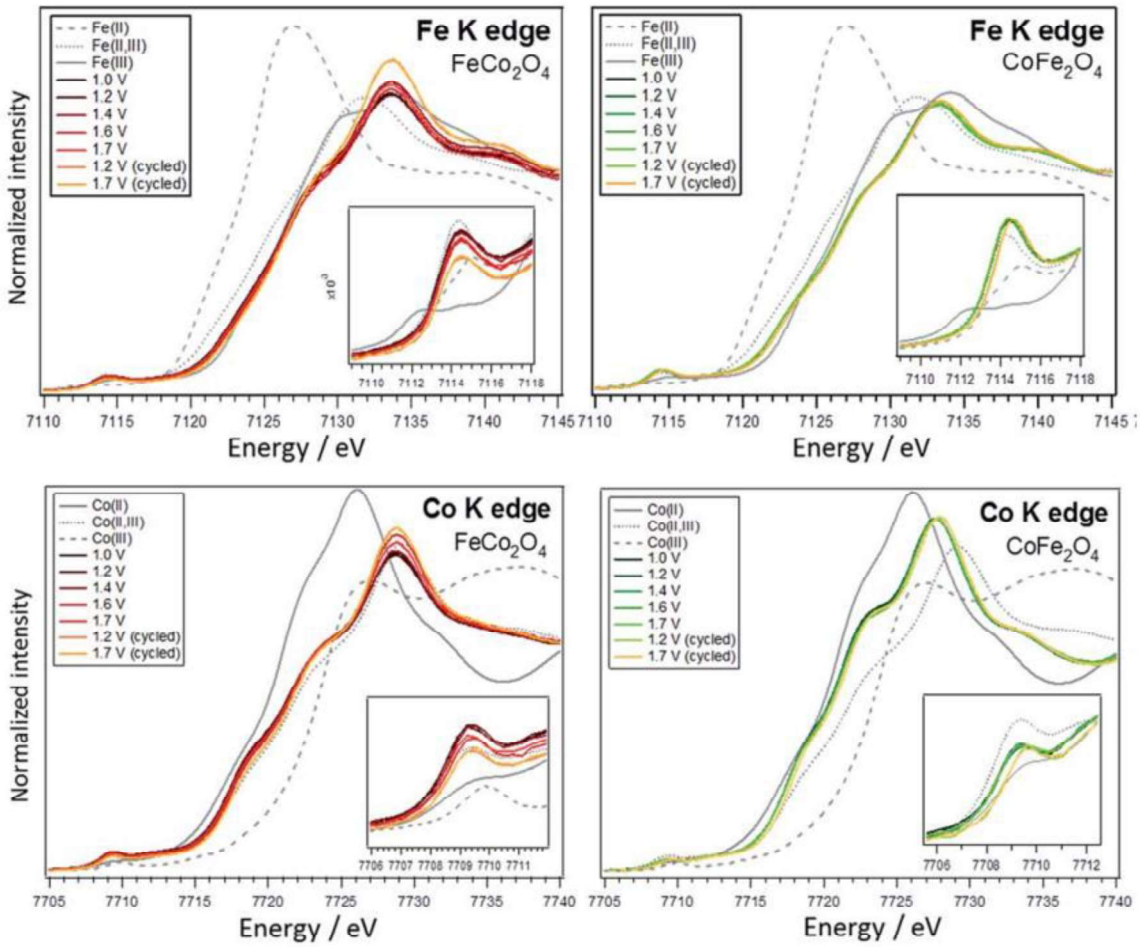

Figure 23: Changes of the Fe K-edge and Co K-edge of cobalt ferrite $CoFe_2O_4$ and iron cobaltite Co_2FeO_4 taken from.[95]

However, they also found that the durability of the material was also depending on the species formed during the OER as iron cobaltite showed the lowest performance loss while in the case of cobalt ferrite a greater loss of activity was observed. This can be attributed to the preferential formation of Co_3O_4 and CoOOH (stable and active) during the OER in the case of Co_2FeO_4 and to the formation of Fe_2O_3 (less active) in the case of cobalt ferrites.

Finally, Saddeler *et al.*[65] recently performed *operando* studies of the behavior of cobalt iron spinel with various iron *vs.* cobalt proportions. Thanks to the changes observed on the Fe K-edge and the Co K-edge (Figure 24 A) for the different materials they synthesized, they were able to conclude that the average Co oxidation state increases for all samples while the average oxidation state of Fe is close to (III) for all samples and doesn't show significant changes, confirming the cobalt is here the active center. They also observed a partial reversibility of this oxidation process. They showed that cobalt reaches Co (III) during the OER for cobalt-rich spinels and shows smaller oxidation state for lower cobalt contents (Figure 24 B).

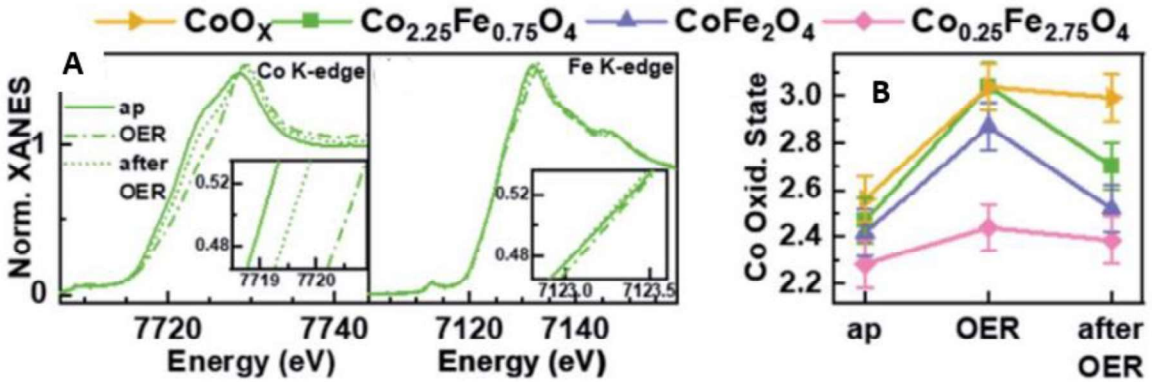

Figure 24: A) Co K-edge and Fe K-edge changes under OER potential. B) Changes in the cobalt oxidation state during the OER for various spinel compositions. Taken from ref[65]. ap= as prepared.

To sum up, the selected examples mentioned above showed that *operando* characterizations helped in understanding the chemical state, phase and oxidation state of the metal cations during the OER. Cobalt-based catalysts have been studied operando for the OER. X-ray absorption techniques in particular can provide valuable insights into the environment and oxidation state of the cations. They exhibited some phase transformations (reversible or not) in the OER potential range. These transformations are accompanied by a change in the oxidation state of the metal cations involved in the reaction. For catalysts containing only cobalt, it seems that the reaction mechanism involves a Co (III) or a Co (IV) intermediate and that the position of the cobalt (Td or octahedral (Oh) sites) has an influence on the transformation occurring. However, for cobalt/iron catalysts, a synergetic effect is suggested between the cobalt and the iron. Various hypotheses were put forward to explain the role of Fe in the OER. One suggests that a Fe-Co ensemble is the active site: iron activates the reaction and helps the cobalt reaching a Co (IV) oxidation state, another is that the iron reaches a Fe (IV) oxidation state and acts as the active site itself. The design of new model catalyst on which the active sites are well defined is then essential for further understanding of the OER mechanism and active sites on cobalt-iron based catalysts.

5) *Nanoparticles: a model catalyst for the OER*

Determining the activity of a catalyst is not as straightforward as it seems: the real electrochemical surface area (ECSA) of the catalysts is often not known, the catalyst can present some composition variations, different surface states (presence of defects, different atomic densities on different crystallographic planes, etc) that will play an important role in the OER activity. To establish a link between structural and electrochemical properties on the one hand and electrocatalytic activity on the other, identify the active sites and compare the catalytic activities, 'ideal' or model systems are needed.

One of the pertinent ways to obtain a model catalyst with a controlled composition, surface state, level of defects, etc… is to use thin films.[42,43] Well-defined thin films deposited on a crystalline substrate present an excellent model system. However, for AEM electrolysis applications the catalyst needs to be deposited on a membrane. As stated before, many of the catalysts studied for the OER are in the form of crystalline NPs, the issue with this type of catalyst is generally that there can be an important size variation, and composition variation. However, some synthesis methods allow for reproducible synthesis of NPs presenting a narrow size distribution. These synthesis methods will be presented in the next parts.

a) *Synthesis and properties of the nanoparticles*

Catalysis being a surface phenomenon, nano-objects which present a high specific surface are usually considered as good materials for the OER. Considering the high tunability in terms of shape, size, and composition of the nanoparticles, they are considered as good candidates for the OER. Different synthesis methods have been developed to synthesize NPs, namely coprecipitation, microemulsion, polyol, hydrothermal and thermal decomposition[96–99]. Table 2 summarizes these various methods and gives their pros and cons.

Table 2: Summary of the different synthesis conditions for nanoparticles taken from.[100]

Synthesis method	Synthesis conditions	Temperature (°C)	Reaction time	Solvent	Size (nm)	Size distribution	Morphology control	Yield
Coprecipitation	Very simple	20-90	Very short	aqueous	<20	Not well controlled	Medium	High
Microemulsion	Difficult	20-50	Short	Aqueous/ organic	<50	Narrow	Good	Low
Polyol	Very simple	>180	Short	Organic	<10	Narrow	Very good	medium
Hydrothermal	Simple	>200	Hours	Aqueous/ ethanol	<1000	Narrow	Very good	medium
Thermal decomposition	Difficult	200-350	Hours	organic	<40	Highly controlled	Very good	high

The coprecipitation synthesis method is one of the most commonly used one where the NPs are synthesized by the addition of a base in an acidic solution of dissolved metal salts that precipitate when the pH of the media changes. This method generates a large amount of NPs in an aqueous media but the size distribution and the extent of aggregation of the NPs is not well controlled. In order to understand better the OER reaction happening at the interface of the electrolyte and the NPs, it is important to have a good control of their morphology, size and composition to obtain a well-defined catalyst that can be used as a model towards a better understanding of the mechanism. For about 20 years the synthesis of NPs via thermal decomposition has been developed and used for the synthesis of NPs as it allows an accurate control of the size distribution and morphology and presents a high synthesis yield despite being realized in organic solvents at high temperatures. This method principles will be described in the next part.

b) The thermal decomposition method

Thermal decomposition is a synthesis method that consists in the decomposition of an organic precursor at high temperature in a solvent that has a high boiling point (typically around 300°C). This synthesis is following the Lamer theory for nucleation and growth[101] presented in Figure 25 . When heated at a high temperature in the presence of a surfactant, the metal precursor decomposes and forms monomers. Typically, the precursors used to perform thermal decomposition synthesis are metal acetylacetonates, oleates or stearates[102–104]. When the precursors decompose, the monomer's concentration in the reaction media during the heating keeps on increasing up to the moment when it reaches the critical supersaturation concentration (S_C). At this point the energy of the system is high

enough to initiate the nucleation step: monomers aggregate in nuclei and the concentration in monomers consequently drops. This is a fundamental step as it will dictate the size of the NPs. Typically, the nucleation has been observed about 250°C for iron oleates and stearates[102,105]. When the concentration reaches a level below S_C then the nucleation step stops and a second step begins: the growth. This step simply consists in the addition of the remaining monomers on the surface of crystal seeds. The energy needed for the growth step being lower than the one for the nucleation step, the growth is easier to perform. The separation of these two steps is the key for the obtention of monodisperse NPs with a controlled size. Another element that plays a key role in the synthesis is the surfactant as it will stabilize the NPs and prevent their aggregation.

If all the nuclei are created at the same time they will undergo the growth step at a similar rate which will allow the formation of NPs homogeneous in size and in shape[106,107]. However, if the reaction continues for a too long time, another type of reaction can occur: the Oswald ripening phenomena when small NPs are being solubilized again and the monomers that constituted them will be used to grow bigger NPs.

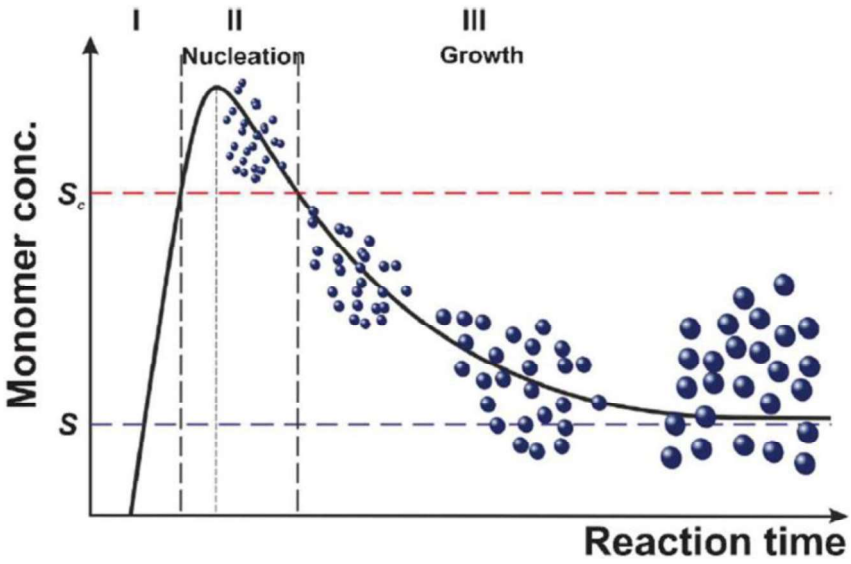

Figure 25: Illustration of the LaMer nucleation and growth steps taken from.[106]

By changing the temperature ramp, the solvent or the precursor it is possible to modify the size, the size distribution, the composition and the shape of NPs. The influence of these parameters will be detailed in the next paragraphs.

- ***Size control***

Van Embden *et al.*[107] have proven that temperature is a key parameter in the nucleation step as the monomer generation rate increases exponentially with the temperature. In the literature, it has been reported that a high temperature will generally produce larger NPs[102,108]. Consequently, the temperature which dependents of the solvent is key point to control the NP size and the synthesis temperature. Also, the nature of the solvent can change the NPs properties: if the precursor is stabilized by the solvent (because of its polarity for example) then its decomposition temperature will be higher and smaller NPs will be produced compared to a non-stabilizing solvent. Also, a parameter that likely plays an even more important role in the NPs size is the heating rate: if it is slow (1°C/min) then the monomer generation rate will also be slow, generating few nuclei and larger NPs compared to a quick temperature ramp that would generate more nuclei but smaller NPs.

The precursor stability and its coordination mode to the metal will change its decomposition parameter. A precursor with a higher decomposition temperature will likely generate smaller NPs.

Finally, the duration of the growth step[107,109] will also have an impact on the NPs size. Long reaction time increases the monomer concentration (anticipating that the precursor was not fully decomposed after the nucleation step and that its decomposition will continue during the growth step) and generates bigger NPs. Furthermore, Ostwald ripening phenomena can occur for longer reaction times. Small NPs dissolve before recrystallization onto the surface of the largest NPs.

- ***Size distribution control***

Wide size distribution can be due to multiple nucleation steps or to its duration (long nucleation usually leads to a wider size distribution). The temperature in the reaction media also has to be homogeneous in order to avoid local nucleation and growth, generating a large size distribution. Figure 26 represents the influence of the nucleation duration on the NPs growth.

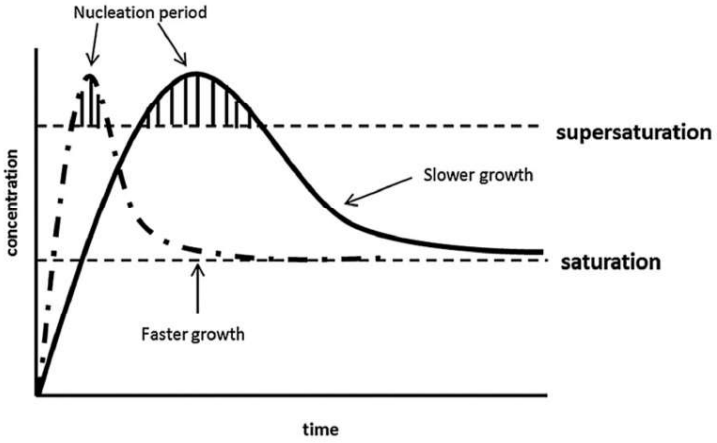

Figure 26: Representation of the nucleation-growth process depending on the kinetics taken from.[110]

- ***Shape control:***

The synthesis of various NPs shapes can be achieved (spheres, cubes, octahedra for example)[102,111,112]. This shape variation and anisotropy is highly interesting for magnetism applications and can also be interesting for electrochemical applications as the activity depends on the exposed crystallographic plane (according to the exposed plane, the number of active sites and their coordination may change). In this work, the spherical shape will be studied as this is the shape that is easier to obtain with a reproducible size and size control.

Tuning all these parameters, it is then possible to obtain NPs with a narrow size distribution and a controlled size and shape. However, the development of core-shell and onion like structures using different precursors to obtain mixed NPs using the thermal decomposition method poses some new challenges that will be detailed un the next part.

c) Core-shell nanoparticles as a catalyst for the electrochemical applications

For electrochemical applications, several publications report on the activity of core-shell NPs for the OER[60–64,67,68,113] in acidic or in alkaline media. Core-shell NPs are of particular interest due to the low amount of catalytically active material needed to synthesize these structures: the core can be composed of an earth-abundant inexpensive material such as iron oxide while the quantity of the catalytically active material (such as cobalt or nickel oxides) localized in the shell is decreased. Additionally, if the core and the shell materials are chosen carefully, the core can, in some cases, participate in the catalytic activity thanks to electronic exchanges between the core and the shell. This has been observed for gold-core and TM shell catalyst[62–64] for which important activities have been

observed (Table 1). An 'ideal' catalyst would then be composed of an iron oxide-based core and a cobalt or nickel oxide shell.

With the thermal decomposition method it is possible to perform successively several thermal decomposition steps in order to obtain a core-shell structure or even an onion-like structure[66,114–116]. This second step is more difficult to realize as it will involve two different precursors: if the precursors used during the synthesis of the shell display the same decomposition temperature, their monomers will deposit on the core in order to grow a shell with homogeneous and stoichiometric chemical composition [107]. It is then possible to tune the shell composition by modifying the ratio of the precursors. However, the elaboration of mixed ferrites MFe_2O_4 is a challenge: the decomposition temperature of the cobalt and iron precursors are different, cobalt (II) stearate has demonstrated a higher decomposition temperature than iron (II) stearate. The concentration of their monomers in the media will then be different. Depending on the decomposition temperature difference between the two precursors used, two observations can be made:

- If the temperature difference is small: a gradient in composition with the metal cation of the lowest decomposition temperature precursor (usually iron) localized in the center, and an increase concentration of the other metal towards the edges of the NPs.[117,118]
- If the temperature difference is large: the oxides of the two different cations will grow one after the other.

Also, in order to obtain a good core-shell structure with high quality of the interface, the materials from the core and from the shell have to display low lattice mismatch with similar cell parameters in order to obtain an epitaxial growth of the shell on the core. In the literature, $Fe_{3-d}O_4$@$CoFe_2O_4$ have been reported (Figure 27) and this could be a good catalyst for the OER[114].

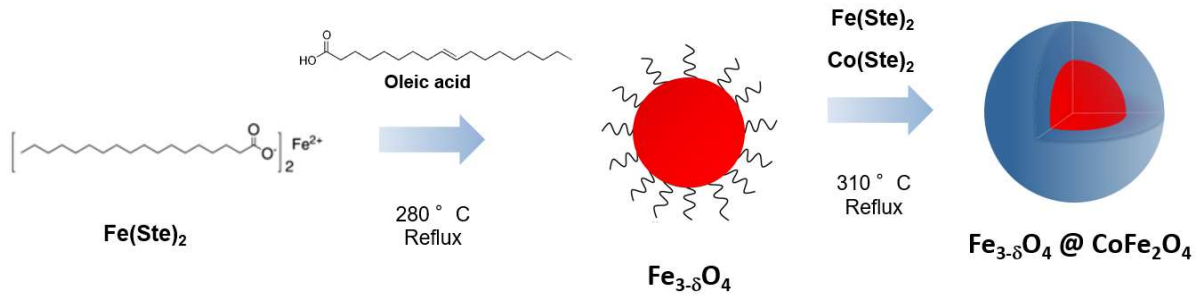

Figure 27: Successive thermal decomposition to form core-shell Fe_3O_4@$CoFe_2O_4$ NPs inspired from.[114]

Last but not least, for electrochemical applications, it is also important to have a conductive catalyst in order to avoid the ohmic losses inherent to a non-conducting or a poorly-conducting

material. When the catalyst is not conductive, it is common to deposit an ink composed of carbon and catalyst on the working electrode; the carbon being conductive, the issue of the ohmic losses in the catalytic layer is then avoided. However, carbon materials are oxidized in the OER potential range. Not only this is detrimental for industrial applications of the catalysts, but also complicates evaluation of the OER activity and understanding of its mechanism. Consequently, utilization of conductive catalysts is one of the key points towards a better understanding of the reaction mechanism.

There are not many spinel oxides that are conductive, and magnetite (Fe_3O_4) is one of them thanks to the hopping of the electrons between the Fe (II) and Fe (III) cations. Indeed, magnetite belongs to the inverse spinel structure (Figure 28) where the oxygen atoms are organized in a cubic closed packed (*ccp*) structure and there are 8 Fe (III) in the T_d sites as well as 8 Fe (III) and 8 Fe (II) in the O_h sites[100] .

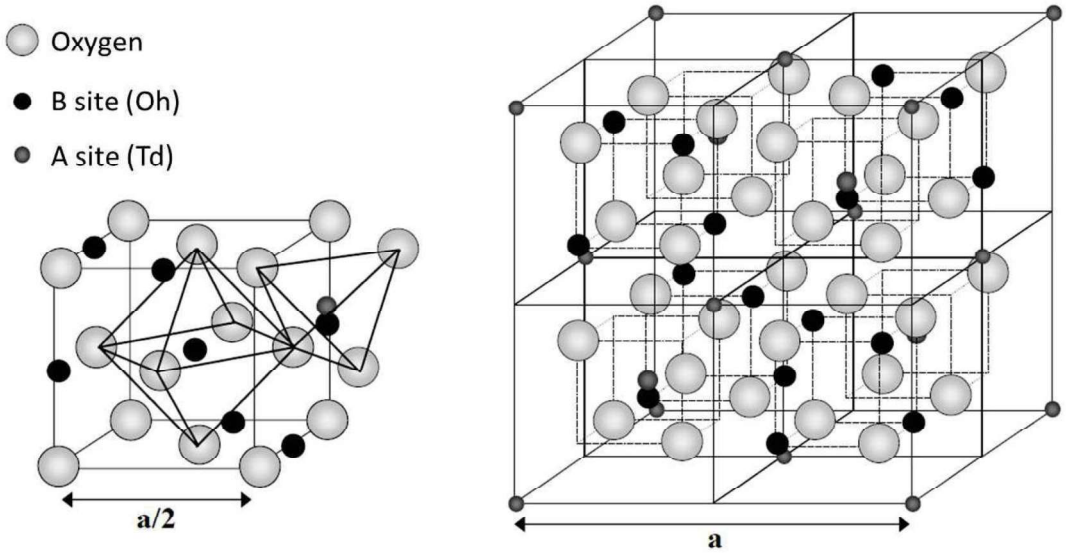

Figure 28: Inverse spinel structure taken from.[100]

However, it was presented in Table 1 that magnetite has almost no activity for the OER. But an element that is quite active for the OER would be Co_3O_4 or cobalt ferrite[25,57,65]. Cobalt ferrite also presents a partially inverse spinel structure and the cell parameters of $CoFe_2O_4$ and Fe_3O_4 are respectively 8.3919 Å (JCPDS card n° 22-1086) and 8.396 (JCPDS card n° 19-062). An epitaxial growth of the ferrite shell on the magnetite core is thus possible. This material would be active for the OER and the conductive core would avoid the use of carbon to increase the conductivity of the system. The decomposition temperature of cobalt stearate and iron stearate precursors in monomers are also similar so it is possible to deposit the monomers at the same time on an already formed core of magnetite and grow a cobalt ferrite shell[114].

To conclude, it is possible to synthesize core-shell NPs with a conductive magnetite core, an electrochemically active cobalt ferrite shell, a controlled size, size distribution, shape and composition via thermal decomposition but the synthesis parameters have to be chosen carefully. These NPs will be synthesized and studied in the next chapters for the OER catalysis applications.

6) Conclusion

To sum up, water electrolysis is an environmentally friendly way to produce hydrogen. Performing this reaction in alkaline media allows to replace the scarce and expensive iridium-based anodes utilized for PEM electrolysis by TMOs such as cobalt, iron or nickel. The OER (half reaction occurring at the anode of a water electolyzer) being more difficult to realize due to four electrons exchange usually presents higher overpotentials than the HER. Hence, finding a good catalyst for this reaction is a bottleneck for future dissemination of the AEM water electrolysis.

Among the transition metal oxides, catalysts presenting a spinel structure are of great interest due to their highly tunable properties. Cobalt, nickel and other transition metal oxides have been studied for the OER in the literature and they seem to present good OER activities. These materials have also been studied *operando, but* the transformations occurring on the catalyst surface are debated. In several publication formation of a CoO_xH_y layer (reversible or not) at the surface of the catalyst has been reported. The nature of the active center and the oxidation state of the transition metal cations are also under discussion. Additionally, the measured activity values greatly vary from one publication to another; a model catalyst is needed to systematically study the OER activities and operando transformations of these catalysts and link them to their chemical structure and oxidation state.

Core-shell structures attract more and more attention: the core can be an earth-abundant inexpensive catalyst while the shell (catalytically active material) quantity is limited. Good catalysts often being scarce on earth, this is a good way to decrease their usage without being detrimental for the OER activity. Additionally, the core can also help in increasing the catalytic activity. Consequently, core-shell Fe_3O_4@$CoFe_2O_4$ NPs seem to be a good candidate for the catalysis of the OER. Iron is indeed known to enhance the OER activity of materials and the conductivity of the magnetite core should make the system conductive and would avoid the use of carbon that would otherwise oxidize in the OER potential range. This structure also uses a lower amount of cobalt, a material that has been classified as “critical raw material” in 2020 by the European union. Additionally, the core and core-shell material both present an inverse spinel structure with almost the same cell parameter, which will allow an epitaxial growth of the shell on the core. These NPs will be synthetized by thermal decomposition, a method that produces NPs with high reproducibility, with a high control of the size, shape and composition.

In this thesis, we aim at developing a model catalyst to evaluate its catalytic properties and link them to the chemical structure but also to understand *operando* the phenomena happening at the surface of the catalyst during the OER. For this purpose, we synthesized four different types of core-

shell cobalt iron oxide NPs, we characterized them electrochemically and then used X-ray absorption spectroscopy to investigate the oxide structure and oxidation states of the metal cations during the OER. In chapter 3 we will focus on the NPs synthesis and their characterizations. In chapter 4, we will investigate the influence of the electrode loading on the activity and highlight the importance of the catalyst conductivity. Once the right loading for measuring accurately the activity has been determined, chapter 5 will focus on the activity determination of the different types of NPs synthesized and will study the impact of the core size on the overall activity. Finally, chapter 6 will investigate the transformations occurring on the catalyst during the OER and study the evolution of the oxidation state of metal cations, and unraveling some synergetic effects between iron and cobalt during the reaction.

Chapter 2: materials and methods

1) NPs and precursors synthesis

The NPs synthesis consists of a two steps thermal decomposition of metallic precursors. Their synthesis protocol and the synthesis protocol of the precursors will be detailed in the next parts of this chapter.

a) Precursors synthesis

Iron (II) stearate:

Iron (II) stearate was synthesized following a protocol that was already published for the iron stearate.[119]

In a 1 L two-necked round-bottom flask, 9.8 g (32 mmol) of sodium stearate (98.8%, TCI) were poured and 320 mL of distilled water were added. The mixture was heated to reflux under magnetic stirring until all the stearate was dissolved. Afterward, 3.80 g (16 mmol) of iron (II) chloride tetrahydrate was dissolved in 160 mL of distilled water and was poured into a round-bottom flask. The mixture was heated to reflux and kept at this temperature for 15 min under magnetic stirring before cooling down to room temperature. The colored precipitate was collected by centrifugation (15 000 rpm, 5 min) and washed by filtration with a Buchner funnel. Finally, the powder was dried in an oven at 65 °C for 15 h.

Cobalt (II) stearate:

Cobalt (II) stearate was synthesized following a protocol that was already published[114].

In a 1 L two-necked round-bottom flask, 9.8 g (32 mmol) of sodium stearate (98.8%, TCI) were poured and 320 mL of distilled water were added. The mixture was heated to reflux under magnetic stirring until all the stearate was dissolved. Afterward, 3.16 g (16 mmol) of cobalt (II) chloride hexahydrate was dissolved in 160 mL of distilled water and was poured into a round-bottom flask. The mixture was heated to reflux and kept at this temperature for 15 min under magnetic stirring before cooling down to room temperature. The colored precipitate was collected by centrifugation (15 000 rpm, 5 min) and washed by filtration with a Buchner funnel. Finally, the powder was dried in an oven at 65 °C for 15 h.

b) Nanoparticles synthesis

Four different types of core-shell NPs were synthetized aiming for different sizes of the core and of the shell. The general protocol is the following:

The first step consists in the core (Fe_3O_4) synthesis. For this step, two different precursors can be used: a homemade iron (II) stearate and a commercial iron (III) stearate. A two-necked round-bottom flask was filled with of iron (II) stearate or the iron (III) stearate, a surfactant (oleic acid 99% Alfa Aesar) and solvent (ether dioctyl or a mix of squalene and dibenzyl ether). The brownish mixture was heated at 100 °C under a magnetic stir for 30 min in order to remove water residues and to homogenize the solution. The magnetic stirrer was then removed and the flask was connected to a reflux condenser before heating the solution to reflux with a heating ramp of 5 °C/min. At the end, the mixture was allowed to cool down to 100 °C. 4mL of the mixture were taken for analysis of the core material following an already published protocol[114]. After cooling at room temperature, this fraction was precipitated by the addition of acetone and washed by agitation with a magnetic stirrer in warm acetone (60°). They were then stored in chloroform.

The second step consists in the shell growth on the core. Cobalt (II) stearate (and in some cases iron (II) stearate), oleic acid, and 1-octadecene were added to the reaction medium. The mixture was heated to 100 °C for 30 min under magnetic stirring to remove water residues and to homogenize the solution. After removal of the magnetic stirrer, the flask was then connected to a reflux condenser to heat the solution at reflux with a heating ramp of 1 °C/min. After cooling down to room temperature, the nanoparticles were precipitated by the addition of acetone and then washed by centrifugation in a mix of chloroform and acetone. They were then stored in chloroform.

The synthesis of the NPs were made following or adapting already published protocols taken from refs[102,113,114,120]. The details of the nature and quantities of the precursors, solvents, surfactant and temperature ramp are given in Table 3.

Table 3: Experimental parameters for the core-shell NPs synthesis

NPs	Parameter	Core synthesis	Shell synthesis
CS-1	Precursors	Iron (II) stearate 1.38 g (2.22 mmol)	Iron (II) stearate 0.585 g (0.94 mmol) and cobalt (II) stearate 0.29 g (0.46 mmol)
	Solvent	20 mL of ether dioctyl	32 mL of 1-octadecene
	Oleic acid	1.254 g (4.44 mmol)	0.791 g (2.8 mmol)
	Temperature	reflux for 2 h with a heating ramp of 5 °C/min	reflux for 2 h with a heating ramp of 1 °C/min
CS-2	Precursors	Iron (II) stearate 1.38 g (2.22 mmol)	Cobalt (II) stearate 0.335g (0.531mmol)
	Solvent	20 mL of ether dioctyl	20 mL of octadecene
	Oleic acid	1.254 g (4.44 mmol)	No addition
	Temperature	reflux for 2 h with a heating ramp of 5 °C/min	reflux for 3 h under air with a heating rate of 1°C/min
CS-3	Precursors	2g (2.2mmol) of commercial iron (III) stearate	1.16g (1.84mmol) of cobalt (II) stearate, 2.36g (3.8mmol) of iron (II) stearate
	Solvent	19.5 mL of squalane and 0.5mL of dibenzyl ether	40 mL of 1-octadecene
	Oleic acid	1.254 g (4.44 mmol)	1.254 g (4.44 mmol)
	Temperature	reflux for 1 h with a heating ramp of 5 °C/min	reflux for 2 h with a heating ramp of 1 °C/min reflux for another 2 h with a heating ramp of 1 °C/min
CS-4	Precursors	2g (2.2mmol) of commercial iron (III) stearate	1.16g (1.84mmol) of cobalt (II) stearate, 2.36g (3.8mmol) of iron (II) stearate
	Solvent	20 mL of ether dioctyl	40 mL of 1-octadecene
	Oleic acid	1.254 g (4.44 mmol)	1.254 g (4.44 mmol)
	Temperature	reflux for 2 h with a heating ramp of 5 °C/min	reflux for 2 h with a heating ramp of 1 °C/min

2) *Thermogravimetric (TG) analysis*

Thermogravimetric analysis is a method of thermal analysis in which the mass of a sample is measured over time as the temperature increases. This analysis gives information about various phenomena such as phase transitions, absorption, adsorption and desorption, chemisorption, or thermal decomposition. In this manuscript, it is used to verify that the decomposition temperature of the iron (II) stearate and cobalt (II) stearate are coherent with the literature and the previous synthesis (see chapter 3).

Thermogravimetry analysis was performed on the cobalt and iron (II) stearates using a SDTQ600 from TA instrument. Measurements were performed on dried powders under air in the temperature range of 20°C to 600°C at a heating rate of 5°C/minute.

3) Transmission electron microscopy (TEM)

To understand the phenomenon occurring on the surface of the NPs, a narrow size distribution and well-defined shape is essential. Transmission electron microscopy (TEM) allows to calculate the mean size of a batch of nanoparticles with a standard deviation, in measuring the size of 200 NPs with the Image J software. The chemical composition of the NPs can also be investigated with energy dispersive spectroscopy (EDS). Additionally, it is possible to obtain a high-resolution image of the NPs and observe the lattice fringes. If the NPs are a single crystal, the fringes will have a regular period across the NPs without defect. The TEM images were obtained on a JEOL 2100 LaB6 instrument with a 0.2 nm point to point resolution. The Fast Fourier Transformation and the microscopy images treating and analysis were done using the Digital Micrograph software.

With the TEM it is also possible to study the atomic distribution on a single NP with electron energy loss spectroscopy (EELS). This technique will confirm the core shell structure. STEM images and EELS data were obtained using a probe-corrected Titan low-base (Thermo Fisher Scientific) equipped with a high-brightness field-emission gun (X-FEG). Convergence angle was 25 mrad and collection angle for high angle annulard dark field (HAADF) imaging was 48 (60) mrad at 300 (80) keV. HRSTEM images were acquired at 300 keV while EELS data was acquired at 80 keV, except for data on sample CS-4 (Figure 6 in SI). A Gatan Image Filter (GIF) Tridiem ESR 865 spectrometer was employed for EELS data acquisition using an energy dispersion of 0.2 eV/pixel and a collection angle of 68 mrad. Spectral range was chosen to encompass O-K edge (520-555 eV), Fe-L_3, L_2 edge (700-730 eV) and Co-L_3, L_2 edge (770-810 eV). Spatially-resolved EELS maps were acquired using DigiScan (Digital Micrograph) with pixel sizes below 5 Angstrom. EELS data was analyzed with a custom Matlab software. Spectrum-images were denoised using principal component analysis (PCA) and quantified by integrating a 30-eV wide window of the background-subtracted spectra and normalizing with calculated scattering cross sections.

Samples for HRSTEM and EELS measurements were prepared by drop-casting of 2 µL on holey-carbon TEM grids from the chloroform-stabilized NP suspensions diluted 1:50 in ethyl alcohol. After

drying, the grids with NPs were washed in a bath of activated carbon and ethyl alcohol similar to the process described by Li *et al.*[121] to minimize contamination.

4) *Scanning electron microscopy (SEM)*

NPs were deposited onto a substrate in order to study the spatial arrangement prior to electrochemical analysis. A Zeiss Gemini SEM 500 scanning electron microscope with a resolution of 1 nm was used. The detector used was a SE-Inlens (secondary electrons), the applied tension 1keV, the working distance 3 mm and the aperture size 15.00µm. Before taking the images, the samples were cleaned thanks to a N_2 plasma generated by an evactron (power 20 W for 2 minutes). Beyond studying the nanoparticle deposited on the substrate from the top, cross sections images were also recorded. In order to observe a cross section, the NPs were deposited on a substrate that was the broken in the middle. A cross polisher IM4000plus was used with a tension of 6 keV to send an argon ion beam on the edge of the substrate and create a clean cut to observe the cross section. Silicon substrates were submitted to the beam for 45 minutes while glassy carbon substrate were for 2 hours. in order to obtain information on the thickness of the NPs layer and the distribution of NPs onto the substrate.

5) *X-ray diffraction (XRD)*

XRD is used to identify the crystallographic phases in the structure thanks to the intensity and the position of the peaks of the diffractogram. The structure can be identified via the position and intensity of the peaks present in the diffractogram. Each peak is the result of the reflection of a Bragg plan of the material which obey the Bragg law:

$$2d_{hkl}\sin(\theta) = n\lambda$$

with d_{hkl} the inter-planar distance, θ the Bragg angle (or half-angle deviation) and n the diffraction order. Usually, the wavelength λ corresponds to the cupper Kα edge of 1.5406 Å. h, k and l are the Miller indices of the different planes.

Thanks to this d_{hkl} value, it is possible to calculate a, the cell parameter of a cubic system, according to the following formula:

$$a = d_{hkl}\sqrt{h^2 + k^2 + l^2}$$

The NPs crystalline structure was investigated by X-ray diffraction (XRD). In the obtained diffractograms, in addition to the peaks that are seen (characteristic of the crystalline lattice mode), the broadness of the peaks can be measured: the width of a peak reflects the crystal size and its narrowing is a consequence of a larger crystal size.

For CS-1 XRD measurements were performed using a Bruker D8 Advance diffractometer equipped with a monochromatic copper radiation (Kα = 0.154056 nm) and a Sol-X detector in the 20–80° 2θ range with a scan step of 0.02°. High-purity silicon powder (a = 0.543082 nm) was systematically used as an internal standard. For CS-3 and CS-2, a Bruker D8 Advance diffractometer equipped with a non-monochromatic copper radiation (Kα = 0.154056 nm) and a Sol-X detector in the 20–80° 2θ range with a scan step of 0.02°. High-purity silicon powder (a = 0.543082 nm) was systematically used as an internal standard. For CS-4 The XRD measurements were carried out on a D8 Discover diffractometer in Bragg Brentano geometry equipped with a Cu Sealed tube ($\lambda K_{\alpha 1}$ = 1.54059 Å), a quartz front monochromator, a motorized anti-scatter screen and an energy resolved Lynxeye XE-T linear detector.

From the diffractograms, it is possible to extract the cell parameter and the crystallite size. These parameters were obtained by fitting the data with fullprof software[122,123].

6) *Fourier transform infrared (FT-IR) spectroscopy*

Fourier transform infrared (FT-IR) spectrometry is a powerful technique that can help in the investigation of the composition of the NPs. It can also evidence the presence of impurities and side products such as the stearate used as a precursor or some free oleic acid used as a surfactant in the reaction. Moreover, after the synthesis of the nanoparticles by thermal decomposition, the NPs are precipitated and washed in warm acetone. After the end of the washing step, FT-IR technique is used to verify if the washing has been successful: one can follow this ratio:

$$\frac{\nu_{as\ and\ s}}{\nu_{M-O}}$$

where $\nu_{s\text{-}as}$ is the symmetric (s) and antisymmetric (as) vibration of C-H bonds from CH_2 group between 2925 and 2855 cm^{-1} and $\nu_{M\text{-}O}$ is the vibration of the metal-oxygen bond centered around 570 cm^{-1} for $Fe_{3-\delta}O_4$. The NPs are considered as clean when this ratio reaches 1 as some oleic acid ligands grafted at the surface of the nanoparticles are still present, allowing their colloidal stability.

FT-IR was performed using a PerkinElmer Spectrum spectrometer in the wavenumber range 4000−400 cm^{-1} on samples diluted in KBr pellets.

7) Granulometry

Stable suspensions are essential for the electrode preparation as aggregates should be avoided in order to have a high surface of the material. The thermal decomposition method allows the nanoparticles to have surfactant (oleic acid) grafted at the surface of the NPs which ensure their stability in suspensions. A first indication of the size of the nanoparticles is given by granulometry measurements also called dynamic light scattering (DLS). It consists in recording the intensity of an incident scattered beam by the nanoparticles. The NPs are in movement in the suspension thanks to the Brownian motion. Measuring the intensity of the beam as a function of the time and using the Stokes-Einstein equation one can determine the hydrodynamic diameter (d_h) which depends on the temperature (T), the carrier liquid viscosity (η) and the diffusion coefficient (D_t):

$$d_h = \frac{K_B T}{3\pi\eta D_t}$$

The hydrodynamic diameter includes the size of the oleic acid ligand grafted at the surface of the NPs. Measurements were performed using a nanosizer Malvern (nano ZS) at a scattering angle of 173°. A measure corresponds to the average of 3 runs of 1 min.

8) Electrode preparation

a) Substrate choice

Different substrates are available for the electrochemical experiments to be performed. In order to determine which substrate was the best for our application, we tried both a plate of polycrystalline gold and a rod of glassy carbon electrode which advantages and drawbacks as well as the electrode preparation will be presented in the next parts.

Glassy carbon electrode:

This electrode was cleaned in HCl 1 M for an hour to make sure that no NPs were left on its surface from previous measurements. Then it was polished for 1 minute using 3 different diameters of alumina

powder: 1µm; 0.3µm; 0.05µm. After the polishing steps; the electrode was rinsed with water and then ultrasonicated for 5 minutes in acetone, for 5 minutes in ethanol and for 5 other minutes in water to remove the traces of alumina powder.

The NPs were then drop casted on the clean glassy carbon electrode (d=0.5 cm) from their suspension in chloroform, the latter was evaporated in air (Figure 29). Different loadings ranging from 0.5 to 100 µg/cm² were deposited on the glassy carbon electrode, the loadings will be indicated in the manuscript when presenting the electrochemical data.

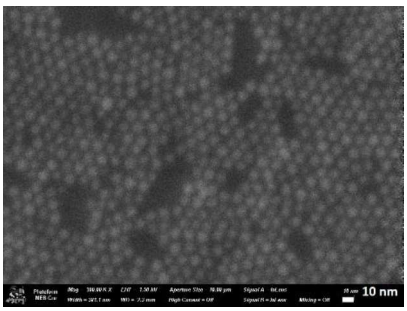

Figure 29: Core-shell NPs CS-1 deposited on a glassy carbon electrode measured with SEM.

Gold electrode:

A polycrystalline gold plate (10 mm by 10 mm and 1 mm thick) was used as the working electrode. First, the gold was cleaned in HCl 1M for an hour and then with ethanol and water. Following this step, both sides of the gold plate were activated by an argon plasma for 2 minutes. Following an already published protocol[124], the gold surface was functionalized for 24 hours in a solution of 11-mercaptoundecanoic acid. The plate was then washed with ethanol to remove all the ligands that are not attached to its surface. Finally, the gold-functionalized plate was placed in the NPs solution for 1 hour and washed with chloroform to remove the NPs that would not be grafted to the surface.

The advantage of using gold as a substrate is that after grafting the NPs it can be annealed to remove the surfactant surrounding the NPs. An annealing step was performed in air for 10 minutes at 300°C in order to remove the organic molecules and make the surface of the NPs available for the OER (Figure 30).

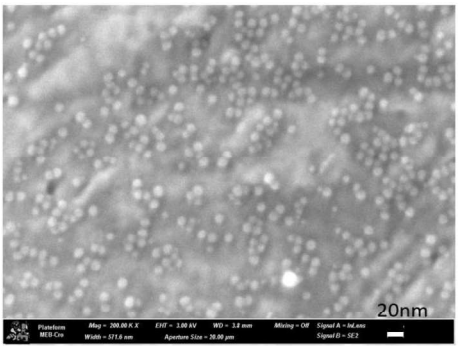

Figure 30: Core-shell NPs CS-1 deposited on a polycrystalline gold plate after annealing at 300°C for 10 minutes, measured with SEM.

In the beginning of my PhD project, the gold substrate was privileged because, in addition to withstand high temperatures that would allow the full removal of the oleic acid surrounding them, it would also allow the study of a submonolayer of non-aggregated NPs and provide for an accurate estimation of the NPs activity. However, the use of the gold substrate was abandoned later. The reason for that was that we have noticed that the activity of the polycrystalline gold substrate evolved in time following successive cycles of NP deposition, annealing, substrate cleaning and polarization to the OER potentials. Unfortunately, the gold plates we had in our possession were not compatible with a polishing machine (which would allow us to renew the surface), and we did not succeed in having Au substrates, which would allow a reproducible surface state. This resulted in a significant irreproducibility of the results as a matter of time. Table 4 summarizes the advantages and drawbacks of each substrate.

Table 4: Pros and cons of a polycrystalline gold plate and a glassy carbon rod as the working electrode to support the NPs

	Glassy carbon	Polycrystalline gold
Annealing possible	No	Yes
Activity estimation	From the volume of NP suspension drop-casted, with cobalt and iron concentration in the suspension obtained by ICP-AES	Number of NPs estimated from the SEM images
Reproducibility	Acceptable (±15%)	Not good (Au substrate becoming more active over time)
Possible electronic interactions with the catalyst	No	Yes
Monolayer	Not easy to obtain, NPs randomly distributed	Yes (submonolayer)

Considering Table 4, even though gold seemed to be a good candidate for the substrate, the fact that due to the annealing, successive chemical treatments and electrochemical measurements, the

gold substrate progressively became more OER active, prompted us to abandon it. Also, research papers indicated that gold could have electronic interactions with the catalyst[69,70], which we preferred to avoid in order to determine the intrinsic activity of our catalyst. In the end, it was decided to move from a gold substrate to a glassy carbon one, even though it could not be annealed, and it was more difficult to control the repartition of the NPs on the electrode. Nevertheless, the glassy carbon substrate allowed us to obtain reproducible results.

On this glassy carbon substrate, two different deposition methods were investigated: spin coating and drop casting.

- Spin coating is an interesting method to obtain a thin layer of the NPs but given the size of the glassy carbon rod (10 mm high and 5 mm diameter), the deposition on the substrate was delicate and not always repeatable. Unfortunately, we did not succeed in optimizing the spin coating procedure, and part of the NPs was removed from the substrate due to the high rotation speed. Thus, the number of NPs on the electrode was then difficult to estimate. Hence, the mass or surface weighted activity of the catalyst was difficult to evaluate using this technique.
- Drop-casting is a deposition method commonly used in electrochemical experiments. It allows better control of the quantity of catalyst deposited on the substrate and is easy to perform. However, it still presents some issues: the distribution of the catalyst on the surface is not well controlled and if the solvent evaporates rapidly (which is the case here as the NPs are stored in chloroform), the layer is not homogeneous. With this technique it is not possible to obtain a monolayer of NPs on the substrate.

As a conclusion of this part, due all the issues above mentioned for the gold substrate, we opted for a glassy carbon substrate using a drop-casting deposition method. Even though this approach is not ideal as the distribution of the NPs on the surface is random, showed a correct repeatability of the cyclic voltammetry experiments.

b) Electrode preparation

The glassy carbon electrode that was chosen to continue the project was prepared according to the following protocol:

- Cleaning step in 1 M HCl for 1 hour to make sure that no NPs were left on the surface from previous experiments.

- Polishing steps for 1 minute on 3 different diameters of alumina powder: 1 µm; 0.3 µm and 0.05 µm.
- After each of the polishing steps, the electrode was rinsed with water and then ultrasonicated for 5 minutes in acetone, for 5 minutes in ethanol and for 5 other minutes in water to remove traces of alumina powder.

10 µL of the NPs solution (with various concentrations) was taken with a micropipette and the droplet was deposited on the clean glassy carbon electrode (d=0.5 cm), the solvent (chloroform) was evaporated in air for about 2 minutes. Different loadings ranging from 0.5 to 100 µg/cm² were deposited on the glassy carbon electrode, the loading will be indicated in the manuscript. Then different dilutions were applied (F=1, 10, 30, 60,100) by adding chloroform to the initial solution of NPs in chloroform and depositing NPs on the electrode to achieve various loadings. The drop-casted volume was kept constant at 10 µL. For the investigation of the surfactant impact on the activity (see chapter 5), 1 µL of oleic acid was added to 1 mL of the original NP dispersion in chloroform.

9) *Electrochemical measurements*

a) *Electrochemical cell*

A 3-electrode glass cell was used with a 0.1 M NaOH electrolyte to characterize the material electrochemically. The working electrode (WE) is the glassy carbon with the NPs, the counter electrode (CE) is a gold wire instead of a more commonly used platinum wire in order to avoid cross-contamination of the WE by platinum, and the reference electrode (RE) is a Hg/HgO electrode which potential vs RHE has been regularly calibrated against a reversible hydrogen electrode to make sure that it was stable and wasn't changing with time.

b) *Impedance spectroscopy measurements*

Electrochemical impedance measurements were performed on a Gamry REF 600 potentiostat at two different potentials: 1.62 and 1.67 V vs RHE. The range of frequency was set from 0.2 Hz to 100 kHz with 10 points per decade.

The Nyquist plots will we used to determine the electrolyte resistance from the high frequency part of the impedance spectrum and to correct the ohmic losses in the cyclic voltammetry

measurements. Figure 31 shows how the electrolyte resistance R_s is determined from the impedance measurements.

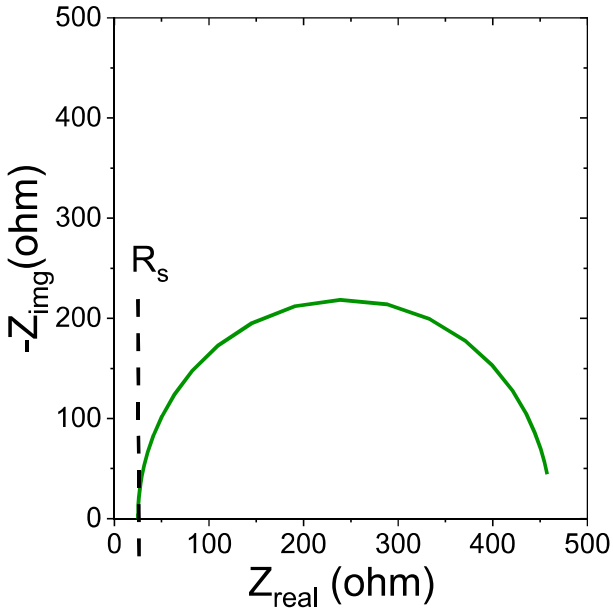

Figure 31: A typical Nyquist plot obtained for the core-shell NPs deposited on a GC electrode. The dashed line illustrates how the electrolyte resistance was determined.

c) Cyclic voltammetry measurements

Cyclic voltammetry measurements were performed on a Gamry potentiostat REF 600. All the experiments were repeated 3 times to ensure their reproducibility. The WE potential was recalculated into the RHE scale and corrected to Ohmic losses, with the electrolyte resistance R_s measured using the impedance spectroscopy. The potential was recalculated as follow (*i* is the current flowing through the cell):

$$E_{RHE} = E_{Hg/HgO} + 0.93 - i \times R_s$$

First 50 CV cycles were done between 0.83 and 1.43 V vs RHE with a scan rate of 100 mV/s in order to clean the surface of the NPs. Then 3 cycles between 0.83 and 1.73 V vs RHE were performed with a 10 mV/s scan rate, which were used to determine the OER activity and the Tafel slope after the iR correction. Figure 32 shows how the correction of the ohmic losses changes the cyclic voltammetry curves. For high currents this change becomes important and can influence greatly the activity determination.

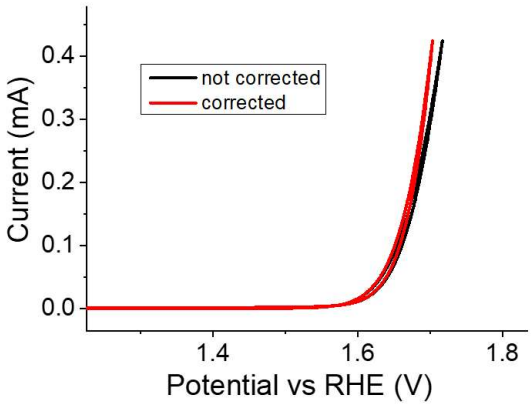

Figure 32: Typical cyclic voltammetry curves measured for core-shell NPs deposited on a GC substrate in 0.1 M NaOH before (black) and after (red) correction of the ohmic losses.

Another factor that we investigated was an eventual influence of oxygen bubbles created on the working electrode. Indeed, as we stated in chapter 4, the creation of bubbles will likely decrease the measured activity. This is why a rotating electrode is usually used in the literature. However, in our case, due to the low NP loadings used and consequently relatively low currents generated, the use of a rotating electrode was not needed. Indeed, Figure 33 does not display any significant change between the measurement performed with and without the WE rotation. Consequently, for all the experiments that will be presented in the following parts, no rotation of the working electrode will be applied.

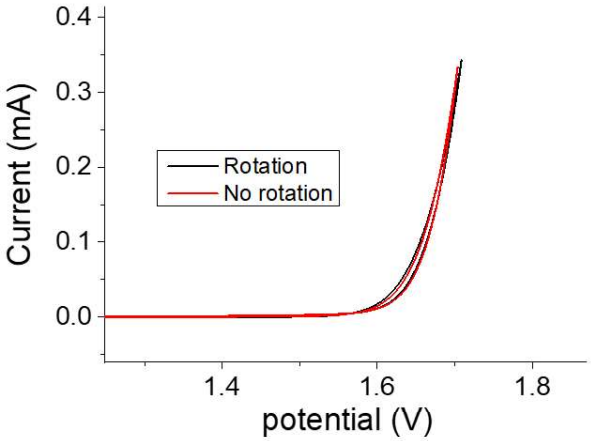

Figure 33: Cyclic voltammetry curves obtained for CS-1 NPs in 0.1 M NaOH at 120µg.cm^{-2} loading without and with (2500 rpm) electrode rotation.

As stated in chapter 1, in order to evaluate the activity of a catalyst and to compare these results with the literature, normalizing the current by the surface of the particles or by their actual mass is imperative. In this study, the concentration of cobalt and iron in a given volume of the NP

suspension has been determined by Inductively Coupled Plasma Atomic Emission Spectroscopy (ICP-AES). From these measurements, the oxide mass was obtained. The surface of the NPs has been calculated thanks to the average diameter of the NPs measured by the TEM, assuming that the NPs were displaying a perfect monomodal distribution and were perfectly spherical. This is an overestimation of the actual electrochemically active surface but is still a good approximation.

The surface weighted activity and the metal oxide mass weighted activity were calculated as follows:

$$surface\ weighted\ activity\ (mA.cm^{-2}) = \frac{current\ (mA)}{oxide\ surface\ (cm^2)}$$

$$metal\ oxide\ mass\ weighted\ activity\ (A.g^{-1}) = \frac{current\ (A)}{oxide\ mass\ (g)}$$

Equation 5: Calculation of the surface weighted activity and the oxide mass weighted activity.

If, as we suppose, the activity of the NPs is arising primarily from the shell, with cobalt being responsible for the activity of the catalyst, another type of activity, normalizing the current by the cobalt mass can be introduced:

$$cobalt\ mass\ weighted\ activity\ (A.g^{-1}) = \frac{current\ (A)}{cobalt\ mass\ (g)}$$

Equation 6: Calculation of the cobalt mass weighted activity.

This indicator may provide a better estimation of the activity of the catalyst as it will consider the low amount of cobalt present in the core-shell NPs and responsible for the activity, and not the entirety of the NPs. These different kinds of activities will be compared for the different types of NPs synthesized for this study.

Cyclic voltammetry experiments were also performed in a 1 M NaOH electrolyte in order to evaluate the influence of the electrolyte concentration and pH on the NPs activity. For these experiments, an Hg/HgO electrode filled with 1 M NaOH and calibrated accordingly was used.

10) Synchrotron measurements

a) Depth profiling

In order to probe the cobalt and iron quantity and their distribution within the NPs, X- ray photoelectron spectroscopy (XPS) can be used in order to measure the Co 2p and Fe 2p peaks at different depths within the NPs by varying the incident photon energy. In this work, two sets of the depth profiling experiments were performed at the ISISS beamline of the BESSY synchrotron facility.

For the first run of experiments (see chapter 6), CS-1 NPs were deposited on a silicon substrate on top of which a thin layer of carbon had been deposited. The measurements were first performed on the initial sample and then it was annealed at 300°C under O_2 atmosphere for 8 hours. The incident energy of photoelectrons was varied from 900 to 1600 eV (corresponding to kinetic energies ranging from 200 to 800 eV). However, in this first run of synchrotron measurements, the depth probed in the NPs was too important, while the number of experimental points was not sufficient to make an unambiguous conclusion regarding the Fe/Co ratio distribution within the NPs.

For the second synchrotron run, CS-1 and CS-3 NPs were drop-casted on a silicon wafer substrate, on this substrate, a thin layer of carbon has been deposited (for the conductivity and to avoid charge effects on the XPS measurements). More measurements were performed with the incident photon energy ranging from 850 eV to 1350 eV (corresponding to kinetic energies ranging from 150 to 550 eV) in order to primarily probe the near-surface region of the NPs. The results of this depth profiling study will be presented in chapter 3. The results obtained for this experimental run at high incident energies agreed with the data obtained for the first depth profiling run.

The average mean free paths for the applied energies were given by QUASES software. The area of the Co 2p and Fe 2p peaks have been integrated thanks to casaXPS software and the proportion of iron vs cobalt has been calculated using the following formula:

$$C_A = \frac{\frac{I_A}{S_A}}{\sum(\frac{I_n}{S_n})}$$

Equation 7: Calculation of the atomic concentration of a given atom A thanks to the area of its XPS peak (I_A) and its sensitivity factor S_A.

where C_A is the atomic concentration of a given element among a number of n elements. I_A---I_n is the area of the peak characteristic of a given element, S_A- - - S_n is the sensitivity factor that depends on the cross-section of the element and also on the flux of the incident source. The cross-sections were

taken from ELETTRA synchrotron website[125] and the flux was taken from the BESSY flux curve. It is worth noting that in the case of the polarized synchrotron radiation, an anisotropy factor should be considered to calculate this ratio. However, while considering the 2p orbitals of cobalt and iron, the error is compensated when the ratio of these two elements is calculated.

b) *In situ and operando* NEXAFS *measurements*

Following the experiments of annealing under an oxidative atmosphere, NEXAFS studies on CS-1 NPs were performed at SOLEIL synchrotron on the TEMPO beamline. The NPs were deposited on a gold substrate. One sample had been annealed for 10 minutes at 300 °C under air and the other was not annealed. Fe L-edge and Co L-edge spectra were measured on the annealed and not annealed samples. The results of this study are presented in chapter 6.

Another NEXAFS study was performed on CS-3 NPs at BESSY synchrotron on the ISISS beamline to study operando the transformations occurring on the Fe L-edge and the Co L-edge as well as the O K-edge. The results of this study will be presented in chapter 6. The cell that was used for *in situ* and *operando* electrochemical studies was designed at the Fritz Haber Institute (FHI, Berlin, Germany) and is presented in Figure 34.

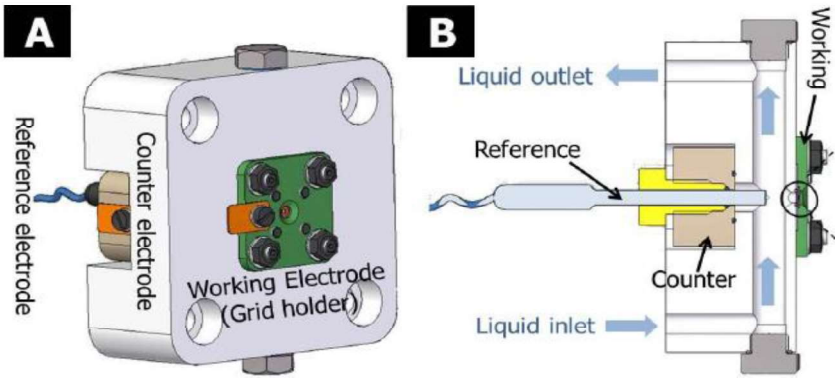

Figure 34: Electrochemical cell developed at FHI taken from.[126]

This cell comprises of a membrane permeable to the electrolyte (in this manuscript an anion exchange membrane) through which it will be able to humidify the catalyst layer deposited at the surface of the membrane and acting as a WE. The counter electrode is a platinum wire and the reference electrode, an Ag/AgCl. This cell allows the application of a potential on the working electrode and the surface of the catalyst can be probed at the same time by NEXAFS or XPS. A gas can also be introduced in the chamber to perform NAP-XPS measurements.

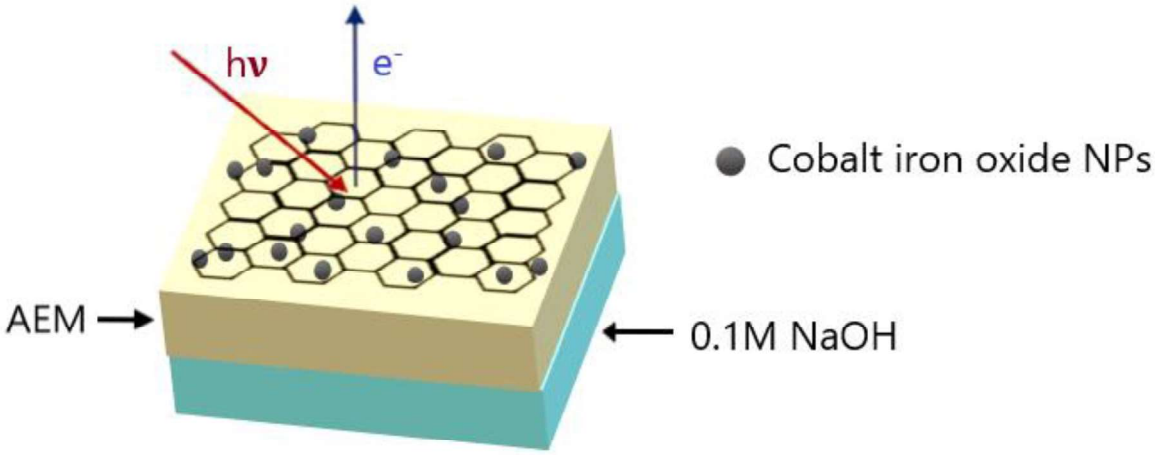

Figure 35: Membrane and catalyst assembly.

The membrane - catalyst assembly is presented in Figure 35. On this figure the catalyst layer is covered by a bilayer of graphene (transparent to photoelectrons) that has two roles[127]:

- acting as an evaporation barrier: the electrolyte will stay between the graphene and the membrane and will humidify the catalyst, making it possible to study the electrochemical reaction.
- providing an electrical contact between the catalyst NPs and the current collector.

This graphene bilayer has been bought from Graphenea company that deposited the graphene thanks to a chemical vapor deposition method. This cell allows the application of a potential to the membrane and catalyst assembly and to study *in situ* the phenomena happening on the surface of the catalyst. It has been previously used to study *operando* the OER in acidic media[127,128]. The NEXAFS measurements are performed in total electron yield (TEY) and Auger electron yield (AEY).

c) *Membrane choice*

Different types of anion exchange membranes exist and can be used. For this work, two different membranes have been tested in order to determine the one that was best-suited for the synchrotron experiments.

The first one is a commercial anion exchange membrane from Fumatech (fumasep® FAS-50) and the second one is an Aemion® anion exchange membrane prepared by the group of S. Holdcroft (Simon Fraser University, Vancouver)[129,130]. Both membranes allowed to obtain decent CV curves for core-shell NPs deposited on their surface and thus seem to be good candidates (Figure 36).

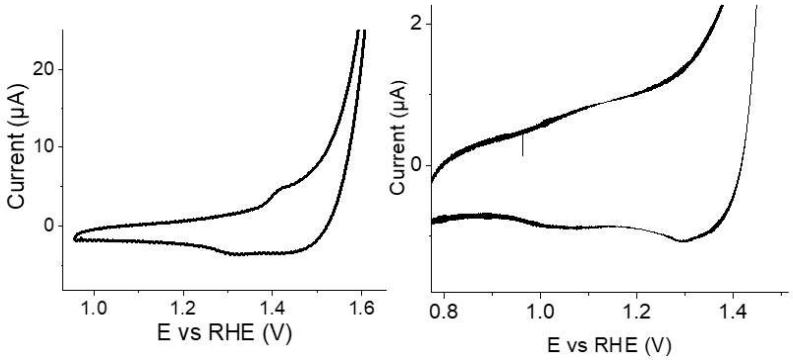

Figure 36: Cyclic voltammetry curves obtained for core-shell CS-1 NPs dropcasted on the Aemion membrane (left) and CS-3 NPs deposited on the Fumatech commercial membrane (right). Note that in addition to the membrane being different, the size of the NPs as well as their loading on the membrane are different, which can explain the differences in the currents observed on the two membrane-electrode assemblies.

CVs measured for the CS-3 sample using both types of membranes exhibit peaks characteristic of the Co (III)/Co (IV) redox transition around 1.3-1.4 V vs. RHE. The membrane developed by the group of S. Holdcroft seems to be a better candidate as for this membrane, the cobalt peaks are more intense compared to the commercial membrane. This difference is probably due to the difference of the ion exchange capacity (IEC) of the membrane and its thickness. Due to these differences, it was decided to first try the *operando* experiments with this membrane. During the preliminary experiments, the MEA was displaying a good behavior and no pressure issues when inserted in the analytical XPS chamber. However, during the synchrotron beamtime, the pressure in the chamber upon insertion of the MEA ($10^{-5/6}$ bars) was too high to perform the experiments safely (the risk of having the membrane breaking and the electrolyte leaking in the analysis chamber were too high). It was then decided to move on to the second candidate (the commercial membrane), for this one the pressure was maintained at a level that was still high (10^{-6}) especially at the end of the experiments but that allowed the experiments to be performed in a safer way for the beamline.

This higher pressure experienced with the Aemion® anion exchange membrane could have been caused by the fact that the non-commercial membrane was needed to be conditioned before use (in a 3 M KOH electrolyte changed regularly for a couple of days), the initial hydration state of the membrane was then probably at fault and the membrane was degassing in the chamber. Even though it was dried for about 30 minutes before inserting in the chamber, it was not possible to dry the membrane more without damaging its properties.

To conclude, the non-commercial membranes seem to be a better candidate but their initial hydration state hinders their use for *operando* investigation. As a consequence, for this run, a commercial Fumatech membrane was used.

Chapter 3: NPs synthesis and characterizations: $Fe_{3-\delta}O_4$ and $Fe_{3-\delta}O_4@Co_{1+x}Fe_{2-x}O_4$

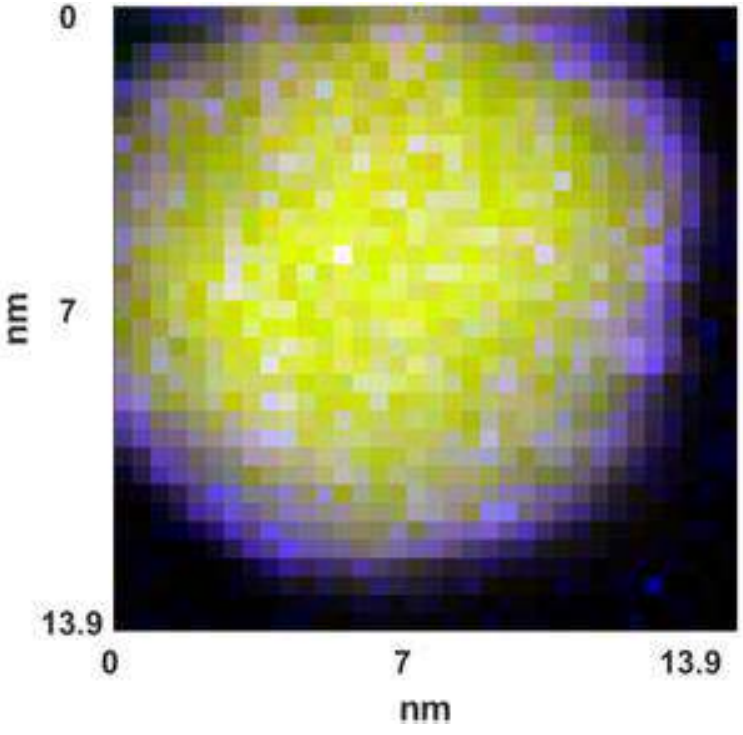

1) *Introduction*

The synthesis of a well-defined catalyst to understand better the phenomena occurring at the interface between the catalyst and the electrolyte is of high importance for the development of future anode materials for the OER. This catalyst has to meet several requirements:

- Be conductive to avoid the use of carbon that is commonly used in the literature to circumvent problems related to the low conductivity of transition metal oxides[25]. The issue is that carbon can't be used in the OER potential range because it corrodes.
- Present a high surface area: catalysis being essentially a surface phenomenon (even if for some (electro)catalytic processes, notably OER, Mars-van-Krevelen-type mechanisms may be involved), it is highly dependent on the surface available for the reaction to happen but also on the surface state and defects of the catalyst.
- Be active for the OER. As we saw in chapter 1, TMO based catalysts with a spinel structure are interesting candidates due to their tunable properties.
- Be stable in the potential range of the OER, in time with repeated cycles and in the alkaline media.

Another important characteristic to consider is the cost of the catalyst and its abundance on earth. Indeed, as it was discussed in chapter 1, the best OER performances are obtained for materials such as iridium and ruthenium oxides that are used in acidic media but due to their scarcity and cost, other alternatives to these catalysts are needed. TMO are good candidates to catalyze the OER in alkaline media. Their properties for the OER were extensively studied in the literature.[25,65,89,93] They exist under different forms: simple oxides/hydroxides (CoOOH, NiOOH), or more complex oxides (spinels, perovskites). Simple oxides and spinels are relatively active for the OER but not conductive (to the exception of Fe_3O_4) while perovskites generally present a higher conductivity. Compared to perovskites, synthesis of spinels is usually performed at a lower temperature, leading to a larger specific surface while the perovskite's one is generally smaller.

The most active materials reported in the literature in alkaline media are cobalt or nickel-based catalysts. However, these materials are not abundant on earth and their prices are consequently quite high. The growing cobalt demand led to its recent classification as critical material by the European Union.[71] In order to investigate the minimum amount of cobalt needed to catalyze efficiently the OER, Saddeler *et al*[65] recently studied the OER activity of $Co_xFe_{3-x}O_4$ compounds and evidenced that the higher activity was reached for Co_2FeO_4 and not Co_3O_4. The cobalt quantity in the catalyst can therefore be decreased but these materials, even though presenting a good OER activity are not conductive.

Catalysis being a surface phenomenon, one way to cut these costs and use less of these materials is to use a core-shell structure where the core consists of inexpensive material and where only the shell that contains these metals is the active component for the OER. Various examples of core-shell NPs for the OER have been investigated in the literature in acidic media[67,68] using elements such as iridium or ruthenium in the shell but also in alkaline media[60,62–64,66] using TMOs in the shell. Among these materials, core-shell NPs presenting a gold core and a TMO shell (CoFeOx[63], $NiCo_2S_4$[64] or Co_3O_4[62]) displayed important activities for the OER of about 10 000 A/g_{TM} for some of the samples. It was suggested that Au enhances the OER activity of TMOs because it induces electronic effects that allow the transformation of the TM in a 4+ oxidation state.[69,70] Although it is not clear yet, iron cations in TMO phases may result in similar synergetic effects with cobalt or nickel atoms which would be responsible for enhanced OER properties[72,73]. Core-shell NPs with an iron conductive core (Fe_3O_4) and a cobalt or nickel-based shell would then present the advantage to decrease the quantity of active material as well as to increase the conductivity in the material. An interaction between this iron core and the shell could also enhance the OER properties of the overall catalyst.

Synthetizing noble metal-free catalysts is then an important challenge for the development of cost-effective catalysts. Another challenge is to control the formation of these objects in order to be able to study systematically their electrochemical properties as a function of their chemical composition and structure. Indeed, according to the size of the conductive core, the thickness of the shell, the valence of the metallic cations, their chemical environment, or their conductivity, the properties of the catalysts may differ.

The catalyst that has been chosen for this study is core-shell cobalt iron oxides NPs: Fe_3O_4@$CoFe_2O_4$. It meets all the criteria above-mentioned: Fe_3O_4 is abundant and stable in the OER conditions, the bulk material conductive at ambient temperature (250 $ohm^{-1}cm^{-1}$)[131] and iron oxide NPs have been proven to be conductive[132,133]. Moreover, $CoFe_2O_4$ is active for the OER and these 2 materials present similar cell parameters, allowing an epitaxial growth of the shell on the core.

These NPs have a core of $Fe_{3-\delta}O_4$ and a shell of $CoFe_2O_4$. Thanks to their spherical shape and their nanosize they present a large specific surface. They are also conductive thanks to the magnetite core[132,133] and the fact that they present a really thin shell of cobalt ferrite. Thus, the addition of carbon with the NPs is not necessary. As it was presented before and in chapter one, TMOs such as cobalt ferrite are known to be active for the OER[24,46] and they are stable in alkaline media in the OER potential interval. Additionally, $Fe_{3-\delta}O_4$ and $CoFe_2O_4$ both present an inverse spinel structure and have almost the same cell parameters so they can grow epitaxially on top of the other. The synthesis approach consists in a seed mediated growth based on the thermal decomposition of metal complexes as

recently reported[114]. Two successive steps of thermal decomposition of metal complexes (iron (II) or (III) stearate in the first step; cobalt (II) and iron (II) stearate in the second step) are performed in a high boiling temperature solvent (about 300°C) and in the presence of a stabilizing agent (oleic acid). The obtained NPs are homogeneous in size, shape, and composition and consist of a good ideally well-defined and model catalyst for the understanding of the phenomena occurring at the NPs/electrolyte interface.

In this chapter, the synthesis strategy of four different types of NPs synthesized with various core sizes and the shell thicknesses will be presented. Their chemical structure will be deeply investigated by a wide panel of characterization techniques including Transmission Electron Microscopy (TEM), Fourier transform infra-red spectroscopy (FT-IR), granulometry, X-ray diffraction (XRD), Thermogravimetric analysis (TGA) electron energy loss spectroscopy (EELS) and X-ray photoelectron spectroscopy (XPS) to verify if they are presenting the right properties to be a good model catalyst for the OER. These synthesis and characterizations of the precursors will be presented in the next section.

2) *Synthesis strategy*

In this work, four different kinds of core-shell NPs have been synthesized, their properties for the OER will be studied in the next chapters. In order to perform a systematic study of the influence of the core size and shell thickness on the electrochemical properties, the operating parameters were varied to control them precisely. For comparison with the core-shell NPs, $Fe_{3-\delta}O_4$ NPs (core material) were also synthesized.

Three parameters were modified:

- ***The core size:***

To study the influence of the core size, two groups of NPs aiming for two different core diameters (8 nm: CS-1; CS-2 and 14 nm: CS-3; CS-4) were designed using two different iron stearate precursors. The activity results obtained for these NPs will shed light on the core role in the behavior of the catalyst.

- ***The shell thickness:***

In order to investigate the influence of the shell thickness, various quantities of cobalt and iron precursors were then added during the second step of the synthesis in order to grow thin and thick shells. For CS-1, CS-3 and CS-4 the precursors quantities added during the second thermal decomposition and consequently, the shell thickness has been gradually increased from 0.46 mmol to 1.84 mmol mmol to generate crystal growth of the shell on top of the core. The second thermal decomposition always consisted in the addition of cobalt and iron stearate precursors stoichiometrically in order to form $CoFe_2O_4$. The activity results obtained for these NPs will be interesting in order to understand the impact of the size of the conductive core and the thickness of the shell.

- ***The growth of the shell:***

The shell synthesis method has been varied in order to investigate the influence of crystalline growth *vs.* diffusion phenomena on the catalytic activity. For CS-2, NPs the synthesis method was different: only cobalt (II) stearate has been added during the second thermal decomposition step. Consequently, the diameter of the core-shell NPs is theoretically similar to the core's one as the cobalt only diffuses in the vacancies present at the surface of the $Fe_{3-\delta}O_4$ core according to the work of Liu *et al*. [113]. The shell should here be localized on the edge of the NPs and the presence of CoO should be controlled. Indeed, if large quantities of cobalt precursors are added, the NPs obtained will be presenting a CoO shell.

3) Precursors synthesis and characterizations

The synthesis of nanoparticles consists in the successive thermal decomposition of iron and cobalt complexes. As we previously discussed in chapter 1, the chemical structures of these precursors significantly affect the reaction kinetics and the size, shape and chemical composition of the NPs.

In order to prepare nanoparticles with a well-defined core-shell structure and spherical shape, homemade iron (II) stearate and cobalt (II) stearate precursors were synthesized by reacting separately sodium oleate and iron of cobalt chloride (Figure 37). The experimental details are given in chapter 2.

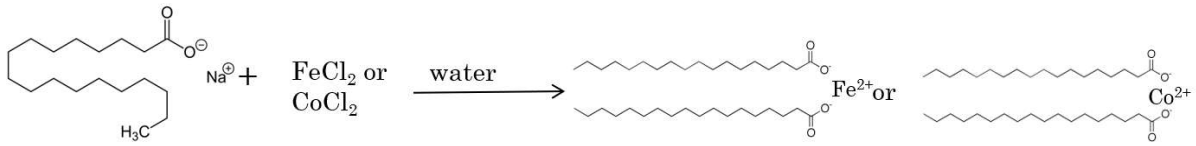

Figure 37: Synthesis of iron (II) and cobalt (II) stearate precursors

For iron (II) stearate, a light brown powder was obtained. For the cobalt (II) stearate, it was a violet powder. The thermal decomposition of these complexes being directly dependent on the chemical structure, thermogravimetry (TG) analysis and by FT-IR spectroscopy.

a) Fourier Transform Infrared spectroscopy (FT-IR)

The FT-IR spectra of iron (II) stearate and cobalt (II) (Figure 38) have been indexed according to the work of Abrahamson and Lukaski on iron stearate[134] as well as the work of Perton *et al.*[135]

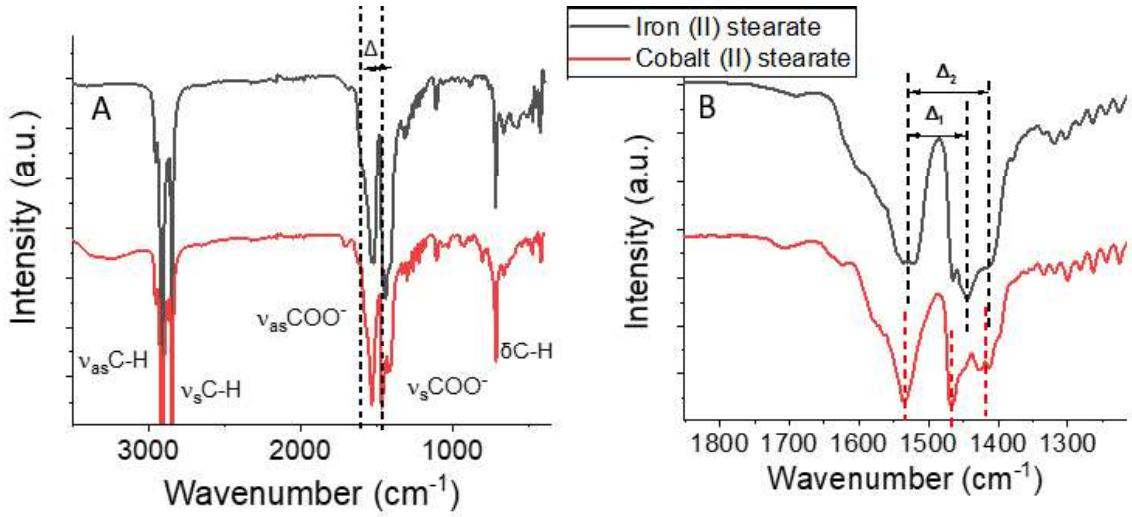

Figure 38: A) FT-IR spectra of iron (II) stearate and cobalt (II) stearate and B) its zoom on the COO^- vibration bands

Bands located at 2917 and 2850 cm^{-1} are characteristic of the symmetric (ν_sC-H) and antisymmetric (ν_{as}C-H) stretching vibrations of the stearate hydrocarbon chains. Peaks centered at 1554 cm^{-1} and 1414 cm^{-1} correspond to the symmetric ($\nu_s COO^-$) and antisymmetric ($\nu_{as} COO^-$) stretching vibrations of the carboxylic acid group. The peak located at 720 cm^{-1} emerges from the H-C-H scissoring of the alkylene chain.

Moreover, the distance Δ between $\nu_{as} COO^-$ and $\nu_a COO^-$ bands can give information on the coordination mode of the ligand with the surface of metal oxides.[136,137] For 200 < Δ < 320 cm^{-1}, the coordination mode is monodentate, for 140 < Δ < 190 cm^{-1} it is bridging bidentate and for Δ < 110 cm^{-1} chelating bidentate. Schemes of these coordination modes are shown in Figure 39.

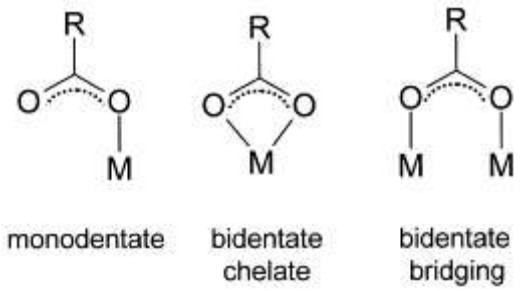

Figure 39: Coordination modes of the metal cation (R is an alkyl chain and M the metallic cation)

Two values of Δ were observed for both iron and cobalt stearate (Table 1). They correspond to bidentate chelate mode (Δ_1) and bidentate bridging mode (Δ_2). It can be seen that there is roughly an equal proportion of bidentate chelate and bidentate bridging for the iron (II) stearate. In contrast, for the cobalt (II) stearate the bidentate chelate mode predominates over the bidentate bridging mode.

Table 1: Δ_1 and Δ_2 values measured for the iron and cobalt stearate precursors

Sample	Δ_1	Δ_2
Iron (II) stearate	85	129
Cobalt (II) stearate	70	125

Hence, FT-IR analysis proved that the synthesis of the precursors has been successfully processed and that the coordination mode for iron (II) and cobalt (II) stearates is a mixture between bridging and chelating bidentate modes. Their decomposition temperature will be investigated in the next part thanks to thermogravimetric analysis.

b) Thermogravimetric (TG) analysis

As previously discussed in the Lamer theory[101], the decomposition temperature of the precursors is a key parameter for the synthesis of the NPs[119] and particularly for the synthesis of a stoichiometric spinel shell. In order to verify the good properties of the precursors in terms of decomposition temperature, thermogravimetric (TG) analyses were performed (Figure 40).

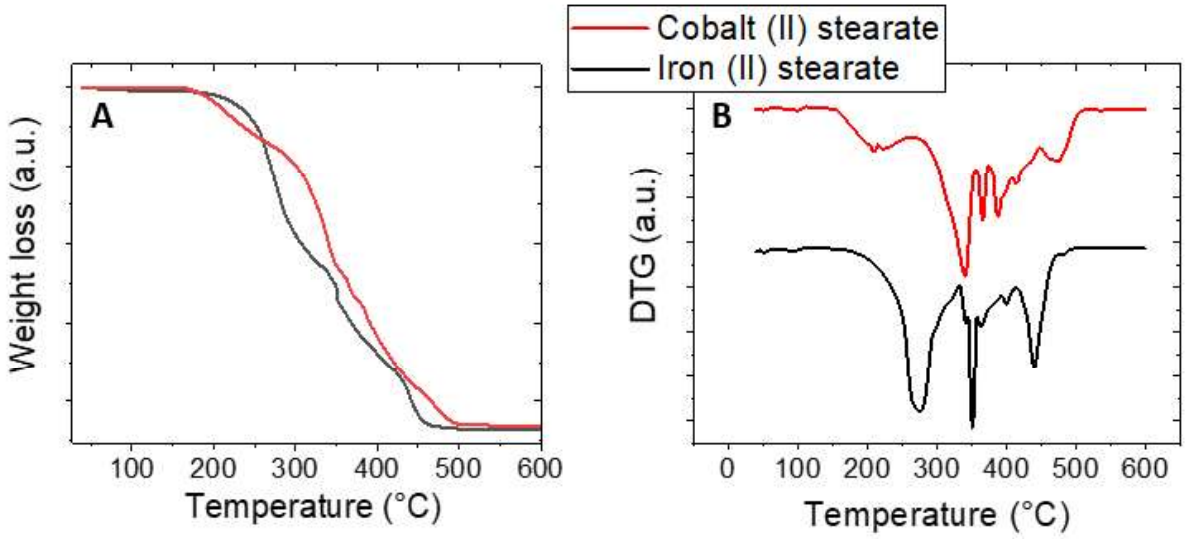

Figure 40: A) TG curves obtained for cobalt (II) and iron (II) stearate precursors measured under air at a rate of 5 °C.min^{-1} with B) their corresponding derivative curves

The iron precursor starts losing weight around 250 °C while for the cobalt one there is a small loss of weight around 200°C at first. This first weight loss observed on cobalt can be attributed to water molecules complexing the metallic center in the cobalt (II) stearate[119]. According to Cotin *et al.*[119] the presence of water molecules complexing the metallic cation in the precursor will stabilize it and consequently increase its decomposition temperature. Indeed, these water molecules don't influence the oxidation state of the metal but they do modify it electronic structure. Then, a constant decrease of the weight can be observed until about 450 °C for iron stearate and 500°C for cobalt stearate. Figure 40 evidences that cobalt stearate has a higher decomposition temperature than iron stearate. These results are consistent with the FT-IR data showing that the cobalt cation was more strongly bonded (more chelating bidentate) to the stearate chains than the iron cation. The derivative of TG analysis (Figure 40B) confirmed that the main weight loss is 280°C for iron stearate while it starts more around 330°C for cobalt stearate, in agreement with the literature on similar precursors[102,138]. This start is generally attributed to the nucleation step. The growth steps then start around 370 °C after which the final weight loss occurring between 400 and 500°C corresponds to the total decomposition of the organic ligands.

This result is in contradiction with the FT-IR results: Bronstein *et al.*[139] studied the influence of iron oleate structure on the formation of iron oxide NPs and concluded that a change in the coordination mode observed thanks to FT-IR spectroscopy corresponds to a change in the nucleation temperature observed on the differential scanning calorimetry curves. They observed that, for higher amount of bridging bidentate coordination modes, the temperature at which the first decomposition of the compound happens (attributed to the nucleation temperature) increased. In our case, the FT-IR spectra are displaying a higher amount of bidentate chelate for cobalt (II) stearate than for iron (II) stearate (hence a lower decomposition temperature for this precursor). The higher decomposition temperature of the cobalt precursor is likely due to its hydration state and the water molecules complexing the metallic center that stabilize it. The hydration state probably has more influence than the coordination mode in that case.

To conclude, the precursors have been successfully synthetized and can be used for the design of core-shell cobalt iron oxide NPs even though they present a difference up to 50°C in their decomposition temperatures. This difference could lead to some gradient of composition in the shell or to some phase segregation. The characterizations of the synthesized NPs using these stearate precursors will be described in the following parts and the composition of the shell will be further analyzed.

4) *Nanoparticles synthesis and characterizations*

NPs were synthesized in order to combine $Fe_{3-d}O_4$ as a conductive core and $CoFe_2O_4$ as an electrocatalytic active shell. The synthesis of core-shell nanoparticles consists in the thermal decomposition of metal precursors in high boiling temperature solvents according to a two-step-seed-mediated growth process (Figure 41). First, iron stearate was decomposed in dioctylether (*bp* 290 °C in order to form pristine $Fe_{3-d}O_4$ nanoparticles. Second, iron and cobalt stearates were decomposed together in octadecene (*bp* 315 °C) in order to grow a $CoFe_2O_4$ shell at the surface of pristine nanoparticles. Each step happened in the presence of oleic acid which acted as a stabilizing agent of metal complex decomposition regulation) and NPs (colloidal stability).

As the core size and the shell thickness are the parameters studied in this work, the NPs were designed using different iron stearate precursors. Indeed, iron (III) stearate presents a higher decomposition temperature than iron (II) stearate and will generate NPs with an increased diameter compared to iron (II) stearate.[135] To investigate the influence of the shell thickness, various quantities of cobalt and iron precursors were then added during the second step of the synthesis in order to grow thin and thick shells. The details of all protocols were given in chapter 2. Four nanoparticles with different core-shell structures were synthesized in order to study systematically the influence of the core structure and the shell thickness on their electrochemical properties (see next chapters).

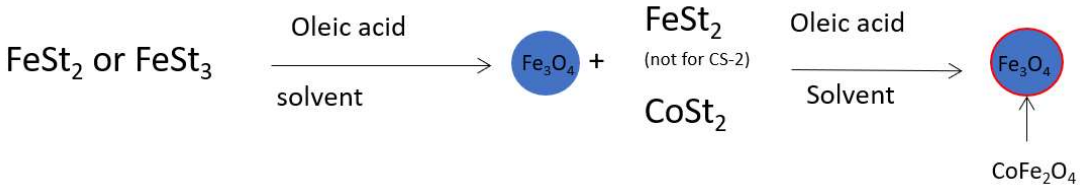

Figure 41: Schematic illustration of the synthesis of the core-shell NPs according to a two-step seed-mediated growth process by completing thermal decomposition of $FeSt_2$ iron (II) stearate; $FeSt_3$ iron (III) stearate and $CoSt_2$ cobalt (II) stearate.

Table 2 presents some experimental details about the NPs synthesis. The full protocol for the NPs synthesis was described in chapter 2.

Table 2: precursors and solvents used for the synthesis of the core-shell NPs. $CoSt_2$: cobalt (II) stearate, $FeSt_2$: iron (II) stearate and $FeSt_3$: iron (III) stearate

Sample name		1st step	2nd step
CS-1	Precursor(s)	$FeSt_2$ 2.2mmol	$CoSt_2$ 0.46mmol and $FeSt_2$ 0.94mmol
	Solvent(s)	dioctyl ether (T_b=290°C)	dioctyl ether (T_b=290°C) and 1-octadecene (T_b=315°C)
CS-2	Precursor(s)	$FeSt_2$ 2.2mmol	$CoSt_2$ 0.531mmol
	Solvent(s)	dioctyl ether (T_b=290°C)	dioctyl ether (T_b=290°C) and 1-octadecene (T_b=315°C)
CS-3	Precursor(s)	$FeSt_3$ 2.2mmol	$CoSt_2$ 0.73mmol and $FeSt_2$ 1.47mmol
	Solvent(s)	Squalane (T_b=421°C) and dibenzyl ether (T_b=298°C)	dioctyl ether (T_b=290°C) and 1-octadecene (T_b=315°C)
CS-4	Precursor(s)	$FeSt_3$ 2.2mmol	$CoSt_2$ 1.84mmol and $FeSt_2$ 3.68mmol
	Solvent(s)	dioctyl ether (T_b=290°C)	dioctyl ether (T_b=290°C) and 1-octadecene (T_b=315°C)

After the synthesis, some washing steps were necessary in order to remove unreacted precursors, intermediate products, the free oleic acid in the solution and the solvents used for the synthesis. A wide panel of techniques was used to characterize the obtained nanoparticles.

a) Transmission electron microscopy (TEM)

The NPs were first characterized by TEM in order to determine the shape and the size distribution of both $Fe_{3-d}O_4$ pristine and core-shell nanoparticles (Figure 42).

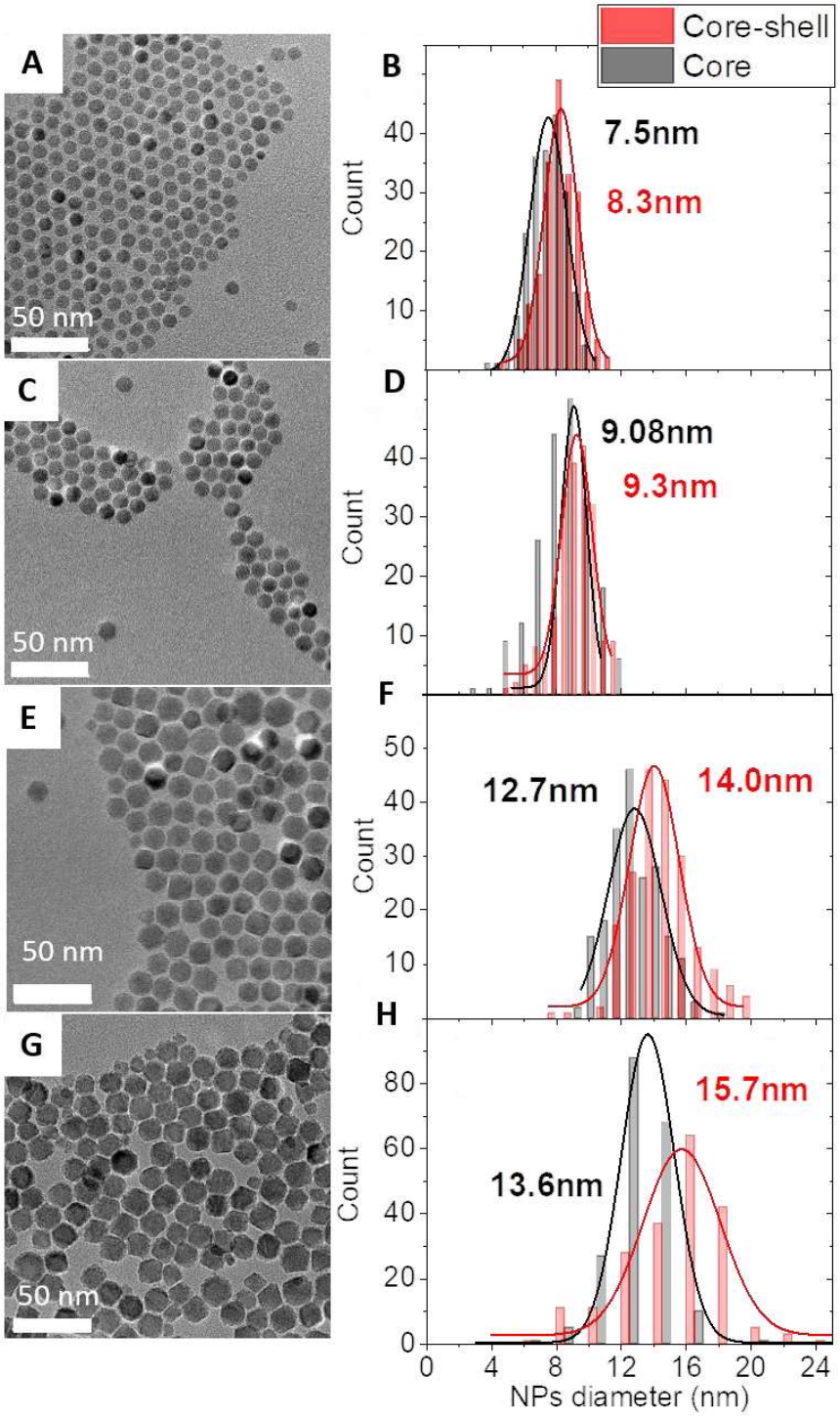

Figure 42: TEM images and size distributions of CS-1 (A, B), CS-2 (C, D), CS-3 (E,F), CS-4 (G,H).

From the TEM images, it can be concluded that the NPs all present a narrow size distribution both for the pristine and the core-shell NPs. The largest NPs (CS-3 and CS-4) display wider size distributions,

although they are narrow enough for the purpose of our study. These NPs are presenting in their majority a spherical shape even though some of them (mainly the CS-3 and CS-4) present some larger facets according to their largest size. In the next parts, the NPs will be assimilated as spheres in order to estimate their volume and surface.

In order to confirm the presence of cobalt in the catalyst, energy dispersive X-ray spectroscopy (EDX) was performed upon TEM analyses. The atomic percentages of cobalt are consistent with the amount of cobalt and iron precursors that were used. They vary from 12 to 19 % depending on the type of NPs (Table 3).

Table 3: Characteristic values of the diameter of pristine $Fe_{3-\delta}O_4$, CS-1, CS-2, CS-3 and CS-4. The estimated shell thickness is the difference between the average core-shell diameter and the average core diameter that is then divided by two. The atomic concentration of cobalt vs. *iron calculation is Co/(Co+Fe).*

Sample	$Fe_{3-\delta}O_4$ diameter (nm)	Core-shell diameter (nm)	Estimated shell thickness (nm)	Atomic % of cobalt *vs.* iron	Expected Atomic % of cobalt *vs.* iron
CS-1	7.5	8.3	0.4	16	9
CS-2	9.1	9.3	0.15	15	3
CS-3	12.7	14.0	0.65	19	9
CS-4	13.6	15.7	1.05	12	12

It can be observed that for CS-1 and CS-2 and CS-3 the atomic proportion of cobalt is higher than expected from the size variation data. Indeed, assuming the NPs were perfectly spherical it was possible to calculate the theoretical ratio of cobalt *vs.* iron in the NPs from the volume of the core and the volume of the shell. From these volumes, their contribution to the total volume of the NPs was calculated thanks to the following calculation (x being the shell or the core):

$$V_x\% = \frac{V_x}{V_{tot}}$$

From these volumes' contribution as in the core there is only iron (100 %) and in the shell there is 66 % of iron, the theoretical proportion of iron vs cobalt in the NPs was calculated. The calculation was the following:

$$V_{shell}\% \times 0.66 + V_{core}\% \times 1 = \%_{at}Fe$$

However, the expected proportion of cobalt was calculated by neglecting the potential diffusion phenomena that can occur during this type of synthesis. In the literature some articles reported the occurrence of diffusion phenomena during NPs synthesis[102,140]. In the case of our core-shell catalyst,

the oxidation in maghemite (Fe_2O_3) at the surface of Fe_3O_4 NPs generates vacancies which favor the diffusion of Co^{2+} (this oxidation layer has been reported to be about 2 nm thick and is due to the oxygen coming from the air as the synthesis is performed under air[102]). Consequently, this difference demonstrates the presence of important diffusion phenomena during the growth of the shell : a thicker cobalt ferrite shell is expected due to this diffusion phenomenon[102,113,114,141]. This diffusion phenomena occurred during all the syntheses but will be particularly visible on small NPs. Consequently, CS-1 that cumulates crystal growth and the diffusion phenomena is expected to display a thicker shell when compared to the one of CS-2 for which only the diffusion will occur. On CS-3 NPs, diffusion also occurs but as the core diameter is larger, the shell should still be well defined. On CS-4 NPs, the expected atomic % of cobalt *vs.* iron is the same as the one measured in EDX, the diffusion becomes negligible even though there should still be some diffusion occurring.

To sum up, TEM images showed that the NPs have been successfully synthesized. They present a well-defined close-to-spherical shape and a narrow size distribution. Their size generally increased after performing the second thermal decomposition of Fe and Co stearate which is consistent with the growth of a shell onto the surface of the pristine $Fe_{3-\delta}O_4$ NPs. Although the size increase for CS-1 and CS-3, the shell thickness is not sufficient to justify the cobalt content measured by EDX. These results agree with the diffusion of metal cations inside the structure during the shell synthesis. Indeed, the pristine $Fe_{3-\delta}O_4$ core is generally oxidized in maghemite on about 2 nm at the surface and during the synthesis the metal cations can diffuse though the vacancies of this oxidized layer[102,113,114,141]. For CS-2 only the diffusion phenomena occurred hence the diameter of the core and the core-shell structure is similar. On CS-4 the crystal growth seems to be predominant over the diffusion.

After verifying the size distribution of the NPs, it was important to make sure that they were properly washed and that no precursors that didn't react or free oleic acid were present in the solvent in which they are stored.

b) *Fourier transform infra-red spectroscopy (FT-IR)*

After the synthesis of the NPs, it is important to wash them chemically in warm acetone to get rid of all the solvents used during the reaction as well as all the stearate precursors that wouldn't have reacted during the reaction. The washing steps are described in chapter 2, they are also used to remove all the free oleic acid that is not attached to the NPs. This molecule acts as a surfactant, its presence allows the NPs to stay as a colloidal solution, i.e. avoiding aggregation. Therefore, some oleic acid should remain at the nanoparticle surface. Therefore, FT-IR was used to monitor the washing step (Figure 43A).

Bands at 2920 and 2850 cm^{-1} are characteristic of symmetric and antisymmetric stretching vibration modes of the alkyl chain (νC-H) belonging to the oleic acid surfactant. The symmetric and antisymmetric stretching vibration modes of the carboxylic acid function (νCOO^-) correspond to bands centered around 1635 cm^{-1} and 1414 cm^{-1} [102,142]. The absence of a peak around 1710 cm^{-1} corresponding to the stretching vibration of free carboxylic acid groups (νC=O) confirms that there is no more free oleic acid. However, the peak at 720 cm^{-1} correspond to C-H scissoring mode of the metal precursor (Figure 43 B).

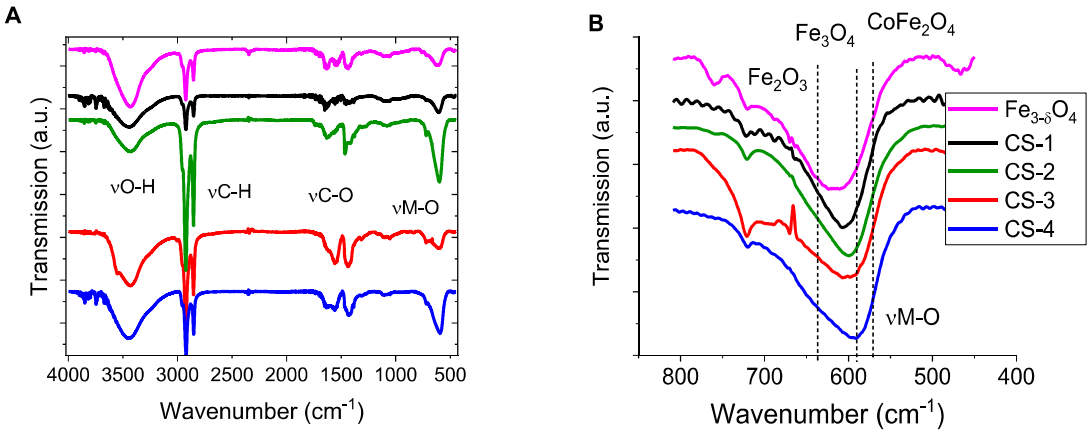

Figure 43: A) FT-IR spectra of the synthesized NPs: $Fe_{3-\delta}O_4$ (8 nm average diameter), CS-1, CS-2, CS-3 and CS-4 B) is a zoom of the metal-oxide band normalized by the peak at 600 cm^{-1} for these NPs.

Moreover, as for the analysis of the precursors, the distance Δ between the two νCOO^- bands can give information on the coordination mode of the ligand at the surface of NPs[136,137,139]. For 200 < Δ < 320 cm^{-1}, the coordination mode is monodentate, for 140 < Δ < 190 cm^{-1}, it is bridging bidentate and for Δ < 110 cm^{-1}, chelating bidentate. However, the multiple peaks and the noise of the signal in this region do not allow the characterization of Δ for the core, CS-1 and CS-4. For CS-2 and CS-3 it is of 135 and 148 cm^{-1} respectively; so, the coordination mode is bridging bidentate. It is likely that the other NPs will present the same coordination mode.

Additionally, the metal oxide stretching band located around 600 cm^{-1} (Figure 43 B) can give information about the chemical composition and oxidation state of the NPs[143]. Indeed, the maghemite (γFe_2O_3) displays several shoulders from 800 cm^{-1} to 600 cm^{-1} exhibiting a maximum at 639 cm^{-1} while magnetite (Fe_3O_4) that presents a higher content in Fe^{2+} presents a single band at 574 cm^{-1} and a shoulder at 700 cm^{-1}. Here, generally on the core-shell NPs, it can be observed that the band is narrower than the core's one. The maximum of the peak seems also shifted to shorter wavenumbers compared to the core's peak which is consistent with the creation of a shell of $CoFe_2O_4$ and the disappearance of the maghemite phase. Additionally, for the core, the maximum can be observed at 615 cm^{-1} and some small shoulders at 720 cm^{-1} and 760 cm^{-1} can be seen, which is consistent with the

potential oxidation of the magnetite into maghemite at the surface of the $Fe_{3-\delta}O_4$ NPs. From these results, it is not possible to evidence the formation of a $CoFe_2O_4$ shell as the bands characteristic of Fe_3O_4 and $CoFe_2O_4$ are too close to be differentiated.

Lastly, the amount of oleic acid surrounding the NPs can be evaluated using the intensity ratio of the two-band characteristic of C-H vibration around 2920 cm^{-1} and M-O around 600 cm^{-1}. When this ratio is close to one for magnetite NPs it means that they are properly washed. Considering the fact that the system studied is not pure magnetite but presents a cobalt ferrite shell and that empirically it has been more difficult to wash (probably due to a different interaction between the cobalt ferrite and the magnetite), this ratio was not possible to obtain for all the NPs. Indeed, if too many washing steps are performed, the oleic acid surrounding the NPs is removed and there are risks of aggregation of the NPs. The aggregation state of the NPs was controlled using granulometry measurements in volume, intensity and number of counts. They will be presented in the following part.

To sum up, the FT-IR analysis showed that the NPs were consisting of a partially oxidized magnetite core ($Fe_{3-\delta}O_4$) on top of which a shell grew. They are correctly washed even though some traces of stearate can be seen and that the ratio of intensity of the M-O band *vs.* the C-H one is not exactly 1-1 but this is due to the presence of cobalt in the shell that makes it more difficult for the oleic acid to be removed from the NPs surface. Further washing can't be realized without risking an aggregation of the NPs. After the verification of the proper washing of the NPs, one other important thing to verify is the aggregation state of the NPs. The objective is to have a stable colloidal solution of the NPs in chloroform and one tool that can be used to characterize the extent of NP aggregation is the granulometry (or dynamic light scattering). This technique will be presented in the next part.

c) *Granulometry measurements*

Granulometry performed by using dynamic light scattering (DLS) is useful to detect the presence of aggregates in colloidal solutions of NPs. Indeed, the electrochemical properties are highly dependent of the surface state of the catalyst and of the surface available for the reaction to occur. An aggregation of the NPs would lead to less surface available for the reaction to happen and consequently to a decrease of the catalytic activity. The NPs are surrounded by oleic acid that is grafted at their surface, this surfactant is the reason for the stability and non-aggregation of the NPs in solvents such as chloroform, toluene, hexane or THF. The hydrodynamic diameter (NPs and oleic acid system) has been measured for the different types of NPs (Figure 44).

There are different ways to measure the distribution of the NPs via DLS:

- The number distribution that shows the number of particles in the different size bins.
- The volume distribution that shows the total volume of particles in the different size bins.
- The intensity distribution that describes how much light is scattered by the particles in the different size bins.

Typically, the difference between these distributions is that intensity distribution gives more importance to large particles, when the number distribution gives more weight to the small particles and the volume distribution only considers the volumetric contribution of a particle of a given size. All these distributions are correct in the sense that they are just different representations of the reality and it depends on how you look at it. In order to compare one sample to the other, it is important to use the same distribution for the representation.

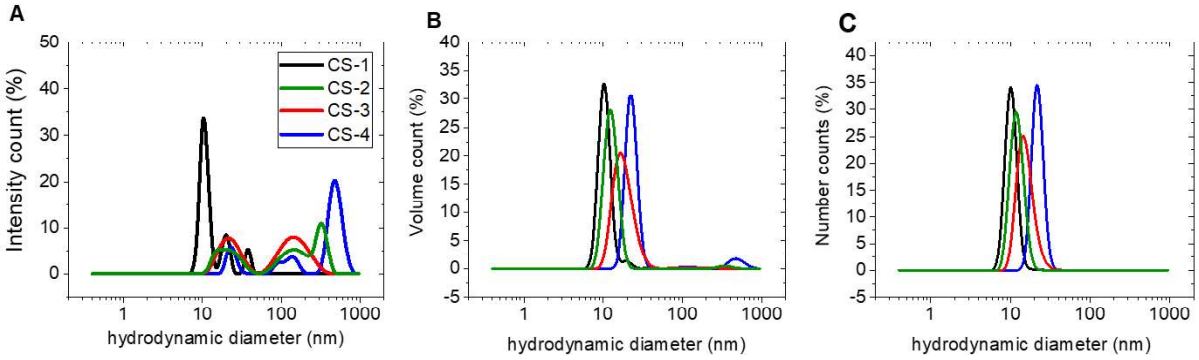

Figure 44: Granulometry measurements. The hydrodynamic diameter is plotted as a function of A) the intensity count, B) the volume count and C) the number count for CS-1, CS-2, CS-3 and CS-4.

Figure 44 evidences a monomodal distribution of the hydrodynamic diameter in number and volume counts for all NPs analyzed. Some additional contributions can be seen in the volume count for CS-2 and CS-4 around 300 nm that are characteristic of a few aggregates. In intensity, these aggregates are dominating the signal. However, these aggregates can be neglected as the major peaks are centered around 10-20 nm for all NPs for the volume and number distribution.

The values obtained for the diameter of the NPs are higher than the sizes measured in TEM because DLS gives the hydrodynamic diameter which is sensitive to both the inorganic NPs and the surfactant (oleic acid) at their surface. Their diameter is then increased by about 2 nm compared to the TEM diameter.

Here the volume distribution and number distribution are close to the sizes measured via TEM so this measurement was privileged for the hydrodynamic diameter (Table 4).

Table 4: Measured maximum of the volume and number distribution hydrodynamic diameters for CS-1, CS-2, CS-3 and CS-4 samples

Sample	Diameter volume counts (nm)	Diameter Number counts (nm)	TEM diameter (nm)
CS-1	10.1	10.1	8.3
CS-2	11.5	11.9	9.3
CS-3	15.8	13.5	14.0
CS-4	21	21.1	15.7

To sum up, granulometry showed that the NPs were non-aggregated, stable in solution in chloroform, and present a monomodal distribution. The NPs crystalline structure can then be characterized.

d) X-Ray diffraction (XRD)

XRD is powerful to characterize the crystalline structure of nanoparticles. The cell parameter and the crystallite size can be calculated from XRD patterns. Experimental details about the diffractometers used to perform the measurements are given in chapter 2.

Using references for Fe_3O_4 (JCPDS card n° 19-062), ɣ-Fe_2O_3 (JCPDS card n° 39-1346) and $CoFe_2O_4$ (JCPDS card n°00-022-1086), it was possible to compare the obtained diffractograms and calculated cell parameters in order to determine the phase and the chemical composition of the NPs. For example, XRD can give information on the oxidation state of pristine iron oxide nanoparticles. Indeed, the surface of magnetite (Fe_3O_4) nanoparticles is usually oxidized in maghemite (ɣ-Fe_2O_3).[102] Both phases belong to the inverse spinel structure but present slightly different cell parameters 8.338 Å for the maghemite and 8.396 Å for magnetite. In that case, it will be possible to determine if the iron oxide NPs have been oxidized or not.

The diffractograms were measured with a reference of silicon added to the NPs (Figure 45) in order to calibrate them and to obtain a better refinement of the cell parameter and the crystallite size.

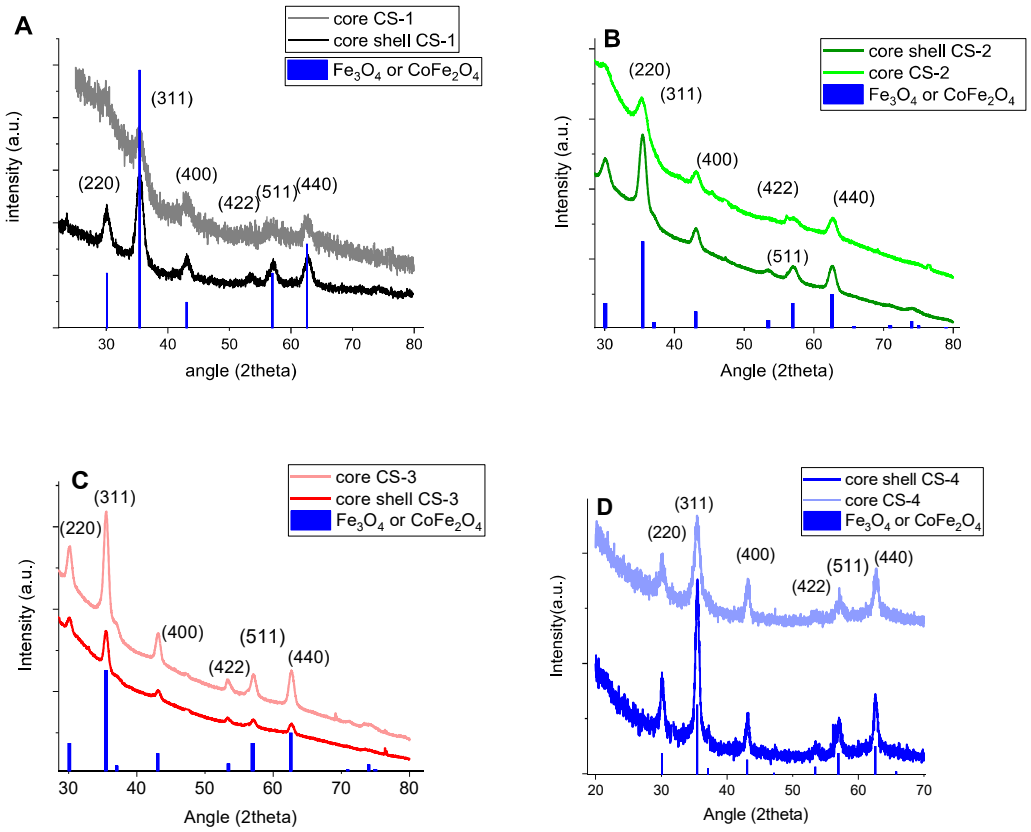

Figure 45: Diffractograms obtained for the core and core-shells systems of CS-1 (A), CS-2 (B), CS-3 (C), and CS-4(D).

Figure 45 shows that all the samples present the peaks characteristics of the inverse spinel structure. The $CoFe_2O_4$ and the Fe_3O_4 both having the same structure with almost the same cell parameter (8.396 Å for magnetite and 8.3919 Å for $CoFe_2O_4$), it is not possible to discriminate them from a diffractogram.

Additionally, one can observe that the peaks are narrowing when the shell has grown. This indicates an increase of the average crystallite sizes (Table 5), which is consistent with the epitaxial growth of a crystalline shell on top of the iron oxide core. The cell parameters of the different NPs were also calculated using Rietveld refinement thanks to the fullprof program[122,123].

Table 5: cell parameters and crystallite sizes calculated for CS-1, CS-2, CS-3 and CS-4 and comparison with the TEM diameters

Sample	Cell parameter (Å)	Crystallite size (Å)	TEM diameter (Å)
CS-1	8.3815 ± 0.0002	54.3± 0.3	93
CS-2	8.3890 ± 0.0003	63.7 ± 2.4	93
CS-3	8.3875 ± 0.0004	112.6± 0.1	140
CS-4	8.3866 ± 0.0004	94.9 ± 1.4	157

The cell parameters calculated for all core-shell NPs are similar. However, this value is inferior to the theoretical one given for either Fe_3O_4 or $CoFe_2O_4$ (about 8.39 Å). This difference could be explained by the partial oxidation of the core which exhibits a smaller cell parameter and would constraint the system. Also, if the size of the crystallites is compared to the TEM measurements for the NPs size (Table 5), one can see that XRD measurements are giving a smaller size for the coherent scattering domains. This difference can be partially explained by the fact that on the TEM images a 2D projection of the NPs is observed, which tend to overestimate the nanoparticle size. Other factors that likely influence the crystallite size is the anisotropy of the NPs and the peak broadening caused by small particles contribution. Also, if the NPs present some structural defects, they are likely to display a smaller crystallite size compared to the TEM images.

To sum up, the XRD patterns showed that all core-shell NPs present an inverse spinel structure, with a cell parameter of about 8.38 Å which is a little smaller than expected according to the growth of a $CoFe_2O_4$ shell[114] (8.41 Å was expected) this is probably due to some constraints in the crystalline structure of the NPs. Apart from CS-2 NPs, the crystallite size in gradually increasing with the size of the NPs and it also increases between the pristine iron oxide and the core-shell NPs which agree with the growth of $CoFe_2O_4$ shell although the cobalt ferrite structure can't be differentiated from the magnetite. Other characterizations techniques are needed to determine the cobalt distribution inside the shell.

e) Scanning transmission electron microscopy with a high-angle annular dark-field (STEM-HAADF) and electron energy loss spectroscopy (EELS) mapping

These measurements were performed by our partner from the "Instituto de Nanociencia y Materiales de Aragón" (INMA). The images obtained thanks to STEM-HAADF allow to see the lattice fringes of the crystallographic planes of the NPs. The latter were then used to analyze the crystallinity and the presence of defects inside the structure. By coupling this technique with the EELS which allows the observation of the iron, cobalt and oxygen spatial distribution within the core-shell NPs, one can have an idea of the surface state of the NPs and prove the existence of a core-shell system. The STEM-HAADF images are presented in Figure 46, the conditions of the measurements are presented in chapter 2.

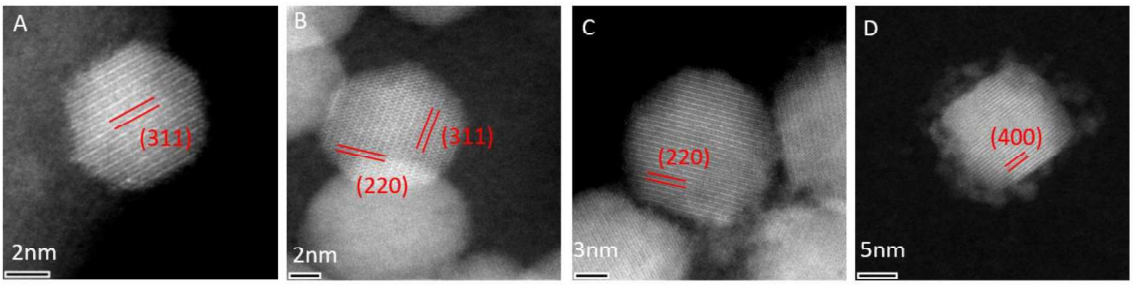

Figure 46: STEM-HAADF images of A) CS-1, B) CS-2, C) CS-3 and D) CS-4.

All NPs present a good crystallinity as shown by well-defined lattice fringes all-across each NP. The planes that are shown on the NPs are the ones characteristic of the spinel structure of iron oxides and assimilated chemical compositions: (311), (220) or (400) depending on the NPs. It can be seen that on CS-4 there seems to be some defects in the structure as the NPs seem rougher and are not as defined as for the other syntheses. Some line defects consisting in one lattice fringes joining another (Figure 47) can be seen but they are equally present in all samples. These defects certainly contribute to the smaller crystallite size compared to the TEM average size that were mentioned in the XRD characterizations.

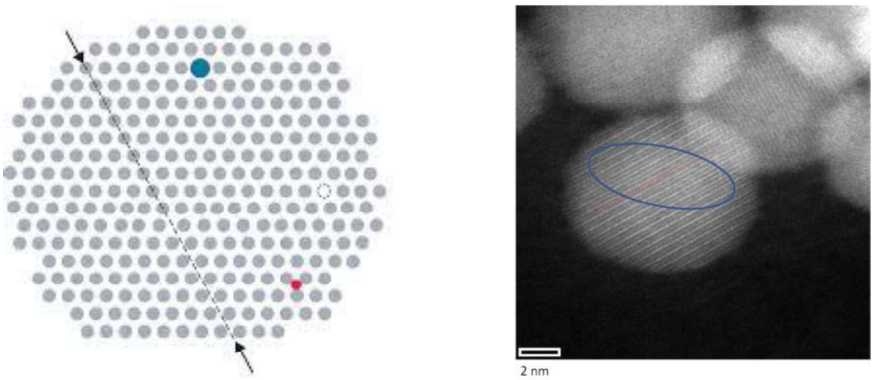

Figure 47: left: 2D illustration of the defects that can be present in a crystal: substitutional (blue) and interstitial (red) impurities, vacancies (white void), and line defects (dashed line) taken from[144]. Right: line defect observed on CS-2

The NPs are crystalline also in the shell. Due to the inverse spinel structure and the close cell parameters of $Fe_{3-\delta}O_4$ and $CoFe_2O_4$ materials, it is not possible to differentiate these two components in the core-shell NPs via these images. Consequently, the core-shell structure was proved by EELS measurements (Figure 48).

Thanks to these images it is possible to observe the cobalt (blue), iron (green), and oxygen (red) distribution in the NPs. From these images the core-shell structure of CS-2, CS-3 and CS-4 is evidenced: the sum of all the atomic contributions of oxygen, cobalt and iron are clearly exhibiting the presence of a thin and sharp cobalt iron oxide shell localized at the edges of the NPs. The shell seems to be about 1 nm thick. It can also be observed that the shell of the NPs is thicker and sharper on the larger NPs

(CS-4 and CS-3) compared to CS-2 NPs. It can also be observed that for CS-2 and CS-4 NPs, the cobalt distribution is rather homogeneous while for CS-3 NPs it seems quite dispersed. In chapter 5, the influence of this distribution will be investigated.

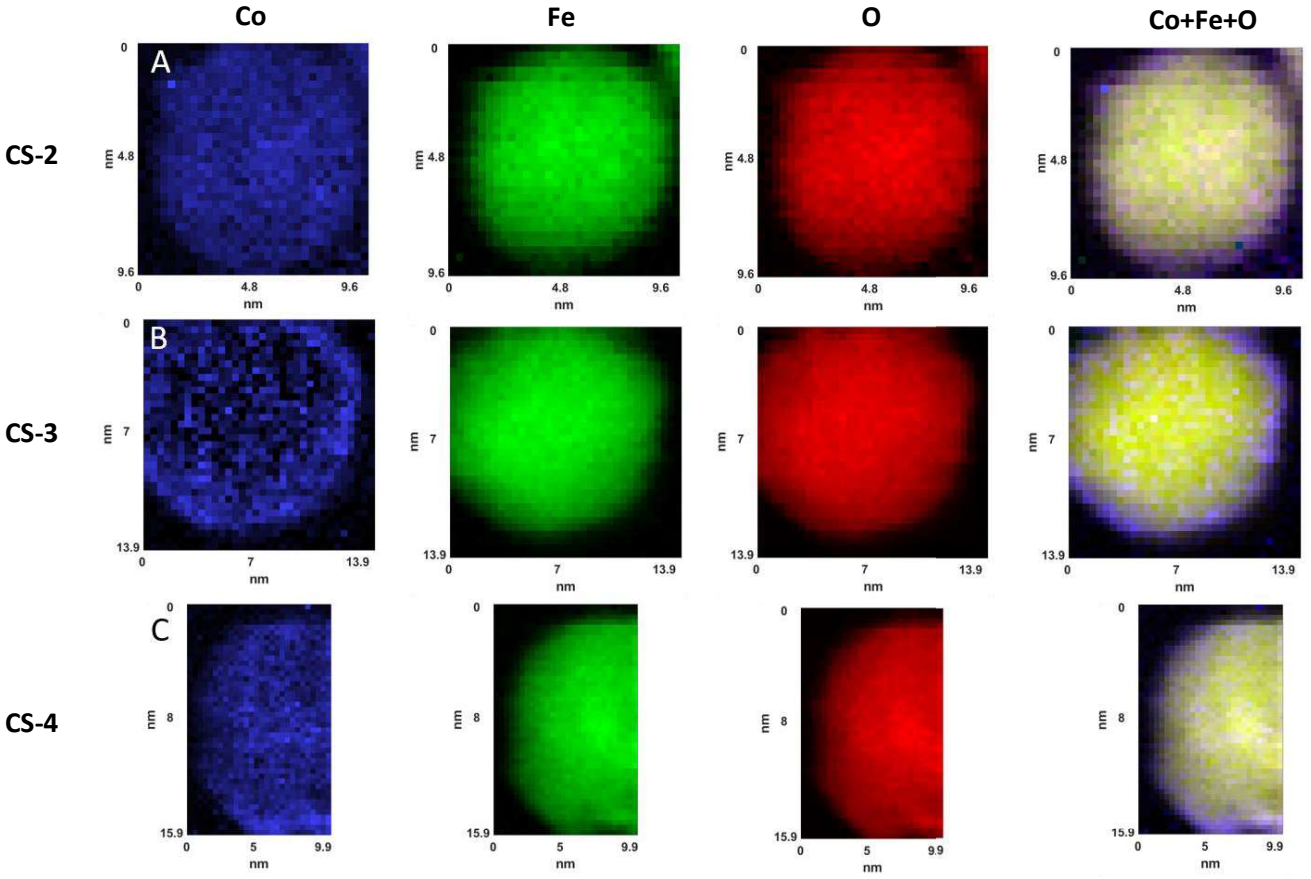

Figure 48: EELS images of A) CS-2, B) CS-3, and C) CS-4 NPs, cobalt is in blue, iron in green, oxygen in red. The image on the right is the sum of all the atomic contributions.

The EELS images also allowed for the quantification of the atoms present in the structure. Consequently, it was possible to plot the profile of the atomic concentration along a cross-section in the NPs (Figure 49 C, F, I, L) in order to get a better idea of the cobalt proportion in the shell. In theory, if the shell is composed of pure $CoFe_2O_4$, it should be composed of about 14 $\%_{at}$ of cobalt, 28 $\%_{at}$ of iron and 57 $\%_{at}$ of oxygen.

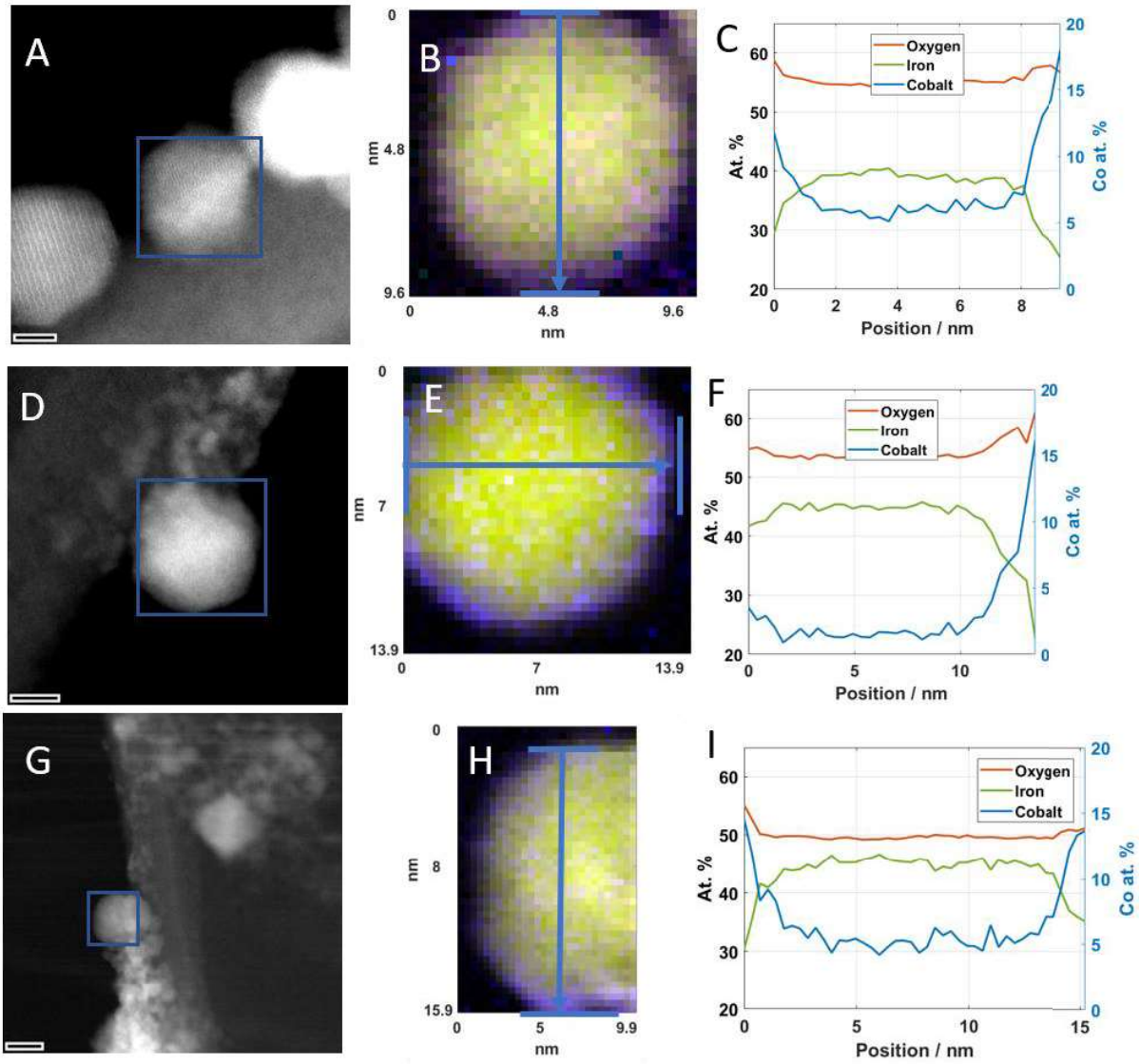

Figure 49: EELS mapping and profile of atomic concentration for CS-2 (A, B, C), CS-3 (D, E, F), and CS-4 (G, H, I). Red: oxygen, green: iron, blue: cobalt. On the profile of concentration, the concentration of cobalt is on the right while the one of iron and oxygen is on the left.

For CS-2 and CS-3 the proportion of cobalt in the shell is higher than the expected one: it reaches about 19 % for CS-2 and 16 % for CS-3. This indicates that there is a gradient in the cobalt content in the shell for these two samples and that the shell is likely $Co_{1+x}Fe_{2-x}O_4$ with x between 0 and 1. This is likely due to the difference in decomposition temperature of the cobalt and iron precursors that was discussed in the TG analysis. The amount of cobalt at the surface reaches 17% for CS-2 while it is 15% for CS-3 and 14% for CS-4. Considering the precision of the measurement (about 1 %) and the fact that EELS is a local analysis, it is likely that the cobalt proportion observed at the surface is similar on all NPs batches. This shell composition with a richer cobalt content at the NPs surface agrees with what has been observed by EELS technique on NPs synthesized with the same method[140].

Additionally, the diffusion could also explain the XRD results for the cell parameter: for all NPs, the cell parameter measured was lower than the expected one for $CoFe_2O_4$. We attributed it to the constraint from the core cell parameter but a higher content of cobalt in the shell ($Co_{1+x}Fe_{2-x}O_4$) would also explain this difference. Indeed, in that case, the cell parameter would be intermediary between the one of $CoFe_2O_4$ (e.g. 8.392 Å) and Co_2FeO_4 (8.244 Å (JCPDS card 04-016-3953)).

To sum up, TEM images have shown that the core-shell NPs were all crystalline and present planes characteristic of the spinel structure. The core-shell structure has been evidenced by EELS images showing the highest content of cobalt on the edge of NPs. The composition profiles of iron cobalt and oxygen in the NPs have been calculated thanks to the EELS images and they displayed a higher proportion of cobalt in the outer shell than the expected one, leading to the conclusion that the shell presented a gradient of cobalt and that its chemical formula was $Co_{1+x}Fe_{2-x}O_4$. However, TEM and EELS are local analysis techniques and only consider isolated NPs and not the whole sample. To get a more accurate estimation of the thickness of the shell and shed light on the diffusion phenomenon, one would need to consider a high number of particles.

f) Depth profiling

The EELS measurements have evidenced the core-shell structure locally and have given an estimation of the amount of cobalt on a single NP. In order to have another estimation of the average iron *vs.* cobalt proportion and confirm the existence of the core-shell structure on a great number of NPs it is possible to use the XPS with a variable energy of photons. Indeed, when acquired using a synchrotron source, one can get a complete quantitative elemental analysis as a function of the analysis depth: 68 % of all photoelectrons will come from within a depth of λ (the inelastic mean free path) and 99.7 % will be arising from a 3λ depth[145,146].

Using the following equation, it is possible to calculate the proportion of a certain element in the material:

$$C_A = \frac{\frac{I_A}{S_A}}{\sum\left(\frac{I_n}{S_n}\right)}$$

Equation 8: Relation between the atomic concentration of a given element and the area of the XPS peaks of the material

C_A is the atomic concentration of a chosen element among a number of n elements. S_A- - - S_n are the sensitivity factors that depend on the cross section of the element and the flux of the incident source. It is worth noting that in the case of the polarized synchrotron radiation, an anisotropy factor

should be considered to calculate this ratio. However, while considering the 2p orbitals of cobalt and iron, the error is compensated when the ratio of these two elements is calculated.

It is then possible with synchrotron radiation to send photoelectrons with various incident energies in order to probe different depths of the NPs (Figure 50) and to correlate it with the area of the cobalt and iron peaks thanks to Equation 8 to obtain the proportion of iron *vs.* cobalt for various depths in the NPs. These measurements were performed on CS-1 and CS-3.

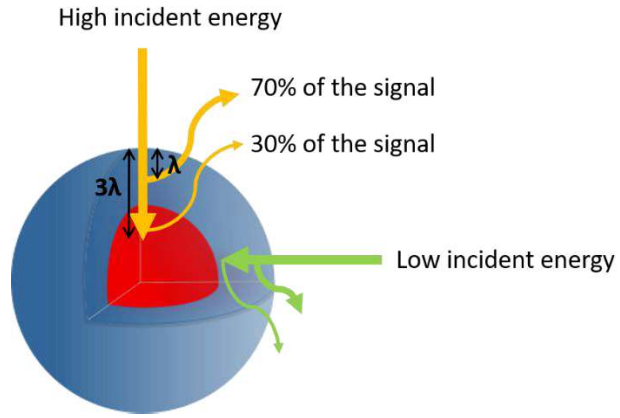

Figure 50: scheme of the depth profiling of a core-shell NP.

The obtained XPS spectra for different depth in the material have been fitted and the area of the Fe2p and Co2p peaks has been calculated (Figure 51). All the parameters of these experiments (incident energy, resulting kinetic energy) were given in chapter 2.

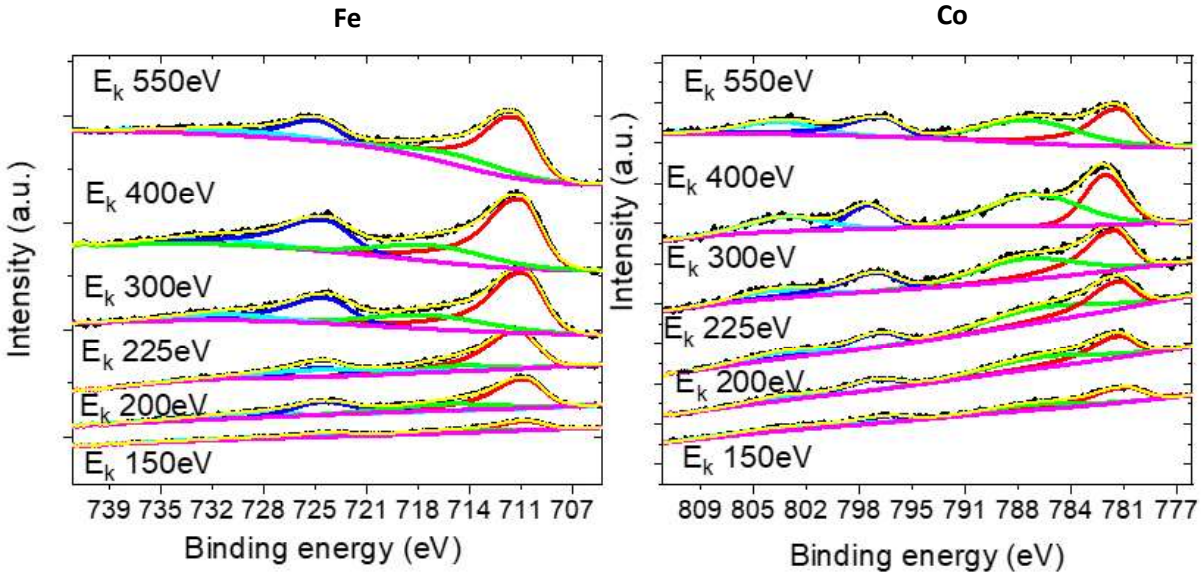

Figure 51: Fe2p (left) and Co2p (right) XP spectra and their fitting for different kinetic energies obtained while performing the depth profiling of CS-3. Black: experimental data, yellow: fitting of the experimental data, sum of all the other peaks: $2p_{3/2}$ (red) and its satellite (green) as well as $2p_{1/2}$ (dark blue) and its satellite (light blue)

The sensitivity factors have been calculated multiplying the flux of the incident source given by BESSY synchrotron and the atomic cross sections given by the elettra synchrotron website for these energies[125]. The ratio of iron vs cobalt has been calculated for these different energies. Figure 52 shows the proportion of iron in CS-1 and CS-3 as a function of λ.

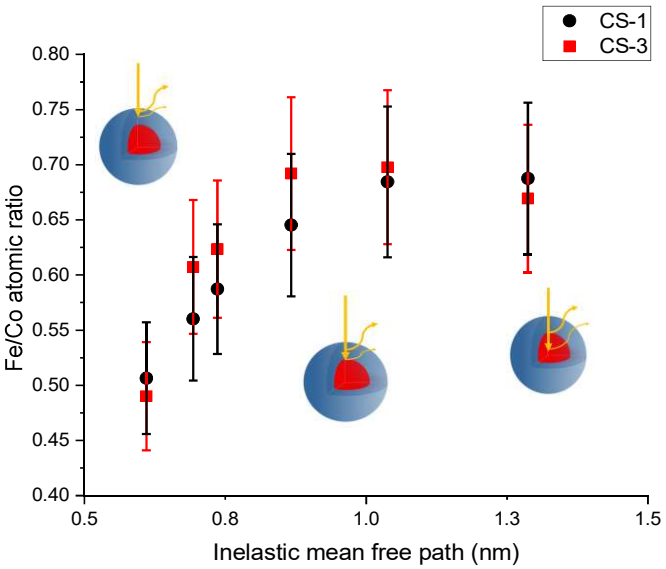

Figure 52: Proportion of iron vs cobalt in CS-1 and CS-3 as a function of the inelastic mean free path of the electrons.

Estimating an error of 10 % on the determination of the iron *vs.* cobalt ratio, it has been determined that cobalt density is higher in the shell than in the core for both types of NPs, which is consistent with the formation of a cobalt ferrite shell.

The depth profiling analysis confirmed the EELS results obtained for CS-3 about the core-shell structure and the same trend can be observed for CS-1. Consequently, both NPs are presenting a core-shell structure. However, for both CS-1 and CS-3 NPs, the Fe/Co atomic ratio at the surface is about 50 % instead of the 66 % that were expected if the deposited material was $CoFe_2O_4$. As the incident energy increases, a more important part of the NP is probed and the proportion of iron increases as not only the shell but also the core is probed. According to the size difference measured between the core and the core-shell NPs on the TEM micrographs, the shell of these NPs should be around 0.5 nm for CS-1 and 0.7 nm for CS-3. However, EELS measurements of CS-3 demonstrated that the shell is thicker than what has been observed on TEM micrographs due to the diffusion phenomenon occurring during the second step of the synthesis. A plateau is reached for a kinetic energy corresponding to an inelastic mean free path of about 0.8 nm for CS-3 and 1 nm for CS-1. As 68 % of the emitted photoelectrons are arising from a depth of λ and 99% from a thickness of 3 λ, it means that the shell of CS-3 has a thickness of about 0.8 mm and that CS-1 about 1 nm.

As for the EELS images, the depth profiling also displayed a higher quantity of cobalt than expected on the edge of the NPs. This could have been due to the presence of CoO on the surface but has been ruled out thanks to the XRD and FT-IR measurements that evidenced the absence of wüstite. Another possibility that agrees with the EELS images is that a gradient of cobalt is present in the NPs. That could be due to the differences in the decomposition temperature of the cobalt and iron stearate precursors (see in the part about the precursors synthesis). Indeed, for a stoichiometric shell, it is necessary to have metal complexes with a close decomposition temperature. In our case, when the shell is synthesized, the core of the NPs is already synthesized and only the growth of the shell will be observed, no nucleation will take place. As it has been presented in the part about the precursors synthesis, cobalt (II) stearate presents a higher decomposition temperature that iron (II) stearate. Consequently, during the second thermal decomposition step, Fe monomers will decompose first resulting in the growth of iron oxide on the surface of the core. Then, the decomposition of Co will start, but by that time the concentration of iron (II) stearate will drop, resulting in the Co enrichment of the outer shell with the composition similar to $Co_{1.5}Fe_{1.5}O_4$. This material would have an intermediate cell parameter to the ones of Co_2FeO_4 and $CoFe_2O_4$ that are respectively 8.244 Å (JCPDS card 04-016-3953) and 8.392 Å (JCPDS card 00-022-1086). As the structure is strained by the magnetite cell parameter of the core, the interatomic distances of $Co_{1.5}Fe_{1.5}O_4$ would be slightly enlarged in order for the shell to grow epitaxially on top of the core.

To conclude, the NPs present a core-shell structure but the shell seems to present a gradient in the cobalt concentration as at the surface the concentration of cobalt *vs.* iron seems to be about 50 % and the more in depth the beam goes in the core, the more it decreases. It is probably due to the difference in the decomposition temperature of the cobalt (II) and iron (II) stearate that are used during the synthesis of the shell.

5) Conclusion

The TEM micrographs have proved that the NPs present a spherical shape and a narrow size distribution. At higher resolutions, it was possible to observe the lattice fringes up to the edges of the NPs confirming their crystallinity. Lattice fringe distances were characteristic of the ones of the spinel structure in agreement with the diffractograms of the NPs that present the peaks characteristic of a spinel phase both for the core and the core-shell system. The cell parameters calculated for these samples correspond to Fe_3O_4. It is not possible to differentiate the core and the shell material neither by XRD nor by HR-TEM due to their similar cell parameters and the constraints on the cell parameter imposed by the core on the shell. Granulometry measurements confirmed this monomodal distribution and proved that the NPs were not aggregated. Apart from CS-2 sample for which the shell is synthetized only though diffusion of cobalt inside the structure[113], the size of the NPs has generally increased between the two thermal decompositions, in agreement with the growth of a shell on the surface of the core. Similar changes on the size of the crystallite have also been observed on the diffractograms of the NPs.

However, the FT-IR analysis of the Fe_3O_4 core NPs showed that they were consisting of a partially oxidized magnetite core ($Fe_{3-\delta}O_4$). This oxidation leaves some vacancies on the surface of the core that will be filled by the diffusion of cobalt or iron atoms during the synthesis of the shell before beginning the crystalline growth of the shell through thermal decomposition. EDX analysis confirmed the presence of cobalt in the core-shell NPs. By calculating the amount of cobalt corresponding to the TEM observed crystal growth, the total content of cobalt should be lower than $15\%_{at}$ in the NPs. Consequently, the crystal growth is not the only phenomenon occurring during the shell growth: diffusion phenomena also occur. The shell will then be thicker than the size difference measured in TEM. This has been confirmed by the depth profiling, EELS images and composition profiles on which the thickness of the shell was evaluated. CS-2 for which no crystal growth was observed exhibited a sharp and well-defined shell of about 1 nm thickness. For CS-1, the depth profiling confirmed the presence of a shell whose thickness is about 1 nm. As to CS-3 and CS-4, the larger diameter of the core limited the diffusion of cobalt atoms to its surface. Their shell is sharp and seems to have a thickness of 1-2 nm.

During the NPs synthesis, the precursors (iron (II) and cobalt (II) stearates) decomposition temperatures have to be similar in order for the shell to grow stoichiometrically at the surface of the core. Thanks to FT-IR and TG characterizations, it was proved that the stearate chains present a mix of two coordination modes to the metal: chelating bidentate and bridging bidentate. TG analysis

showed that the decomposition temperature of the cobalt precursor is higher than the iron one, this has been attributed to complexed water molecules surrounding the metallic center that were observed in the cobalt (II) stearate precursor which increased its decomposition temperature by stabilizing it. This difference in decomposition temperature led to some gradient in the amount of cobalt in the shell observed thanks to the EELS composition profiles and the XPS depth profiling performed on the NPs: the external part of the shell seems to be composed of $Co_{1.5}Fe_{1.5}O_4$ and the cobalt content decreases when going deeper in the shell.

Consequently, four different types of core-shell cobalt iron oxide NPs have been successfully synthetized and characterized. Two samples are presenting a core of 8-9 nm (CS-1 and CS-2) and two others a larger core of 13-14 nm (CS-3 and CS-4). Two synthesis methods have been used: the crystal growth of the shell on the core (CS-1, CS-3 and CS-4) and the diffusion of cobalt in the vacancies of the core (CS-2) that should generate a sharper and thinner shell. Both synthesis approaches resulting in different chemical structure (defects, crystallographic planes, cobalt vs iron proportion) of the $CoFeO_x$ shell, electrochemical activity of these nanoparticles will be investigated in the next chapters.

The design of NPs with core-shell structure is an elegant way to produce efficient catalysts for the OER reaction. The $Fe_{3-d}O_4$ core size and the CoFe oxide shell thickness being key structural parameters to control the electrocatalytic properties, their systematic variation should shed light on the mechanisms occurring at the interface between the catalyst and the electrolyte. Additionally, they meet two of the four requirements for a good catalyst that were stated in the introduction:

- They should be conductive thanks to their magnetite core and allow us to avoid the use of carbon that is commonly used in the literature to increase the conductivity of the catalyst[25]. The use of carbon would make the system more complex and the surface transformations more difficult to understand than on a carbon-free catalyst.
- Thanks to their small size (8-16 nm) they present a high surface area, their specific surface has been evaluated and for all NPs it is about 100 m^2g^{-1}. Catalysis being a surface phenomenon, it is highly dependent on the surface available for the reaction to happen.

Moreover, these core-shell NPs limit the use of cobalt (only present in the thin shell). As this material was classified as a critical material by the European union in 2017[71], it is highly interesting for future electrocatalysis applications to limit its usage. TMOs such as cobalt ferrite are known to be active for the OER[24,46] and are stable. The OER properties of the NPs will be investigated in the next chapters of this manuscript by studying the redox properties and the electrochemical activity of the NPs during the OER as well as the transformations occurring at their surfaces.

Chapter 4: Experimental investigation and modelling of the electrochemical properties of cobalt iron oxide core-shell nanoparticle multilayers in alkaline medium

This work has been awarded a poster prize at the 31st ISE Topical Meeting "Theory and Computation in Electrochemistry: Seeking Synergies in Methods, Materials and Systems", which took place in Aachen (Germany) on May 2022. The chapter is based on the invited manuscript, which is prepared for submission to the Virtual Special Issue of Electrochimica Acta associated with the Topical Meeting in Aachen.

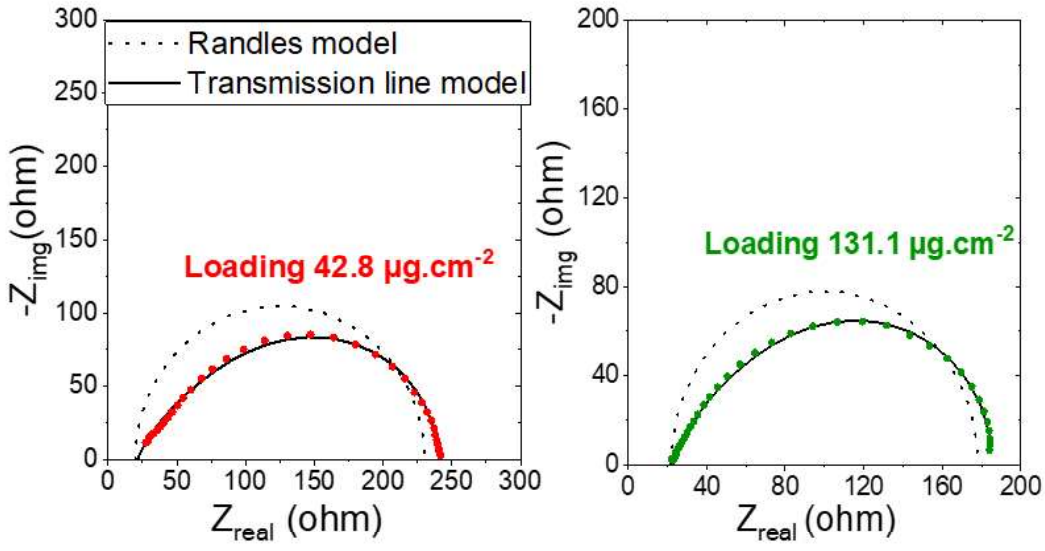

1) *Introduction*

Anion exchange water electrolysis is an attractive alternative to PEM water electrolysis allowing the replacement of the iridium anodes by more abundant 3d transition metal oxides (TMO) based on nickel, cobalt, iron or manganese[7,15]. TMOs with spinel structure constitute a promising class of oxygen evolution reaction (OER) catalysts due to their high activity, a relatively low synthesis temperature (allowing the preparation of high surface area catalysts) and their composition-dependent and widely tunable properties.

The catalytic layers commonly used in electrolyzers often present a complex 3D porous architecture. In the case of the OER in an AEM electrolyzers, the performance of the catalyst layer can be limited by:

- ✓ the water /OH^- transport in the catalyst layer;
- ✓ the efficiency of the O_2 removal and eventually the formation of O_2 bubbles that might block the access to catalytic active sites;
- ✓ local changes of the pH affecting the stability and the activity of the layer;
- ✓ electronic conduction across layer which depends on the intrinsic conductivity of the materials composing the layer and/or on the contact resistance between the catalyst particles.

TMOs are usually not very conductive. Thus, to compensate for this lack of conductivity, carbon is often added to the catalytic layers for benchmarking of TMOs. However, carbon materials are oxidized at high anodic potentials required for the OER[147]. Hence carbon could be eventually used to determine the activity of TMOs but it won't be possible to use it at an industrial scale. Another possibility is to develop TMOs with intrinsic electronic conductivity such as Fe_3O_4, that is conductive thanks to an electron hopping between the Fe (II) and Fe (III) cations[148]. However, even if Fe_3O_4 nanoparticles (NPs) possess high intrinsic conductivity, the conductivity of NP networks may be low due to the contact resistance between the NPs, the conductivity mainly arising from the tunneling effect[132,133]. Thus, to accurately calculate electrocatalytic activity of materials it is critically important to consider charge propagation through the catalytic layer and understand whether the entire surface of material is involved in the electrochemical reaction.

As we presented in chapter 1, numerous TMO based catalyst for the OER have been studied in the literature and these materials generally presented a low conductivity if no carbon was added to the catalytic layer[7,15]. In order to understand better the effect of the catalyst conductivity, Chung *et al.*[149] reported on how the electrical resistance of the catalytic layer affects its electrocatalytic activity. They

investigated poorly conductive amorphous and crystalline MoS_2 (loading 0.25 mg/cm²) mixed with various amounts of carbon and demonstrated that both the overpotential and the Tafel slope are affected by underutilization of the active material and the ohmic losses. Indeed, increase of the ohmic resistance resulted in an increase of the overpotential (required to reach a 10 $mA.cm^{-2}$ current density) 0.15 to 0.35 V and Tafel slope from 40 to 75 $mV.dec^{-1}$. They concluded that even though electrical conductivity is often neglected in electrocatalytic studies, it should be considered as one of the important criteria when designing electrocatalysts. Additionally, for poorly conductive catalysts they observed an inflexion in the Tafel plots that deviated from a linear behavior and became convex. Moreover, Papaderakis *et al.*[150] studied the OER on porous iridium oxide catalytic layers and used the transmission line model with various constant phase elements to evaluate the charge transfer resistance and capacitance for different loadings. By studying the impedance curves before the OER and in the potential range of the OER, they concluded that impedance studies of porous IrO_2 electrodes can give an estimate of their total capacitance C_t and that this capacitance decreases during the OER due to pore clogging by evolved O_2. These studies were performed in acidic medium, which is not compatible with TMOs. Consequently, more in-depth analysis for electrocatalytic reactions utilizing poorly conducting materials in alkaline media is needed to adequately evaluate and understand their properties.

In the case of the oxygen evolution reaction (OER) in alkaline media on TMO catalysts, such issues as the electrical conductivity of the catalysts, the interparticle resistance, the pore clogging with the evolved oxygen, may also affect the measured electrocatalytic activity. As we previously stated, one way to evaluate the importance of these factors is to measure the electrochemical impedance and to determine the solution resistance, the charge transfer resistance, the ionic and electronic resistance as well as the capacitance of the material. Electrochemical impedance spectroscopy is a commonly used characterization technique but its interpretation is not always straightforward due to the effect of charge transport, storage, and polarization but also to the fact that all the above-mentioned phenomena can be modified depending on the position of the particle in the catalyst layer (close to the electrode/electrolyte interface, in the middle of the layer, close to the current collector). In that case, one has to consider a distributed impedance within a porous catalyst. The distributed impedance approach has been applied to polymer films,[27] but can also be used for oxide materials, and impedance spectroscopy has been extensively utilized in the literature especially for porous electrodes.[151–153] Heim *et al.*[153] for example recently studied porous electrodes and concluded that it as possible to translate the transmission line equivalent circuit model into independent distribution of time constants with a model containing two or three R||C chains.

We report here on electrochemically active nanoparticles (NPs) which combine a magnetite core and a cobalt ferrite shell: Fe_3O_4@$CoFe_2O_4$. These well-defined NPs with a narrow size distribution and controlled shape and composition both for the core and the core-shell were synthesized via a seed-mediated growth based on the thermal decomposition of metal complexes as recently reported[113,114]. Such a core-shell structure allows combining an electrochemically active phase (Co-Ferrite) at the nanoparticle surface and a conductive Fe_3O_4 core.[132,133] Even though the shell is not conductive, this conductive core is expected to enhance the electron transport between the electrode and the interface between the nanoparticles and the electrolyte. They also present the advantage of using low amounts of cobalt, a material which demand is exploding worldwide and has been classified as critical material by the European union recently[71]. The diameter of these NPs (core size and shell thickness) will be modified in order to evaluate the importance of these parameters on the resistance and on the electrochemical activity. The behavior of the catalytic layer of different thickness was studied by impedance spectroscopy in order to get a better understanding of the influence of the resistance within the catalytic layer. We will first present the characterization of the catalytic layer thanks to scanning electron microscopy (SEM), then the electrochemical characterization for different thicknesses of the catalytic layer (cyclic voltammetry curves, their corresponding Tafel slopes, OER activity and impedance spectroscopy measurements). The results will only be exploited for a small overpotential to avoid the influence of the O_2 bubble formation and the mass transport issues. Finally, the impedance spectroscopy curves will be fitted thanks to two different models: the Randles model (for thin catalytic layers) and the transmission line model (for thick catalytic layers), a simulation of the current and potential distribution within the catalytic layer will also be presented.

2) Results and discussion

a) Characterization of the NPs and NP films

In this work two types of NPs will be used: CS-2 and CS-3. The characterizations from chapter 3 showed that the NPs are homogeneous in size, shape, and composition. Their size, structure and crystallinity have been confirmed by X- ray diffraction (Figure 53 A), transmission electron microscopy (Figure 53 B, C, E, F) and the core-shell structure has been demonstrated thanks to electron energy loss spectroscopy (see chapter 3). They display an average diameter of 9.3 nm and 14 nm respectively (Figure 53 D) and are presenting peaks characteristic of the spinel structure.

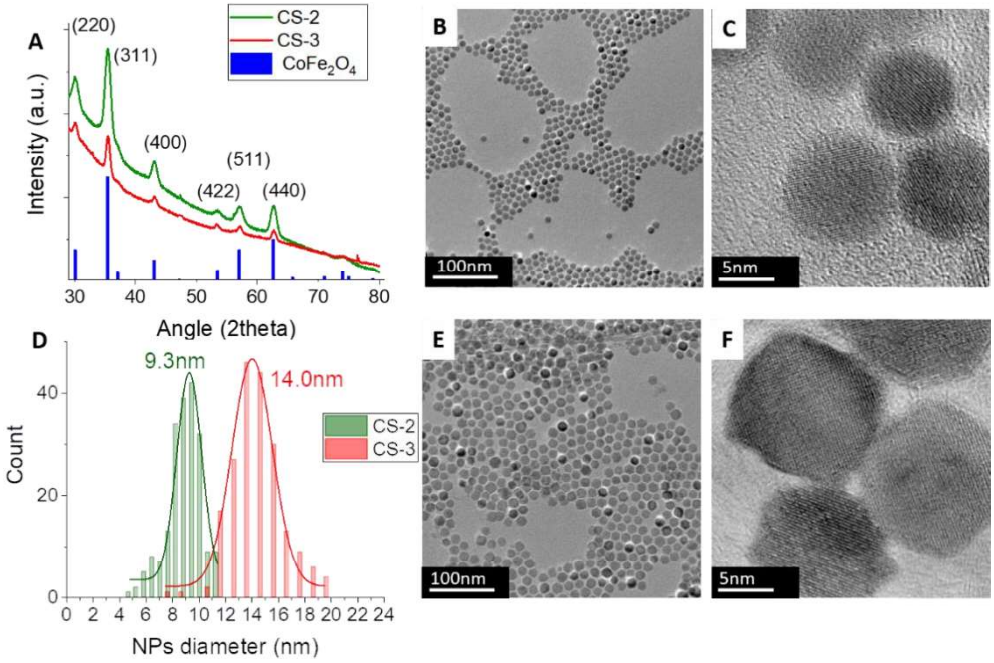

Figure 53: A) Diffractograms of the NPs, B) TEM micrograph and C) HR TEM micrograph of CS-2. D) Average diameter of the NPs CS-2 and CS-3 F) TEM micrograph and G) HR-TEM micrograph CS-3.

Various mass of catalysts have been dropcasted on a glassy carbon electrode to obtain catalytic layers composed of core-shell NPs with different thicknesses. In order to observe the thickness of the catalytic layer and the organization of the NPs on the surface, different NPs loadings were deposited on either a thin glassy carbon plate or a silicon wafer substrate that was then crossed polished thanks to an ion beam, leaving the cross-section of the material exposed and ready to be characterized by scanning electron microscopy (SEM). Since the quality of the cross-sectional images was much higher when using the flat silicon wafer substrate, they will be presented in Figure 54, which shows the SEM images of the cross section for three different loadings of NPs. On these images, the important thickness variation of the catalytic layer is confirmed: for a loading of 63 µg/cm² (average thickness 200 nm) there are a lot of NPs stacked on top of each other while for 6.3 µg/cm² (average thickness 50

nm) there seems to be between 4/5 and 10 monolayers of NPs on the surface. For a loading of 0.63 µg/cm² (average thickness 10 nm) there is 2 monolayers of NPs at most and in some places no NPs are present on the substrate. These irregularities are due to the deposition method (dropcasting) and the fast evaporation rate of the solvent in which the NPs are in suspension (chloroform). Indeed, this fast evaporation will favorize some irregularities in the layer thickness.

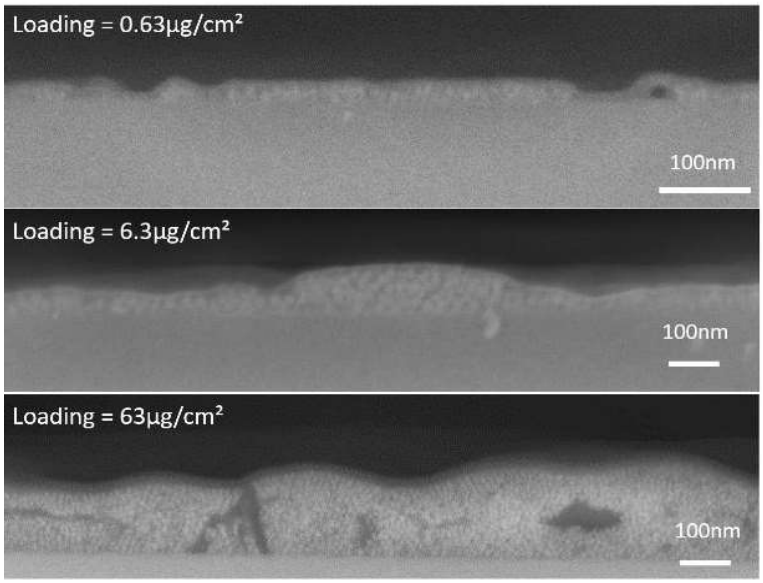

Figure 54: SEM image of a cross section of different loadings of the NPs dropcasted on a silicon wafer substrate.

b) Electrochemical data

After the characterization of the catalyst and the catalyst film, cyclic voltammetry experiments were performed in a 3-electrode cell and a 0.1 M NaOH electrolyte. All experiments were repeated 3 times to study the reproducibility of the experiments and the curves were corrected from the ohmic losses by measuring the electrolyte resistance thanks to impedance spectroscopy.

Figure 55 A and D present the cyclic voltammetry curves obtained for the two types of NPs studied in this chapter. On both types of NPs the diminution of the loading implies a diminution of the overall reaction current. From these curves, by taking the anodic contribution, Tafel plots were built (Figure 55 B and E). The Tafel slopes are in agreement with the results obtained for similar compounds in the literature[7]. In agreement with Chung *et al*[149], an increase of the loading leads to an increase of the Tafel slope that can be explained by the ohmic resistance built across the catalyst film. Thus, when the loading increases, some zones of the catalytic layer become less involved in the reaction as they are not submitted fully to the applied potential. Another phenomenon can be observed, namely nonlinearity of the Tafel plots. Indeed, the Tafel slopes incurvate and become convex: at low

overpotential the slope is lower than the one at high potential (Table 5).

Table 5: Tafel slope measured as function of the loading for CS-2 and CS-3 NPs at two values of the electrode potential: 1.62 1.67 V vs RHE

Sample	Loading ($\mu g.cm^{-2}$)	Tafel slope at 1.62 V (mV/decade)	Tafel slope at 1.67 V (mV/decade)
CS-2	131.1	72± 7	98±9
	13.1	55±5	82±8
	4.4	54±5	80±8
	2.2	49±5	73±7
	1.3	60±6	75±7
CS-3	42.8	62±6	87±9
	4.3	52±5	74±7
	1.4	62±6	72±7
	0.7	59±6	64±6

As expected from the linear sweep voltammograms, the current measured at a given potential increases with the loading. However, if the activity per unit mass is plotted (Figure 55 F) by dividing the current obtain at 1.67 V *vs.* RHE by the actual mass of the catalyst, then the mass-weighted activity is constant (as expected) up to a loading of about 5 $\mu g.cm^{-2}$, but decreases by a factor of 10 at higher loadings. In an ideal case, if all of the NPs within the catalyst layer are involved in the reaction, the mass-weighted activity should be constant. Here it is not the case, so in agreement with the Tafel plots, these results are suggesting that the NPs are not fully involved in the reaction when the loading is too high.

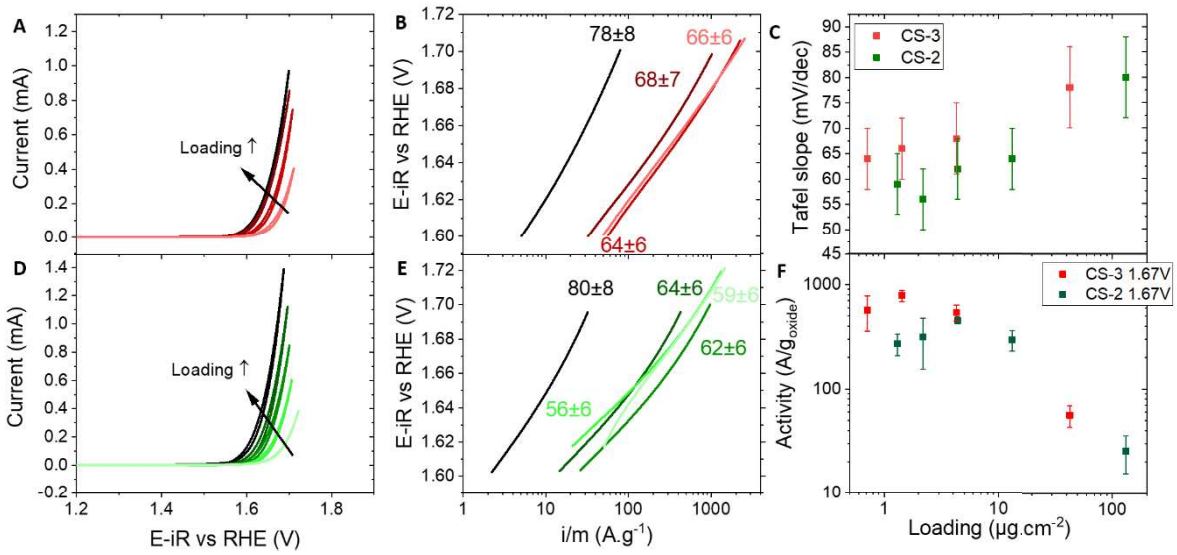

Figure 55: A) Cyclic voltammetry curves obtained for CS-3 NPs in 0.1M NaOH, scan rate 10 mV/s. Dark colors are for high loadings and light ones for lower loadings. B) Tafel plots obtained for CS-3 NPs (the values of the Tafel slopes are indicated in mV/decade). C) Tafel slopes measured for CS-2 and CS-3 for various loadings. D) Cyclic voltammetry curves obtained for CS-2 NPs in 0.1M NaOH, scan rate 10 mV/s. E) Tafel slopes obtained for CS-2 (mV/decade). F) Activity per unit mass of oxide measured at 1.67 V vs RHE for CS-2 (green) and CS-3 (red)

This diminution of the activity for high loadings could be due to the formation of oxygen bubbles blocking the surface. Indeed, the formation of O_2 bubbles might block the access of water to the catalysts surface and thus result in a decrease of the overall current with the loading. To analyze the possible influence of the O_2 generation, we measured the activity for 2 different potentials: one at which the OER has just started (1.62 V, Figure 56) and one at a higher potential (1.67 V Figure 55 F) at which the OER has fully begun. By seeing the same trend for both potentials, we are able to conclude that the observed loss of activity is not linked to the formation of O_2 bubbles. It is also instructive to analyze the activity vs. loading plot shown in Figure 55F. The slope of this plot for high loadings can give an indication of the NPs involvement in the activity. Indeed, a slope of -1 would mean that an increase of the loading does not lead to an increase in the measured OER current. For both CS-2 and CS-3 samples the slope was estimated as – 0.91 at 1.67 V vs RHE and decreased down to – 0.81 at 1.62 V vs RHE. These values demonstrate that the NPs are becoming less and less involved in the OER reaction while the loading increases, and that this phenomenon aggravates with the increase of the electrode potential.

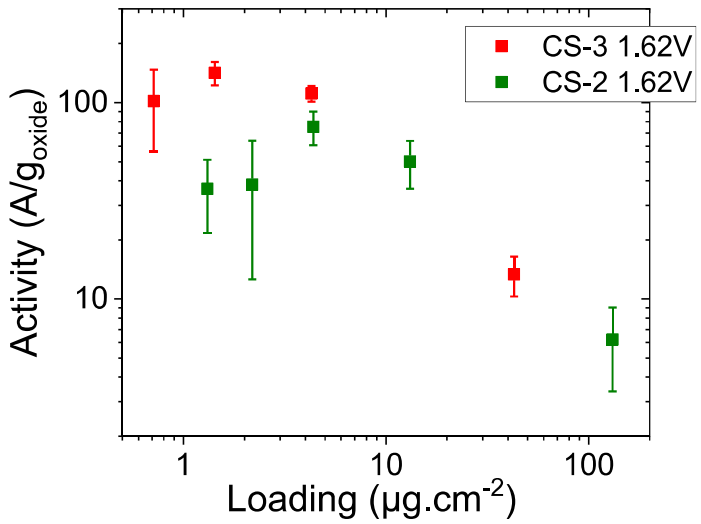

Figure 56: Activity measured at 1.62 V vs. RHE for CS-2 and CS-3 NPs as a function of their NP loading on a GC electrode.

In order to investigate the electrical properties of the catalytic layer, electrochemical impedance spectroscopy measurements were performed for the various loadings of both NPs. The Nyquist plots of the different loadings have also been plotted (Figure 59 and Figure 58). On these curves it can be observed that for high loadings the semi-circles present some asymmetry at high frequencies. This could be linked to an additional resistance in the catalytic layer that could either be an electronic or ionic resistance.

c) *Modelling*

Impedance measurements can be modeled thanks to an electric circuit. In this work, two different models will be considered: the Randles model and the transmission line model. As a first approximation Randles circuit (Figure 57 A), applies to flat electrodes, it is well adapted when the catalyst layer deposited on the electrode is very conductive and all the particles of the catalyst are available to participate in the reaction. Thanks to this model the catalytic layer can be considered homogeneous, in which the ohmic resistance (Rs, usually related to the electrolyte resistance) and the charge-transfer resistance (R_2) do not vary across the film thickness.

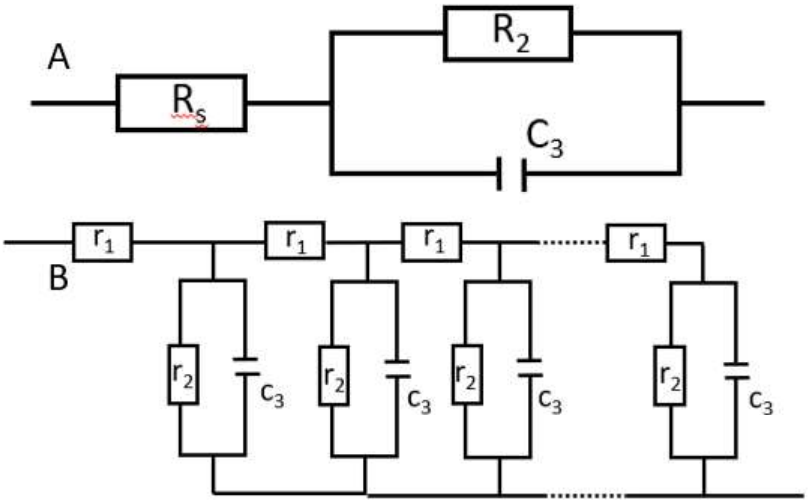

Figure 57: Randles model (A) and transmission line model (B) inspired from[28].

However, when the catalyst layer becomes thicker and/or when the catalytic material is not sufficiently conductive to assure fast charge transport across the layer, one can consider a distributed repartition of the charge transfer at the catalyst/electrolyte interface and electrochemical capacitance according to the region of the catalyst. The catalyst can then be separated into different layers and the modelling can be done using a transmission line model[28] (Figure 57 B). This model considers three different parameters: an apparent resistance R_1, which may comprise of either the ionic or the electronic resistance or both, R_2 the charge transfer resistance, and C_3 the capacitance. It has been developed for porous polymer and electrocatalyst layers and can thus be applied to porous catalyst films that present a certain resistivity (either ionic or electronic). The equations used to model the circuits were the following:

$$Z_{Randles} = \frac{R_2}{1 + jR_2C_3\omega} + R_s \ (1)$$

$$Z_{Transmission\ line} = \left[\frac{R_1R_2}{1 + (j\frac{\omega}{\omega_2})}\right]^{1/2} \times \coth\left(\left(\frac{\omega_2}{\omega_L}\right)^{1/2}\left[1 + (j\frac{\omega}{\omega_2})\right]^{1/2}\right) + R_s (2)$$

Equations used to fit the impedance data for the Randles model (1) and the transmission line model (2).

The fitting was performed considering a pure capacitance, the phase constant element exponent (α) value is 1. First, the impedance Nyquist curves were fitted at low loadings for which the Randles model can be used (loadings about 1 µg.cm^{-2}). This allowed the determination of R_2 (the total charge transfer resistance) and C_3 the capacitance of about a monolayer of nanoparticles. Then, it was possible to fit the Nyquist plots obtained for higher loadings, for which the Randles model was not appropriate,

with the transmission line model. The values of the different parameters used in are given in the equations below.

$$\omega_2 = \frac{1}{r_2 c_3} = \frac{1}{R_2 C_3} \quad (3)$$

$$\omega_L = \frac{1}{r_1 c_3 L^2} = \frac{1}{R_1 C_3} \quad (4)$$

$$R_1 = r_1 \times L \quad (5)$$

$$R_2 = \frac{r_2}{L} \quad (6)$$

$$C_3 = c_3 \times L \quad (7)$$

Equations used to calculate the different parameters of the impedance measurement with the transmission line model: ω_2 (3), ω_L (4), R_1 the ionic and electronic resistance (5), R_2 the charge transfer resistance (6) and C_3 the capacitance (7). L is the thickness of the layer.

With the transmission line model there were often several solutions possible for the various parameters of the fit using the method of the least squares. In order to select the right solution, we used the value $R_2=r_2/L$ (equation 6) as initial value for the nonlinear least squares fitting process. r_2 was estimated thanks to the fitting of the impedance data at low electrocatalyst loading using the Randles model. Thus, among the different possible solutions for the transmission line model, the one presenting the closest R_2 value to the one estimated from Equation (6) as initial conditions was then selected. The capacitance of the catalytic layer C_3 can also be determined thanks to this model. Figure 58 presents Nyquist plots for CS-2 and CS-3 fitted with the Randles model for low loadings and the transmission line model for high loadings.

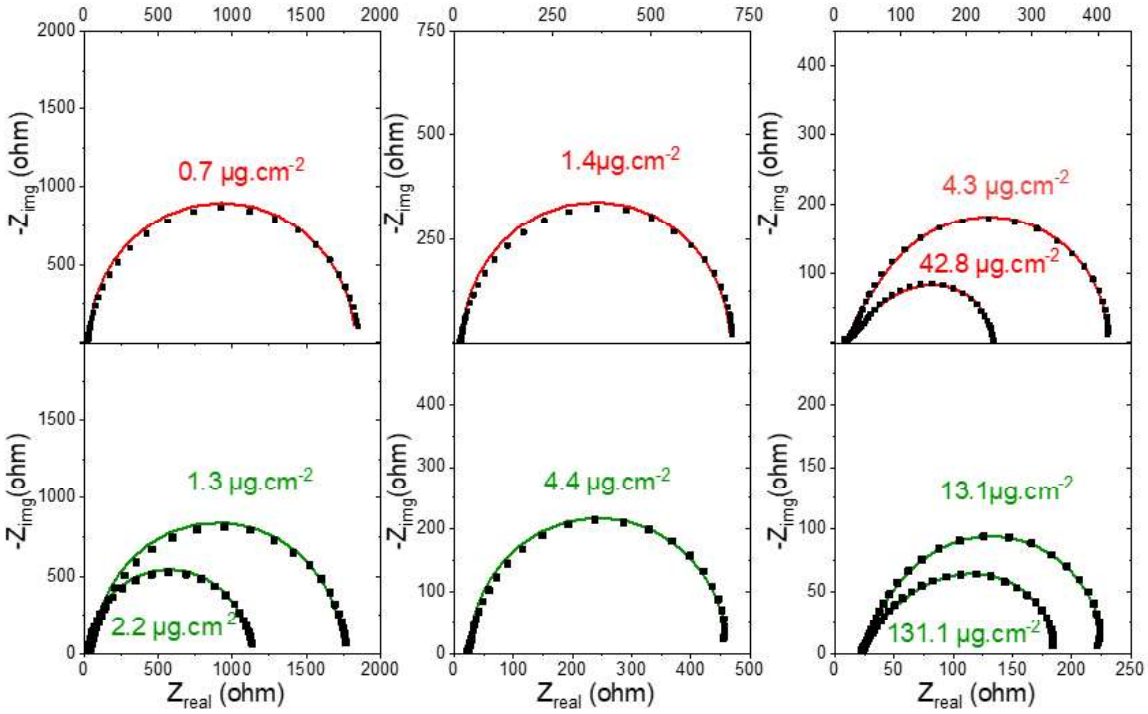

Figure 58: Experimental (black squares) Nyquist curves for different loadings of NPs on the electrode modelled thanks to the Randles model for low loadings (left and middle) and the transmission line model (right) for high loadings on CS-3 (red) and CS-2 (green) NPs at 1.62 V vs RHE.

These results evidenced that for low loadings (about one or two monolayers), the Randles model fits the experimental results: the catalytic layer can be considered as a homogeneous layer in which the charge-transfer resistance is the same throughout the whole thickness. However, when the loading increases and more monolayers of NPs are present on the electrode, then the Randles model doesn't fit the experimental results anymore and one has to consider the transmission line model that will consider the electronic and ionic resistance between the catalyst layers (Figure 59).

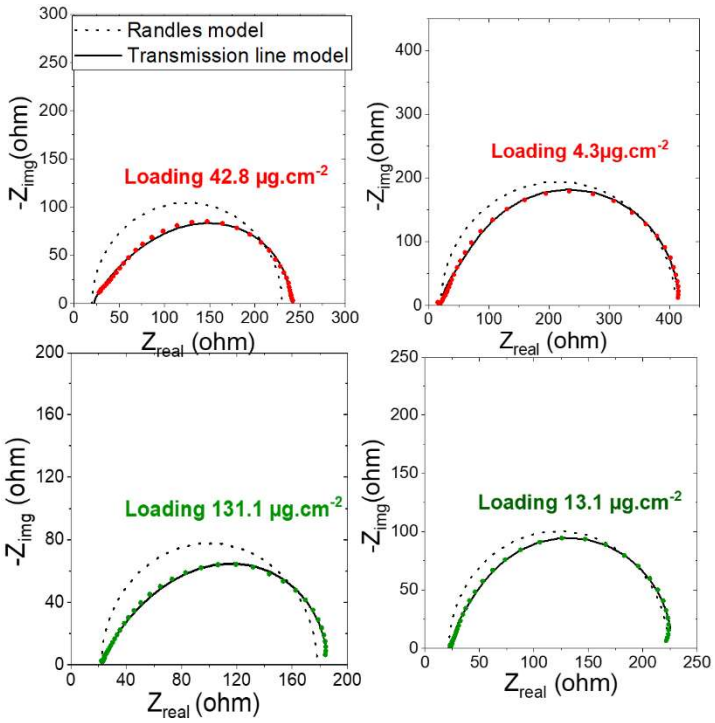

Figure 59: Transmission line model (solid line) and Randles model (dotted line) fitting of the experimental data (green and red dots) for high loadings of CS-2 (green) and CS-3 (red) NPs.

On Figure 59 it can be observed that for high loadings, the Randles model is not able to provide an accurate description of the experimental data while the transmission line model can, confirming the existence of an additional parameter: resistance R_1 (ionic and/or electronic) to the charge transport across the layer. From these fittings it was possible to extract the value of R_1, the charge transfer resistance (R_2) and the capacitance of the layer (C_3). All these parameters are given in Table 6.

Table 6: R_3, R_1, and C_3 parameters obtained thanks to the fitting of the Nyquist curves

Sample	Loading (µg.cm^{-2})	R_2 (ohm)	R_1 (ohm)	C_3 (µF)
CS-2	131.1	20±5	1317±330	2790±700
	13.1	144±36	191±50	142±40
	4.4	437±110	/	118±30
	2.2	1090±270	/	46±11
	1.3	1690±420	/	22±5
CS-3	42.8	30±8	1575±400	870±220
	4.3	304±75	293±75	72±20
	1.4	679±170	/	46±11
	0.7	1800±450	/	28±7

The results shown in Table 6 are demonstrating an influence of the layer thickness for loadings above 5 μg.cm^{-2} (which corresponds to 10-20 NP monolayers). The value of R_2 decreases with the loading while R_1 and C_3 increase. This was to be expected as a greater number of NPs leads to a higher overall rate of charge transfer across the interface (and hence the OER current) and higher capacitance.

Figure 60 shows the evolution of R_2 and C_3 as a function of the electrode roughness factor defined here as the total surface of NPs (calculated from their mean size) and the geometric surface on the GC electrode ($cm^2_{NPs}.cm^{-2}_{electrode}$). On these graphs it can be observed that for larger NPs (CS-3), the charge transfer resistance R_2 is lower than the one measured for small particles (CS-2). This difference can be attributed to the larger core (CS-3 over CS-2 NPs) facilitating charge transfer across the interface (hence the OER), and hinting to a synergy between the cobalt in the shell and the iron in the core, as it will be presented later in chapter 6.

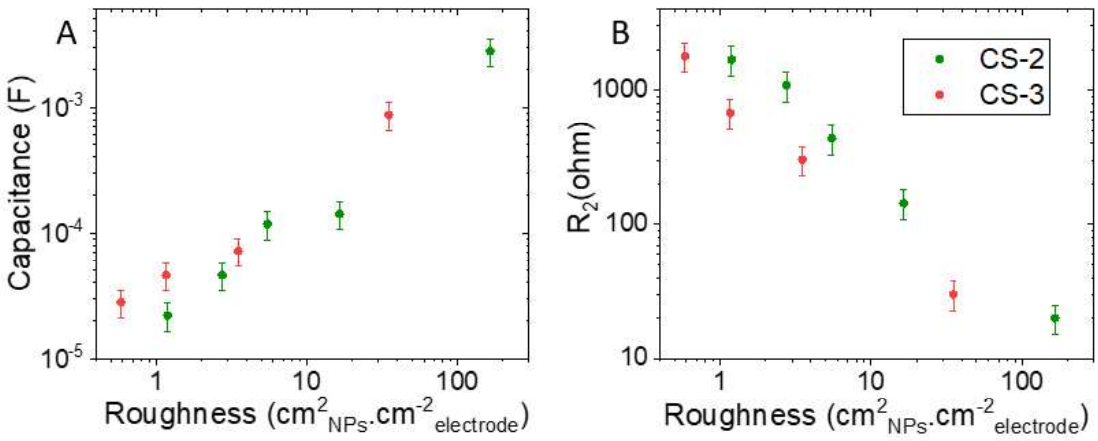

Figure 60: Evolution of the capacitance C_3 (A) and the charge transfer resistance R_2 (B) as a function of the roughness of the catalytic layer defined as the total surface of NPs (calculated from their mean size) and the geometric surface on the GC electrode ($cm^2_{NPs}.cm^{-2}_{electrode}$)

Using various R_1 values it is also possible to model the linear sweep voltammograms and their respective Tafel slopes for various R_1 values (Figure 61). In order to perform these simulations, the Telegrapher's equations[154] (see below) adapted for this model were used. Note that the charge-transfer step is modelled as an exponent (see Eq. 9) with the transfer coefficient of 1 (in agreement with the 60 mV/decade Tafel slope for thin NP films).

$$\frac{\partial V}{\partial x} = -R_1 \times I \quad (8)$$

$$\frac{\partial I}{\partial x} = -V \times k e^{\frac{FV}{RT}} + j\omega C_3 - C_3 \frac{\partial V}{\partial t} \quad (9)$$

$$\frac{\partial V}{\partial t} = v \quad (10)$$

Telegraphers equations used to simulate the linear sweep voltammetry curves. V is the applied voltage, C the capacitance, I the current, k the reaction rate constant (has the dimension of a conductance), T the temperature, R the ideal gas constant and F the Faraday constant.

On these simulated linear sweep voltammetry curves a decrease in the current can be observed when the R_1 value increases (Figure 61A). Also, the Tafel plots deviate from an ideal linear

behavior and are becoming convex when R_1 increases. These observations agree with the experimental data presented above. These results are confirming that the catalytic activity cannot be determined accurately for high loadings if the catalyst layer presents resistance to charge transport across the layer. This resistance may arise from an insufficient electronic conductivity of the catalytic layer (poorly conducting catalyst particles or high contact resistance between the catalytic particles) or, alternatively, from ionic resistance of the electrolyte within the pores of the catalytic layer. Also, this highlights the impact of the loading on the Tafel slope, the latter being often used for mechanistic interpretations. Indeed, these interpretations are likely to be inaccurate for high loadings, notably for poorly conductive catalysts and/or electrolytes of low conductivity.

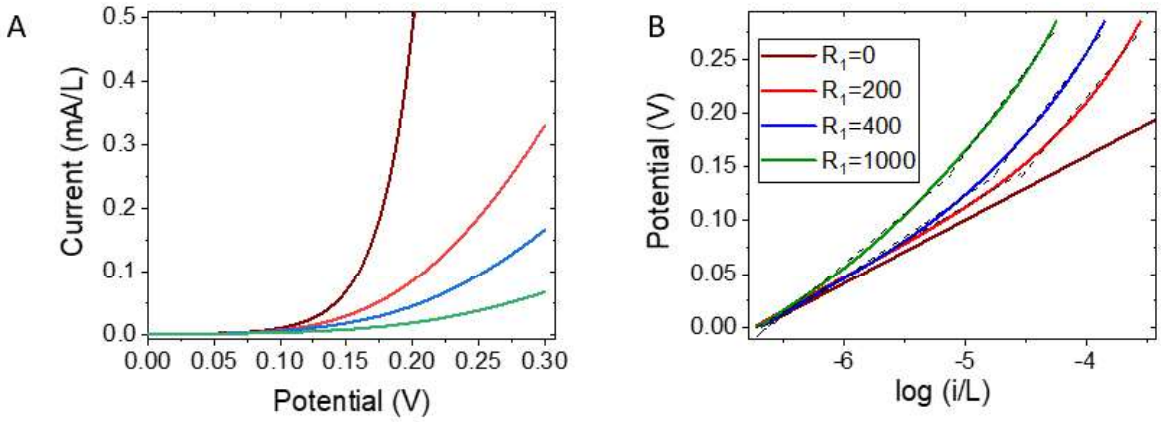

Figure 61: Simulated linear sweep voltammetry curves (A) and their corresponding Tafel plots (B). The dashed lines correspond to a linear fitting of the Tafel slopes for high and low potentials. It can be observed that the Tafel slope increases at high potentials.

The simulated currents normalized by the number of elements (N) for two different potentials (0.12 and 0.17 V) were then plotted against the transmission line length (L) (Figure 62). We note that as the number of elements increases (and thus the resistance across the layer, R_1, increases), the normalized current drops and the slope on the log i vs log N changes with the applied potential from -0.68 at 0.12 V to -0.9 at 0.17 V. The overall trend and the simulated values are in reasonable agreement with the experimental data presented above.

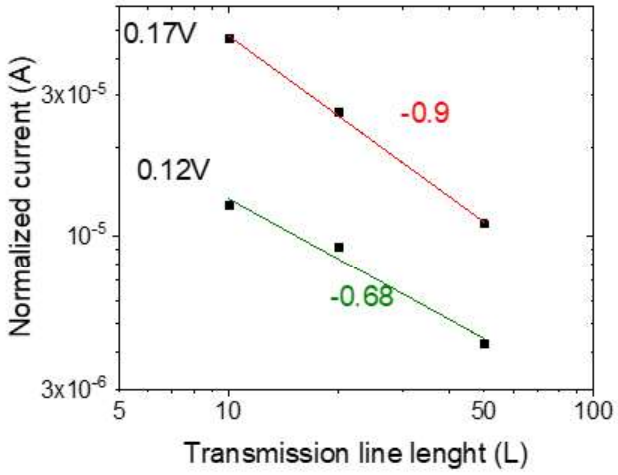

Figure 62: Simulated currents normalized by the number of elements at 0.12 and 0.17 V against the transmission line length in the transmission line model.

Finally, in Figure 63 the current and the potential distribution inside the catalytic layer have been plotted for a high value of R_1=1000 Ω and high applied potential of 0.3 V.

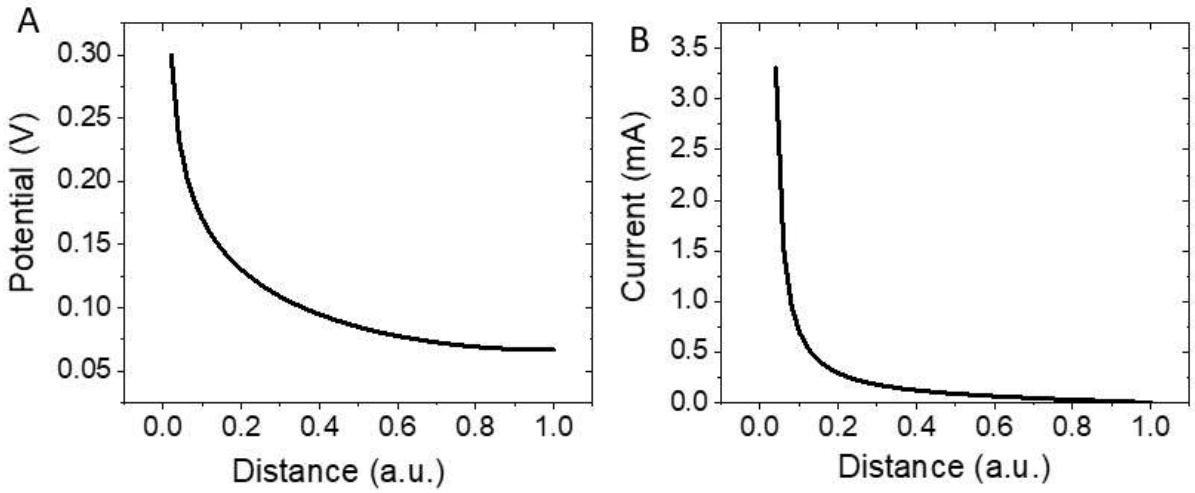

Figure 63: Simulation of the potential (A) and current (B) distribution within the catalyst layer for a potential applied on the working electrode of 0.3 V and an R_1 resistance of 1000 Ω.

This figure demonstrates that the potential within a catalytic layer is applied in an inhomogeneous manner. If the apparent R_1 resistance is primarily electronic, then the highest potential is applied to the catalyst particles adjacent to the substrate (GC in the experiment) decaying towards the exterior of the catalyst layer. On the contrary, if the apparent R_1 resistance is primarily ionic, then the highest potential is applied to the exterior of the catalyst layer, facing the electrolyte, decaying towards the interior of the catalyst layer. As a result, the current generated due to the electrocatalytic reaction will be the highest in the interior of the catalyst layer (electronic resistance) or in the exterior of the catalyst layer (ionic resistance). This confirms that for high loadings the NPs are not entirely involved in the OER.

3) *Conclusions*

To conclude, in this work we studied the OER activity of two different sizes of core-shell cobalt iron oxide NPs for different thicknesses of the catalytic layer. For both types of NPs, it was observed that the apparent activity of the NPs at a given potential strongly depends on the layer's thickness and that the Tafel plots deviate from the linear behavior and present an important variation (from 60 to 80 mV/decade depending on the loading). It was concluded that in order to measure accurately the activity of a catalyst, thin layers are needed, notably for catalyst layers that are not highly conductive. This loss of activity can be attributed to either contact resistance between the NPs or to electrolyte resistance in the voids between the NPs. In order to distinguish between these two alternatives, additional experiments are required, notably with variable electrolyte conductivity. Experiments with different supporting electrolyte (higher concentration and hence higher conductivity) were performed and are currently being analyzed.

In order to get a better understanding of the influence of the resistance across the catalyst layer on the measured electrochemical characteristics (mass-weighted activity and Tafel slope), impedance spectroscopy measurements were performed. These measurements demonstrated asymmetry appearing on the Nyquist plots at high frequencies for high loadings. Consequently, we used the transmission line model to extract the apparent resistance (ionic and/or electronic) value from the fitting of these impedance curves and used the resistance value to simulate the linear sweep voltammetry curves for various R_1 values. These simulations agreed with the experimental data as for higher resistance the normalized current was lower and the Tafel plots were deviating from an ideal linear behavior, confirming that mechanistic interpretations of the Tafel slopes are only accurate if the catalyst is highly conductive (negligible resistance to the charge transport across the catalyst layer) or if the loading on the electrode is low. Finally, the current and potential distribution throughout the catalytic layer was also simulated and displayed an exponential decay when the resistance was important, confirming that the particles within the layer were not submitted to the same potential and consequently that if the catalytic layer is too thick not all the particles will be equally involved in the electrocatalytic reaction.

Chapter 5: Combining conductivity and electrochemical properties in unique core-shell $Fe_{3-\delta}O_4$@$CoFe_2O_4$ nanoparticles for enhanced oxygen evolution reaction

This chapter is based on the article "Combining conductivity and electrochemical properties in unique core-shell $Fe_{3-\delta}O_4$@$CoFe_2O_4$ nanoparticles for enhanced oxygen evolution reaction" by L. Royer, S. Hettler, R. Arenal, T. Asset, B. Rotonnelli, B. Pichon, A.Bonnefont and E. Savinova submitted to Angewandte Chemie.

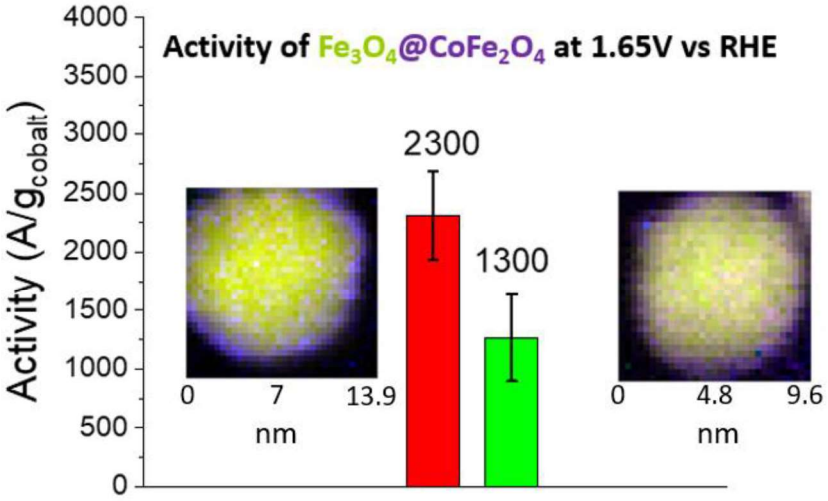

1) *Introduction*

Water electrolysis provides an environmentally friendly way to store renewable energies through the H_2 production. While proton exchange membrane water electrolysis is well suited to the renewable energy storage, it relies on the utilization of scarce and expensive Ir to accelerate the sluggish kinetics of the anodic oxygen evolution reaction (OER). Thanks to the recent progress in the development of anion-exchange membranes (AEM), transition metal oxides (TMOs) appear as promising substitutes for noble metals.[19,93,155,156] Various approaches were proposed to enhance their OER activity, notably varying the composition, particle size, defect concentration, or, recently, forming core-shell structures.[60,62–64,66]

Owing to their composition-dependent and widely tunable properties, TMOs with spinel structures became very attractive. While Co_3O_4 and CoOOH thin films deposited on an Au(111) substrate were reported to significantly enhance the OER activity,[43] core-shell nanoparticles (NPs) combining a gold core and a TMO shell reached 10 000 A/g_{TM} at 1.65 V *vs.* RHE. Such a high OER activity of TMOs may result from an electronic effect of gold that favors the oxidation of TM up to the 4+ state.[69,70] The use of core-shell nanoparticles might be an efficient way to reduce the amount of expensive and rare electrocatalysts by circumscribing them to a thin shell,[67,68] the exclusive use of cost-effective and abundant materials is the next challenge for the worldwide dissemination of water electrolysis.

Although most of TMOs are insulating, magnetite (Fe_3O_4) is conductive thanks to electron hopping between Fe (II) and Fe (III). Therefore, it may be considered as a promising support material to avoid carbons, which are often added to circumvent the lack of conductivity of TMOs catalysts, but are unstable under the anode operation conditions. Furthermore, iron cations in TM oxide phases may result in synergetic effects with the surrounding atoms, thus enhancing the OER[72,73]. All of the above makes Fe_3O_4 an excellent candidate as the core of noble metal-free OER catalysts.

TMO nanoparticles are also of significant interest since the catalytic activity can be greatly enhanced by adapting their size, i.e. the active surface area. The fine-tuning of the size of the conductive core, the thickness of the catalyst shell, the valence of the metallic cations, and their chemical environment may be also critical parameters to consider for enhancing the OER activity. Consequently, the challenge lies not only in identifying the chemical structure of NPs, but also in controlling their formation in order to systematically study their electrochemical properties Beyond the fine control of narrow size distribution and well-defined shape, recent advances in nanoparticle

synthesis in liquid media avoid aggregation which favors high surface area, *i.e.* enhanced mass-weighted catalytic activity.

Here we report on an original approach to design a new type of carbon-free, noble-metal-free nanostructured material for the OER. The core-shell structure of $Fe_{3-\delta}O_4$@$CoFe_2O_4$ NPs allows the combination of a conductive magnetite core and a catalytically active cobalt ferrite shell. Such a cost-effective material resulted in an excellent OER activity per unit mass of Co. The fine control of the core size and the shell thickness led us to investigate the influence of the core-shell structure on the OER which is markedly enhanced by a larger conductive core. The influence of the pH and concentration of the electrolyte as well as the addition of oleic acid ligand on the electrocatalytic activity are also investigated. Higher pH and lower quantities of ligands seem to have a positive impact on the catalytic activity.

The NPs used for this study are CS-1, CS-2, CS-3 and CS-4 which have been previously presented in chapter 3. As a consequence, only a quick reminder of the most important features of these NPs will be made here.

2) *NPs synthesis and characterizations*

Four types of core-shell nanoparticles were synthesized thanks to the decomposition of two precursors in a high temperature boiling solvent to induce seed-mediated growth and in the presence of a surfactant to keep the NPs from aggregating. They were synthesized *via* two different approaches: The first one is based on the epitaxial crystal growth (CG) of a $CoFe_2O_4$ shell on a $Fe_{3-\delta}O_4$ core as we recently reported[114]. The second approach relied on the diffusion (D) of cobalt into the core vacancies as we previously reported [113]. All the synthesis protocols are presented in chapter 2.

NPs were characterized by several analysis techniques which confirmed their structure, composition and suitability for electrochemical characterizations:

- TEM micrographs showed that the NPs were quasi-spherical and presented a narrow size distribution. The EDX also showed the presence of cobalt in the structure.
- Granulometry measurements demonstrated that the core-shell NPs were a stable non-aggregated suspension.
- X-ray diffraction (XRD) patterns display peaks corresponding to the spinel crystal structure both for the core and the core-shell NPs, demonstrating the crystallinity of the catalyst.
- The crystallinity of the NPs was also confirmed by Scanning Transmission Electron Microscopy with a High Angle Annular Dark Field detector (STEM-HAADF) images which showed lattice fringes all-across each core-shell NP.
- The local composition of these NPs was then further investigated by Electron Energy Loss Spectroscopy (EELS) analysis that demonstrated the presence of a sharp and defined shell on these NPs. This technique also demonstrated an iron depletion at the surface of the NPs and a gradient of cobalt concentration inside the structure.
- While EELS provided information regarding local composition of the NPs, X-ray photoelectron spectroscopy (XPS) depth profiling measurements were performed to probe the average near-surface composition of the sample and also evidences the core-shell structure. Also, in agreement with the EELS results, an iron depletion at the surface of the NPs and a gradient of cobalt concentration inside the shell was observed.

All the parameters of the NPs are summed up in Table 6 .

Table 6: Mean size of the $Fe_{3-\delta}O_4$ core and $Fe_{3-\delta}O4@CoFe_2O_4$ core-shell nanoparticles and the corresponding Co:Fe atomic ratio. Epitaxial crystal growth (CG), diffusion (D)

Sample	$Fe_{3-\delta}O_4$ size (nm)	$Fe_{3-\delta}O_4@CoFe_2O_4$ size (nm)	Co:Fe at. %	Synthesis method	Cell parameter $Fe_{3-\delta}O_4@CoFe_2O_4$
CS-1	7.5	8.3	15	CG	8.3815 ± 0.001
CS-2	9.1	9.3	16	D	8.386 ± 0.002
CS-3	12.7	14.0	19	CG	8.387 ± 0.004
CS-4	13.6	15.7	12	CG	8.3797 ± 0.006

Such an excess of Co at the nanoparticle surface may be explained by the faster decomposition of the Fe complex compared to the Co one. Indeed Fe(II) stearate presents a lower decomposition temperature than the Co(II) stearate[115]. The Fe oxide thus starts growing at the surface before the beginning of the Co oxide growth, which creates a gradient of Co concentration in the shell. However, their decomposition temperature is close enough so that no phase segregation in wüstite or CoO is observed on the diffractograms[140].

The NPs were then characterized electrochemically and their redox properties as well as their activities will be studied in the next part.

3) Electrochemical characterizations

a) Activity determination

After determining the optimal loading of NPs in order to evaluate accurately their activity (chapter 4), electrochemical characterizations of all four types of the core-shell NPs were performed to determine their activity for the OER.

More details on the cyclic voltammetry experiments are given in chapter 2. Cyclic voltammetry experiments were performed in a three electrodes cell in 0.1M NaOH electrolyte by dropcasting a thin layer of NPs on a glassy carbon substrate. All the experiments were repeated three times to study their reproducibility and all potentials were then corrected to the RHE by regularly calibrating the electrode reference (around 0.93 V) and the electrolyte resistance R_s was measured thanks to impedance spectroscopy in order to correct the ohmic losses. The potential was recalculated as follow (i is the current generated by the reaction):

$$E_{RHE} = E_{Hg/HgO} + 0.93 - i \times R_s$$

As stated in chapter 1, in order to evaluate the activity of a catalyst and compare these results to the literature, normalizing the current by the surface of the particles or by their actual mass is imperative. In this study, the concentration of cobalt and iron in a given volume has been determined by Inductively coupled plasma atomic emission spectroscopy (ICP- AES). From these measurements the oxide mass was obtained. The surface of the NPs has been calculated thanks to the average diameter of the NPs measured by the TEM, considering the NPs were displaying a perfect monomodal distribution and were perfectly spherical. This is an overestimation of the actual electrochemically active surface but is still a good approximation.

The surface weighted activity and the oxide mass weighted activity were calculated as follow:

$$surface\ weighted\ activity\ (mA.cm^{-2}) = \frac{current\ (mA)}{oxide\ surface\ (cm^2)}$$

$$oxide\ mass\ weighted\ activity\ (A.g^{-1}) = \frac{current\ (A)}{oxide\ mass\ (g)}$$

Equation 9: calculation of the surface weighted activity and the oxide mass weighted activity

On the cyclic voltammetry curves of Figure 64, the current measured has been divided by the NPs mass. It can be observed that the core's material ($Fe_{3-\delta}O_4$) is not active. Indeed, at 1.65V the OER has not started yet while at this potential, core-shell NPs already display an important activity. Hence, as expected, it is the cobalt ferrite shell that imparts the NPs OER activity.

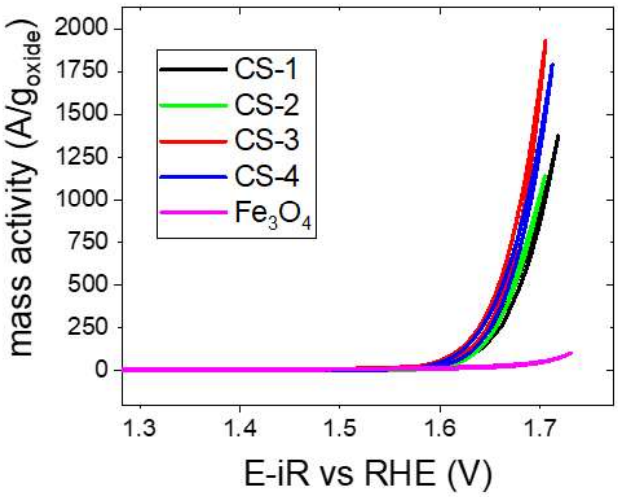

Figure 64: Cyclic voltammetry measurements performed on CS-1, CS-2, CS-3 and CS-4 deposited on a glassy carbon electrode (oxide loading about 1µg/cm²), in 0.1M NaOH, scan rate 10mV/s. The current has been divided by the oxide mass

As the cobalt is the atom responsible for the activity of the catalyst and is only present in the shell, another type of activity, normalizing the current by the cobalt mass can be introduced:

$$cobalt\ mass\ weighted\ activity\ (A.g^{-1}) = \frac{current\ (A)}{cobalt\ mass\ (g)}$$

Equation 10: calculation of the cobalt mass weighted activity

This indicator will be a better estimation of the activity of the catalyst as it will consider the low amount of cobalt present in the structure responsible for the activity and not the entirety of the NPs. These different kinds of activities will be studied on the different types of NPs synthesized for this study. From the cyclic voltammetry curves, another indicator of the activity of a catalyst was extracted from the anodic scans of the cyclic voltammograms (Figure 65): the Tafel slope. From this graph, it can be observed that Fe_3O_4 NPs present a high Tafel slope, further confirming their low OER activity. In the meantime, core-shell NPs all display Tafel slopes of about 60 mV/decade which is coherent with the literature for similar compounds (see Table 7).

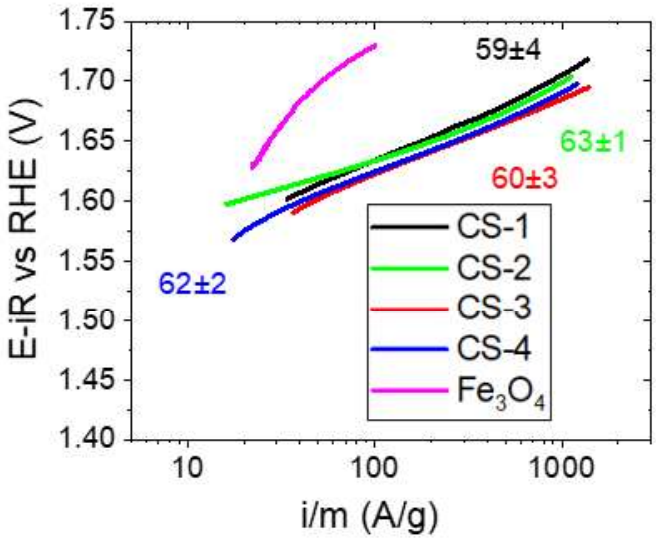

Figure 65: Tafel slopes (in mV/decade) of CS-1, CS-2, CS-3 and CS-4 extracted from the anodic scan of the cyclic voltammetry curves presented above.

b) Core diameter influence on the NPs activity

Thanks to the calculations mentioned in Equation 5 and Equation 6, the current observed at 1.65 V was divided by the mass of cobalt, the NPs surface area and by the mass of oxide to evaluate their activity. 1.65 V is a high potential compared to the potential values usually used in the literature to determine the activity but it was chosen considering the low NPs loading on the substrate. The Co mass-, surface- and oxide mass- weighted OER activities at 1.65V are plotted in Figure 66 A, B and C respectively.

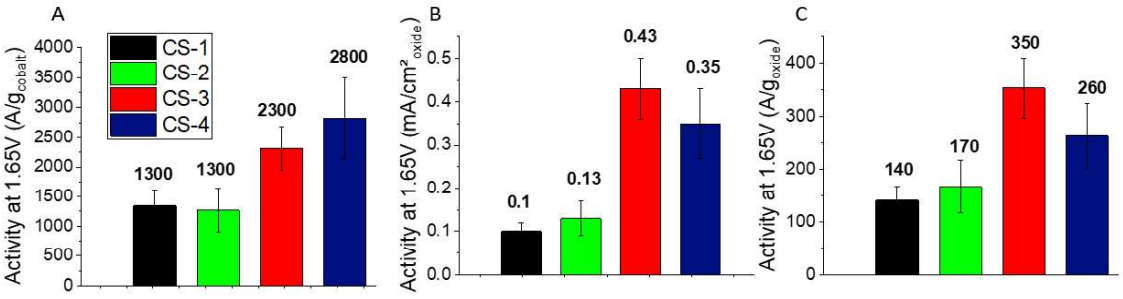

Figure 66: Co mass (A), surface(B) and oxide mass (C) weighted OER activities at 1.65V vs. the real hydrogen electrode (RHE, all subsequent potentials are given vs. this reference)

While all core-shell NPs studied in this work demonstrate excellent OER activities, larger NPs seem to be better candidates. Indeed, the OER activity at 1.65 V is about 1300 A/g_{cobalt} for CS-1 and CS-2 (Figure 66 A) and it is about doubled for CS-3 and CS-4 (2300 and 2800 A/g_{cobalt} respectively). The same trend can be observed for the surface-weighted activity (Figure 66 B) where it is increased by a

3-4-fold factor for larger NPs. Finally, for the oxide-mass weighted activity the same observation is made: the activity of larger NPs is increased by a 2-fold factor compared to small NPs.

With a record activity at 2800 A/g_{cobalt} for CS-4, the $Fe_{3-\delta}O_4$@$CoFe_2O_4$ core-shell NPs greatly outperform most of the TMO catalysts for alkaline OER reported in the literature, with a uniform structure or with a Fe_3O_4-core-shell structure (Table 7).

*Table 7: Mass activities calculated from the literature for different type of catalysts and their Tafel slopes compared to the activities obtained in this work. Data with * have been extrapolated thanks to the values of the Tafel slopes.*

Catalyst	Mass activity(A/g)	Tafel slope (mV/decade)	Loading (µg/cm²)	Carbon	Electrolyte concentration	Reference
$Co(OH)_2$	125*	59	204	Graphene	0.1M KOH	58
CoFe layered double hydroxide	185*	43				
$CoFe_2O_4$ NFs	16	82	429	No carbon	0.1M KOH	59
$CoFe_2O_4$ NPs	2	223				
$CuFe_2O_4$ NFs	0.3	93				
Fe_2O_3 NFs	0.2	148				
$NiFe_2O_4$ NFs	3.4	98				
$CoCr_2O_4$	23.4	177	204	No carbon	0.1M KOH	45
Co_2TiO_4	2.1	83				
$MgCo_2O_4$	120	70				
Co_3O_4	51.6*	61				
Co_3O_4	9.6	83	210	No carbon	0.1M KOH	44
$Co(OH)_2$	12	63				
Fe_3O_4	21	96	960	No carbon	1M KOH	46
Co_3O_4	78	72				
$CoFe_2O_4$	182	58				
Co_3O_4@CoO@Co	56	92	127	No carbon	0.1M KOH	60
Fe_3O_4@CoO	77A/g_{oxide} 154 A/g_{cobalt}*	89	300 (catalyst)	Vulcan XC-72	0.1M KOH	61
Au@Co_3O_4	312A/g_{oxide} 500A/g_{cobalt}*	60	200 (catalyst+carbon) 64 (catalyst) 40 (Co_3O_4)	Vulcan XC-72	0.1M KOH	62
Au@$CoFeO_x$	16 200A/g_{TM}*	58	56 (TM)	Vulcan XC-72	1M KOH	63
Au@$NiCo_2S_4$	50 000 A/g_{oxide}*	44.5	200	Carbon black	1M KOH	64
Fe_3O_4	15 A/g_{oxide}	105	100	No carbon	1M KOH	65
$Co_{0.25}Fe_{2.75}O_4$	50 A/g_{oxide} 600 A/g_{cobalt}	80				

$Co_{0.5}Fe_{2.5}O_4$	90 A/g_{oxide} 540 A/g_{cobalt}	45				
$Co_{0.75}Fe_{2.25}O_4$	170 A/g_{oxide} 680 A/g_{cobalt}	46				
$CoFe_2O_4$	170 A/g_{oxide} 510 A/g_{cobalt}	45				
$Co_{1.25}Fe_{1.75}O_4$	220 A/g_{oxide} 528 A/g_{cobalt}	48				
$Co_{1.5}Fe_{1.5}O_4$	310 A/g_{oxide} 620 A/g_{cobalt}	46				
$Co_{1.75}Fe_{1.25}O_4$	350 A/g_{oxide} 600 A/g_{cobalt}	50				
Co_2FeO_4	450 A/g_{oxide} 675 A/g_{cobalt}	50				
$Co_{2.25}Fe_{0.75}O_4$	500 A/g_{oxide} 666 A/g_{cobalt}	52				
$Co_{2.5}Fe_{0.5}O_4$	430 A/g_{oxide} 516 A/g_{cobalt}	47				
$Co_{2.75}Fe_{0.25}O_4$	300 A/g_{oxide} 327 A/g_{cobalt}	56				
Co_3O_4	150 A/g_{oxide}	61				
Co_3O_4	123*A/g_{oxide}	61.2	300	No carbon	1M NaOH	[25]
Co_3O_4	240*A/g_{oxide}	80	15	Sibunit		
Co_3O_4	152*A/g_{oxide}	65	15	BDD		
$CoO_x(OH)_y$ 9nm	5000* A/g_{cobalt}	37	2.98	No carbon	0.1M KOH	[57]
$CoO_x(OH)_y$ 6nm	5000* A/g_{cobalt}	39	0.82			
$CoO_x(OH)_y$ 4nm	11 000* A/g_{cobalt}	43	0.82			
$CoO_x(OH)_y$ 1nm	14 000* A/g_{cobalt}	43	0.25			
CS-1	0.1 mA/cm^2_{oxide} 140 A/g_{oxide} 1300 A/g_{cobalt}	59	Between 0.6µg/$cm^2_{electrode}$ and 5.5µg/$cm^2_{electrode}$	No carbon	0.1M NaOH	This work
CS-2	0.13 mA/cm^2_{oxide} 170 A/g_{oxide} 1300 A/g_{cobalt}	63				
CS-3	0.43 mA/cm^2_{oxide} 350 A/g_{oxide} 2300 A/g_{cobalt}	60				
CS-4	0.35 mA/cm^2_{oxide} 260 A/g_{oxide} 2800 A/g_{cobalt}	62				

One example of a higher OER activity for a uniform structure reported in the literature is that of $CoO_x(OH)_y$ NPs[57] where the activities values reported were from 5 000 to 14 000 A/g for NPs diameters ranging from 1 to 9 nm. Their small size can partly explain their high efficiency for the OER. Additionally, it is worth noting that the activities were measured for low loading (often inferior to 1µg/cm²) which as we proved in chapter 4 can lead to higher activity values.

Considering the core-shell, structures, the only material that has been reported with a higher OER activity is NPs with a gold core[63,64] (Au@$CoFeO_x$ and Au@$NiCo_2S_4$) which activities were reaching 10^4 A/g_{TM}. However, these activities were measured in 1M KOH electrolyte (and not 0.1M NaOH like in our study, the influence of the electrolyte concentration will be investigated later) by mixing the catalyst with carbon black, the latter leading to a better dispersion and thus higher site accessibility (on top of the Au-induced activity improvement thanks to the core of the NPs) but being detrimental for practical applications as the carbon oxidizes in the OER potential range[147]. Additionally, gold is an expensive and rare metal, which makes the development of this catalyst at a larger scale less likely.

The two-fold factor difference in activity between CS-1 and CS-2 *vs*. CS-3 and CS-4 likely originates from the differences in core sizes (7.5 – 9.1 nm *vs.* 12.7 – 13.6 nm). This incidentally explains the low activity observed for Fe_3O_4@CoO (154 A/g_{cobalt}) nanocubes with a small core diameter of 4.5 nm [61]. Large Fe_3O_4 NPs have been proved to be conductive[132,133] and small NPs are often less conductive due to their surface oxidation in maghemite. Consequently, the core conductivity is likely to be essential for reaching high OER activity.

We also presume a synergistic effect between the Fe_3O_4 core and $CoFe_2O_4$ shell where Fe (II) cations from the core act as efficient electron donors to the Co (II) cations from the shell. This synergistic effect and the transformations of the NP structure during the OER will be developed in chapter 6 which presents the detailed *operando* study of CS-3 NPs under synchrotron radiation studying the iron L-edge, cobalt L-edge and Oxygen K-edge.

A few other parameters such as the pH, the electrolyte concentration or the quantity of ligand surrounding the NPs can have an impact on the catalyst activity. They have been investigated and the results will be presented in the next paragraphs.

c) *Influence of the NaOH electrolyte concentration on the catalytic activity*

Another factor that can influence the apparent electrocatalytic activity is the electrolyte, notably its type, concentration, and its pH. Firstly, an increased concentration of the electrolyte usually results in a higher conductivity of the electrolyte, hence less ohmic losses. Second, the type of electrolyte and its concentration can also influence the reaction kinetics. Indeed, Duan *et al.*[47] recently worked on TMO catalysts in alkaline media and, as presented in chapter 1, observed important differences in the catalytic activities depending on the electrolyte that was used (LiOH, NaOH, KOH, CsOH) but also on its concentration. They observed an important cation (Li^+, Na^+, K^+, Cs^+) effect on CoOOH and on $Fe_{0.5}Co_{0.5}OOH$ activity and important changes on CoOOH activity as a function of the

electrolyte concentration. Generally in the literature, an increase in the electrolyte concentration has been linked to an increase in the catalytic activity[48,49,157].

Giordano et al.[51] also studied the pH influence on the OER on TMO catalysts and concluded on the importance of measuring the cyclic voltammetry curves with respect to the RHE as a pH-dependent, which allows one to conveniently separate thermodynamic and kinetic effects in electrocatalysis. They also suggested that for systems containing transition metal oxides, which can sustain certain degree of charge buildup accommodated by a change in the TM oxidation state, decoupling of proton and electron transfers during the OER reaction is possible. It has been suggested by M. Koper[52] that the pH dependence of the OER activity points to the presence of non-concerted proton–electron transfer steps during the OER. Grimaud et al. [53] studied perovskite compounds for the OER and, by increasing the pH, they obtained higher OER activities. They concluded that non-concerted proton–electron transfer steps are coupled to the activation of lattice oxygen redox reactions in their catalyst. Kim et al.[54] studied the OER on perovskite catalysts and concluded that both the lattice oxygen evolution and the conventional OER occurring on the oxide surface occur simultaneously, the former dominating at high pH. The influence of the electrolyte composition and concentration and pH is thus highly debated in the literature and it would be interesting to study their influence on the OER on core-shell NPs as it could give more insights into the OER mechanism.

While detailed investigation of the electrolyte concentration on the catalytic activity of CS-3 NPs is beyond the scope of this thesis, in what follows we will compare OER activity in 1.0 and 0.1 M NaOH electrolytes. The experiments were performed on CS-3 NPs in a 0.1 M NaOH and a 1 M NaOH electrolyte with two different Hg/HgO reference electrodes calibrated for these pHs. Even if more experiments on other samples for different loadings and in a wider range of pH would be needed to confirm this trend, the cyclic voltammetry curves obtained for a higher electrolyte concentration, clearly exhibited better OER performance (Figure 67). Indeed, in 1.0 M electrolyte the activity normalized by the cobalt mass of the catalyst is increased by a factor of 2-3. Following Ref[52,53], the increase of the OER current with pH could be tentatively attributed to a OER mechanism involving a non-concerted proton–electron transfer step as the rate determining step. It would also hint at the involvement of lattice oxygen in the electrocatalytic reaction. However, the latter is in contradiction to the OER mechanism discussed in Chapter 6 (*operando* study of the transformations occurring on the NPs during the OER), whereby no formation of electron-deficient oxygen species was detected (cf. O-K-edge spectra).

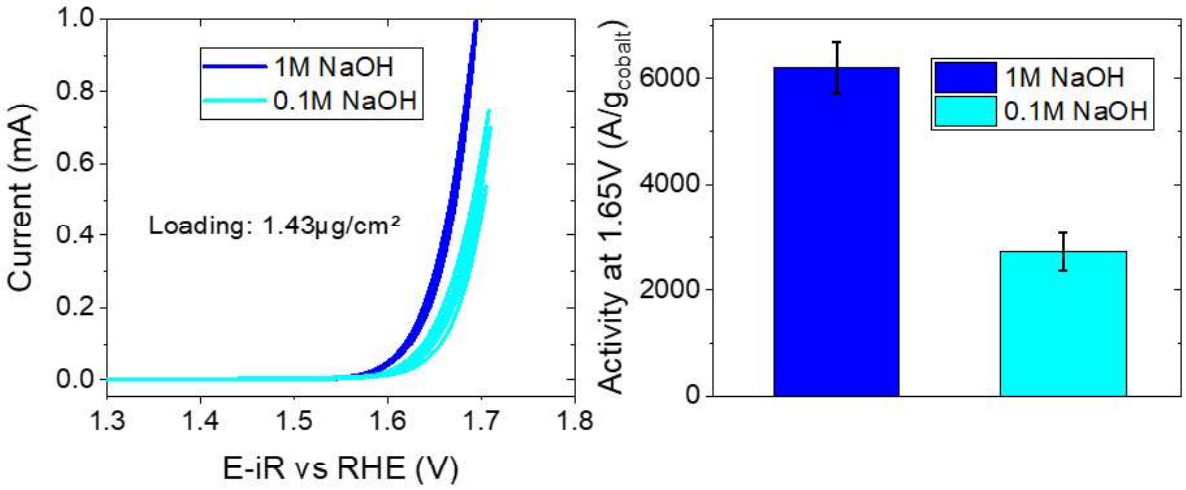

Figure 67: Left: cyclic voltammetry curves obtained for the same loadings (1.43 µg/cm²) in 1 M and in 0.1 M NaOH electrolyte and their corresponding activities (right) normalized by the cobalt mass.

The Tafel plots corresponding to the two different pHs have also been extracted from the anodic part of the cyclic voltammetry curves (Figure 68). They don't display significative differences and the mechanism is likely the same at both electrolyte concentrations. Due to the low catalyst loading on the electrode, it was not possible to observe the redox peaks of cobalt in these experiments. In the future, it would be interesting to evaluate the influence of the electrolyte concentration on the cobalt redox peaks by performing experiments with higher loadings.

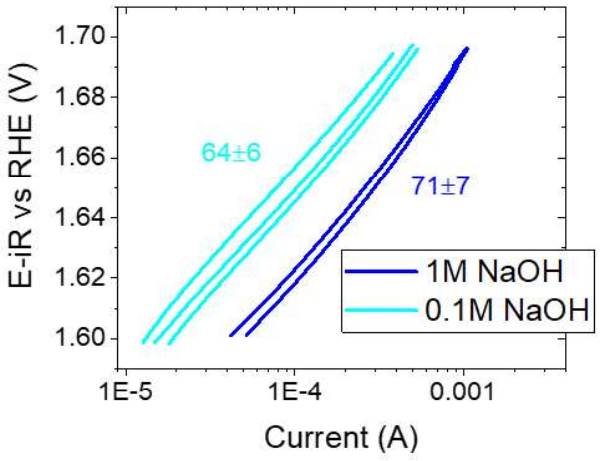

Figure 68: Tafel slopes of CS-3 NPs in 0.1 M (light blue) and 1.0 M (dark blue) NaOH electrolyte. Loading 1.43 µg/cm².

To sum up, the electrolyte concentration has an important influence on the catalytic activity, hinting to a non-concerted proton–electron transfer steps as the rate determining step. Indeed, the activity in a 1.0 M electrolyte has been multiplied by 2-3 compared to a 0.1 M electrolyte. However, from these preliminary experiments, it is difficult to draw definite conclusion regarding the lattice oxygen involvement in the OER mechanism. Indeed, along with the pH, the concentration of Na^+

cations could also affect the OER kinetics. Indeed, Duan *et al.*[47] suggested that the counter ion (K^+, Na^+, Li^+) can have a high impact on the catalytic activity, especially for iron-containing catalysts. Further investigation on the influence of the electrolyte on the OER activity of core-shell NPs (pH effect at a constant Na^+ concentration and Na^+ concentration at a constant pH) would be interesting to carry out in the future as it could shed some light on the OER mechanism.

d) Influence of the presence of oleic acid

Another factor presented in chapter 1 that can influence the catalytic activity is the ligand surrounding the NPs. Li *et al*.[55] suggested that the presence of a surfactant such as oleic acid or oleylamine may be detrimental for electrocatalytic reactions. They studied the case of platinum particles for the ORR and obtained a more than three-fold increase of the ORR activity between the untreated sample and the sample on which they removed the oleylamine surfactant. In order to remove the surfactant, they used three different methods: chemical washings, UV irradiation or annealing, the more efficient was the annealing. It is worth noting that with this annealing, it is likely that the surface reconstructs to become more crystalline and that is has an impact on the electrochemical properties of the material. More recently, a similar effect was also observed on iridium particles for the OER in acidic media[56].

In order to avoid their aggregation, the synthesis of the NPs presented in this work was performed in the presence of oleic acid. They have been chemically washed with warm acetone in order to remove a major part of the oleic acid but some is still present at the NPs surface to provide some colloidal stability to the suspension. In order to evaluate the importance of the oleic acid presence around the NPs, 1 µL of oleic acid was added to the NPs in suspension. Their concentration was then divided by a factor of 10 (corresponding to an added oleic acid concentration of $3.17\ 10^{-7}$ $mol.L^{-1}$ ($0.1\mu L.mL^{-1}$)) and they were deposited on the working electrode. The activity of the catalyst was determined in presence of added oleic acid and without added oleic acid (Figure 69).

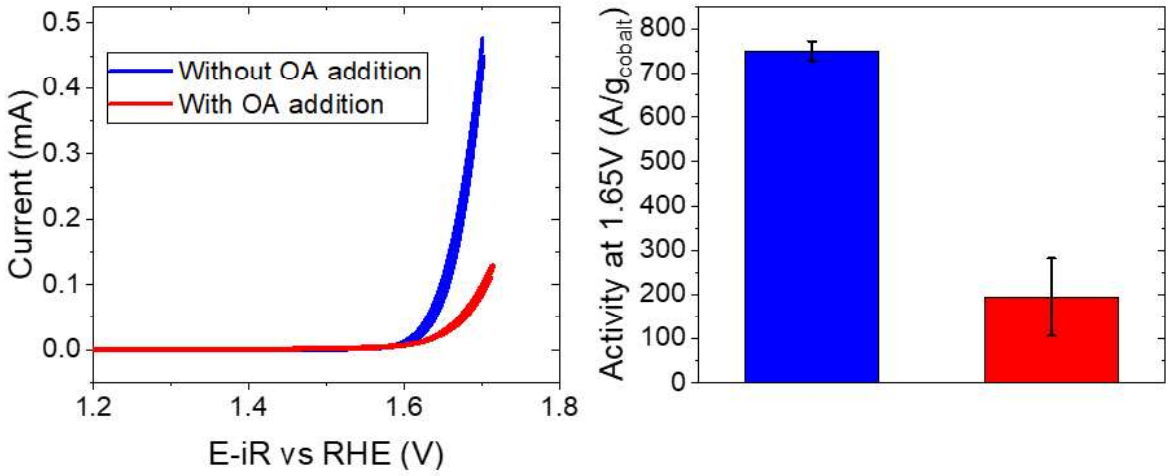

Figure 69: Left: cyclic voltammetry curves obtained for a 3.2 µg/cm² loading of CS-1 NPs on the electrode and their corresponding activities at 1.65 V vs. RHE normalized by the cobalt mass (right) without and with the addition of 0. 1 µL.mL^{-1} of oleic acid (OA).

The cyclic voltammetry curves of Figure 69 display important changes depending on whether oleic acid has been added to the colloidal NPs suspension or not. The activity of the NPs without the addition of oleic acid is higher by a factor of 4 compared to the ones with added oleic acid. This would need to be investigated further but it confirms that an excess of ligands is detrimental for practical applications. Thanks to the washing steps after the synthesis, all the unnecessary oleic acid is removed from the NPs surface but it is still present at their surface in order to avoid their aggregation and could have an influence on the activity. This lower activity for a higher amount of ligand is also confirmed by the Tafel slopes extracted from the anodic part of the cyclic voltammetry curves (Figure 70), that are higher when some oleic acid has been added to the NPs suspension.

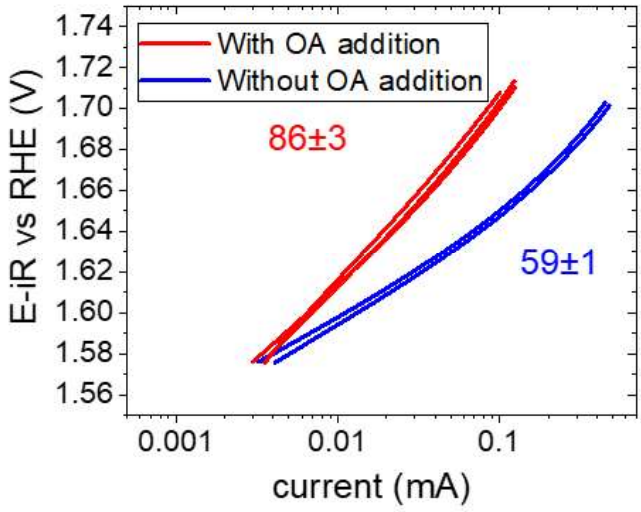

Figure 70: Tafel Slopes of CS-1 with and without the addition of oleic acid (OA). Loading 3.2µg/cm².

To conclude, the presence of oleic acid ligands around the NPs has a high impact on their activity as in the presence of added oleic acid, the NPs present an activity divided by a factor of four compared to the NPs for which no oleic acid has been added in the suspension. This can be explained by the fact that when more oleic acid surrounds the NPs, less of their surface is then involved in the OER. In this work, the impact of the oleic acid has been reduced as much as possible thanks to thorough washing of the NPs with warm acetone after their synthesis and the NPs are displaying a high activity at least at the level of the values observed in the literature (and even far more important than these values if only the cobalt mass is considered when normalizing the current to obtain the activity). It was consequently assumed that if the oleic acid was playing a role, it would likely be negligible.

Li *et al.*[55] suggested that the surfactant removal could be performed using different methods such as chemical washing (which has been done on our catalyst), heating at a temperature high enough for the ligand to decompose, or irradiating the sample by UV radiations. There are consequently other methods to remove the surfactant from the NPs surface but not all these solutions are applicable on our system. In this study the NPs are deposited on a glassy carbon electrode that can't withstand high temperatures without degrading, annealing is thus impossible. Another substrate would then be needed to study the influence of this parameter. A gold substrate has been studied as it can be heated to high temperatures, the NPs were grafted on a the gold substrate[124] (see chapter 2). The oleic acid was removed thanks to a thermal treatment at 300°C for 10 minutes and a submonolayer of NPs was obtained. Their properties for the OER were evaluated (Figure 71).

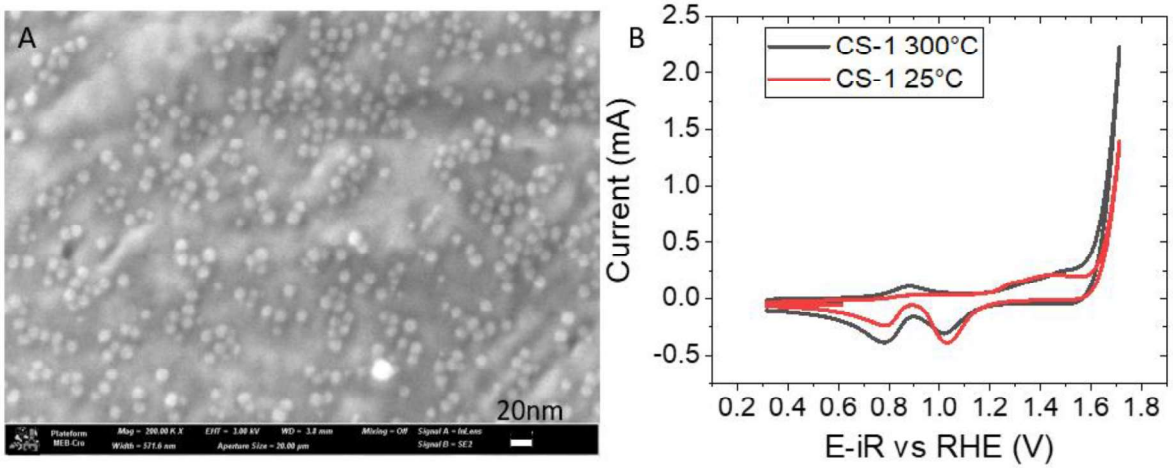

Figure 71: A) SEM image of a sub monolayer of NPs grafted on a gold substrate, B) Cyclic voltammetry curves obtained on core-shell NPs CS-1 annealed at 300°C under air for 10 minutes and not annealed.

Figure 71 displays a more important current for the annealed NPs. As the experiments were performed on two gold plates presenting the same surface and as the functionalization times were similar the coverage is supposed to be similar for both samples, hence annealed samples are likely to present a better activity. However, upon the successive annealing and cleaning processes performed

on the gold substrates, it was observed that the gold activity was increasing, progressively becoming active for the OER. This was problematic as the role of the substrate is to ensure conductivity but if it is active for the OER, its contribution should be removed from the activity measurements. As the substrate contribution is not straightforward to evaluate, a substrate which does not display OER activity (glassy carbon) was chosen and the use of a gold substrate was abandoned. Additionally, gold has been reported for OER activity enhancement in the literature[69,70] which would be better to avoid in order to get a better understanding of the phenomena occurring at the surface of the NPs. In the future, it would be interesting to try to irradiate the NPS with UV radiations in order to see if this has an influence on the activity.

4) Conclusion and perspectives

To sum up, core-shell Fe_3O_4@$CoFe_2O_4$ NPs with a uniform size distribution have been successfully synthesized through two alternative approaches (diffusion and crystal growth). They present excellent OER activities per unit mass of cobalt (ranging from 1300 to 2800 A/g_{cobalt}), and greatly outperform most of the OER activities of transition metal oxide nanoparticles reported in the literature.

Along with the core-shell structure, the size of the core plays key role in the OER activity, which is tentatively attributed to the conductivity of Fe_3O_4 and a synergistic effect between the core and the shell (that will be developed in chapter 6). However, the synthesis method does not seem to have an influence on the obtained activity. Thus, controlled synthesis of core-shell nanostructures seems to be a viable approach for designing promising alkaline OER catalysts. In the future, the influence of different shapes (cubic, plates) on the OER activity should be investigated in order to understand if some crystallographic plans are better than others for the reaction to occur. Also, the comparison between core-shell and pure $CoFe_2O_4$ NPs is something that should be done to confirm the conductivity role of the core. However, due to the differences in decomposition temperature of the cobalt and iron (II) stearates, and the fact that the nucleation is a more difficult step than the growth, all the synthesis we tried failed and were not magnetic or presented two different populations of nanoparticles with different compositions. Finally, one last experiment that would be of high interest is the replacement of the cobalt ferrite shell by a nickel ferrite one and the investigation of the properties of a cobalt/nickel core-shell NP (Fe_3O_4@$Co_xNi_{1-x}Fe_2O_4$). Indeed, nickel is known to be active for the OER and would be a good candidate for the catalysis of the OER.

Further studies should be performed on the influence of the electrolyte concentration and on the pH on the basis of preliminary and promising results correlating the catalytic activity to the electrolyte concentration. However, higher electrolytes concentrations (and pH) seem to be better for the OER activity. Indeed, with a NaOH concentration of 1 M (pH= 14), the activity of the NPs was three times higher than for a concentration of 0.1 M (pH=13). The dependence of the OER activity to pH has been linked to a non-concerted proton–electron transfer steps as the rate determining step and the involvement of lattice oxygen in the redox reaction in the literature.[52,53] However, from the experiments presented above, it was not possible to determine if the activity was influenced by a higher concentration in Na^+ or OH^- (or both) ions. In the future, deeper investigation of the electrolyte nature, the impact of the counter ion, and its concentration on the OER activity should be performed to get a better understanding of the OER on these samples.

Preliminary experiments focusing on the evaluation of how the surfactant (oleic acid) surrounding the NPs was impacting the OER activity demonstrated that low concentrations of surfactants seem to be better for the OER activity. When oleic acid was added to the NPs suspension, its activity was divided by four. It was assumed that the chemical washing steps were enough to evaluate the activity of the NPs. Indeed, they displayed a more important activity than most of the catalysts reported in the literature. However, to make sure that the ligand removal is efficient enough, more analysis on another substrate than gold (which use has been abandoned due to all the above-mentioned factors) would be interesting. A substrate that would not present possible interaction with the catalyst or that wouldn't be subjected to reconstruction upon annealing or the application of a potential would be interesting. in order to make sure that the ligand removal was efficient enough with the chemical washing. Exposing the sample to UV radiations could also be another way to remove the leftover oleic acid while avoiding coalescence of NPs. It could be performed on a glassy carbon electrode to assess the need for additional surfactant removal.

In the next chapter, the transformations occurring on the NPs surface during the OER will be investigated thanks to synchrotron radiations to get a better understanding of the iron and cobalt interaction in these types of structures.

Chapter 6: *in situ* and *operando* studies of the NPs upon potential application and annealing in O_2 atmosphere

This chapter is based on the manuscript "Cooperative red-ox transitions drive electrocatalysis of the oxygen evolution reaction on cobalt-iron core-shell nanoparticles" by L. Royer, A. Bonnefont, T. Asset, B. Rotonnelli, J. Velasco-Velez, S. Holdcroft, S. Hettler, R. Arenal, B. Pichon, and E. Savinova, ACS catalysis, accepted.

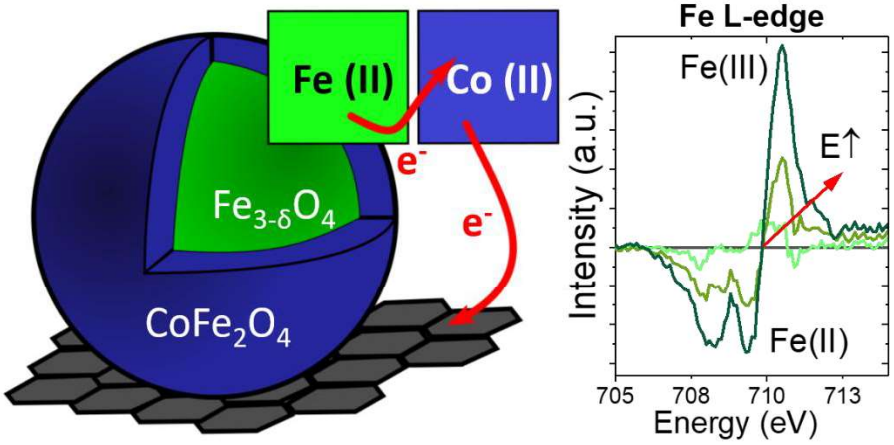

1) *Introduction*

Anion exchange membrane water electrolysis is an attractive alternative to proton exchange membrane electrolysis as it allows the replacement of iridium or ruthenium at the anode with more abundant 3d (Ni, Co, Fe, Mn) transition metal oxides (TMO).[129,130] TMOs possessing a spinel structure constitute a promising class of oxygen evolution reaction (OER) catalyst due to their high activity, relatively low synthesis temperature (allowing preparation of high surface area catalysts without coalescence), their composition-dependent and widely tunable properties. However, the nature of the active sites which is connected to the evolution of the surface structure and the composition under the OER conditions are not fully understood. These knowledge gaps hamper building correlations between the chemical structure of materials on the one hand and their OER activity/durability on the other hand, ultimately impeding the development of active and stable catalysts for the anode of the AEMWE.

Bergmann *et al.*[87] studied nanocrystalline Co_3O_4 films during the OER using *in situ* X-ray diffraction and '*quasi-in situ'* absorption spectroscopy (samples were freeze-quenched under potential control). They found that in the potential interval of the OER the Co (II) ions were oxidized into octahedrally (Oh) coordinated, di-μ-O(H)-bridged Co (III/IV) species resulting in a reversible formation of a sub-nanometer thick amorphous $CoO_x(OH)_y$ shell. In contrast, Ortiz-Pena *et al.*[41] studied Co_3O_4 nanoparticles (NPs) *in situ* by transmission electron microscopy under potential control (EC-TEM) and found that this amorphization is irreversible. In the meantime, Reikowski *et al.*[43] applied *operando* surface X-ray diffraction to study structurally well-defined epitaxial cobalt oxide thin Co_3O_4(111) film electrodeposited on Au(111). They observed fast and fully reversible Co_3O_4(111)/CoOOH (001) transformation at potentials 300 mV negative of the 'onset' of the OER, and thus concluded that the observed structural transformation was not OER-driven. By comparing the OER activity of Co_3O_4(111) and CoOOH (001) epitaxial crystalline films the authors argued against di-μ-oxo bridged Co cations being responsible for the OER activity of Co oxides. In the case of $Co(OH)_2$ particles, Mefford *et al.*[89], by using *operando* scanning probe and X-ray microscopy techniques, documented Co (II) into Co (III) oxidation leading to the formation of β-CoOOH under OER conditions and concluded that Co (III) at the particle edges were the OER active catalytic sites. Recently, Haase *et al.*[57] studied transformations of $CoO_x(OH)_y$ NPs with the average size ranging from 1.6 to 9.3 nm during the OER with *operando* X-ray absorption spectroscopy and density functional theory (DFT). The authors arrived to the conclusion that during the OER an electron 'hole' resides on oxygen (the so-called 'anion-redox' OER mechanism) ions rather than Co cations, leading to the formation of electron-deficient 'oxyl' rather than Co (IV) species (similar to what has been previously proposed for IrO_x-catalyzed OER[91,92]), and that this charge

redistribution between the cobalt and oxygen atoms is particle size-dependent. From the aforementioned works, it appears that (i) the oxidation degree of the Co during the OER, namely the occurrence of the Co (II) to Co (III) and Co (III) to Co (IV) transitions, and (ii) the formation of the CoOOH phase and its reversibility, are rather controversial in the literature. This complexifies even further when addressing the Co-Fe based catalysts for the OER.

Numerous studies have revealed the crucial role of iron in enhancing the OER activity of Ni and Co-based TMO[93] catalysts with further controversies regarding the reasons for this enhancement. Since iron oxide itself presents a low activity for the OER, it was suggested that a synergetic effect between iron and other TMs such as nickel or cobalt[73] is at the origin of the observed enhancement. Using Hubbard model DFT+U calculations, Wang *et al*[158] demonstrated that, for Fe-doped Ni hydroxide, a local arrangement of Fe (III) with two Ni (IV) ions plays an important role in the OER activity, and that charge transfer during the OER occurs from Fe (III) to the OER intermediates. Xiao *et al.* also suggested a synergy between Fe and Ni where Fe (IV) catalyzes formation of an O radical intermediate and Ni (IV) catalyzes the O-O coupling[159]. It was also argued that the presence of iron modifies the e_g orbital filling[74], generating more active materials towards the OER. DFT+U calculations were also applied to elucidate the influence of iron on the OER activity of Co_3O_4[160,161]. They revealed influence of Fe on the oxidation state of Co and will be discussed in what follows. Although many studies have investigated transformations of cobalt-based catalysts during the OER, few have studied Co/Fe catalysts. Calvillo *et al.*[95] studied the Fe K-edge and the Co K-edge to scrutinize the chemical and structure changes of a Co-Fe spinel powder during the OER. They demonstrated that the samples suffered irreversible oxidation under the OER conditions leading to the formation of a layer consisting of Co_3O_4, CoOOH and Fe_2O_3. They also stated that these were Co (II) cations in tetrahedral (Td) sites which were experiencing changes during the OER. Saddeler *et al.*[65] recently studied cobalt iron spinel catalysts of different composition and thanks to the changes of the Co and Fe K-edge concluded that during the OER cobalt was oxidized to Co (III) while iron maintained its Fe (III) oxidation state.

In this work, we report on the cooperative red-ox behavior of core-shell cobalt iron oxide nanoparticles (Fe_3O_4@$CoFe_2O_4$), with a conductive Fe_3O_4 core and OER active $CoFe_2O_4$ shell. The use of core-shell nanoparticles where Co is present only in the shell has the advantage to drastically reduce the Co loading in the electrocatalyst. Furthermore, an improved OER performance may be expected if the particle core has beneficial impact on the shell properties[62,63]. More details about the synthesis and characterization of the NPs used in this study (CS-3) have been previously presented and can be found in chapter 2 and in chapter 3 respectively. The synthesis consisted in a seed-mediated growth based on the thermal decomposition of metal complexes as recently reported[114]. The obtained spinel Fe_3O_4@$CoFe_2O_4$ NPs are homogeneous in size, shape, and composition and possess an average

diameter of ca. 14 nm with a shell thickness of ca.1.5 nm. As it was discussed in chapter 5, these NPs present high activity for the OER.

2) *Membrane electrode assembly*

The membrane electrode assembly was used in the *operando* liquid spectro-electrochemical cell of the ISIS Beamline at Bessy synchrotron. The procedure for the membrane electrode assembly was the following: 10 µL (4.2 µg) of NPs CS-3 dispersed in chloroform were drop-casted either on the surface of a Fumatech anion exchange membrane (fumasep® FAS-50) or on the surface of an Aemion® anion exchange membrane. Then, following procedure developed by Velasco-Velez et al,[126,162] covered by a graphene bilayer, the latter establishing electric contact between the particles and the current collector. A 0.1M NaOH electrolyte was flowing behind the membrane in order to humidify the NPs, the reference electrode used was a silver/silver chloride (Ag/AgCl) electrode and the counter electrode a platinum wire. More details about the electrochemical cell used for these measurements have been presented in chapter 2.

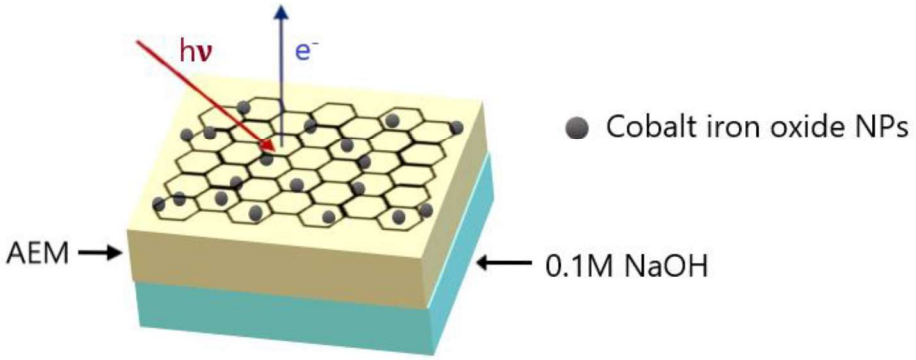

Figure 72: Membrane electrode assembly used for the synchrotron measurements

Cyclic voltammetry curves have then been measured on both membranes. The shape of current-potential curves obtained with the two types of anion exchange membranes was similar as the redox peaks characteristic of cobalt could be seen on both membranes. However, on the Aemion membrane, the peaks were more intense, which might be tentatively attributed to higher ion exchange capacity (IEC) of this type of membrane (see chapter 2). These membranes would have been a better candidate than the commercial Fumatech membrane but their initial hydration state made the pressure in the analysis chamber upon insertion too high to perform the experiments safely. As a consequence, the commercial Fumatech membrane was used.

The redox behavior of Fe_3O_4@$CoFe_2O_4$ core-shell and Fe_3O_4 core NPs was studied *operando* in a wide potential interval by monitoring the evolution of the Near Edge Absorption Fine Structure (NEXAFS) spectra recorded for cobalt and iron L-edge and oxygen K-edge in total electron yield mode as a function of the applied potential.

3) *Reduction experiments*

We start our discussion with the analyses of red-ox transformations occurring at low electrode potentials. Figure 73 shows that on Fe_3O_4 NPs, when the potential is decreased, a pair of anodic (P_A) and cathodic (P_C) redox peaks is observed in the CV at ca. 0.2 and at -0.2 V *vs.* the reversible hydrogen electrode (RHE), respectively. These peaks were attributed to the oxidation and reduction of iron.

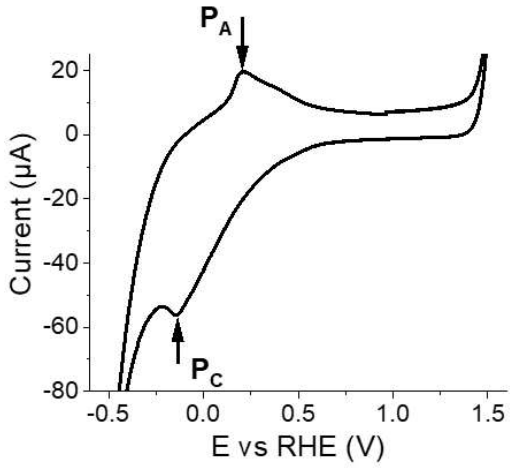

Figure 73: Cyclic voltammetry curves at low potential of Fe_3O_4 NPs (right) dropcasted on the Fumatech membrane. Electrolyte: 0.1M NaOH; scan rate 20mV s^{-1}

For the core shell NPs CS-3, the same redox peaks were observed on the cyclic voltammetry curves (Figure 74 A). The corresponding NEXAFS Fe L-edge, Co L-edge and O K-edge spectra measured in the interval from 1.0 down to -0.5 V *vs*. RHE are presented in Figure 74 B, C and D respectively. All NEXAFS measurements are performed in total electron yield which has higher surface sensitivity compared to the fluorescence yield. The Fe L_3 and L_2-edge peaks (Figure 74 B) are centered at 711 eV and 724 eV respectively and are sensitive to the valence and redox state of the atoms. At 1.0 V *vs.* RHE, the fine structure of the Fe L_3-edge shows a shoulder at 709 eV, which is attributed to Fe(II), while the main peak at 711 eV is attributed to Fe(III).[164] The Co L-edge spectra (Figure 74 C) confirm the presence of Co (II) in the shell as expected for $CoFe_2O_4$.

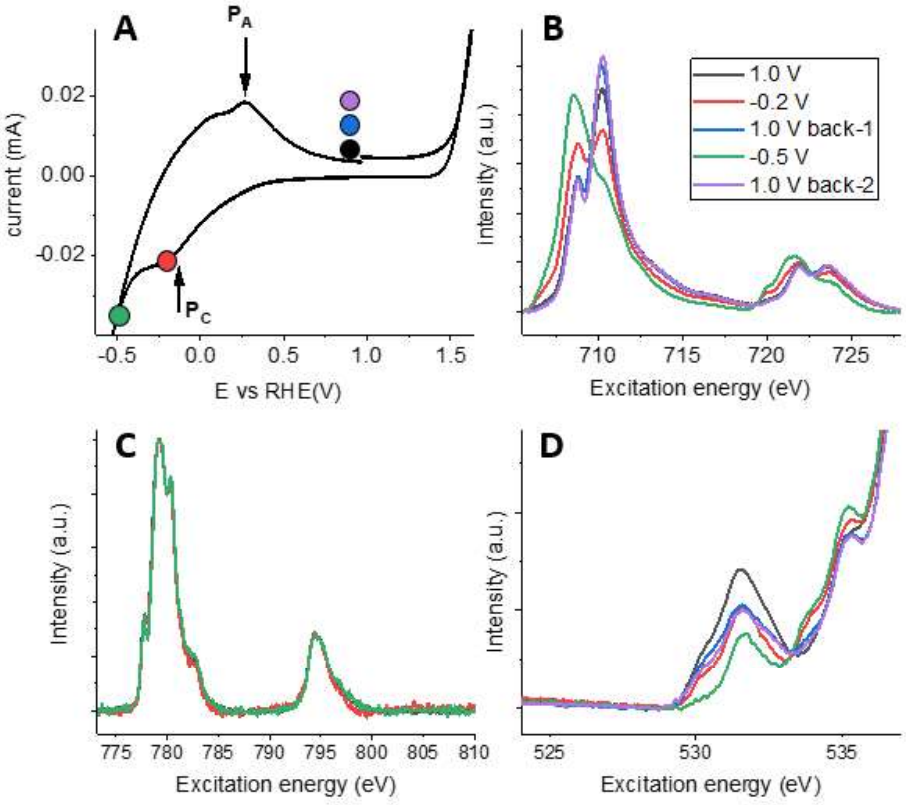

Figure 74: A) Cyclic voltammetry curves obtained for core-shell NPs dropcasted on a Fumatech membrane in 0.1 M NaOH electrolyte, scan rate 20 mV s^{-1}. B) Area-normalized NEXAFS Fe-$L_{2,3}$ edge spectra for core-shell NPs at different applied potentials. C) Area-normalized NEXAFS Co-$L_{2,3}$ edge spectra for core-shell NPs at different applied potentials. D) Baseline corrected O K-edge spectra for core-shell NPs at different applied potentials.

The red-ox peaks of Figure 73 can be assigned with the help of the NEXAFS spectra. In the Fe L_3-edge spectra measured at -0.2 *vs.* RHE (Figure 74 B), a significant increase of the Fe (II) peak and a pronounced decrease of the Fe (III) peak are clearly observed. Moreover, another shoulder at 705 eV, characteristic of the formation of FeO[162], emerges a low potentials. These changes are accentuated at -0.5 V *vs*. RHE. Similar changes are also seen on the L_2 peaks at 720 eV, 722 eV, and 724 eV. Thus, the majority of the Fe (III) cations in the Fe_3O_4 core and in the $CoFe_2O_4$ shell is reduced into FeO at potentials negative of the cathodic peak P_C. It should be mentioned that the Co L-edge spectra are not modified even for potentials as low as -0.5 V *vs.* RHE suggesting that Co (II) is not reduced at these potentials (Figure 74 C) while the O K-edge spectra evidenced some changes related to the transformation of the spinel structure into the rock salt (Figure 74 D). Furthermore, no signature corresponding to the reduction to metallic iron was observed in the NEXAFS spectra contrary to what has been reported in some previous publications.[164] Note that if the potential was scanned further negative, the CV became irreversible (not shown), which we tentatively attribute to the reduction of Fe_3O_4 to metallic Fe. When the potential is brought back to its initial value (1.0 V *vs.* RHE) the Fe (II)/Fe (III) ratio returns to the initial one. Consequently, chemical transformation of Fe_3O_4 into FeO and back seems to be essentially reversible.

The ratio between the Fe (II) and Fe (III) peaks for core-shell NPs is 0.59, slightly lower than the Fe (II)/Fe (III) ratio of 0.61 observed for the Fe_3O_4 core NPs, pointing to smaller Fe (III) fraction in core-shell NPs. Furthermore, no signature of the reduction to metallic iron has been observed in the NEXAFS spectra.

Finally, STEM-HAADF micrographs, TEM micrographs and EELS mappings before (Figure 75) and after (Figure 76) the application of -0.5 V *vs.* RHE for 30 min are presented.

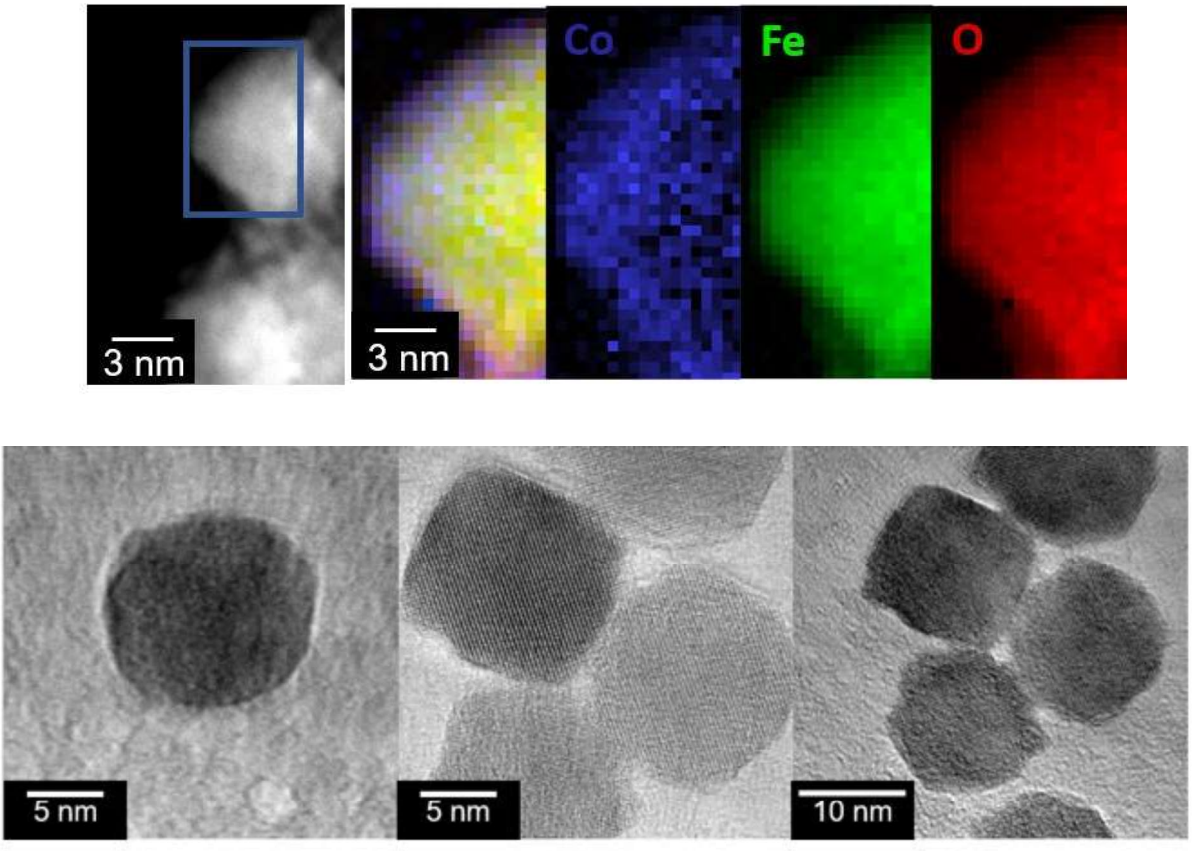

Figure 75: STEM-HAADF and EELS images (top), TEM micrographs (bottom) of the core-shell NPs CS-3 before the application of a potential. Cobalt is in blue, iron in green and oxygen in red.

It is worth noting that even after reduction the NPs are still crystalline. However, they seem to have undergone structural changes. The differences in the TEM and EELS images provide evidence for Co redistribution inside the core-shell NPs, likely resulting from the atomic diffusion inside the core and indicating that while being compositionally reversible, the red-ox cycling results in some structural irreversibility of the core-shell NPs.

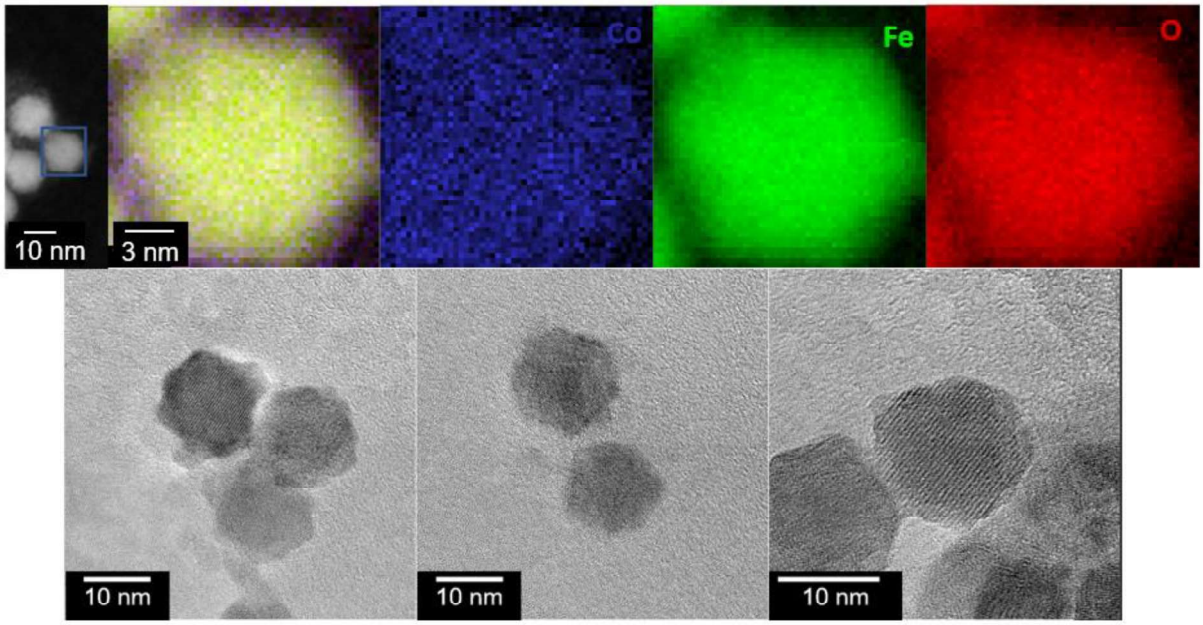

Figure 76: STEM-HAADF and EELS images (top), TEM micrographs (bottom) of the core-shell NPs CS-3 after the application of -0.5V vs RHE for 30 minutes. Cobalt is in blue, iron in green and oxygen in red

Last but not least, the important changes observed in the Fe L-edge spectra also underline that the NPs probed by the X-ray beam are electrically connected to the graphene bilayer, confirming that this spectro-electrochemical cell can be successfully utilized to assess *operando* changes during the OER.

4) *Oxidation experiments*

Armed with the knowledge that the NPs are well connected to the membrane and that they can undergo reversible redox changes, we turn to the analyses of NEXAFS spectra acquired above 1.0 V *vs.* RHE in the OER potential range. Cyclic voltammogram of Figure 77 shows a pair of low intensity peaks ($P_{A,1}$ and $P_{C,1}$) around 1.05 V *vs.* RHE, which are usually attributed to Co (II/III) transition in Co_3O_4 or $Co(OH)_2$ materials (Figure 77)[43,89]. Additionally, a cathodic peak usually attributed to the Co (IV/III) transition[43,89] is observed at high potentials, around 1.3 V *vs.* RHE ($P_{C,2}$). The oxidation peak is hidden by the OER and is consequently not seen. The cyclic voltammetry curve obtained for Fe_3O_4 NPs (Figure 77) does not exhibit these peaks around 1.1 and 1.4 V, further confirming that these peaks are indeed due to the cobalt presence in the shell of the NPs.

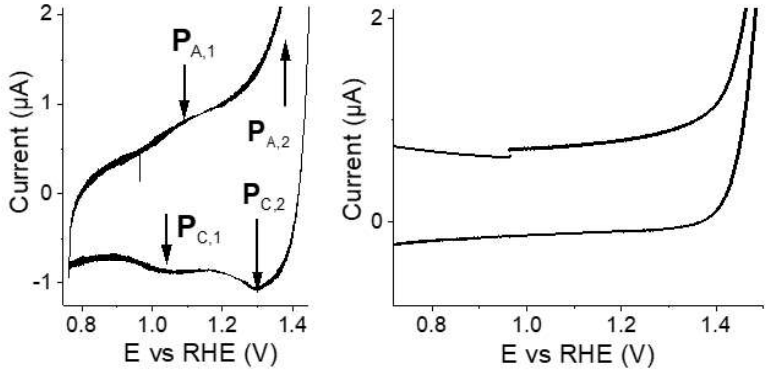

Figure 77: Left: cyclic voltammetry curve obtained for CS-3 NPs in 0.1 M NaOH, scan rate 20 mV s^{-1}. Right: cyclic voltammetry curve obtained for Fe_3O_4 NPs in 0.1 M NaOH, scan rate 20 mV s^{-1}.

Since the intensity of these CV peaks is low (compared to the peaks observed at low potentials), the changes in the NEXAFS spectra are also expected to be smaller. The NEXAFS spectra under potential for the Fe L-edge, Co L-edge and O K-edge are presented in Figure 78.

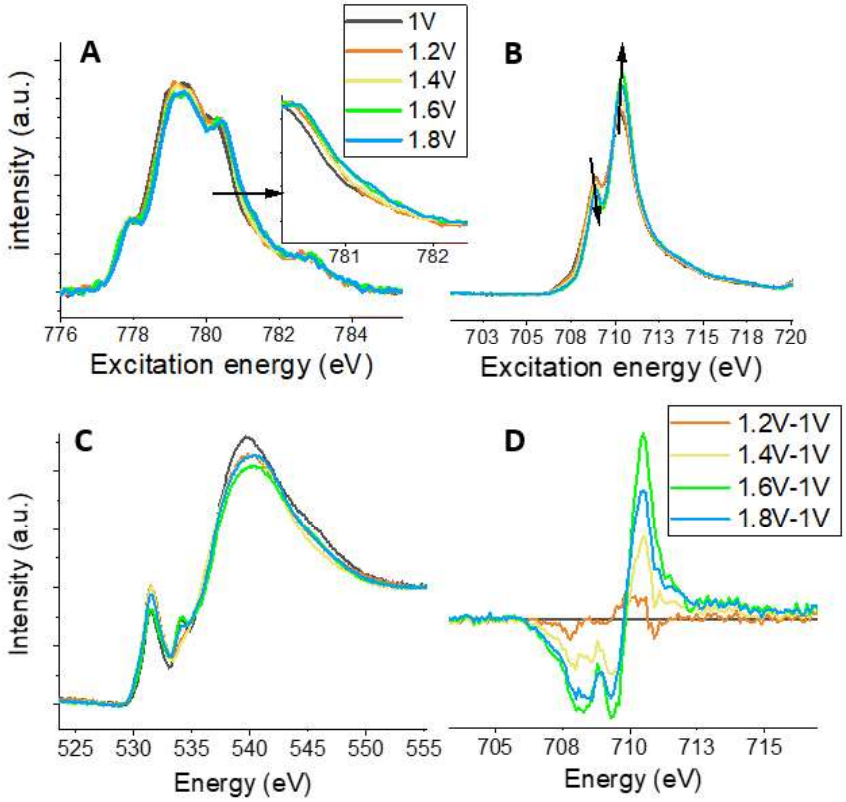

Figure 78: Area-normalized Co-L_3 edge (A), Fe-L_3 edge (B), and O K-edge (C) NEXAFS spectra for core-shell NPs at different applied potentials. D) Fe-L_3 edge NEXAFS spectra to which the spectrum at 1 V vs. RHE has been subtracted.

At 1.0 V *vs.* RHE, the Co L_3-edge NEXAFS spectrum exhibits shape characteristic of Co (II). By comparing the spectrum at 1 V with the simulated L-edge spectra of Co in Oh and Td sites[163] it is estimated that roughly 75% of cobalt resides in the Oh and 25% in the Td sites as expected for the $CoFe_2O_4$ inverse spinel structure (Figure 79).

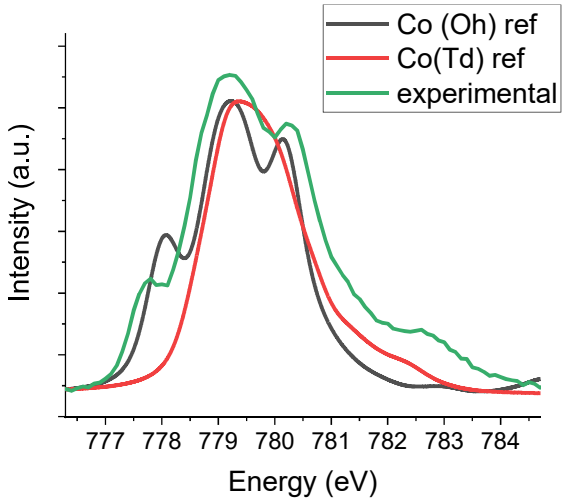

Figure 79: Co L_3- edge spectra of the core-shell NPs at 1.0 V vs RHE compared to Co L_3- edge spectra simulated for Co(II) in Oh and Td sites taken from Ref.[164]

Surprisingly, when the potential is increased in 0.2 V increments up to 1.8 V *vs*. RHE (Figure 78 A), the Co (II) signal is still largely observed in NEXAFS spectra revealing that the spinel structure is preserved even under the OER conditions. However, it is worth noticing that the L_3 peak slightly shifts to higher energies when the applied potential increases, suggesting that a small fraction of Co (II) is transformed into Co (III). Potential-induced changes observed at the Fe-L_3 edge (Figure 78 B) are more significant with (i) the characteristic Fe (II)/Fe(III) peak ratio decreasing to 0.46 at 1.8 V *vs*. RHE and (ii) the disappearance of the 707 eV shoulder, both evidencing oxidation of a fraction of Fe(II) present in the NPs core into Fe(III).[164] As iron in the Fe (II) oxidation state is only present in the Fe_3O_4 core (in the shell it is Fe (III)), we thus conclude that the Fe_3O_4 core is strongly influencing the chemical properties of the $CoFe_2O_4$ shell, as this oxidation likely results from an electron transfer from the Fe (II) in the core to reduce the electrochemically oxidized Co (III) species in the shell and thus essentially maintain its Co(II) state.

Additionally, STEM HAADF micrographs, EELS mappings and TEM micrographs of the NPs after the oxidation (Figure 80) demonstrate that the crystallinity and the presence of the Co-containing shell have been preserved even after the application of 1.75 V for 30 minutes.

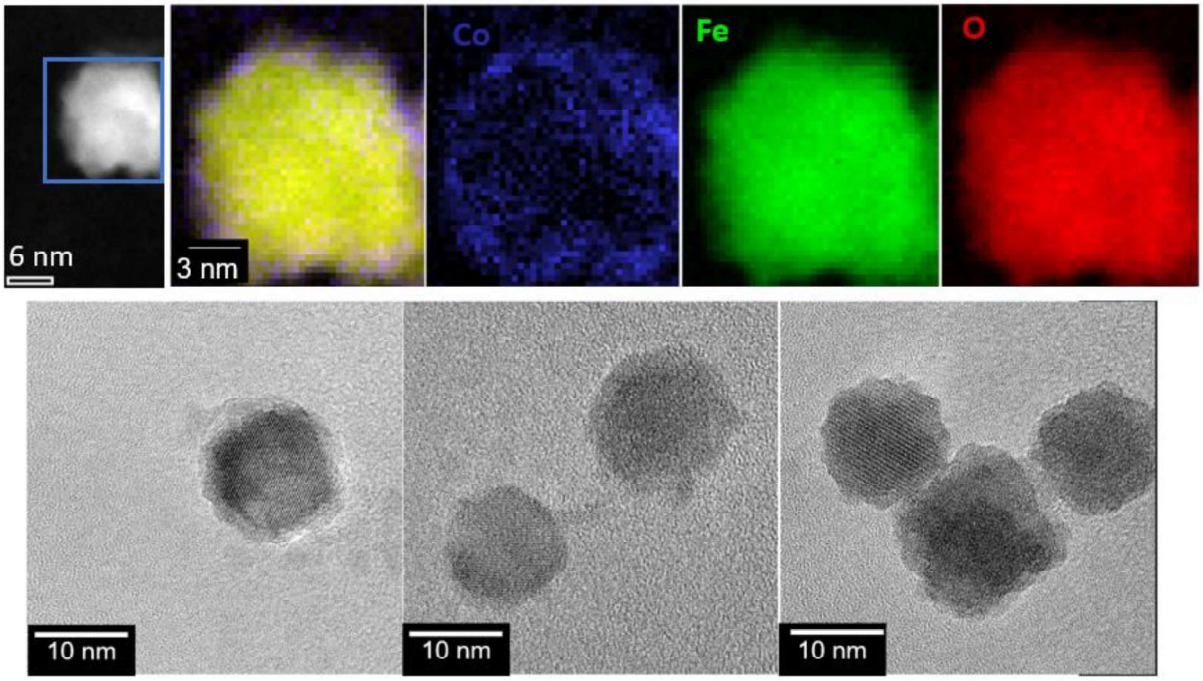

Figure 80: STEM-HAADF and EELS images (top), TEM micrographs (bottom) of the core-shell NPs CS-3 after the application of 1.75 V vs RHE for 30 minutes. Cobalt is in blue, iron in green and oxygen in red.

However, the NPs appear to be rougher and the edges are not as neat as before applying the anodic potential (Figure 80). Such roughening may be attributed to the NP restructuring driven by the migration of excess Fe (III) cations from the core to the shell of the NPs. This hypothesis is supported

by the reported evidence of the inverse spinel structure Fe_3O_4 (magnetite) that can easily transform into γ-Fe_2O_3 (maghemite) which is deficient spinel, with vacancies in the octahedral sublattice[166]. For example, oxidation of Fe (II) of magnetite NPs into Fe (III) by molecular oxygen involves electron hopping along with migration of Fe(III) cations through the lattice framework, generating vacancies in the octahedral sublattice (and their migration) in order to preserve the charge balance.[166]

It is interesting to notice that no changes were observed in the low excitation energy region (in the interval from 527 to 530 eV) of the O K-edge spectra when the potential was increased from 1.0 to 1.8 V *vs*. RHE (Figure 78C for the full spectra and Figure 81 for the zoom). Thus, an anion red-ox mechanism involving the formation of an electrophilic oxygen species O^{I-} as an OER intermediate can be discarded.

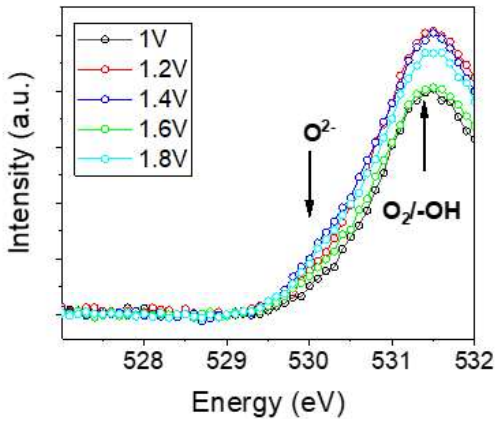

Figure 81: Zoom of the O K-edge of core-shell NPs evolution upon potential application.

On the other hand, a small peak around 714 eV emerges in the Fe L-edge spectra at *E* > 1.6 V *vs*. *RHE* (Figure 78 B and D) and might be tentatively attributed to the formation of Fe (IV), since broadening of the L_3 peak has been shown in the literature to correspond to Fe (IV)[166,168]. Subtracting the spectrum obtained at 1 V *vs. RHE* from the spectra at higher potentials (Figure 78 D) better highlights this peak. The presence of this peak agrees with a cation red-ox OER mechanism involving participation of Fe(IV) in the OER active site as it was suggested by Enman et al upon *operando* hard-X-ray investigation of Co(Fe)O_xH_y oxyhydroxide.[90] Note that on the core alone (Fe_3O_4, Figure 82), which is much less OER-active and which has been proven to be stable during oxidation[169], almost no changes are seen on the Fe L-edge under the OER conditions.

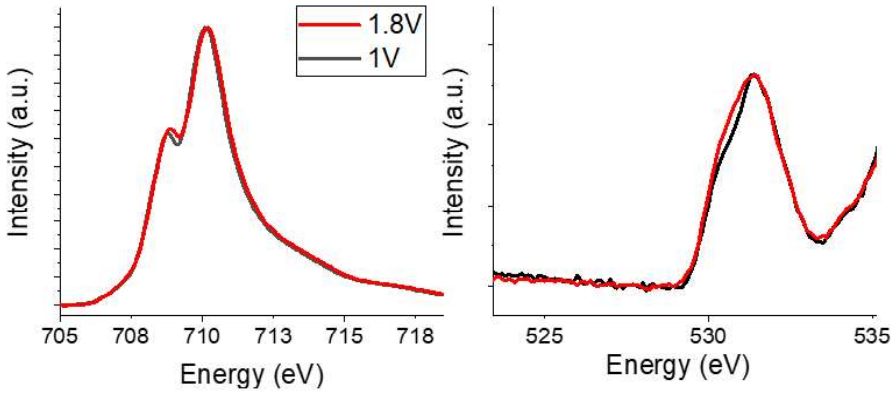

Figure 82: Fe L_3-edge (left) and O K-edge (right) of Fe_3O_4 NPs upon oxidation. The Fe L_3-edge spectra have been normalized by the area of the peaks.

This hindered Fe_3O_4 core compared to Fe_3O_4@$CoFe_2O_4$ core-shell NP oxidation may be attributed to the presence of a thin layer of γ-Fe_2O_3 on the surface of the Fe_3O_4 NPs acting as a passivating layer.[26]

5) *Transformations of core-shell NPs with potential*

Considering this observation, we can conclude that in the core-shell NPs a small fraction of Fe (II) from the core, likely localized in the close proximity to the shell, is oxidized to Fe (III) to maintain the Co (II) state above 1.1 V *vs.* RHE. To preserve electroneutrality in the core, this Fe (III) cation probably migrates from the core towards the surface of the NPs, leaving behind a vacancy in the core and leading to a roughening of the NP surface. It is interesting to note that stabilization of the Co(II) state at high applied potential by the nearby Fe was already invoked dealing with DFT+U calculations of Co_3O_4(001) and $CoFe_2O_4$ (001) surfaces with and without an additional half or full monolayer of Fe. It was concluded that the OER active site is octahedral Co, both in the presence and in the absence of a Fe monolayer. However, while for the Fe-free surface Co is oxidized to reach a Co (IV) state[160], the presence of a Fe monolayer (for example, on the $CoFe_2O_4$ (001) surface) stabilizes the Co (II) state[161] while itself relaxing to octahedral sites and accepting the Fe (III) oxidation state under the OER potential. In this case, the OER catalytic cycle would involve the oxidation of a surface-active site composed of Co (II) interacting with a nearby Fe (III), into Co (III). Formation of short-lived Co (IV) as it has been suggested in the literature on similar compounds[94,158] cannot be fully discarded. However, considering that only a small fraction of Co (II) is transformed into Co (III) during the OER, such a scenario is quite unlikely for the core-shell NPs. In the meantime, the anion red-ox mechanism previously proposed for IrOx[91,92] and Co_3O_4[65] anodes involving electron-deficient oxygen as an active intermediate is rather unlikely. Figure 83 presents the transformations that are susceptible to occur on the core shell NPs.

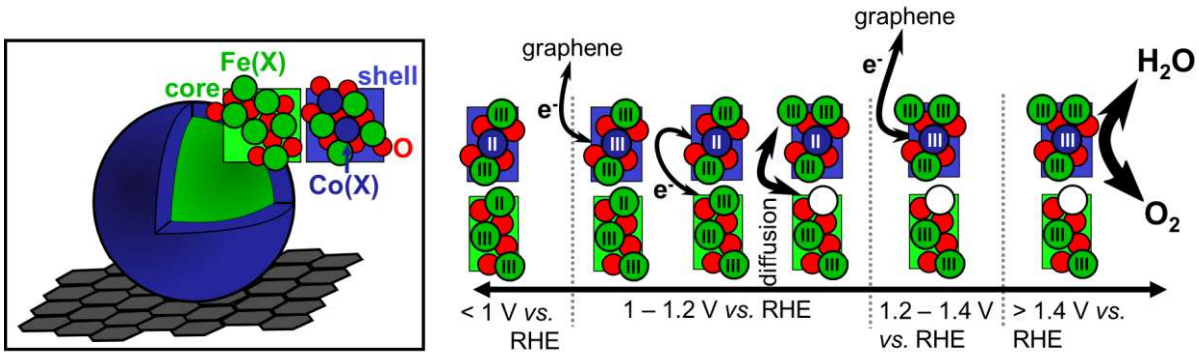

Figure 83: Proposed redox transformations on core-shell NPs depending on the applied potential. Step 1: At E=1.0 V vs. RHE, Fe (II) and Fe (III) are coexisting in the core, and the shell is composed of Co (II) and Fe (III). Step 2: At 1.0<E <1.2 V vs RHE, an electron is transferred from Co (II) in the particle shell to the current collector. However, Co (III) is not observed by NEXAFS since it is reduced back to Co (II) due to an electron transfer from Fe (II) (residing in the NP core in the close proximity to the shell) resulting in the Fe (III) formation. This Fe (III) cation then likely migrates to the surface, leaving behind a cationic vacancy in the particle core. Step 3: Above 1.2 V vs RHE, Co (II) in the shell is partly oxidized to Co (III). Step 4: OER occurs on an active center comprised of Co (III) and Fe (III). However, one cannot exclude formation of active Fe (IV) species above 1.4 V vs RHE. Oxygen atoms are in red, cobalt in blue and iron in green.

6) *Transformation of core-shell NPs upon annealing in O_2 atmosphere*

To complement the studies of NP transformations with the electrode potential, we have also investigated NEXAFS and XPS changes occurring upon their annealing at 300°C under air or a 1mbar O_2 atmosphere. The latter could also help to better understand phenomena occurring when the NPs were annealed to remove the oleic acid from their surface as explained in chapter 2.

The NPs used for this study are CS-1 NPs, the experiments were realized at BESSY and SOLEIL synchrotron on either a gold substrate (SOLEIL) or a silicon wafer covered by a carbon layer to insure its conductivity (BESSY). Although, the results that will be presented in this part are quite preliminary, additional measurement will be performed soon on the TEMPO beamline (SOLEIL synchrotron).

a) Depth profiling experiments

First, to clarify whether the core-shell structure is stable against annealing, depth profiling experiments were performed for CS-1 NPs using different incident photon energy (from 900 eV to 1600 eV, corresponding to kinetic energies of photoelectrons ranging from 200 eV to 800 eV) before and after heating at 300 °C under an O_2 atmosphere 1 mbar for 8 hours. These experiments were realized at BESSY synchrotron on ISISS beamline. Similar to what has been discussed in chapter 3, the XPS spectra of the Co 2p and Fe 2p peaks were analyzed (Figure 84). Note that changes in the XPS peak intensity are not only due to the variation of the excitation energy but also to the fact that spectra were taken from different zones of the sample (to avoid beam damage).

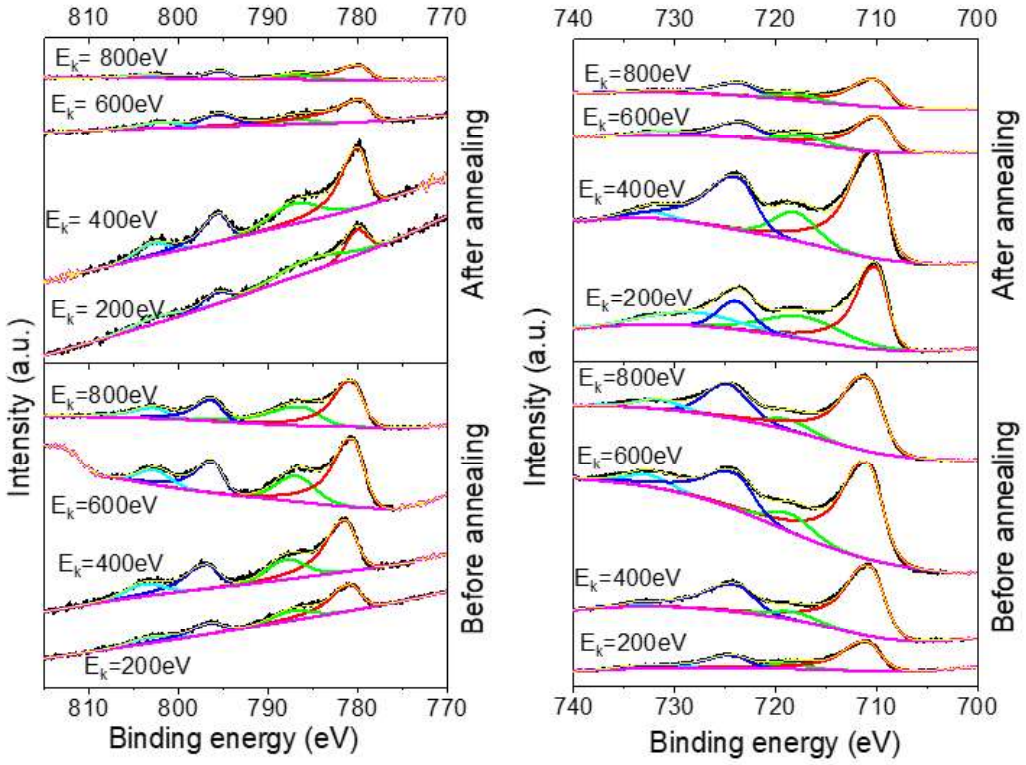

Figure 84: Co 2p (left) and Fe 2p (right) XP spectra and their fitting for different kinetic energies obtained while performing the depth profiling of CS-1 NPs before (bottom) and after (top) annealing under 1 mbar O_2 for 8 hours. Experimental data (black); $2p_{3/2}$ (red) and its satellite (green), $2p_{1/2}$ (dark blue) and its satellite (light blue): sum of all fitted peaks (yellow).

From the area of these peaks normalized to the synchrotron flux and to the respective cross sections, it was possible to determine the Fe:Co (Figure 85) at different depths (see chapter 2 for more details about the calculation). The spectra measured on not annealed CS-1 NPs presented in chapter 3 for more photoelectrons incident energies have been added to the graph. Indeed, as the measurements have been performed on the same line, they are comparable.

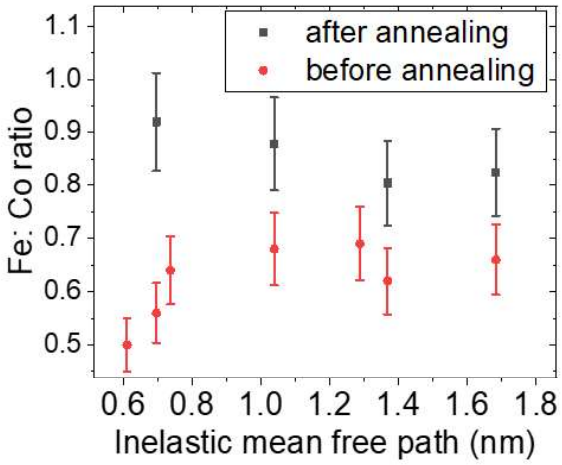

Figure 85: Fe:Co ratio calculated from depth profiling experiments realized on the particles CS-1 before (red) and after (black) annealing at 300 °C for 8 hours in 1 mbar O_2 atmosphere and plotted against the inelastic mean free path

For NPs before annealing, in agreement with what has been discussed in Chapter 3, one may observe lower Fe:Co ratio at small values of the inelastic mean free path (hence small probing depth). This confirms the core-shell structure with Co preferentially localized in the particle shells. However, after annealing the Fe:Co distribution changes drastically. Even though more points at lower incident energies for the annealed sample would be needed to confirm this, Figure 85 seems to display a higher proportion of iron in the shell after annealing. Thus, the core-shell structure does not seem to be preserved after annealing at 300 °C for 8 hours. The proportion of iron *vs.* cobalt seems higher for lower incident energies, likely indicating the diffusion of iron atoms toward the surface and of cobalt atoms in the center of the NPs.

While the depth-profiling experiments have demonstrated redistribution of Fe and Co in the core-shell NPs as a result of annealing in O_2 atmosphere, they did not show any clear indication of the change in the average oxidation state of either Co or Fe. Since L-edge spectra are more sensitive to the oxidation state and to the environment of Co and Fe than the 2p XPS spectra, in what follows we present the results of the Co and Fe L-edge NEXAFS studies performed before and after annealing of the NPs.

b) NEXAFS experiments

The L-edge of cobalt and iron have also been measured before and after annealing at SOLEIL synchrotron on TEMPO beamline. Their spectra are presented in Figure 86. For these experiments, the NPs have been deposited on a polycrystalline gold substrate.

On the iron L-edge spectra, it can be observed that iron experienced partial oxidation: the decrease of the peak at 708 eV and the increase of the one at 710 eV is characteristic of more Fe (III) and less Fe (II) after annealing[163]. Additionally, the shoulder at 707 eV characteristic of Fe_3O_4 decreased[163,166]. This change is characteristic of the Fe_3O_4 transformation in γ-Fe_2O_3 at the surface of the NPs.

For the Co L-edge, much smaller changes were observed. The difference between the two spectra is mainly related to the peak at 781 eV which is more intense before annealing than after. This difference could arise from the migration of Co(II) in Td sites to the Oh sites (see Figure 79 for the simulated spectra of Co(II) in Oh and in Td sites taken from Ref.[164]). Indeed, as we discussed in the previous sections, cobalt is initially present both in the Td sites (about 25%) and in the Oh sites (about 75%) even though in theory it is only supposed to be in the Oh sites. Here we suppose that to reach a more stable configuration of a $CoFe_2O_4$ spinel, the cobalt migrates from the Td to the Oh sites upon annealing. This would agree with the changes observed on the depth profiling and Fe-L edge as the Fe (II) and Fe (III) would then migrate to the Td sites. No changes related to the Co (II) oxidation could be evidenced from the Co L-edge spectra taken after annealing.

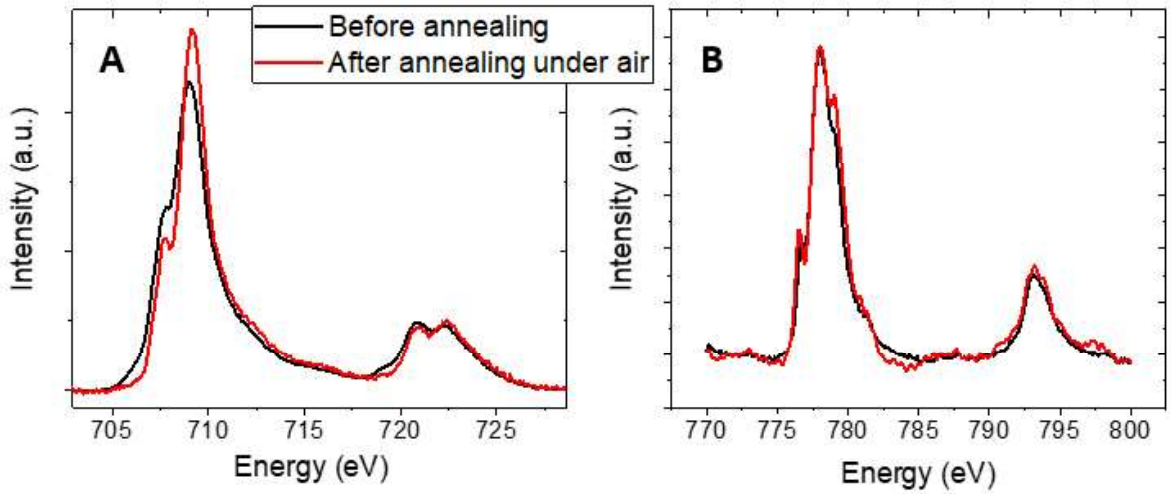

Figure 86: a) Fe L-edge (left) and b) Co L-edge (right) spectra of core-shell NPs CS-1 before (black curve) and after (red curve) annealing at 300°C under air for 10 minutes at SOLEIL synchrotron on TEMPO beamline. NPs were deposited on a gold substrate.

On these NEXAFS spectra measured at SOLEIL synchrotron, the energy values for the iron and cobalt peaks are not the same as the ones observed at BESSY. This is due to a calibration in energy that

should be performed. However, that does not have an impact on the changes observed on the shape of the peaks and their relative intensity, the only change is in the energy value. To conclude, the NEXAFS observations agree with the depth profiling measurements; hinting at a diffusion of the metal cations upon annealing. To sum up, the NEXAFS results present important changes upon annealing. More experiments at different temperatures and under various atmospheres would be needed to understand better the phenomena occurring during the NPs annealing and in order to shed light on these transformations. In order to continue in this direction, NPs CS-3 were analyzed studying the K-edge of iron and cobalt during the annealing at ESRF synchrotron and these results are currently being analyzed. Additionally, a synchrotron beamtime on the TEMPO beamline is planned in the beginning of 2023 to study the transformations occurring during annealing under O_2 and under H_2.

7) Conclusion

To conclude, we performed an *operando* study using soft X-ray absorption spectroscopy in a wide potential range spanning from -0.5 V *vs*. RHE up to the OER interval on membrane electrode assemblies containing cobalt iron oxide spinel core-shell nanoparticles (CS-3, Fe_3O_4@$CoFe_2O_4$) covered by a graphene bilayer. This approach turned out to be well-suited to study potential-induced redox transformations of these NPs. The work sheds light onto the interactions between the core and the shell, thus providing insights into the synergies that might exist within these NPs. We document strong influence of the Fe_3O_4 core on the red-ox behavior of the $CoFe_2O_4$ shell under the OER conditions.

Compared to previously investigated Co_3O_4 or $Co(OH)_2$ NPs[41,43,87,89], core-shell Fe_3O_4@$CoFe_2O_4$ NPs behave differently: most of the cobalt atoms in the shell remains in a Co (II) oxidation state in the potential interval where significant OER current is achieved. In addition, the presence of Co in the shell favors the oxidation of some fraction of Fe (II) into Fe (III) in the NPs core. Hence, these results suggest the occurrence of a cation-red-ox OER mechanism involving cooperative red-ox behavior between Co and Fe atoms. It is remarkable that the core-shell spinel structure is essentially preserved under the OER conditions but can hardly withstand cathodic polarization down to – 0.5 V *vs*. RHE.

To complement electrochemical studies, annealing NPs in different environments could also be of interest. XPS depth profiling experiments of core-shell NPs before and after annealing at 300°C in the presence of O_2 suggesting that there is a diffusion of the iron and cobalt atoms through the NPs resulting in a higher density of iron on the surface of the NPs. More measurements would be needed to clarify above which temperature the loss of core-shell structure occurs. Such studies may be interesting to perform in the future in order to clarify whether annealing is suitable for removing the oleic acid (that could impact their OER activity) from the surface of NPs. Additionally, the NEXAFS Fe L-edge spectra indicate partial oxidation of Fe (II) to Fe (III). In the meantime, Co L-edge spectra are displaying some changes that would be characteristic of cobalt migration from the Td sites to the Oh sites upon annealing. In order to confirm these observations, the iron and cobalt K-edge were studied *in situ* at ESRF synchrotron and the results are currently being analyzed. Another beamtime at the TEMPO beamline of SOLEIL synchrotron is also planned to study the influence of annealing at various temperatures in various atmospheres in order to simulate oxidation and a reduction of core-shell NPs.

General conclusions and outlook

The aim of the present thesis was to develop well-defined nanoparticulated TMOs-based catalysts for the OER in alkaline media, which could, on the one hand, serve as a model system to study the OER, and, on the other hand, to have a potential to replace iridium and ruthenium-based anode catalysts commonly used in acidic media. This catalyst should both be active for the OER and present an intrinsic conductivity to avoid the use of carbon. This catalyst was then characterized electrochemically to determine its OER activity and *operando* with NEXAFS spectroscopy to shed light on the phenomena occurring at its surface during the reaction. The strategy to develop such a catalyst was to synthesize and characterize core-shell cobalt iron oxide NPs and study their electrochemical properties.

In this work, we studied four types of core-shell NPs (Fe_3O_4@$CoFe_2O_4$) that meet the criteria of an 'ideal' catalyst:

- ✓ Conductivity: the core Fe_3O_4 is conductive
- ✓ Activity: the shell $CoFe_2O_4$ is electrochemically active
- ✓ Large specific surface: the nano-size of the objects gives it a large specific surface for the OER to occur.
- ✓ Stability: the material is stable in alkaline media and in OER conditions.

Additionally, this catalyst presents other advantages: it is synthesized at a relatively low temperature, the shell can grow epitaxially on top of the core as both materials present a similar cell parameter, and interactions between Co and Fe or Ni and Fe have been reported as favorable for the OER but are not fully understood yet. Finally, the synthesis method (thermal decomposition) can also be modified to tune the core size, shell thickness and modify the shell growth (diffusion or crystalline growth) using different solvents, precursors, temperature ramps...This type of synthesis produces NPs that present a narrow size distribution, a sharp shell rich in cobalt at its surface, the cobalt content will then decrease inside the NPs. This composition gradient is due to the decomposition temperature difference of the iron and cobalt stearate precursors used to synthesize the shell.

The NPs have then been studied electrochemically thanks to cyclic voltammetry and impedance spectroscopy techniques and their activity for the OER was evaluated. By characterizing the activity of the catalytic layers, we were able to show that for high NPs loadings on the electrode even though the overall current was increasing, the activity per mass of oxide was decreasing when it should have been constant. These results indicated that, at high NP loadings, the NPs were not equally involved in the OER despite the conductivity of their core. This could be attributed to either a contact resistance between NPs or an electrolyte resistance within the catalytic layer. This resistance affects

the Tafel slopes that become non-linear. Below a loading of about 5 $\mu g.cm^{-2}$ the activity was reaching a plateau. For a couple of monolayers, all the NPs were then involved in the OER. The impedance data obtained at 1.62 V vs RHE at low current densities (to avoid blocking the layer by O_2 bubbles) were fitted for various layer thicknesses. Two different models were used for simulating the experimental data: the Randles model and the transmission line model. Thanks to this analysis, it was possible to evaluate the charge transfer resistance, the capacitance, and ionic/electronic resistance within the catalytic layer. It was demonstrated that the charge transfer resistance was decreasing with the loading while the electronic and ionic resistance as well as the capacitance was increasing. The conclusion was that for important loadings, an ionic and/or electronic resistance builds up across the catalytic layer, causing the mass-weighted activity to drop. This phenomenon must be considered in order to evaluate accurately the electrocatalytic activity. Some simulations of the linear-sweep voltammetry have also been done using various values for the ionic and electronic resistance and they are coherent with the experimental data by showing a drop in the mass-weighted activity for high resistance in the catalytic layer. From these simulated linear-sweep voltammetry curves, the Tafel plots were extracted. For high values of resistance, a deviation from a linear behavior was observed sometimes resulting in two different Tafel slopes, which agrees once again with the experimental data. As the Tafel slopes are often used to determine the nature of the rate-determining step and the reaction mechanism, ohmic losses in the catalytic layer is an important factor to consider when performing this type of analysis in order to avoid eventual misinterpretations.

Once the optimal amount of NPs to deposit on the electrode has been determined, then the NPs OER activity was determined. Comparison of the OER activity of the core-shell NPs with that of the Fe_3O_4 core NPs confirmed significantly higher activity of the former. Three types of activity were considered: the surface-weighted activity, the oxide mass-weigthed activity, and the cobalt mass-weighted activity (the overall current was divided either by the surface of the NPs, by their mass, or by the mass of cobalt present in the shell of the NPs as it is the element that imparts them their activity). The activity values obtained for the core-shell NPs in 0.1 M NaOH at 1.65 V vs RHE were ranging from 140 $A.g^{-1}_{oxide}$, 0.1 $mA.cm^{-2}_{oxide}$ or 1300 $A.g^{-1}_{cobalt}$ for the NPs presenting a small core (about 8 nm) to 350 $A.g^{-1}_{oxide}$, 0.4 $mA.cm^{-2}_{oxide}$ 2800 $A.g^{-1}_{cobalt}$ for NPs presenting a larger core (about 13 nm). These activity values are among the highest activities that can be found in the literature: 240 $A.g^{-1}_{oxide}$ for Co_3O_4, 500 $A.g^{-1}_{cobalt}$ for Au@Co_3O_4 particles, or 154 $A.g^{-1}_{cobalt}$ for Fe_3O_4@CoO particles at 1.65V *vs.* RHE for example. It is worth noting that the electrolyte was not the same for all these measurements and can have an impact on the activity. From these results, it was then concluded that along with the core-shell structure, the size of the core plays an important role in the OER activity. This is tentatively attributed to the conductivity of Fe_3O_4 and a synergistic effect between the core and the shell. Thus, controlled

synthesis of core-shell nanostructures seems to be a viable approach for designing promising alkaline OER catalysts. However, the approach used to form the shell around the Fe_3O_4 core (diffusion against crystal growth) does not seem to have a significant influence on the obtained activity.

In order to get a better understanding of the OER mechanism and of the transformations occurring on the catalyst during the OER, NPs with a large core that presented an excellent OER activity were then characterized *operando* using soft X-ray absorption spectroscopy. In order to do so they were deposited on an anion-exchange membrane and covered by a graphene bilayer. This approach turned out to be well-suited to study potential-induced redox transformations of these NPs. The NPs were then submitted to a wide potential range spanning from -0.5 V *vs*. RHE up to 1.8 V vs RHE. The work sheds light on the interactions between the core and the shell, thus providing insights into the synergies that might exist within these NPs. We document the strong influence of the Fe_3O_4 core on the redox behavior of the $CoFe_2O_4$ shell under the OER conditions. Compared to previously investigated Co_3O_4 or $Co(OH)_2$ NPs[41,43,87,89], core-shell Fe_3O_4@$CoFe_2O_4$ NPs behave differently: most of the cobalt atoms in the shell remain in a Co (II) oxidation state in the potential interval where significant OER current is achieved. This was attributed to the electron transfer from iron to cobalt cations, resulting in the oxidation of some fraction of Fe (II) into Fe (III) in the NPs core and protecting cobalt from formation of CoOOH. Additionally, the O K-edge spectra are not modified in the OER conditions, so an anion redox mechanism has been ruled out. Hence, these results suggest the occurrence of a cation-red-ox OER mechanism involving cooperative red-ox behavior between Co and Fe atoms. It is remarkable that the core-shell spinel structure is essentially preserved under the OER conditions but can hardly withstand cathodic polarization down to – 0.5 V *vs*. RHE.

In the future, several perspectives can be envisioned for the development of the OER catalysts:

- Comparing the activity between core-shell NPs and pure $CoFe_2O_4$ NPs is something that should be done to confirm the role of the core conductivity. However, due to the differences in decomposition temperature of the cobalt and iron (II) stearates, and the fact that nucleation is a more difficult step than growth, all the syntheses of $CoFe_2O_4$ NPs using the thermal decomposition method failed.
- As nickel is known to be active for the OER, replacing the cobalt ferrite shell by a nickel ferrite one and investigating the properties of a cobalt/nickel core-shell NP (Fe_3O_4@$Co_xNi_{1-x}Fe_2O_4$) could also be interesting.
- Changing the shape of the nano object and using Fe_3O_4 nanofibers for the growth of the Co and/or Ni shell would also be interesting, as nanofibers seems to show better performances for the OER.

Also, in order to understand better the catalytic properties of core-shell NPs and ameliorate them, the study of the electrolyte pH and electrolyte concentration effect as well as the impact of full removal of the surfactant surrounding the NPs would be something to consider. The role of the core in the OER activity should be investigated deeper with other *operando* studies on different core-shell NPs: It would be interesting to study the interaction between the core and the shell with a nickel-based shell to see if the interactions seen with the cobalt are also observed with nickel. Finally, the long-term stability of the core-shell NPs under the OER conditions should also be investigated to shed light on the durability of the catalyst.

To complement electrochemical studies, annealing NPs in different environments could also be of interest. XPS depth profiling experiments of core-shell NPs before and after annealing at 300°C in the presence of O_2 suggested that there is a diffusion of the iron and cobalt atoms through the NPs resulting in a higher density of iron on the surface of the NPs after annealing. More measurements would be needed to clarify above which temperature the loss of core-shell structure occurs. Such studies may be interesting to perform in the future in order to clarify whether annealing is suitable for removing the oleic acid (that could impact their OER activity) from the surface of NPs. Additionally, the NEXAFS Fe L-edge spectra indicate partial oxidation of Fe (II) to Fe (III). In the meantime, Co L-edge spectra are displaying some changes that would be characteristic of cobalt migration from the Td sites to the Oh sites upon annealing.

References

(1) Aneke, M.; Wang, M. Energy Storage Technologies and Real Life Applications – A State of the Art Review. *Applied Energy* **2016**, *179* (C), 350–377.

(2) Ursua, A.; Gandia, L. M.; Sanchis, P. Hydrogen Production From Water Electrolysis: Current Status and Future Trends. *Proceedings of the IEEE* **2012**, *100* (2), 410–426. https://doi.org/10.1109/JPROC.2011.2156750.

(3) Møller, K. T.; Jensen, T. R.; Akiba, E.; Li, H. Hydrogen - A Sustainable Energy Carrier. *Progress in Natural Science: Materials International* **2017**, *27* (1), 34–40. https://doi.org/10.1016/j.pnsc.2016.12.014.

(4) Dincer, I.; Zamfirescu, C. *Sustainable Hydrogen Production*; Elsevier, 2016.

(5) Christophe Coutanceau, Steve Baranton, Thomas Audichon. *Hydrogen Electrochemical Production* -.

(6) Dincer, I.; Zamfirescu, C. *Sustainable Hydrogen Production*; Elsevier, 2016.

(7) Peng, J.; Dong, W.; Wang, Z.; Meng, Y.; Liu, W.; Song, P.; Liu, Z. Recent Advances in 2D Transition Metal Compounds for Electrocatalytic Full Water Splitting in Neutral Media. *Materials Today Advances* **2020**, *8*, 100081. https://doi.org/10.1016/j.mtadv.2020.100081.

(8) Christophe Coutanceau, Steve Baranton, Thomas Audichon. *Hydrogen Electrochemical Production* -.

(9) Dekel, D. R. Review of Cell Performance in Anion Exchange Membrane Fuel Cells. *Journal of Power Sources* **2018**, *375*, 158–169. https://doi.org/10.1016/j.jpowsour.2017.07.117.

(10) Thomas, O. D.; Soo, K. J. W. Y.; Peckham, T. J.; Kulkarni, M. P.; Holdcroft, S. Anion Conducting Poly(Dialkyl Benzimidazolium) Salts. *Polym. Chem.* **2011**, *2* (8), 1641–1643. https://doi.org/10.1039/C1PY00142F.

(11) Holdcroft, S.; Fan, J. Sterically-Encumbered Ionenes as Hydroxide Ion-Conducting Polymer Membranes. *Current Opinion in Electrochemistry* **2019**, *18*, 99–105. https://doi.org/10.1016/j.coelec.2019.10.014.

(12) Wright, A. G.; Weissbach, T.; Holdcroft, S. Poly(Phenylene) and m-Terphenyl as Powerful Protecting Groups for the Preparation of Stable Organic Hydroxides. *Angew. Chem. Int. Ed. Engl.* **2016**, *55* (15), 4818–4821. https://doi.org/10.1002/anie.201511184.

(13) Jamesh, M.-I.; Sun, X. Recent Progress on Earth Abundant Electrocatalysts for Oxygen Evolution Reaction (OER) in Alkaline Medium to Achieve Efficient Water Splitting – A Review. *Journal of Power Sources* **2018**, *400*, 31–68. https://doi.org/10.1016/j.jpowsour.2018.07.125.

(14) Dau, H.; Limberg, C.; Reier, T.; Risch, M.; Roggan, S.; Strasser, P. The Mechanism of Water Oxidation: From Electrolysis via Homogeneous to Biological Catalysis. *ChemCatChem* **2010**, *2* (7), 724–761. https://doi.org/10.1002/cctc.201000126.

(15) Song, F.; Bai, L.; Moysiadou, A.; Lee, S.; Hu, C.; Liardet, L.; Hu, X. Transition Metal Oxides as Electrocatalysts for the Oxygen Evolution Reaction in Alkaline Solutions: An Application-Inspired Renaissance. *J. Am. Chem. Soc.* **2018**, *140* (25), 7748–7759. https://doi.org/10.1021/jacs.8b04546.

(16) Bockris, J. O. Kinetics of Activation Controlled Consecutive Electrochemical Reactions: Anodic Evolution of Oxygen. *J. Chem. Phys.* **1956**, *24* (4), 817–827. https://doi.org/10.1063/1.1742616.

(17) Man, I. C.; Su, H.-Y.; Vallejo, F. C.; Hansen, H. A.; Martinez, J. I.; Inoglu, N. G.; Kitchin, J.; Jaramillo, T. F.; Nørskov, J. K.; Rossmeisl, J. Universality in Oxygen Evolution Electrocatalysis on Oxide Surfaces. *Chemical Catalysis Catalytical Chemistry* **2011**, *3* (7), 1159–1165. https://doi.org/10.1002/cctc.201000397.

(18) Wei, C.; Sun, S.; Mandler, D.; Wang, X.; Qiao, S. Z.; Xu, Z. J. Approaches for Measuring the Surface Areas of Metal Oxide Electrocatalysts for Determining Their Intrinsic Electrocatalytic Activity. *Chem. Soc. Rev.* **2019**, *48* (9), 2518–2534. https://doi.org/10.1039/C8CS00848E.
(19) Kim, J. S.; Kim, B.; Kim, H.; Kang, K. Recent Progress on Multimetal Oxide Catalysts for the Oxygen Evolution Reaction. *Advanced Energy Materials* **2018**, *8* (11), 1702774. https://doi.org/10.1002/aenm.201702774.
(20) Shinagawa, T.; Garcia-Esparza, A. T.; Takanabe, K. Insight on Tafel Slopes from a Microkinetic Analysis of Aqueous Electrocatalysis for Energy Conversion. *Sci Rep* **2015**, *5* (1), 13801. https://doi.org/10.1038/srep13801.
(21) Trasatti, S. Electrocatalysis in the Anodic Evolution of Oxygen and Chlorine. *Electrochimica Acta* **1984**, *29* (11), 1503–1512. https://doi.org/10.1016/0013-4686(84)85004-5.
(22) Zeng, K.; Zhang, D. Recent Progress in Alkaline Water Electrolysis for Hydrogen Production and Applications. *Progress in Energy and Combustion Science* **2010**, *36* (3), 307–326. https://doi.org/10.1016/j.pecs.2009.11.002.
(23) George, K.; van Berkel, M.; Zhang, X.; Sinha, R.; Bieberle-Hütter, A. Impedance Spectra and Surface Coverages Simulated Directly from the Electrochemical Reaction Mechanism: A Nonlinear State-Space Approach. *J. Phys. Chem. C* **2019**, *123* (15), 9981–9992. https://doi.org/10.1021/acs.jpcc.9b01836.
(24) Li, M.; Xiong, Y.; Liu, X.; Bo, X.; Zhang, Y.; Han, C.; Guo, L. Facile Synthesis of Electrospun MFe2O4 (M = Co, Ni, Cu, Mn) Spinel Nanofibers with Excellent Electrocatalytic Properties for Oxygen Evolution and Hydrogen Peroxide Reduction. *Nanoscale* **2015**, *7* (19), 8920–8930. https://doi.org/10.1039/C4NR07243J.
(25) Kéranguéven, G.; Filimonenkov, I. S.; Savinova, E. R. Investigation of the Stability of the Boron-Doped Diamond Support for Co3O4-Based Oxygen Evolution Reaction Catalysts Synthesized through in Situ Autocombustion Method. *Journal of Electroanalytical Chemistry* **2022**, 116367. https://doi.org/10.1016/j.jelechem.2022.116367.
(26) *Electrokinetic Analysis of Poorly Conductive Electrocatalytic Materials | ACS Catalysis*. https://pubs.acs.org/doi/abs/10.1021/acscatal.0c00960 (accessed 2022-04-28).
(27) Bisquert, J.; Belmonte, G. G.; Santiago, F. F.; Ferriols, N. S.; Yamashita, M.; Pereira, E. C. Application of a Distributed Impedance Model in the Analysis of Conducting Polymer Films. *Electrochemistry Communications* **2000**, *2* (8), 601–605. https://doi.org/10.1016/S1388-2481(00)00089-8.
(28) Fletcher, S. An Electrical Model Circuit That Reproduces the Behaviour of Conducting Polymer Electrodes in Electrolyte Solutions. *Journal of Electroanalytical Chemistry* **1992**, *337* (1), 127–145. https://doi.org/10.1016/0022-0728(92)80533-A.
(29) Bisquert, J.; Fabregat-Santiago, F.; Ferriols, N. S.; Bogdanoff, P.; Pereira, E. C. Doubling Exponent Models for the Analysis of Porous Film Electrodes by Impedance. Relaxation of TiO2 Nanoporous in Aqueous Solution. 12.
(30) Gebreslase, G. A.; Martínez-Huerta, M. V.; Lázaro, M. J. Recent Progress on Bimetallic NiCo and CoFe Based Electrocatalysts for Alkaline Oxygen Evolution Reaction: A Review. *Journal of Energy Chemistry* **2022**, *67*, 101–137. https://doi.org/10.1016/j.jechem.2021.10.009.
(31) Suen, N.-T.; Hung, S.-F.; Quan, Q.; Zhang, N.; Xu, Y.-J.; Chen, H. M. Electrocatalysis for the Oxygen Evolution Reaction: Recent Development and Future Perspectives. *Chem. Soc. Rev.* **2017**, *46* (2), 337–365. https://doi.org/10.1039/C6CS00328A.
(32) Subbaraman, R.; Tripkovic, D.; Chang, K.-C.; Strmcnik, D.; Paulikas, A. P.; Hirunsit, P.; Chan, M.; Greeley, J.; Stamenkovic, V.; Markovic, N. M. Trends in Activity for the Water Electrolyser Reactions on 3d M(Ni,Co,Fe,Mn) Hydr(Oxy)Oxide Catalysts. *Nat Mater* **2012**, *11* (6), 550–557. https://doi.org/10.1038/nmat3313.
(33) Liu, G.; Chen, H.; Xia, L.; Wang, S.; Ding, L.-X.; Li, D.; Xiao, K.; Dai, S.; Wang, H. Hierarchical Mesoporous/Macroporous Perovskite La0.5Sr0.5CoO3–x Nanotubes: A Bifunctional Catalyst with Enhanced Activity and Cycle Stability for Rechargeable Lithium Oxygen Batteries. *ACS Appl. Mater. Interfaces* **2015**, *7* (40), 22478–22486. https://doi.org/10.1021/acsami.5b06587.

(34) Zhu, Y.; Zhou, W.; Yu, J.; Chen, Y.; Liu, M.; Shao, Z. Enhancing Electrocatalytic Activity of Perovskite Oxides by Tuning Cation Deficiency for Oxygen Reduction and Evolution Reactions. *Chem. Mater.* **2016**, *28* (6), 1691–1697. https://doi.org/10.1021/acs.chemmater.5b04457.
(35) Chen, C.-F.; King, G.; Dickerson, R. M.; Papin, P. A.; Gupta, S.; Kellogg, W. R.; Wu, G. Oxygen-Deficient BaTiO3−x Perovskite as an Efficient Bifunctional Oxygen Electrocatalyst. *Nano Energy* **2015**, *13*, 423–432. https://doi.org/10.1016/j.nanoen.2015.03.005.
(36) Wang, H.; Zhou, M.; Choudhury, P.; Luo, H. Perovskite Oxides as Bifunctional Oxygen Electrocatalysts for Oxygen Evolution/Reduction Reactions – A Mini Review. *Applied Materials Today* **2019**, *16*, 56–71. https://doi.org/10.1016/j.apmt.2019.05.004.
(37) *Description de la structure spinelle*. http://ressources.univ-lemans.fr/AccesLibre/UM/Pedago/chimie/04/mcu12/spinelle.html (accessed 2020-05-07).
(38) Szotek, Z.; Temmerman, W. M.; Ködderitzsch, D.; Svane, A.; Petit, L.; Winter, H. Electronic Structures of Normal and Inverse Spinel Ferrites from First Principles. *Phys. Rev. B* **2006**, *74* (17), 174431. https://doi.org/10.1103/PhysRevB.74.174431.
(39) Wang, H.-Y.; Hsu, Y.-Y.; Chen, R.; Chan, T.-S.; Chen, H. M.; Liu, B. Ni3+-Induced Formation of Active NiOOH on the Spinel Ni–Co Oxide Surface for Efficient Oxygen Evolution Reaction. *Advanced Energy Materials* **2015**, *5* (10), 1500091. https://doi.org/10.1002/aenm.201500091.
(40) Tung, C.-W.; Hsu, Y.-Y.; Shen, Y.-P.; Zheng, Y.; Chan, T.-S.; Sheu, H.-S.; Cheng, Y.-C.; Chen, H. M. Reversible Adapting Layer Produces Robust Single-Crystal Electrocatalyst for Oxygen Evolution. *Nat Commun* **2015**, *6*, 8106. https://doi.org/10.1038/ncomms9106.
(41) Ortiz Peña, N.; Ihiawakrim, D.; Han, M.; Lassalle-Kaiser, B.; Carenco, S.; Sanchez, C.; Laberty-Robert, C.; Portehault, D.; Ersen, O. Morphological and Structural Evolution of Co3O4 Nanoparticles Revealed by in Situ Electrochemical Transmission Electron Microscopy during Electrocatalytic Water Oxidation. *ACS Nano* **2019**, *13* (10), 11372–11381. https://doi.org/10.1021/acsnano.9b04745.
(42) Wiegmann, T.; Pacheco, I.; Reikowski, F.; Stettner, J.; Qiu, C.; Bouvier, M.; Bertram, M.; Faisal, F.; Brummel, O.; Libuda, J.; Drnec, J.; Allongue, P.; Maroun, F.; Magnussen, O. M. Operando Identification of the Reversible Skin Layer on Co3O4 as a Three-Dimensional Reaction Zone for Oxygen Evolution. *ACS Catal.* **2022**, *12* (6), 3256–3268. https://doi.org/10.1021/acscatal.1c05169.
(43) Reikowski, F.; Maroun, F.; Pacheco, I.; Wiegmann, T.; Allongue, P.; Stettner, J.; Magnussen, O. M. Operando Surface X-Ray Diffraction Studies of Structurally Defined Co3O4 and CoOOH Thin Films during Oxygen Evolution. *ACS Catal.* **2019**, *9* (5), 3811–3821. https://doi.org/10.1021/acscatal.8b04823.
(44) Masa, J.; Weide, P.; Peeters, D.; Sinev, I.; Xia, W.; Sun, Z.; Somsen, C.; Muhler, M.; Schuhmann, W. Amorphous Cobalt Boride (Co2B) as a Highly Efficient Nonprecious Catalyst for Electrochemical Water Splitting: Oxygen and Hydrogen Evolution. *Advanced Energy Materials* **2016**, *6* (6), 1502313. https://doi.org/10.1002/aenm.201502313.
(45) Liu, Z.; Wang, G.; Zhu, X.; Wang, Y.; Zou, Y.; Zang, S.; Wang, S. Optimal Geometrical Configuration of Cobalt Cations in Spinel Oxides to Promote Oxygen Evolution Reaction. *Angewandte Chemie International Edition* **2020**, *59* (12), 4736–4742. https://doi.org/10.1002/anie.201914245.
(46) Guo, D.; Kang, H.; Wei, P.; Yang, Y.; Hao, Z.; Zhang, Q.; Liu, L. A High-Performance Bimetallic Cobalt Iron Oxide Catalyst for the Oxygen Evolution Reaction. *CrystEngComm* **2020**, *22* (25), 4317–4323. https://doi.org/10.1039/D0CE00401D.
(47) Duan, Y.; Dubouis, N.; Huang, J.; Dalla Corte, D. A.; Pimenta, V.; Xu, Z. J.; Grimaud, A. Revealing the Impact of Electrolyte Composition for Co-Based Water Oxidation Catalysts by the Study of Reaction Kinetics Parameters. *ACS Catal.* **2020**, *10* (7), 4160–4170. https://doi.org/10.1021/acscatal.0c00490.
(48) Huang, Z.-F.; Song, J.; Du, Y.; Xi, S.; Dou, S.; Nsanzimana, J. M. V.; Wang, C.; Xu, Z. J.; Wang, X. Chemical and Structural Origin of Lattice Oxygen Oxidation in Co–Zn Oxyhydroxide Oxygen

Evolution Electrocatalysts. *Nat Energy* **2019**, *4* (4), 329–338. https://doi.org/10.1038/s41560-019-0355-9.

(49) Zhou, Y.; Sun, S.; Song, J.; Xi, S.; Chen, B.; Du, Y.; Fisher, A. C.; Cheng, F.; Wang, X.; Zhang, H.; Xu, Z. J. Enlarged Co□O Covalency in Octahedral Sites Leading to Highly Efficient Spinel Oxides for Oxygen Evolution Reaction. *Advanced Materials* **2018**, *30* (32), 1802912. https://doi.org/10.1002/adma.201802912.

(50) Garcia, A. C.; Touzalin, T.; Nieuwland, C.; Perini, N.; Koper, M. T. M. Enhancement of Oxygen Evolution Activity of Nickel Oxyhydroxide by Electrolyte Alkali Cations. *Angewandte Chemie International Edition* **2019**, *58* (37), 12999–13003. https://doi.org/10.1002/anie.201905501.

(51) Giordano, L.; Han, B.; Risch, M.; Hong, W. T.; Rao, R. R.; Stoerzinger, K. A.; Shao-Horn, Y. PH Dependence of OER Activity of Oxides: Current and Future Perspectives. *Catalysis Today* **2016**, *262*, 2–10. https://doi.org/10.1016/j.cattod.2015.10.006.

(52) Koper, M. T. M. Theory of Multiple Proton–Electron Transfer Reactions and Its Implications for Electrocatalysis. *Chem. Sci.* **2013**, *4* (7), 2710–2723. https://doi.org/10.1039/C3SC50205H.

(53) Grimaud, A.; Diaz-Morales, O.; Han, B.; Hong, W. T.; Lee, Y.-L.; Giordano, L.; Stoerzinger, K. A.; Koper, M. T. M.; Shao-Horn, Y. Activating Lattice Oxygen Redox Reactions in Metal Oxides to Catalyse Oxygen Evolution. *Nature Chem* **2017**, *9* (5), 457–465. https://doi.org/10.1038/nchem.2695.

(54) Kim, B.-J.; Fabbri, E.; Borlaf, M.; F. Abbott, D.; E. Castelli, I.; Nachtegaal, M.; Graule, T.; J. Schmidt, T. Oxygen Evolution Reaction Activity and Underlying Mechanism of Perovskite Electrocatalysts at Different PH. *Materials Advances* **2021**, *2* (1), 345–355. https://doi.org/10.1039/D0MA00661K.

(55) Li, D.; Wang, C.; Tripkovic, D.; Sun, S.; Markovic, N. M.; Stamenkovic, V. R. Surfactant Removal for Colloidal Nanoparticles from Solution Synthesis: The Effect on Catalytic Performance. *ACS Catal.* **2012**, *2* (7), 1358–1362. https://doi.org/10.1021/cs300219j.

(56) Arminio-Ravelo, J. A.; Quinson, J.; Pedersen, M. A.; Kirkensgaard, J. J. K.; Arenz, M.; Escudero-Escribano, M. Synthesis of Iridium Nanocatalysts for Water Oxidation in Acid: Effect of the Surfactant. *ChemCatChem* **2020**, *12* (5), 1282–1287. https://doi.org/10.1002/cctc.201902190.

(57) Haase, F. T.; Bergmann, A.; Jones, T. E.; Timoshenko, J.; Herzog, A.; Jeon, H. S.; Rettenmaier, C.; Cuenya, B. R. Size Effects and Active State Formation of Cobalt Oxide Nanoparticles during the Oxygen Evolution Reaction. *Nat Energy* **2022**, 1–9. https://doi.org/10.1038/s41560-022-01083-w.

(58) Han, X.; Yu, C.; Yang, J.; Zhao, C.; Huang, H.; Liu, Z.; Ajayan, P. M.; Qiu, J. Mass and Charge Transfer Coenhanced Oxygen Evolution Behaviors in CoFe-Layered Double Hydroxide Assembled on Graphene. *Advanced Materials Interfaces* **2016**, *3* (7), 1500782. https://doi.org/10.1002/admi.201500782.

(59) Li, M.; Xiong, Y.; Liu, X.; Bo, X.; Zhang, Y.; Han, C.; Guo, L. Facile Synthesis of Electrospun MFe2O4 (M = Co, Ni, Cu, Mn) Spinel Nanofibers with Excellent Electrocatalytic Properties for Oxygen Evolution and Hydrogen Peroxide Reduction. *Nanoscale* **2015**, *7* (19), 8920–8930. https://doi.org/10.1039/C4NR07243J.

(60) Chou, S.-C.; Tso, K.-C.; Hsieh, Y.-C.; Sun, B.-Y.; Lee, J.-F.; Wu, P.-W. Facile Synthesis of Co3O4@CoO@Co Gradient Core@Shell Nanoparticles and Their Applications for Oxygen Evolution and Reduction in Alkaline Electrolytes. *Materials* **2020**, *13* (12). https://doi.org/10.3390/ma13122703.

(61) Zhou, L.; Deng, B.; Jiang, Z.; Jiang, Z.-J. Shell Thickness Controlled Core–Shell Fe3O4@CoO Nanocrystals as Efficient Bifunctional Catalysts for the Oxygen Reduction and Evolution Reactions. *Chem. Commun.* **2019**, *55* (4), 525–528. https://doi.org/10.1039/C8CC09140D.

(62) Zhuang, Z.; Sheng, W.; Yan, Y. Synthesis of Monodispere Au@Co3O4 Core-Shell Nanocrystals and Their Enhanced Catalytic Activity for Oxygen Evolution Reaction. *Advanced Materials* **2014**, *26* (23), 3950–3955. https://doi.org/10.1002/adma.201400336.

(63) Strickler, A. L.; Escudero-Escribano, M.; Jaramillo, T. F. Core–Shell Au@Metal-Oxide Nanoparticle Electrocatalysts for Enhanced Oxygen Evolution. *Nano Lett.* **2017**, *17* (10), 6040–6046. https://doi.org/10.1021/acs.nanolett.7b02357.
(64) Lv, Y.; Duan, S.; Zhu, Y.; Yin, P.; Wang, R. Enhanced OER Performances of Au@NiCo2S4 Core-Shell Heterostructure. *Nanomaterials* **2020**, *10* (4), 611. https://doi.org/10.3390/nano10040611.
(65) Saddeler, S.; Bendt, G.; Salamon, S.; Haase, F. T.; Landers, J.; Timoshenko, J.; Rettenmaier, C.; Jeon, H. S.; Bergmann, A.; Wende, H.; Cuenya, B. R.; Schulz, S. Influence of the Cobalt Content in Cobalt Iron Oxides on the Electrocatalytic OER Activity. *J. Mater. Chem. A* **2021**, *9* (45), 25381–25390. https://doi.org/10.1039/D1TA06568H.
(66) Luo, Z.; Martí-Sànchez, S.; Nafria, R.; Joshua, G.; de la Mata, M.; Guardia, P.; Flox, C.; Martínez-Boubeta, C.; Simeonidis, K.; Llorca, J.; Morante, J. R.; Arbiol, J.; Ibáñez, M.; Cabot, A. Fe3O4@NiFexOy Nanoparticles with Enhanced Electrocatalytic Properties for Oxygen Evolution in Carbonate Electrolyte. *ACS Appl. Mater. Interfaces* **2016**, *8* (43), 29461–29469. https://doi.org/10.1021/acsami.6b09888.
(67) Gloag, L.; Benedetti, T. M.; Cheong, S.; Webster, R. F.; Marjo, C. E.; Gooding, J. J.; Tilley, R. D. Pd–Ru Core–Shell Nanoparticles with Tunable Shell Thickness for Active and Stable Oxygen Evolution Performance. *Nanoscale* **2018**, *10* (32), 15173–15177. https://doi.org/10.1039/C8NR03341B.
(68) Nong, H. N.; Gan, L.; Willinger, E.; Teschner, D.; Strasser, P. IrOx Core-Shell Nanocatalysts for Cost- and Energy-Efficient Electrochemical Water Splitting. *Chem. Sci.* **2014**, *5* (8), 2955–2963. https://doi.org/10.1039/C4SC01065E.
(69) Gorlin, Y.; Chung, C.-J.; Benck, J. D.; Nordlund, D.; Seitz, L.; Weng, T.-C.; Sokaras, D.; Clemens, B. M.; Jaramillo, T. F. Understanding Interactions between Manganese Oxide and Gold That Lead to Enhanced Activity for Electrocatalytic Water Oxidation. *J. Am. Chem. Soc.* **2014**, *136* (13), 4920–4926. https://doi.org/10.1021/ja407581w.
(70) Yeo, B. S.; Bell, A. T. Enhanced Activity of Gold-Supported Cobalt Oxide for the Electrochemical Evolution of Oxygen. *J. Am. Chem. Soc.* **2011**, *133* (14), 5587–5593. https://doi.org/10.1021/ja200559j.
(71) *Actualisation de la liste des substances critiques pour l'UE | MineralInfo*. https://www.mineralinfo.fr/fr/actualite/actualite/actualisation-de-liste-des-substances-critiques-pour-lue (accessed 2022-06-21).
(72) Anantharaj, S.; Kundu, S.; Noda, S. "The Fe Effect": A Review Unveiling the Critical Roles of Fe in Enhancing OER Activity of Ni and Co Based Catalysts. *Nano Energy* **2021**, *80*, 105514. https://doi.org/10.1016/j.nanoen.2020.105514.
(73) Li, M.; Gu, Y.; Chang, Y.; Gu, X.; Tian, J.; Wu, X.; Feng, L. Iron Doped Cobalt Fluoride Derived from CoFe Layered Double Hydroxide for Efficient Oxygen Evolution Reaction. *Chemical Engineering Journal* **2021**, *425*, 130686. https://doi.org/10.1016/j.cej.2021.130686.
(74) Suntivich, J.; May, K. J.; Gasteiger, H. A.; Goodenough, J. B.; Shao-Horn, Y. A Perovskite Oxide Optimized for Oxygen Evolution Catalysis from Molecular Orbital Principles. *Science* **2011**, *334* (6061), 1383–1385. https://doi.org/10.1126/science.1212858.
(75) Dionigi, F.; Zeng, Z.; Sinev, I.; Merzdorf, T.; Deshpande, S.; Lopez, M. B.; Kunze, S.; Zegkinoglou, I.; Sarodnik, H.; Fan, D.; Bergmann, A.; Drnec, J.; Araujo, J. F. de; Gliech, M.; Teschner, D.; Zhu, J.; Li, W.-X.; Greeley, J.; Cuenya, B. R.; Strasser, P. In-Situ Structure and Catalytic Mechanism of NiFe and CoFe Layered Double Hydroxides during Oxygen Evolution. *Nat Commun* **2020**, *11* (1), 2522. https://doi.org/10.1038/s41467-020-16237-1.
(76) Silva, V. D.; Ferreira, L. S.; Simões, T. A.; Medeiros, E. S.; Macedo, D. A. 1D Hollow MFe2O4 (M = Cu, Co, Ni) Fibers by Solution Blow Spinning for Oxygen Evolution Reaction. *J Colloid Interface Sci* **2019**, *540*, 59–65. https://doi.org/10.1016/j.jcis.2019.01.003.
(77) *Photoelectron spectroscopy (article)*. Khan Academy. https://www.khanacademy.org/science/ap-chemistry-beta/x2eef969c74e0d802:atomic-

structure-and-properties/x2eef969c74e0d802:photoelectron-spectroscopy/a/photoelectron-spectroscopy (accessed 2022-03-07).
(78) Briggs, D.; Grant, J. T.; SurfaceSpectra Limited. *Surface Analysis by Auger and X-Ray Photoelectron Spectroscopy.*; IM Publications: Chichester, 2003.
(79) Northrup, P.; Leri, A.; Tappero, R. Applications of "Tender" Energy (1-5 KeV) X-Ray Absorption Spectroscopy in Life Sciences. *Protein & Peptide Letters 23* (3), 300–308.
(80) Bak, S.-M.; Shadike, Z.; Lin, R.; Yu, X.; Yang, X.-Q. In Situ/Operando Synchrotron-Based X-Ray Techniques for Lithium-Ion Battery Research. *NPG Asia Mater* **2018**, *10* (7), 563–580. https://doi.org/10.1038/s41427-018-0056-z.
(81) Hähner, G. Near Edge X-Ray Absorption Fine Structure Spectroscopy as a Tool to Probe Electronic and Structural Properties of Thin Organic Films and Liquids. *Chem. Soc. Rev.* **2006**, *35* (12), 1244–1255. https://doi.org/10.1039/B509853J.
(82) Alp, E. E.; Mini, S. M.; Ramanathan, M. X-Ray Absorption Spectroscopy: EXAFS and XANES - A Versatile Tool to Study the Atomic and Electronic Structure of Materials. 12.
(83) Chen, J. G. NEXAFS Investigations of Transition Metal Oxides, Nitrides, Carbides, Sulfides and Other Interstitial Compounds. *Surface Science Reports* **1997**, *30* (1), 1–152. https://doi.org/10.1016/S0167-5729(97)00011-3.
(84) Stöhr, J. Principles, Techniques, and Instrumentation of NEXAFS. In *NEXAFS Spectroscopy*; Stöhr, J., Ed.; Springer Series in Surface Sciences; Springer: Berlin, Heidelberg, 1992; pp 114–161. https://doi.org/10.1007/978-3-662-02853-7_5.
(85) Saveleva, V. Investigation of the Anodes of PEM Water Electrolyzers by Operando Synchrotron-Based Photoemission Spectroscopy. These de doctorat, Strasbourg, 2018.
(86) Favaro, M.; Yang, J.; Nappini, S.; Magnano, E.; Toma, F. M.; Crumlin, E. J.; Yano, J.; Sharp, I. D. Understanding the Oxygen Evolution Reaction Mechanism on CoOx Using Operando Ambient-Pressure X-Ray Photoelectron Spectroscopy. *J. Am. Chem. Soc.* **2017**, *139* (26), 8960–8970. https://doi.org/10.1021/jacs.7b03211.
(87) Bergmann, A.; Martinez-Moreno, E.; Teschner, D.; Chernev, P.; Gliech, M.; de Araújo, J. F.; Reier, T.; Dau, H.; Strasser, P. Reversible Amorphization and the Catalytically Active State of Crystalline Co3O4 during Oxygen Evolution. *Nat Commun* **2015**, *6* (1), 8625. https://doi.org/10.1038/ncomms9625.
(88) Bergmann, A.; Jones, T. E.; Martinez Moreno, E.; Teschner, D.; Chernev, P.; Gliech, M.; Reier, T.; Dau, H.; Strasser, P. Unified Structural Motifs of the Catalytically Active State of Co(Oxyhydr)Oxides during the Electrochemical Oxygen Evolution Reaction. *Nat Catal* **2018**, *1* (9), 711–719. https://doi.org/10.1038/s41929-018-0141-2.
(89) Mefford, J. T.; Akbashev, A. R.; Kang, M.; Bentley, C. L.; Gent, W. E.; Deng, H. D.; Alsem, D. H.; Yu, Y.-S.; Salmon, N. J.; Shapiro, D. A.; Unwin, P. R.; Chueh, W. C. Correlative Operando Microscopy of Oxygen Evolution Electrocatalysts. *Nature* **2021**, *593* (7857), 67–73. https://doi.org/10.1038/s41586-021-03454-x.
(90) Enman, L. J.; Stevens, M. B.; Dahan, M. H.; Nellist, M. R.; Toroker, M. C.; Boettcher, S. W. Operando X-Ray Absorption Spectroscopy Shows Iron Oxidation Is Concurrent with Oxygen Evolution in Cobalt–Iron (Oxy)Hydroxide Electrocatalysts. *Angewandte Chemie International Edition* **2018**, *57* (39), 12840–12844. https://doi.org/10.1002/anie.201808818.
(91) Pfeifer, V.; E. Jones, T.; Wrabetz, S.; Massué, C.; Vélez, J. J. V.; Arrigo, R.; Scherzer, M.; Piccinin, S.; Hävecker, M.; Knop-Gericke, A.; Schlögl, R. Reactive Oxygen Species in Iridium-Based OER Catalysts. *Chemical Science* **2016**, *7* (11), 6791–6795. https://doi.org/10.1039/C6SC01860B.
(92) Saveleva, V. A.; Wang, L.; Teschner, D.; Jones, T.; Gago, A. S.; Friedrich, K. A.; Zafeiratos, S.; Schlögl, R.; Savinova, E. R. Operando Evidence for a Universal Oxygen Evolution Mechanism on Thermal and Electrochemical Iridium Oxides. *J. Phys. Chem. Lett.* **2018**, *9* (11), 3154–3160. https://doi.org/10.1021/acs.jpclett.8b00810.
(93) Feng, C.; Faheem, M. B.; Fu, J.; Xiao, Y.; Li, C.; Li, Y. Fe-Based Electrocatalysts for Oxygen Evolution Reaction: Progress and Perspectives. *ACS Catal.* **2020**, *10* (7), 4019–4047. https://doi.org/10.1021/acscatal.9b05445.

(94) Smith, R. D. L.; Pasquini, C.; Loos, S.; Chernev, P.; Klingan, K.; Kubella, P.; Mohammadi, M. R.; Gonzalez-Flores, D.; Dau, H. Spectroscopic Identification of Active Sites for the Oxygen Evolution Reaction on Iron-Cobalt Oxides. *Nat Commun* **2017**, *8* (1), 2022. https://doi.org/10.1038/s41467-017-01949-8.
(95) Calvillo, L.; Carraro, F.; Vozniuk, O.; Celorrio, V.; Nodari, L.; Russell, A. E.; Debellis, D.; Fermin, D.; Cavani, F.; Agnoli, S.; Granozzi, G. Insights into the Durability of Co–Fe Spinel Oxygen Evolution Electrocatalysts via Operando Studies of the Catalyst Structure. *J. Mater. Chem. A* **2018**, *6* (16), 7034–7041. https://doi.org/10.1039/C7TA10892C.
(96) Dong, H.; Chen, Y.-C.; Feldmann, C. Polyol Synthesis of Nanoparticles: Status and Options Regarding Metals, Oxides, Chalcogenides, and Non-Metal Elements. *Green Chem.* **2015**, *17* (8), 4107–4132. https://doi.org/10.1039/C5GC00943J.
(97) Chen, D.; Xu, R. Hydrothermal Synthesis and Characterization of Nanocrystalline Fe3O4 Powders. *Materials Research Bulletin* **1998**, *33* (7), 1015–1021. https://doi.org/10.1016/S0025-5408(98)00073-7.
(98) Lopez-Perez, J. A.; Lopez-Quintela, M. A.; Mira, J.; Rivas, J. Preparation of Magnetic Fluids with Particles Obtained in Microemulsions. *IEEE Transactions on Magnetics* **1997**, *33* (5), 4359–4362. https://doi.org/10.1109/20.620446.
(99) Lu, A.-H.; Salabas, E. L.; Schüth, F. Magnetic Nanoparticles: Synthesis, Protection, Functionalization, and Application. *Angewandte Chemie International Edition* **2007**, *46* (8), 1222–1244. https://doi.org/10.1002/anie.200602866.
(100) Sartori, K. Studying the Interfacial Exchange Coupling within Ferrite Based Magnetic Nanoparticles Prepared Following to a Succession of Thermal Decomposition Synthesis. These de doctorat, Strasbourg, 2019.
(101) LaMer, V. K.; Dinegar, R. H. Theory, Production and Mechanism of Formation of Monodispersed Hydrosols. *J. Am. Chem. Soc.* **1950**, *72* (11), 4847–4854. https://doi.org/10.1021/ja01167a001.
(102) Baaziz, W.; Pichon, B. P.; Fleutot, S.; Liu, Y.; Lefevre, C.; Greneche, J.-M.; Toumi, M.; Mhiri, T.; Begin-Colin, S. Magnetic Iron Oxide Nanoparticles: Reproducible Tuning of the Size and Nanosized-Dependent Composition, Defects, and Spin Canting. *J. Phys. Chem. C* **2014**, *118* (7), 3795–3810. https://doi.org/10.1021/jp411481p.
(103) Lak, A.; Kraken, M.; Ludwig, F.; Kornowski, A.; Eberbeck, D.; Sievers, S.; Litterst, F. J.; Weller, H.; Schilling, M. Size Dependent Structural and Magnetic Properties of FeO–Fe3O4 Nanoparticles. *Nanoscale* **2013**, *5* (24), 12286–12295. https://doi.org/10.1039/C3NR04562E.
(104) Redl, F. X.; Black, C. T.; Papaefthymiou, G. C.; Sandstrom, R. L.; Yin, M.; Zeng, H.; Murray, C. B.; O'Brien, S. P. Magnetic, Electronic, and Structural Characterization of Nonstoichiometric Iron Oxides at the Nanoscale. *J. Am. Chem. Soc.* **2004**, *126* (44), 14583–14599. https://doi.org/10.1021/ja046808r.
(105) Hyeon, T.; Lee, S. S.; Park, J.; Chung, Y.; Na, H. B. Synthesis of Highly Crystalline and Monodisperse Maghemite Nanocrystallites without a Size-Selection Process. *J. Am. Chem. Soc.* **2001**, *123* (51), 12798–12801. https://doi.org/10.1021/ja016812s.
(106) Schladt, T. D.; Schneider, K.; Schild, H.; Tremel, W. Synthesis and Bio-Functionalization of Magnetic Nanoparticles for Medical Diagnosis and Treatment. *Dalton Trans.* **2011**, *40* (24), 6315. https://doi.org/10.1039/c0dt00689k.
(107) van Embden, J.; Chesman, A. S. R.; Jasieniak, J. J. The Heat-Up Synthesis of Colloidal Nanocrystals. *Chem. Mater.* **2015**, *27* (7), 2246–2285. https://doi.org/10.1021/cm5028964.
(108) Demortière, A.; Panissod, P.; P. Pichon, B.; Pourroy, G.; Guillon, D.; Donnio, B.; Bégin-Colin, S. Size-Dependent Properties of Magnetic Iron Oxide Nanocrystals. *Nanoscale* **2011**, *3* (1), 225–232. https://doi.org/10.1039/C0NR00521E.
(109) Herman, D. A. J.; Cheong-Tilley, S.; McGrath, A. J.; McVey, B. F. P.; Lein, M.; Tilley, R. D. How to Choose a Precursor for Decomposition Solution-Phase Synthesis: The Case of Iron Nanoparticles. *Nanoscale* **2015**, *7* (14), 5951–5954. https://doi.org/10.1039/C5NR00718F.

(110) Keating, M.; Chen, Y.; Larmour, I. A.; Faulds, K.; Graham, D. Growth and Surface-Enhanced Raman Scattering of Ag Nanoparticle Assembly in Agarose Gel. *Meas. Sci. Technol.* **2012**, *23* (8), 084006. https://doi.org/10.1088/0957-0233/23/8/084006.
(111) Shavel, A.; Liz-Marzán, L. M. Shape Control of Iron Oxide Nanoparticles. *Phys. Chem. Chem. Phys.* **2009**, *11* (19), 3762–3766. https://doi.org/10.1039/B822733K.
(112) Wang, H.; Shrestha, T. B.; Basel, M. T.; Pyle, M.; Toledo, Y.; Konecny, A.; Thapa, P.; Ikenberry, M.; Hohn, K. L.; Chikan, V.; Troyer, D. L.; Bossmann, S. H. Hexagonal Magnetite Nanoprisms: Preparation, Characterization and Cellular Uptake. *J. Mater. Chem. B* **2015**, *3* (23), 4647–4653. https://doi.org/10.1039/C5TB00340G.
(113) Liu, X.; Pichon, B. P.; Ulhaq, C.; Lefèvre, C.; Grenèche, J.-M.; Bégin, D.; Bégin-Colin, S. Systematic Study of Exchange Coupling in Core–Shell Fe3−δO4@CoO Nanoparticles. *Chem. Mater.* **2015**, *27* (11), 4073–4081. https://doi.org/10.1021/acs.chemmater.5b01103.
(114) Sartori, K.; Musat, A.; Choueikani, F.; Grenèche, J.-M.; Hettler, S.; Bencok, P.; Begin-Colin, S.; Steadman, P.; Arenal, R.; Pichon, B. P. A Detailed Investigation of the Onion Structure of Exchanged Coupled Magnetic Fe3−δO4@CoFe2O4@Fe3−δO4 Nanoparticles. *ACS Appl. Mater. Interfaces* **2021**, *13* (14), 16784–16800. https://doi.org/10.1021/acsami.0c18310.
(115) Baaziz, W.; Pichon, B. P.; Liu, Y.; Grenèche, J.-M.; Ulhaq-Bouillet, C.; Terrier, E.; Bergeard, N.; Halté, V.; Boeglin, C.; Choueikani, F.; Toumi, M.; Mhiri, T.; Begin-Colin, S. Tuning of Synthesis Conditions by Thermal Decomposition toward Core–Shell CoxFe1–XO@CoyFe3–YO4 and CoFe2O4 Nanoparticles with Spherical and Cubic Shapes. *Chem. Mater.* **2014**, *26* (17), 5063–5073. https://doi.org/10.1021/cm502269s.
(116) Baaziz, W.; Pichon, B. P.; Lefevre, C.; Ulhaq-Bouillet, C.; Greneche, J.-M.; Toumi, M.; Mhiri, T.; Bégin-Colin, S. High Exchange Bias in Fe3−δO4@CoO Core Shell Nanoparticles Synthesized by a One-Pot Seed-Mediated Growth Method. *J. Phys. Chem. C* **2013**, *117* (21), 11436–11443. https://doi.org/10.1021/jp402823h.
(117) Peddis, D.; Yaacoub, N.; Ferretti, M.; Martinelli, A.; Piccaluga, G.; Musinu, A.; Cannas, C.; Navarra, G.; Greneche, J. M.; Fiorani, D. Cationic Distribution and Spin Canting in CoFe2O4 Nanoparticles. *J Phys Condens Matter* **2011**, *23* (42), 426004. https://doi.org/10.1088/0953-8984/23/42/426004.
(118) Deatsch, A. E.; Evans, B. A. Heating Efficiency in Magnetic Nanoparticle Hyperthermia. *Journal of Magnetism and Magnetic Materials* **2014**, *354*, 163–172. https://doi.org/10.1016/j.jmmm.2013.11.006.
(119) Cotin, G.; Kiefer, C.; Perton, F.; Boero, M.; Özdamar, B.; Bouzid, A.; Ori, G.; Massobrio, C.; Begin, D.; Pichon, B.; Mertz, D.; Begin-Colin, S. Evaluating the Critical Roles of Precursor Nature and Water Content When Tailoring Magnetic Nanoparticles for Specific Applications. *ACS Appl. Nano Mater.* **2018**, *1* (8), 4306–4316. https://doi.org/10.1021/acsanm.8b01123.
(120) Perton, F. Architecture de Nanoparticules Hybrides Pour Une Imagerie et/Ou Thérapie Multimodales. thesis, Strasbourg, 2019.
(121) Li, C.; Tardajos, A. P.; Wang, D.; Choukroun, D.; Van Daele, K.; Breugelmans, T.; Bals, S. A Simple Method to Clean Ligand Contamination on TEM Grids. *Ultramicroscopy* **2021**, *221*, 113195. https://doi.org/10.1016/j.ultramic.2020.113195.
(122) Thompson, P.; Cox, D. E.; Hastings, J. B. Rietveld Refinement of Debye–Scherrer Synchrotron X-Ray Data from Al2O3. *Journal of Applied Crystallography* **1987**, *20* (2), 79–83. https://doi.org/10.1107/S0021889887087090.
(123) Rodríguez-Carvajal, J. Recent Advances in Magnetic Structure Determination by Neutron Powder Diffraction. *Physica B: Condensed Matter* **1993**, *192* (1), 55–69. https://doi.org/10.1016/0921-4526(93)90108-I.
(124) Pichon, B. P.; Demortière, A.; Pauly, M.; Mougin, K.; Derory, A.; Bégin-Colin, S. 2D Assembling of Magnetic Iron Oxide Nanoparticles Promoted by SAMs Used as Well-Addressed Surfaces. *J. Phys. Chem. C* **2010**, *114* (19), 9041–9048. https://doi.org/10.1021/jp101872u.
(125) *WebCrossSections*. https://vuo.elettra.eu/services/elements/WebElements.html (accessed 2022-06-01).

(126) Velasco-Velez, J. J.; Pfeifer, V.; Hävecker, M.; Weatherup, R. S.; Arrigo, R.; Chuang, C.; Stotz, E.; Weinberg, G.; Salmeron, M.; Schlögl, R.; Knop-Gericke, A. Photoelectron Spectroscopy at the Graphene–Liquid Interface Reveals the Electronic Structure of an Electrodeposited Cobalt/Graphene Electrocatalyst. *Angew. Chem. Int. Ed.* **2015**, *54* (48), 14554–14558. https://doi.org/10.1002/anie.201506044.

(127) Mom, R.; Frevel, L.; Velasco-Vélez, J.-J.; Plodinec, M.; Knop-Gericke, A.; Schlögl, R. The Oxidation of Platinum under Wet Conditions Observed by Electrochemical X-Ray Photoelectron Spectroscopy. *J. Am. Chem. Soc.* **2019**, *141* (16), 6537–6544. https://doi.org/10.1021/jacs.8b12284.

(128) Frevel, L. J.; Mom, R.; Velasco-Vélez, J.-J.; Plodinec, M.; Knop-Gericke, A.; Schlögl, R.; Jones, T. E. In Situ X-Ray Spectroscopy of the Electrochemical Development of Iridium Nanoparticles in Confined Electrolyte. *J. Phys. Chem. C* **2019**, *123* (14), 9146–9152. https://doi.org/10.1021/acs.jpcc.9b00731.

(129) Holdcroft, S.; Fan, J. Sterically-Encumbered Ionenes as Hydroxide Ion-Conducting Polymer Membranes. *Current Opinion in Electrochemistry* **2019**, *18*, 99–105. https://doi.org/10.1016/j.coelec.2019.10.014.

(130) Thomas, O. D.; Soo, K. J. W. Y.; Peckham, T. J.; Kulkarni, M. P.; Holdcroft, S. Anion Conducting Poly(Dialkyl Benzimidazolium) Salts. *Polym. Chem.* **2011**, *2* (8), 1641–1643. https://doi.org/10.1039/C1PY00142F.

(131) Miles, P. A.; Westphal, W. B.; Von Hippel, A. Dielectric Spectroscopy of Ferromagnetic Semiconductors. *Rev. Mod. Phys.* **1957**, *29* (3), 279–307. https://doi.org/10.1103/RevModPhys.29.279.

(132) Pauly, M.; Dayen, J.-F.; Golubev, D.; Beaufrand, J.-B.; Pichon, B. P.; Doudin, B.; Bégin-Colin, S. Co-Tunneling Enhancement of the Electrical Response of Nanoparticle Networks. *Small* **2012**, *8* (1), 108–115. https://doi.org/10.1002/smll.201100931.

(133) Rydzek, G.; Toulemon, D.; Garofalo, A.; Leuvrey, C.; Dayen, J.-F.; Felder-Flesch, D.; Schaaf, P.; Jierry, L.; Begin-Colin, S.; Pichon, B. P.; Boulmedais, F. Selective Nanotrench Filling by One-Pot Electroclick Self-Constructed Nanoparticle Films. *Small* **2015**, *11* (36), 4638–4642. https://doi.org/10.1002/smll.201500639.

(134) Abrahamson, H. B.; Lukaski, H. C. Synthesis and Characterization of Iron Stearate Compounds. *Journal of Inorganic Biochemistry* **1994**, *54* (2), 115–130. https://doi.org/10.1016/0162-0134(94)80025-1.

(135) Perton, F.; Cotin, G.; Kiefer, C.; Strub, J.-M.; Cianferani, S.; Greneche, J.-M.; Parizel, N.; Heinrich, B.; Pichon, B.; Mertz, D.; Begin-Colin, S. Iron Stearate Structures: An Original Tool for Nanoparticles Design. *Inorg. Chem.* **2021**, *60* (16), 12445–12456. https://doi.org/10.1021/acs.inorgchem.1c01689.

(136) Ren, Y.; Iimura, K.; Kato, T. Structure of Barium Stearate Films at the Air/Water Interface Investigated by Polarization Modulation Infrared Spectroscopy and Π−A Isotherms. *Langmuir* **2001**, *17* (9), 2688–2693. https://doi.org/10.1021/la000872e.

(137) Nakamoto, K. Part B: Applications in Coordination, Organometallic, and Bioinorganic Chemistry. 30.

(138) Ding, X.; Bao, L.; Jiang, J.; Gu, H. Colloidal Synthesis of Ultrathin γ-Fe2O3 Nanoplates. *RSC Adv.* **2014**, *4* (18), 9314–9320. https://doi.org/10.1039/C3RA46728G.

(139) Bronstein, L. M.; Huang, X.; Retrum, J.; Schmucker, A.; Pink, M.; Stein, B. D.; Dragnea, B. Influence of Iron Oleate Complex Structure on Iron Oxide Nanoparticle Formation. *Chem. Mater.* **2007**, *19* (15), 3624–3632. https://doi.org/10.1021/cm062948j.

(140) Sartori, K.; Cotin, G.; Bouillet, C.; Halté, V.; Bégin-Colin, S.; Choueikani, F.; Pichon, B. P. Strong Interfacial Coupling through Exchange Interactions in Soft/Hard Core–Shell Nanoparticles as a Function of Cationic Distribution. *Nanoscale* **2019**, *11* (27), 12946–12958. https://doi.org/10.1039/C9NR02323B.

(141) Sartori, K.; Gailly, D.; Bouillet, C.; Grenèche, J.-M.; Dueñas-Ramirez, P.; Begin-Colin, S.; Choueikani, F.; Pichon, B. P. Increasing the Size of Fe3-ΔO4 Nanoparticles by Performing a

Multistep Seed-Mediated Growth Approach. *Crystal Growth & Design* **2020**, *20* (3), 1572–1582. https://doi.org/10.1021/acs.cgd.9b01300.
(142) Zhang, L.; He, R.; Gu, H.-C. Oleic Acid Coating on the Monodisperse Magnetite Nanoparticles. *Applied Surface Science* **2006**, *253* (5), 2611–2617. https://doi.org/10.1016/j.apsusc.2006.05.023.
(143) Daou, T. J.; Grenèche, J. M.; Pourroy, G.; Buathong, S.; Derory, A.; Ulhaq-Bouillet, C.; Donnio, B.; Guillon, D.; Begin-Colin, S. Coupling Agent Effect on Magnetic Properties of Functionalized Magnetite-Based Nanoparticles. *Chem. Mater.* **2008**, *20* (18), 5869–5875. https://doi.org/10.1021/cm801405n.
(144) *12.4: Defects in Crystals*. Chemistry LibreTexts. https://chem.libretexts.org/Bookshelves/General_Chemistry/Book%3A_General_Chemistry%3A_Principles_Patterns_and_Applications_(Averill)/12%3A_Solids/12.04%3A_Defects_in_Crystals (accessed 2022-06-26).
(145) Carlson, T. A.; McGuire, G. E. Study of the X-Ray Photoelectron Spectrum of Tungsten—Tungsten Oxide as a Function of Thickness of the Surface Oxide Layer. *Journal of Electron Spectroscopy and Related Phenomena* **1972**, *1* (2), 161–168. https://doi.org/10.1016/0368-2048(72)80029-X.
(146) Strohmeier, B. R. An ESCA Method for Determining the Oxide Thickness on Aluminum Alloys. *Surface and Interface Analysis* **1990**, *15* (1), 51–56. https://doi.org/10.1002/sia.740150109.
(147) Wang, W.; Luo, J.; Chen, S. Carbon Oxidation Reactions Could Misguide the Evaluation of Carbon Black-Based Oxygen-Evolution Electrocatalysts. *Chem. Commun.* **2017**, *53* (84), 11556–11559. https://doi.org/10.1039/C7CC04611A.
(148) Skomurski, F. N.; Kerisit, S.; Rosso, K. M. Structure, Charge Distribution, and Electron Hopping Dynamics in Magnetite (Fe3O4) (100) Surfaces from First Principles. *Geochimica et Cosmochimica Acta* **2010**, *74* (15), 4234–4248. https://doi.org/10.1016/j.gca.2010.04.063.
(149) Chung, D. Y.; Park, S.; Lopes, P. P.; Stamenkovic, V. R.; Sung, Y.-E.; Markovic, N. M.; Strmcnik, D. Electrokinetic Analysis of Poorly Conductive Electrocatalytic Materials. *ACS Catal.* **2020**, *10* (9), 4990–4996. https://doi.org/10.1021/acscatal.0c00960.
(150) Papaderakis, A.; Tsiplakides, D.; Balomenou, S.; Sotiropoulos, S. Electrochemical Impedance Studies of IrO2 Catalysts for Oxygen Evolution. *Journal of Electroanalytical Chemistry* **2015**, *757*, 216–224. https://doi.org/10.1016/j.jelechem.2015.09.033.
(151) Tröltzsch, U.; Kanoun, O. Generalization of Transmission Line Models for Deriving the Impedance of Diffusion and Porous Media. *Electrochimica Acta* **2012**, *75*, 347–356. https://doi.org/10.1016/j.electacta.2012.05.014.
(152) Cooper, S. J.; Bertei, A.; Finegan, D. P.; Brandon, N. P. Simulated Impedance of Diffusion in Porous Media. *Electrochimica Acta* **2017**, *251*, 681–689. https://doi.org/10.1016/j.electacta.2017.07.152.
(153) Heim, C.; Wagner, N.; Friedrich, K. A. Analytical Distribution Function of Relaxation Times for Porous Electrodes and Analysis of the Distributions of Time Constants. *Solid State Ionics* **2022**, *383*, 115960. https://doi.org/10.1016/j.ssi.2022.115960.
(154) Masoliver, J.; Weiss, G. H. Telegrapher's Equations with Variable Propagation Speeds. *Phys. Rev. E* **1994**, *49* (5), 3852–3854. https://doi.org/10.1103/PhysRevE.49.3852.
(155) Jamesh, M.-I.; Sun, X. Recent Progress on Earth Abundant Electrocatalysts for Oxygen Evolution Reaction (OER) in Alkaline Medium to Achieve Efficient Water Splitting – A Review. *Journal of Power Sources* **2018**, *400*, 31–68. https://doi.org/10.1016/j.jpowsour.2018.07.125.
(156) Suen, N.-T.; Hung, S.-F.; Quan, Q.; Zhang, N.; Xu, Y.-J.; Chen, H. M. Electrocatalysis for the Oxygen Evolution Reaction: Recent Development and Future Perspectives. *Chem. Soc. Rev.* **2017**, *46* (2), 337–365. https://doi.org/10.1039/C6CS00328A.
(157) Duan, Y.; Sun, S.; Sun, Y.; Xi, S.; Chi, X.; Zhang, Q.; Ren, X.; Wang, J.; Ong, S. J. H.; Du, Y.; Gu, L.; Grimaud, A.; Xu, Z. J. Mastering Surface Reconstruction of Metastable Spinel Oxides for Better Water Oxidation. *Advanced Materials* **2019**, *31* (12), 1807898. https://doi.org/10.1002/adma.201807898.

(158) Wang, L.; Saveleva, V. A.; Eslamibidgoli, M. J.; Antipin, D.; Bouillet, C.; Biswas, I.; Gago, A. S.; Hosseiny, S. S.; Gazdzicki, P.; Eikerling, M. H.; Savinova, E. R.; Friedrich, K. A. Deciphering the Exceptional Performance of NiFe Hydroxide for the Oxygen Evolution Reaction in an Anion Exchange Membrane Electrolyzer. **2022**, 10.

(159) Xiao, H.; Shin, H.; Goddard, W. A. Synergy between Fe and Ni in the Optimal Performance of (Ni,Fe)OOH Catalysts for the Oxygen Evolution Reaction. *Proceedings of the National Academy of Sciences* **2018**, *115* (23), 5872–5877. https://doi.org/10.1073/pnas.1722034115.

(160) Peng, Y.; Hajiyani, H.; Pentcheva, R. Influence of Fe and Ni Doping on the OER Performance at the Co3O4(001) Surface: Insights from DFT+U Calculations. *ACS Catal*. **2021**, 11 (9), 5601–5613. https://doi.org/10.1021/acscatal.1c00214 .

(161) Hajiyani, H.; Pentcheva, R. Surface Termination and Composition Control of Activity of the CoxNi1– XFe2O4(001) Surface for Water Oxidation: Insights from DFT+U Calculations. *ACS Catal*. **2018**, 8 (12), 11773–11782. https://doi.org/10.1021/acscatal.8b00574

(162) Falling, L. J.; Mom, R. V.; Sandoval Diaz, L. E.; Nakhaie, S.; Stotz, E.; Ivanov, D.; Hävecker, M.; Lunkenbein, T.; Knop-Gericke, A.; Schlögl, R.; Velasco-Vélez, J.-J. Graphene-Capped Liquid Thin Films for Electrochemical Operando X-Ray Spectroscopy and Scanning Electron Microscopy. *ACS Appl. Mater. Interfaces* **2020**, *12* (33), 37680–37692. https://doi.org/10.1021/acsami.0c08379.

(162) Sassi, M.; Pearce, C. I.; Bagus, P. S.; Arenholz, E.; Rosso, K. M. First-Principles Fe L2,3-Edge and O K-Edge XANES and XMCD Spectra for Iron Oxides. *J. Phys. Chem. A* **2017**, *121* (40), 7613–7618. https://doi.org/10.1021/acs.jpca.7b08392.

(163) Regan, T. J.; Ohldag, H.; Stamm, C.; Nolting, F.; Lüning, J.; Stöhr, J.; White, R. L. Chemical Effects at Metal/Oxide Interfaces Studied by x-Ray-Absorption Spectroscopy. *Phys. Rev. B* **2001**, *64* (21), 214422. https://doi.org/10.1103/PhysRevB.64.214422.

(164) Accogli, A.; Bertoli, L.; Panzeri, G.; Gibertini, E.; Pesce, R.; Bussetti, G.; Magagnin, L. Electrochemical Characterization of Magnetite (Fe3O4) Nanoaggregates in Acidic and Alkaline Solutions. *ACS Omega* **2021**, *6* (41), 26880–26887. https://doi.org/10.1021/acsomega.1c03142.

(164) Papaefthimiou, V.; Dintzer, T.; Dupuis, V.; Tamion, A.; Tournus, F.; Hillion, A.; Teschner, D.; Hävecker, M.; Knop-Gericke, A.; Schlögl, R.; Zafeiratos, S. Nontrivial Redox Behavior of Nanosized Cobalt: New Insights from Ambient Pressure X-Ray Photoelectron and Absorption Spectroscopies. *ACS Nano* **2011**, *5* (3), 2182–2190. https://doi.org/10.1021/nn103392x.

(165) Zhou, S.; Potzger, K.; Xu, Q.; Kuepper, K.; Talut, G.; Markó, D.; Mücklich, A.; Helm, M.; Fassbender, J.; Arenholz, E.; Schmidt, H. Spinel Ferrite Nanocrystals Embedded inside ZnO: Magnetic, Electronic, and Magnetotransport Properties. *Phys. Rev. B* **2009**, *80* (9), 094409. https://doi.org/10.1103/PhysRevB.80.094409.

(166) Jolivet, J.-P.; Tronc, E.; Chanéac, C. Iron Oxides: From Molecular Clusters to Solid. A Nice Example of Chemical Versatility. *Comptes Rendus Geoscience* **2006**, *338* (6), 488–497. https://doi.org/10.1016/j.crte.2006.04.014.

(167) Ikeno, H.; Tanaka, I.; Miyamae, T.; Mishima, T.; Adachi, H.; Ogasawara, K. First Principles Calculation of Fe *L*_{2,3}-Edge X-Ray Absorption Near Edge Structures of Iron Oxides. *Materials Transactions* **2004**, *45* (5), 1414–1418. https://doi.org/10.2320/matertrans.45.1414.

(168) Abbate, M.; de Groot, F. M. F.; Fuggle, J. C.; Fujimori, A.; Strebel, O.; Lopez, F.; Domke, M.; Kaindl, G.; Sawatzky, G. A.; Takano, M.; Takeda, Y.; Eisaki, H.; Uchida, S. Controlled-Valence Properties of La 1 − x Sr x FeO 3 and La 1 − x Sr x MnO 3 Studied by Soft-x-Ray Absorption Spectroscopy. *Phys. Rev. B* **1992**, *46* (8), 4511–4519. https://doi.org/10.1103/PhysRevB.46.4511.

(169) Müllner, M.; Riva, M.; Kraushofer, F.; Schmid, M.; Parkinson, G. S.; Mertens, S. F. L.; Diebold, U. Stability and Catalytic Performance of Reconstructed Fe3O4(001) and Fe3O4(110) Surfaces during Oxygen Evolution Reaction. *J. Phys. Chem. C* **2019**, *123* (13), 8304–8311. https://doi.org/10.1021/acs.jpcc.8b08733.

Résumé de la thèse en français

1) Introduction

L'électrolyse de l'eau est une technique prometteuse pour le stockage des énergies renouvelables. Cette technique consiste en la décomposition de la molécule d'eau en dioxygène et dihydrogène, la molécule d'intérêt étant celle d'hydrogène qui permet de stocker l'énergie électrique sous forme d'énergie chimique. Le stockage d'énergie sous forme d'hydrogène est en effet particulièrement intéressant car il dispose d'une densité énergétique supérieure à trois fois celle du pétrole (45.8 kJ/g)[1,2]. Le dispositif d'électrolyse de l'eau consiste en une cellule électrochimique composée d'électrodes séparées par un électrolyte alcalin et une membrane échangeuse d'ions afin de séparer les gaz formés, cette réaction peut se produire aussi bien en milieu acide qu'en milieu basique. Deux réactions ont lieu à l'interface entre l'électrolyte et les électrodes : à la cathode la réaction de dégagement de l'hydrogène (HER) et à l'anode la réaction de dégagement de l'oxygène (OER).

Plusieurs verrous doivent cependant être levés pour permettre à cette technique d'être développée à l'échelle industrielle. Notamment le rendement énergétique de la réaction l'OER qui n'est pas spontanée et requière une surtension élevée : 1.23V *vs.* RHE minimum. Cependant à cause de la cinétique lente de l'OER, les surtensions à appliquer sont généralement bien plus importantes. De nombreux catalyseurs sont à l'étude afin de diminuer le plus possible cette surtension. Le catalyseur anodique en milieu acide le plus efficace jusqu'à présent est un métal rare et cher : l'iridium. Ce matériau a beaucoup été utilisé du fait de la stabilité des membranes échangeuses d'ions limitées au milieu acide[3–5] mais grâce à de récents progrès, des membranes échangeuses d'anions[6,7] permettent dès à présent de réaliser l'électrolyse de l'eau en milieu basique. Cette avancée technologique ouvre ainsi des perspectives intéressantes pour remplacer l'iridium par des oxydes métalliques à base de métaux de transition comme les oxydes de fer, de nickel ou de cobalt qui sont plus abondants sur terre et par conséquent moins chers. Cependant, les valeurs d'activité relevées dans la littérature pour ces types de matériaux sont assez contradictoires selon les matériaux utilisés, la charge de catalyseur présente sur l'électrode ou encore le pH/concentration/nature de l'électrolyte utilisé[8].

De plus, les mécanismes réactionnels ayant lieu à la surface des électrodes sont également mal connus. Même si des études *in situ* et *operando* de ces matériaux ont été réalisées[9–11], la nature des sites actifs et des intermédiaires réactionnels n'est donc pas encore bien comprise. Cela empêche donc leur développement pour l'électrolyse en milieu basique. Il est donc nécessaire de développer un catalyseur pour l'OER qui puisse servir de système modèle afin de mieux comprendre ces phénomènes. Ce catalyseur doit donc remplir plusieurs critères : (i) il doit être stable chimiquement dans les conditions opératoires (pH, température, électrolyte, potentiel), (ii) conducteur pour permettre le transfert des charges, (iii) avoir une structure électronique adaptée pour catalyser la réaction à une tension la plus basse possible, (iv) présenter une grande surface spécifique pour permettre un bon rendement de la réaction et limiter les problèmes de transfert de masse.

Les oxydes métalliques présentant une structure de type spinelle sont prometteurs car ils peuvent être synthétisés à une température relativement basse, de plus leurs compositions chimiques et leurs propriétés peuvent être facilement modifiées. Cependant, de nombreux oxydes de métaux de transition ont une faible conductivité électrique, ce qui complique leur utilisation en électrocatalyse. Par exemple, alors que le spinelle de cobalt Co_3O_4 est connu pour être actif pour l'OER, sa basse conductivité électrique requiert l'addition de carbone[12]. Ce qui réduit donc la possibilité qu'il soit utilisé à grande échelle dans l'industrie car le carbone s'oxyde dans les conditions de l'OER. Inversement, Fe_3O_4 a une plus grande conductivité électrique mais est

moins actif pour l'OER. La combinaison des propriétés de ces deux composés permettrait donc de créer un catalyseur efficace pour l'OER et constituerait une alternative à l'usage d'iridium.

L'objectif des travaux de thèses décrits dans ce mémoire est donc de proposer une alternative efficace à l'usage d'iridium en tant que constituant de l'anode des électrolyseurs. L'approche utilisée consiste à concevoir des nanoparticules (NPs) présentant une structure cœur-coquille selon Fe_3O_4@$CoFe_2O_4$ pour combiner la conductivité du cœur de magnétite (Fe_3O_4) avec l'activité catalytique de la ferrite de cobalt ($CoFe_2O_4$). Ces nanoparticules ont été synthétisées via la décomposition thermique de précurseurs métalliques dans des solvants aux alentours de 300 °C[13]. Cette technique a l'avantage de générer des nanoparticules présentant une distribution de tailles étroite et donc de s'affranchir des effets de tailles influençant les propriétés électrochimiques. De plus, cette approche permet de limiter l'usage de cobalt seulement dans la coquille pour ainsi réduire les risques de rupture d'approvisionnement. De plus, il a été montré dans la littérature que la présence de fer dans un catalyseur pouvait aider à augmenter l'activité pour l'OER[14]. Les raisons de cette amélioration ne sont pas encore très bien comprises mais la présence de fer dans le cœur pourrait donc être un avantage pour le catalyseur.

Des NPs présentant des tailles de cœur et des épaisseurs de coquilles différentes ont été synthétisées. La manière de faire croitre la coquille (par diffusion ou par croissance cristalline) a également été étudiée. La structure chimique de ces NPs a été étudiée de façon approfondie en mobilisant une large gamme de techniques présente dans les laboratoires (Microscopie à balayage électronique, microscopie à transmission électronique, diffraction des rayons X, spectroscopie infra-rouge, granulométrie, analyse thermo gravimétrique). Les résultats obtenus nous ont permis d'étudier l'influence de la structure cœur-coquille des NPs sur leurs propriétés électrochimiques. Nous avons pu ainsi confirmer le potentiel de ces nanoparticules cœur-coquille comme catalyseur efficace pour réaliser la réaction d'OER. Par la suite, des études *operando* ont été menées à l'aide de la technique NEXAFS (Near edge absorption fine structure) dans le but de mieux comprendre les mécanismes réactionnels se produisant à l'interface des nanoparticules et de l'électrolyte durant l'OER.

2) Résultats et discussion

a) Synthèse et caractérisation

Quatre types de nanoparticules (NPs) ont été synthétisées suite à la décomposition thermique de précurseurs métalliques (stéarates de fer et de cobalt). L'approche consiste en la formation d'une première nanoparticule d'oxyde de fer à la surface de laquelle est formée une coquille de ferrite de cobalt via le principe de nucléation-croissance (Figure 1) [13,15,16].

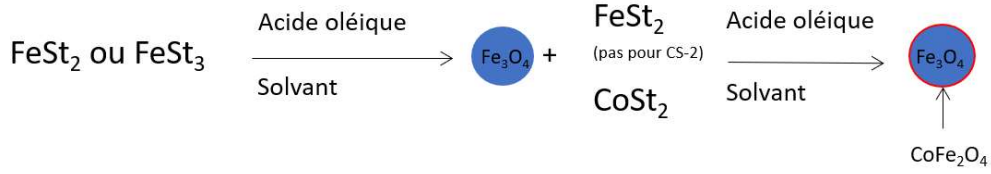

Figure 1: protocole opératoire pour la synthèse des NPs cœur-coquille étudiées dans ce manuscrit $FeSt_2$: stéarate de fer, $CoSt_2$ stéarate de cobalt.

Des NPs cœur-coquille (CS-1, CS-2, CS-3 et CS-4) cristallines présentant une forme quasi-sphérique et une taille homogène ont été obtenues et caractérisées à l'aide d'un microscope à transmission électronique (MET) (Figure 2 A, B, D, E, G, H, J, K). La taille de la coquille et du cœur de ces NPs ont été modifiées afin de pouvoir étudier l'influence de ces deux paramètres sur l'activité. Une analyse de la suspension des NPs par granulométrie a permis de montrer que les NPs n'étaient pas agglomérées et stables en suspension. En parallèle, des analyses de diffraction des rayons X (DRX), et de MET haute résolution ont également montré que ces NPs étaient cristallines et présentaient uns structure spinelle. Cependant il n'était pas possible de différencier le cœur de la coquille par ces techniques de caractérisations car les paramètres de maille de Fe_3O_4 et $CoFe_2O_4$ sont très proches.

La formation de la coquille a pu être démontrée sur un grand nombre de particules grâce à une étude par la spectroscopie de photoélectrons X (X-ray photoelectron spectroscopy, XPS) dans laquelle des photons de différentes énergies incidentes permettaient de sonder l'échantillon en profondeur (Figure 2 C). Cette étude a permis de prouver la présence d'une coquille dont l'épaisseur est de l'ordre de 1-2 nm mais aussi de quantifier la proportion de fer et de cobalt dans la coquille. Il semblerait que la surface de la coquille soit plus riche en cobalt que prévu : à la surface des NPs nous trouvons un ratio atomique Fe:Co de 50/50. Cela tend donc à montrer qu'il y a un gradient de concentration de cobalt dans la coquille. L'existence de la coquille a également été prouvée par des images de spectroscopie de perte d'énergie des électrons (EELS) qui montrent clairement que le cobalt est localisé sur les bords des NPs (Figure 2 F, I, L). Les profils de concentrations de ces NPs sont en accord avec les observations faites en XPS par rapport à la composition de la coquille : la surface de la coquille semble être plus riche en cobalt. Ce gradient de concentration en cobalt est dû à la différence de température à laquelle les précurseurs (stéarate de cobalt et stéarate de fer) se décomposent. En effet en général le stéarate de cobalt présente une température de décomposition plus élevée que le stéarate de fer. Ces résultats ont également été observés dans la littérature pour des NPs similaires[17].

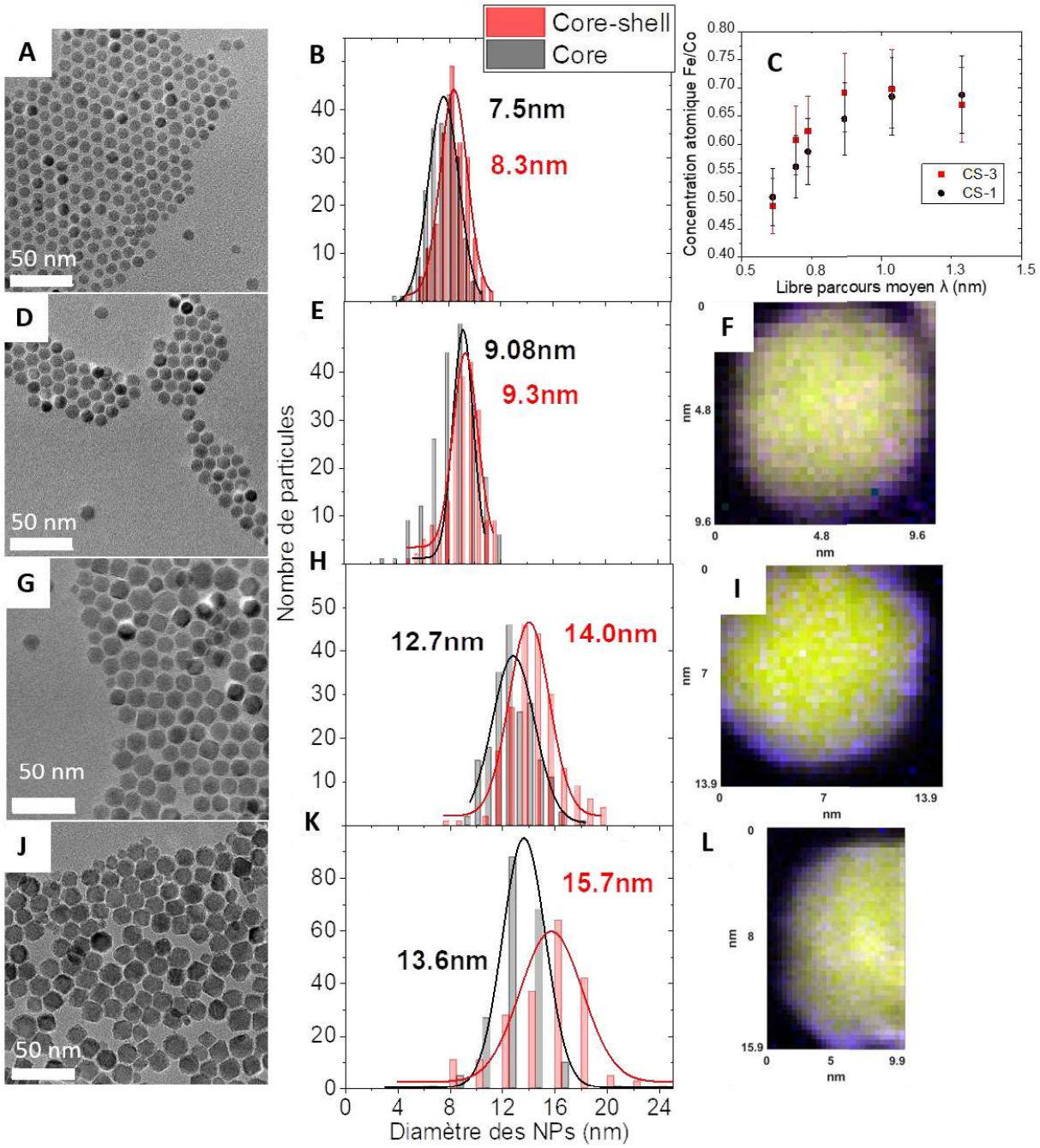

Figure 2 : A, D, G, J) Image MET des NPs CS-1, CS-2, CS-3 et CS-4 respectivement. B, E, H, K) Répartitions de tailles de ces NPs. C) Etude de la répartition de Fe:Co en profondeur dans les NPs CS-1 et CS-3. F, I, L) Images EELS de la répartition des atomes dans les NPs CS-2, CS-3 et CS-4 respectivement. Le cobalt est en bleu, le fer en vert et l'oxygène en rouge.

b) Études électrochimiques

Dans le but d'évaluer l'activité catalytique de ces NPs, différentes quantités ont été déposées sur l'électrode pour obtenir des couches catalytiques de différentes épaisseurs allant d'une charge de 0.6 µg.cm^{-2} (environ une monocouche des NPs) à une charge de 100 µg.cm^{-2} (plusieurs monocouches les unes sur les autres). L'activité massique à différents potentiels a été déterminée en divisant le courant obtenu à ce potentiel par la masse de catalyseur déposé sur l'électrode (Figure 3).

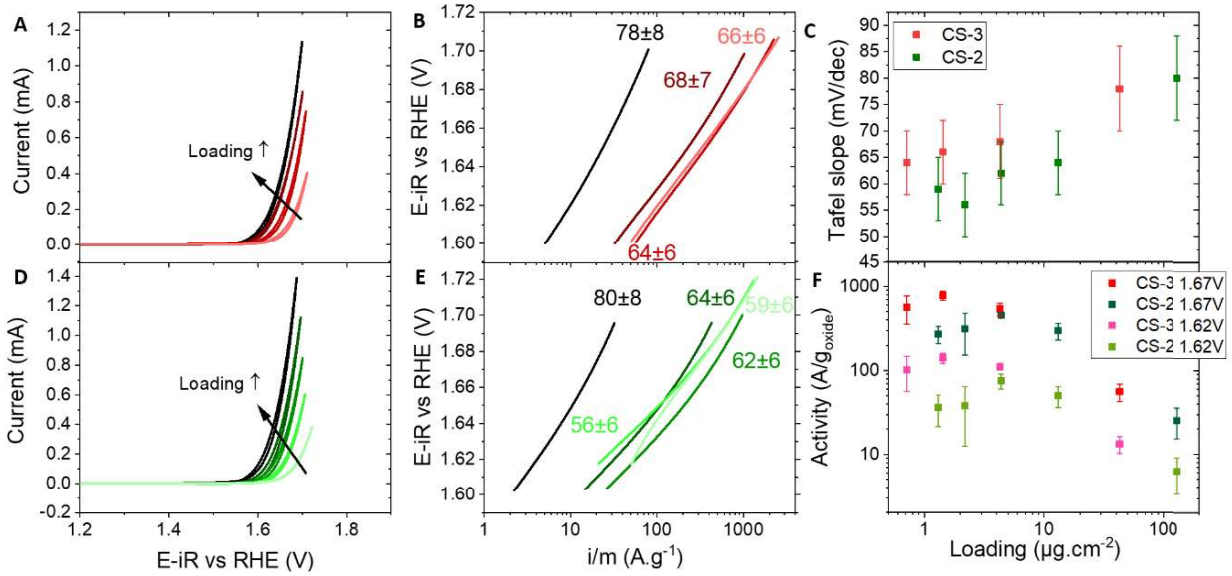

Figure 3: A) courbes de voltampérométrie cyclique obtenues pour différentes charges de NPs CS-3 and B) les pentes de Tafel tirées de ces courbes (en mV/décade). C) Pentes de Tafel pour les NPs CS-2 et CS-3 à différentes charges. D) courbes de voltampérométrie cyclique obtenues pour différentes charges de NPs CS-2 and E) les pentes de Tafel tirées de ces courbes (en mV/décade). F) Activités massiques apparentes par gramme d'oxyde mesurées à 1.62 et 1.67 V vs RHE pour les NPs CS-2 et CS-3.

Cette figure met en évidence que l'activité massique apparente varie en fonction de la masse déposée et que pour une masse déposée faible on a une activité massique plus importante. Il faut cependant noter que si toutes les NPs sont accessibles et participent à la réaction, cette activité massique devrait être constante. De plus, les pentes de Tafel semblent dévier de la linéarité pour devenir convexes et que la valeur de la pente de Tafel augmente lorsque l'épaisseur de la couche catalytique augmente. Ces résultats semblent donc signifier que toutes les NPs ne sont pas soumises au potentiel ou actives pour l'OER lorsque la couche catalytique est trop épaisse.

Ce phénomène a pu être étudié à l'aide de la technique de spectroscopie d'impédance dont les résultats sont présentés en Figure 4. Des courbes Nyquist sont alors obtenues et il peut être observé que pour d'importantes charges, une asymétrie du demi-cercle est présente aux hautes fréquences. Ce phénomène peut être expliqué par une résistance ionique et/ou électronique présente entre les NPs. Des modélisations ont été réalisées en assimilant la cellule electrochimique à un circuit électrique constitué de résistances et de capacités à l'aide de deux modèles différents :

- Le modèle de Randles (bien adapté pour des matériaux conducteurs ou pour des couches catalytiques fines)

- Le modèle lignes de transmissions[18] (valable pour des couches catalytiques plus épaisses) dans lequel les différentes sous-couches de la couche catalytique sont considérées et où un paramètre de résistance R_1 (ionique ou électronique) est considéré entre les NPs.

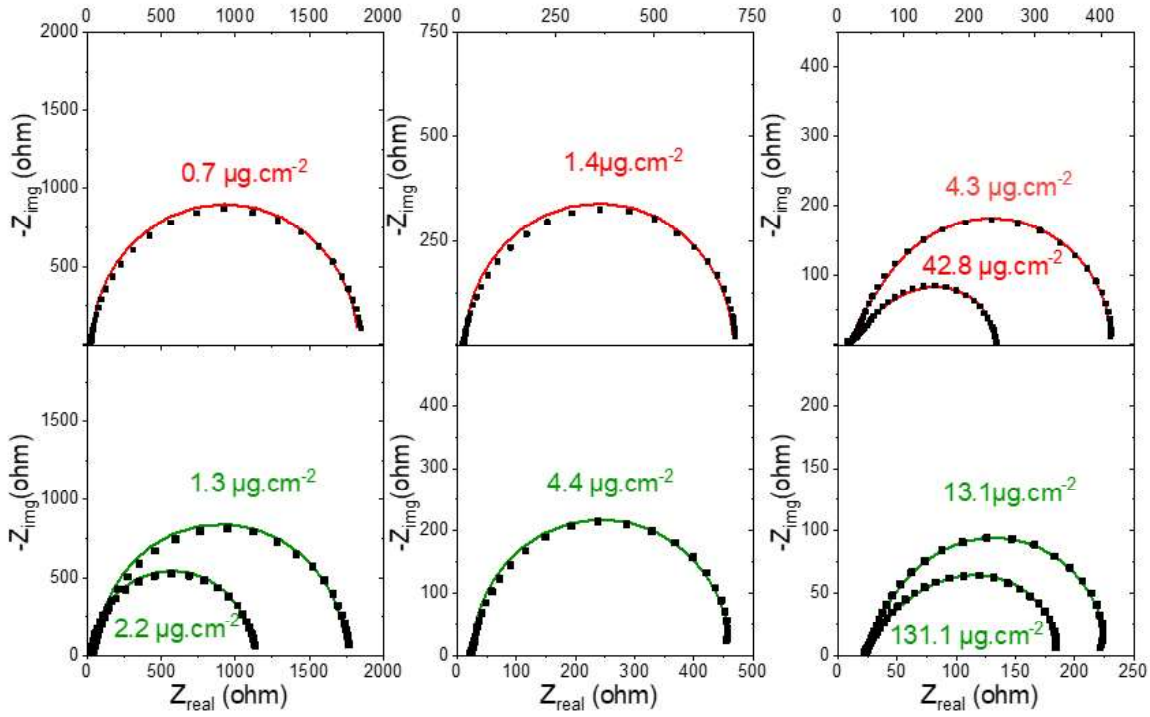

Figure 4: Modèles de Randles et de ligne de transmission pour modéliser les courbes d'impédance Nyquist expérimentales (carrés noirs) pour les NPs CS-2 (vert) et CS-3 (rouge).

Grâce à ces simulations, il a été possible de déterminer la valeur de la résistance au transfert de charge (qui diminue avec la charge de NPs), la capacité (qui augmente avec la charge de NPs) ainsi que la résistance ionique et électronique (qui augmente avec la charge pour de hautes charges seulement). Il a également été possible de simuler les courbes de voltammétrie à balayage linéaire et leurs pentes de Tafel correspondantes (Figure 5) pour différentes valeurs de résistance.

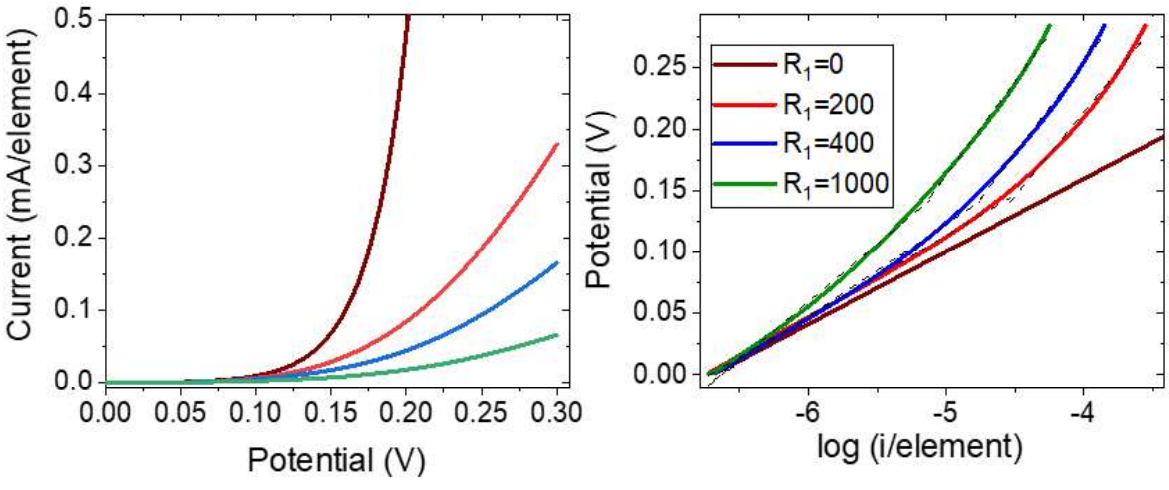

Figure 5: simulation des CVs et des pentes de Tafel pour une résistance R_1 variable

Ces simulations mettent en valeur l'influence importante de la résistance ionique et électronique sur l'activité apparente et les pentes de Tafel, elles sont cohérentes avec ce qui a été observé expérimentalement (diminution de l'activité massique avec la résistance qui augmente et déformation de la linéarité des pentes de Tafel).

L'étude d'impédance ayant permis de mieux comprendre les phénomènes de transport de masse et de transport de charge sur l'électrode, l'activité massique a pu être déterminée pour une charge suffisamment faible de manière à ce que l'activité massique ne soit plus dépendante de la masse de catalyseur déposée à la surface de l'électrode. Les résultats de voltampérométrie cyclique et les pentes Tafel des différents types de nanoparticules sont présentés en Figure 6. Cette figure met en évidence le fait que les NPs cœur-coquille sont bien plus actives que le cœur seul. En effet, la pente de Tafel correspondants aux nanoparticules d'oxyde de fer sans coquille est plus importante et la surtension qu'il faut appliquer pour initier de l'OER est beaucoup plus importante.

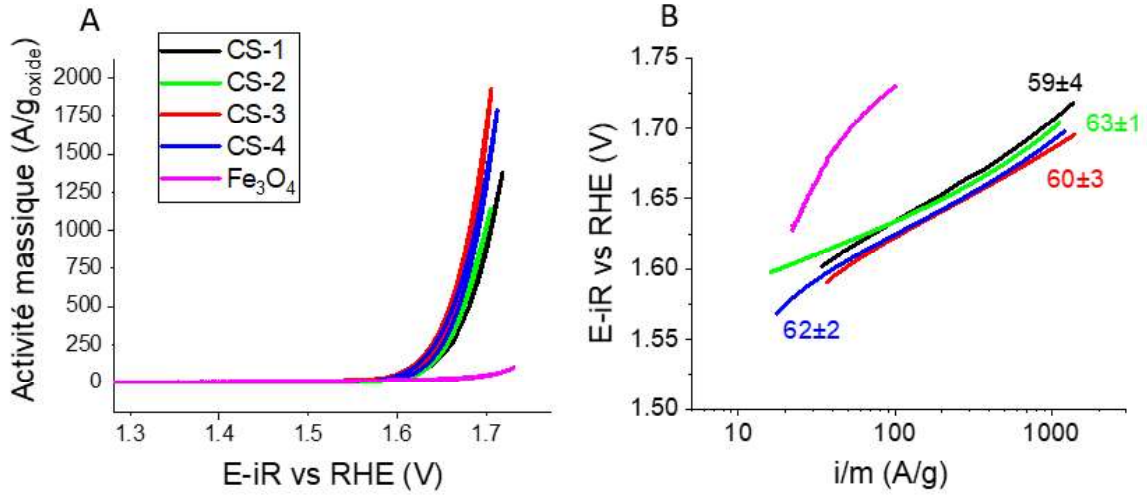

Figure 6: A) courbe de voltampérométrie cyclique obtenue pour les différents types de nanoparticules synthétisées. B) pentes de Tafel (en mV/décade) de ces mêmes NPs

Les activités massiques par gramme de cobalt, par unité de surface et par masse d'oxyde de ces NPs ont été mesurées à 1.65 V vs RHE (Figure 7) et comparées à ce qui a pu être obtenu dans la littérature pour des composés similaires. Les activités massiques par gramme d'oxyde obtenues pour les NPs (entre 160 et 410 A/g_{oxyde}) sont cohérentes avec ce qui a pu être observé dans la littérature pour des composés similaires. Cependant, comme il a été prouvé que seule la coquille est responsable de l'activité des NPs, il est alors possible de normaliser l'activité par la masse de cobalt (composé actif). Dans ce cas, les valeurs d'activité mesurées par gramme de cobalt sont beaucoup plus importantes que celles mesurées dans la littérature et les valeurs obtenues sont de l'ordre de 2000 A/g_{cobalt} à 1.65 V vs RHE, ce qui représente une activité électrocatalytique exceptionnelle. Les NPs cœur-coquille constituent donc un matériau prometteur pour l'OER. De plus, entre les NPs, les valeurs d'activité ne sont pas toujours similaires, les NPs présentant les plus grosses tailles (CS-3 et CS-4) semblent être de meilleures candidates. Ces résultats peuvent être expliqués par le fait que les NPs CS-3 et CS-4 ont un cœur conducteur plus grand que celui de CS-1 et CS-2, ce qui donne une meilleure conduction au catalyseur.

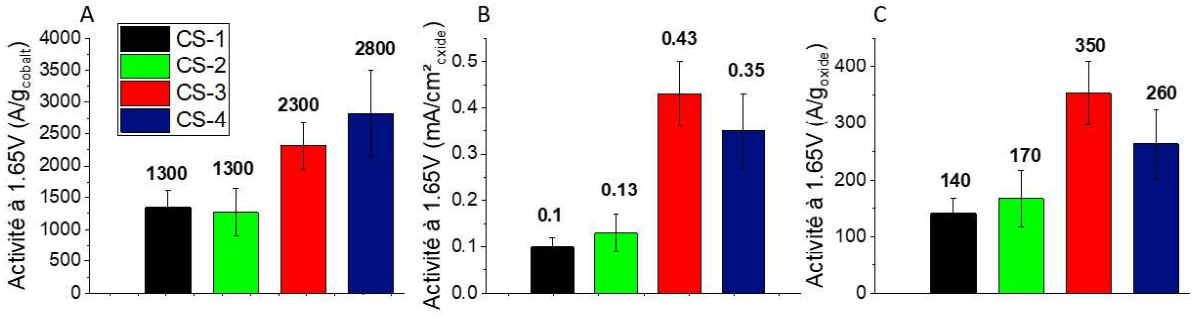

Figure 7: Activité massique des NPs à 1.65 V vs RHE. A gauche normalisée par la masse d'oxyde et à droite normalisée par la masse de cobalt contenue dans les nanoparticules.

L'impact de la concentration de l'électrolyte et de la quantité de ligands entourant les NPs a également été mesuré. Un pH plus important et une plus faible quantité de ligands (acide oléique) autour des NPs sont bénéfiques pour l'activité du catalyseur. Il faudrait le confirmer avec plus d'études mais il semblerait que les lavages à l'acétone chaud réalisés sur les NPs sont suffisant pour retirer la majorité des ligands et donc que la quantité d'acide oléique entourant les NPs n'a pas d'influence sur l'activité.

c) Études NEXAFS operando pendant l'OER

Les NPs CS-3 ayant montré d'excellents résultats d'activité ont été étudiées *operando* durant l'OER au synchrotron. Les NPs ont été analysées d'abord en électrochimie puis en NEXAFS.

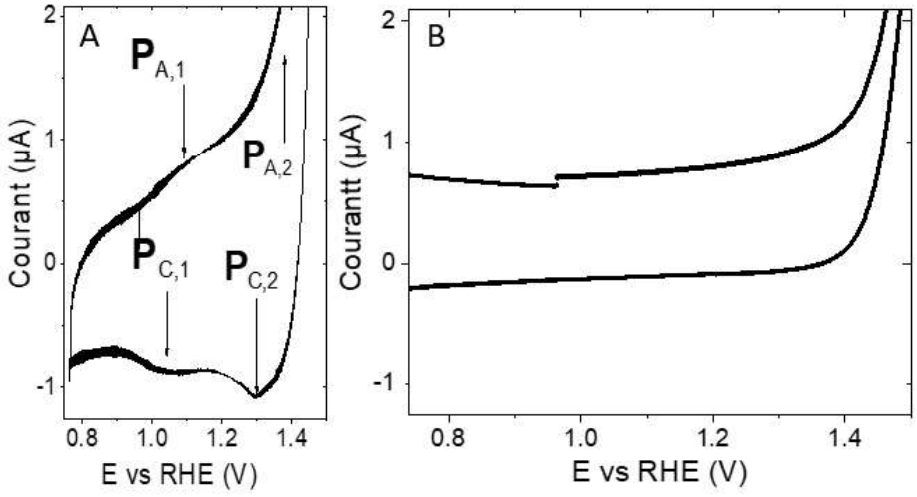

Figure 8: Courbes de voltampérométrie cyclique obtenue pour les NPs CS-3 (A) et Fe_3O_4 (B) sur une membrane polymère échangeuse d'anions fumatech dans un électrolyte NaOH 0.1M avec une vitesse de balayage de 20mV/s

Sur les courbes de voltampérométrie cyclique pour les NPs CS-3 (Figure 8A) on peut voir des pics redox qui ne sont pas observés sur les NPs de Fe_3O_4 (Figure 8B) et qui dans la littérature sont caractéristiques du cobalt[9]. Le cobalt change donc d'état d'oxydation durant l'OER. Afin d'étudier les changements se produisant dans les NPs cœur-coquille quand un potentiel est appliqué, différents potentiels fixes ont alors été appliqués et des spectres NEXAFS pour le seuil L du cobalt et du fer ont pu être mesurés. Ils sont présentés en Figure 9 sur laquelle on voit que le cobalt reste globalement dans un état d'oxydation Co (II) et qu'il y a une très petite transformation en Co (III)[10]. D'autre part, le Fe (II) est remplacé par du Fe (III) lors de l'oxydation[19,20].

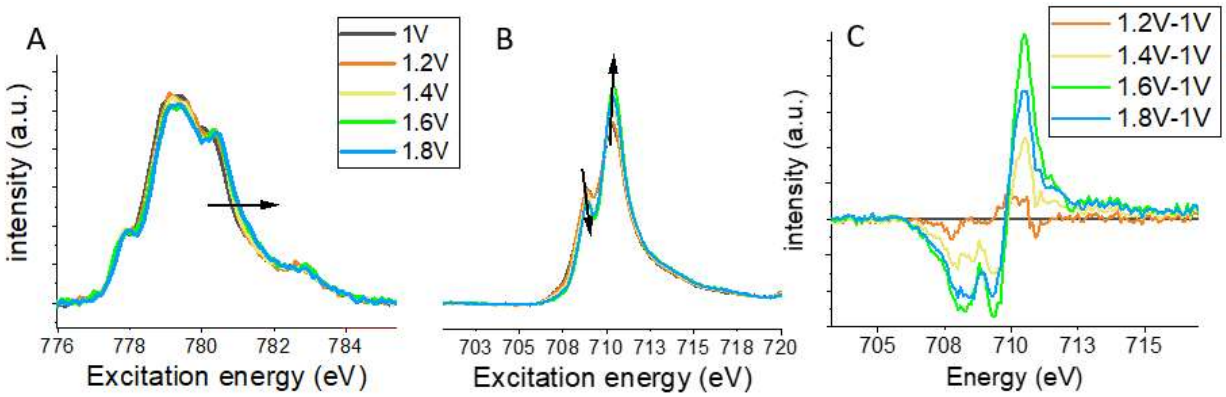

Figure 9: Seuil L du cobalt (A) et du fer (B) pour différents potentiels appliqués aux NPs CS-3. C) est le résultat de la soustraction de la courbe obtenue à 1 V à la courbe obtenue à un autre potentiel.

Ces résultats montrent qu'il y a un effet conjoint du fer et du cobalt qui agissent dans l'OER : au-dessus de 1 V, le cobalt passe de Co (II) à Co (III) mais il est alors directement réduit en Co (II) par le Fe (II) présent dans la NP qui s'oxyde lui en Fe (III) et migre vers la surface de la particule. Au-dessus de 1.4 V, le cobalt ou le fer peuvent passer d'un état d'oxydation (III) vers un état d'oxydation IV avant d'être réduits par l'OER. Ces échanges redox sont résumés en Figure 10.

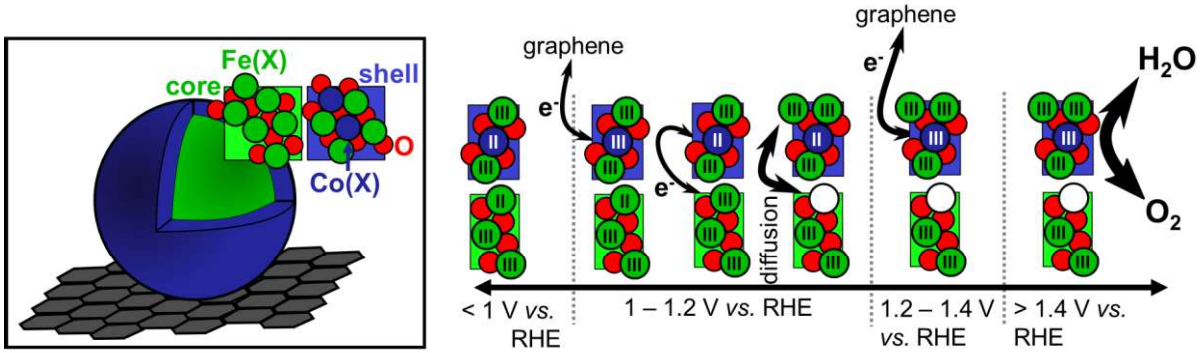

Figure 10: Schéma résumant les transformations se produisant dans les NPs lors de l'OER. Etape 1 – Pour E =1 V vs. RHE fe(II) et Fe(III) coexistent dans le cœur et la coquille est composée de Co(II) et Fe(III). Etape 2 : entre 1.0 et 1.2V vs. RHE, un électron est transféré de Co (II) dans la coquille au collecteur de courant (graphène). Cependant Co (III) n'est pas observé en NEXAFS car il est directement réduit en Co (II) grâce à un transfert d'électron depuis le Fe (II) dans le cœur (dans la partie du cœur proche de la coquille) résultant en la formation de Fe (III). Ce cation de Fe (III) migre ensuite probablement vers la surface laissant une lacune dans le cœur. Etape 3 : au-dessus de 1.2V vs. RHE Co (II) dans la coquille est partiellement oxydé en Co (III). Etape 4 : l'OER se produit sur un centre actif composé de Co (III) et Fe (III). Cependant on ne peut pas exclure la formation de Fe (IV) actif pour l'OER au-dessus de1.4V vs. RHE. Les atomes d'oxygène sont en rouge, le cobalt en bleu et le fer en vert.

Bien que dans la littérature sur des NPs de Co_3O_4, il ait été observé la formation d'une couche de CoOOH en surface lors de l'OER, ici la structure spinelle de la NP semble être conservée, le cobalt reste dans un état d'oxydation Co (II). Un mécanisme faisant intervenir l'oxygène de la maille a été également écarté car aucun changement n'a été vu sur le seuil K de l'oxygène lors de l'OER.

3) Conclusion

Dans ce travail nous avons synthétisé différents types de catalyseurs pour l'OER sous forme de NPs cœur-coquille $Fe_3O_4@Co_xFe_{2-x}O_4$. Cette approche originale a pour intérêt de maximiser la surface de matériau catalytiquement actif (coquille) tout en limitant la quantité du cobalt. Cette coquille est combinée avec un cœur conducteur de Fe_3O_4 sur lequel la coquille peut croitre de manière épitaxiée. Quatre types de NPs qui peuvent être assimilées à des catalyseurs modèles ont été synthétisés par décomposition thermique de précurseurs métalliques et la taille du cœur ainsi que l'épaisseur de la coquille ont été modifiés afin de pouvoir étudier l'influence de ces paramètres sur les propriétés électrochimiques des NPs. La méthode de décomposition thermique est intéressante car elle permet l'obtention de NPs dont la taille, la distribution de taille, la composition et la forme sont bien définies et contrôlées.

Avant de procéder aux caractérisations électrochimiques des NPs, leur structure a été étudiée à l'aide de différentes techniques d'analyse qui ont mis en évidence la présence d'une structure cœur-coquille comme nous nous y attendions. Cependant la stœchiométrie de la coquille n'est pas d'exactement $CoFe_2O_4$ mais plutôt $Co_xFe_{2-x}O_4$: un gradient de concentration de cobalt est donc présent dans la coquille. Ce résultat peut être expliqué par la température de décomposition des précurseurs (stéarates de cobalt et de fer) utilisés pour la synthèse des NPs. En effet le stéarate de cobalt présente une température de décomposition plus faible, le fer commencera donc à croitre en premier à la surface de la coquille puis le cobalt croit également à la surface, créant un gradient de cobalt avec la surface de la coquille riche en cobalt.

Une fois ces caractérisations réalisées, les NPs ont été caractérisées électrochimiquement à l'aide de techniques de voltampérométrie cyclique et d'impédance. Lors de cette étude, il a pu être observé que l'activité massique apparente des NPs n'est pas constante en fonction de la charge déposée sur l'électrode : elle diminue fortement lorsque la masse est trop importante et que les NPs forment alors plusieurs couches

superposées. La conclusion logique de cette observation est que toutes les NPs ne sont alors plus accessibles de la même façon. A l'aide de simulations réalisées sur les données expérimentales de spectroscopie d'impédance, il a pu être démontré l'existence d'une résistance de contact qui se crée entre les couches de NPs. Les modélisations ont été réalisées à l'aide de deux modèles : le modèle de Randles et le modèle de lignes de transmission. Ainsi cette étude a prouvé que pour avoir une valeur correcte de l'activité il faut donc mesurer les NPs avec une charge basse sur l'électrode (qui correspond à une couche catalytique mince).

Comparativement à la littérature, les NPs cœur-coquille ont toutes montré une bonne activité pour l'OER. De plus, le cœur des NPs, constitué uniquement de Fe_3O_4 est lui très peu actif, c'est donc bien le cobalt dans la structure spinelle qui donne l'activité au système. Il est donc possible de normaliser le courant généré par les NPs par la masse de cobalt seulement et non pas la masse totale des NPs. Lorsque l'on considère les activités massiques par gramme de cobalt alors les NPs présentent une activité allant de 1300 $A.g^{-1}_{cobalt}$ pour les NPs présentant un cœur de petite taille (7-8 nm) à 2800 $A.g^{-1}_{cobalt}$ pour celles qui présentent un cœur dont la taille est plus importante (13-14 nm). Ces activités sont bien supérieures à la majorité des activités reportées dans la littérature. Ces différences d'activité en fonction de la taille du cœur des NPs sont probablement dues au fait que le cœur donne au système une conductivité suffisante pour que le catalyseur soit conducteur. L'épaisseur de la coquille ne semble pas avoir un effet important sur l'activité mais il faudrait réaliser ces expériences avec une coquille dont l'épaisseur serait bien plus importante pour s'en assurer.

Enfin les analyses NEXAFS *operando* réalisées au synchrotron ont mis en évidence une action conjointe du fer dans le cœur et du cobalt lors de la réaction de l'OER. Il a été observé que dans les conditions de l'OER le fer s'oxydait en Fe (III) alors que le cobalt lui restait majoritairement dans un état d'oxydation Co (II). Une transformation en CoOOH comme cela a été souvent proposé dans la littérature pour des catalyseurs de Co_3O_4 a alors été écartée. De même, un mécanisme faisant intervenir l'oxygène de la maille a été écarté car aucun changement n'a pu être observé au seuil K de l'oxygène lors de l'OER. Les transformations se produisant dans les NPs ont été expliquées par la potentielle intervention d'un atome de Fe (IV) dont la durée de vie est très courte et qui n'est donc que très peu observé en NEXAFS qui pourrait constituer un cluster avec le cobalt et serait le site actif.

Dans le futur il sera intéressant de changer la composition des NPs en remplaçant le cobalt par du nickel, lui aussi connu pour être actif pour l'OER mais aussi de regarder au microscope électronique à transmission comment les NPs sont affectées par l'application d'un potentiel pour vérifier s'il y a une reconstruction de la nanoparticule et de la diffusion des atomes de cobalt et de fer ou si la structure cœur-coquille initiale est belle et bien conservée.

4) Références

(1) Christophe Coutanceau, Steve Baranton, Thomas Audichon. *Hydrogen Electrochemical Production* -.

(2) Dincer, I.; Zamfirescu, C. *Sustainable Hydrogen Production*; Elsevier, 2016.

(3) Arminio-Ravelo, J. A.; Quinson, J.; Pedersen, M. A.; Kirkensgaard, J. J. K.; Arenz, M.; Escudero-Escribano, M. Synthesis of Iridium Nanocatalysts for Water Oxidation in Acid: Effect of the Surfactant. *ChemCatChem* **2020**, *12* (5), 1282–1287. https://doi.org/10.1002/cctc.201902190.

(4) Pfeifer, V.; E. Jones, T.; Wrabetz, S.; Massué, C.; Vélez, J. J. V.; Arrigo, R.; Scherzer, M.; Piccinin, S.; Hävecker, M.; Knop-Gericke, A.; Schlögl, R. Reactive Oxygen Species in Iridium-Based OER Catalysts. *Chemical Science* **2016**, *7* (11), 6791–6795. https://doi.org/10.1039/C6SC01860B.

(5) Saveleva, V. A.; Wang, L.; Teschner, D.; Jones, T.; Gago, A. S.; Friedrich, K. A.; Zafeiratos, S.; Schlögl, R.; Savinova, E. R. Operando Evidence for a Universal Oxygen Evolution Mechanism on Thermal and Electrochemical Iridium Oxides. *J. Phys. Chem. Lett.* **2018**, *9* (11), 3154–3160. https://doi.org/10.1021/acs.jpclett.8b00810.

(6) Thomas, O. D.; Soo, K. J. W. Y.; Peckham, T. J.; Kulkarni, M. P.; Holdcroft, S. Anion Conducting Poly(Dialkyl Benzimidazolium) Salts. *Polym. Chem.* **2011**, *2* (8), 1641–1643. https://doi.org/10.1039/C1PY00142F.

(7) Wang, L.; Weissbach, T.; Reissner, R.; Ansar, A.; Gago, A. S.; Holdcroft, S.; Friedrich, K. A. High Performance Anion Exchange Membrane Electrolysis Using Plasma-Sprayed, Non-Precious-Metal Electrodes. *ACS Appl. Energy Mater.* **2019**, *2* (11), 7903–7912. https://doi.org/10.1021/acsaem.9b01392.

(8) Peng, J.; Dong, W.; Wang, Z.; Meng, Y.; Liu, W.; Song, P.; Liu, Z. Recent Advances in 2D Transition Metal Compounds for Electrocatalytic Full Water Splitting in Neutral Media. *Materials Today Advances* **2020**, *8*, 100081. https://doi.org/10.1016/j.mtadv.2020.100081.

(9) Reikowski, F.; Maroun, F.; Pacheco, I.; Wiegmann, T.; Allongue, P.; Stettner, J.; Magnussen, O. M. Operando Surface X-Ray Diffraction Studies of Structurally Defined Co3O4 and CoOOH Thin Films during Oxygen Evolution. *ACS Catal.* **2019**, *9* (5), 3811–3821. https://doi.org/10.1021/acscatal.8b04823.

(10) Mefford, J. T.; Akbashev, A. R.; Kang, M.; Bentley, C. L.; Gent, W. E.; Deng, H. D.; Alsem, D. H.; Yu, Y.-S.; Salmon, N. J.; Shapiro, D. A.; Unwin, P. R.; Chueh, W. C. Correlative Operando Microscopy of Oxygen Evolution Electrocatalysts. *Nature* **2021**, *593* (7857), 67–73. https://doi.org/10.1038/s41586-021-03454-x.

(11) Wiegmann, T.; Pacheco, I.; Reikowski, F.; Stettner, J.; Qiu, C.; Bouvier, M.; Bertram, M.; Faisal, F.; Brummel, O.; Libuda, J.; Drnec, J.; Allongue, P.; Maroun, F.; Magnussen, O. M. Operando Identification of the Reversible Skin Layer on Co3O4 as a Three-Dimensional Reaction Zone for Oxygen Evolution. *ACS Catal.* **2022**, *12* (6), 3256–3268. https://doi.org/10.1021/acscatal.1c05169.

(12) Kéranguéven, G.; Filimonenkov, I. S.; Savinova, E. R. Investigation of the Stability of the Boron-Doped Diamond Support for Co3O4-Based Oxygen Evolution Reaction Catalysts Synthesized through in Situ Autocombustion Method. *Journal of Electroanalytical Chemistry* **2022**, 116367. https://doi.org/10.1016/j.jelechem.2022.116367.

(13) Sartori, K.; Musat, A.; Choueikani, F.; Grenèche, J.-M.; Hettler, S.; Bencok, P.; Begin-Colin, S.; Steadman, P.; Arenal, R.; Pichon, B. P. A Detailed Investigation of the Onion Structure of Exchanged Coupled Magnetic Fe3−δO4@CoFe2O4@Fe3−δO4 Nanoparticles. *ACS Appl. Mater. Interfaces* **2021**, *13* (14), 16784–16800. https://doi.org/10.1021/acsami.0c18310.

(14) Anantharaj, S.; Kundu, S.; Noda, S. "The Fe Effect": A Review Unveiling the Critical Roles of Fe in Enhancing OER Activity of Ni and Co Based Catalysts. *Nano Energy* **2021**, *80*, 105514. https://doi.org/10.1016/j.nanoen.2020.105514.

(15) Liu, X.; Pichon, B. P.; Ulhaq, C.; Lefèvre, C.; Grenèche, J.-M.; Bégin, D.; Bégin-Colin, S. Systematic Study of Exchange Coupling in Core–Shell Fe3−δO4@CoO Nanoparticles. *Chem. Mater.* **2015**, *27* (11), 4073–4081. https://doi.org/10.1021/acs.chemmater.5b01103.

(16) Perton, F. Architecture de Nanoparticules Hybrides Pour Une Imagerie et/Ou Thérapie Multimodales. thesis, Strasbourg, 2019.

(17) Sartori, K.; Cotin, G.; Bouillet, C.; Halté, V.; Bégin-Colin, S.; Choueikani, F.; Pichon, B. P. Strong Interfacial Coupling through Exchange Interactions in Soft/Hard Core–Shell Nanoparticles as a Function of Cationic Distribution. *Nanoscale* **2019**, *11* (27), 12946–12958. https://doi.org/10.1039/C9NR02323B.

(18) Fletcher, S. An Electrical Model Circuit That Reproduces the Behaviour of Conducting Polymer Electrodes in Electrolyte Solutions. *Journal of Electroanalytical Chemistry* **1992**, *337* (1), 127–145. https://doi.org/10.1016/0022-0728(92)80533-A.

(19) Zhou, S.; Potzger, K.; Xu, Q.; Kuepper, K.; Talut, G.; Markó, D.; Mücklich, A.; Helm, M.; Fassbender, J.; Arenholz, E.; Schmidt, H. Spinel Ferrite Nanocrystals Embedded inside ZnO: Magnetic, Electronic, and Magnetotransport Properties. *Phys. Rev. B* **2009**, *80* (9), 094409. https://doi.org/10.1103/PhysRevB.80.094409.

(20) Regan, T. J.; Ohldag, H.; Stamm, C.; Nolting, F.; Lüning, J.; Stöhr, J.; White, R. L. Chemical Effects at Metal/Oxide Interfaces Studied by x-Ray-Absorption Spectroscopy. *Phys. Rev. B* **2001**, *64* (21), 214422. https://doi.org/10.1103/PhysRevB.64.214422.

Lisa ROYER

Nanoparticules cœur-coquille d'oxyde de fer et de cobalt pour l'électrocatalyse de la réaction de dégagement de l'oxygène

Résumé

Cette thèse étudie un nouveau type de catalyseur visant à abaisser le potentiel d'activation de la réaction de dégagement de l'oxygène (OER) en milieu alcalin tout en remplaçant les métaux nobles utilisés communément en milieu acide par des oxydes métalliques. Ce catalyseur combine les propriétés conductrices d'un cœur de magnétite (Fe_3O_4) à l'activité électrocatalytique d'une coquille de ferrite de cobalt ($CoFe_2O_4$) dans une structure cœur-coquille Fe_3O_4@$CoFe_2O_4$. Les propriétés électrochimiques de ces nanoparticules (NPs) ont été étudiées systématiquement en modifiant la taille du cœur et l'épaisseur de la coquille. Les NPs constituées d'un cœur de taille supérieur à 12 nm ont permis d'atteindre une activité de 2800 $A.g^{-1}_{cobalt}$ à 1.65 V *vs.* RHE qui est généralement au-delà des valeurs reportées dans la littérature pour des composés similaires. Les mécanismes se déroulant à la surface des nanoparticules lors de la réaction d'OER ont été étudiées *operando* et l'étude de la structure électronique des métaux en fonction de leur environnement a permis de suivre l'évolution de leurs degrés d'oxydation et de mettre en évidence la synergie entre les cations de fer (II) et de cobalt (II) pendant l'OER. De plus, l'analyse par microscopie électronique à transmission (STEM HAADF et EELS) a montré que la structure cœur-coquille est conservée lors de cette réaction et qu'elle permet d'éviter la formation de CoOOH en surface dans la gamme de potentiel de l'OER.

Mots clés : Réaction de dégagement de l'oxygène (OER) ; oxyde de cobalt ; oxyde de fer ; nanoparticule cœur coquille ; *operando* spectroscopie de structure près du seuil d'absorption de rayons X (NEXAFS)

Résumé en anglais

This thesis studies a novel type of catalyst aiming for lowering the overpotential of the oxygen evolution reaction in alkaline media while replacing the noble metals oxide commonly used in acidic media by transition metal oxides. This catalyst combines the conductive properties of a magnetite core (Fe_3O_4) and the electrocatalytic activity of a cobalt ferrite shell using core-shell Fe_3O_4@$CoFe_2O_4$ nanoparticles. The electrochemical properties of these nanoparticles have been systematically studied modifying the core size and the shell thickness. The particles presenting a core diameter superior to 12nm reached an activity of 2800 $A.g^{-1}_{cobalt}$ at 1.65 V *vs.* RHE which is by far superior to the activity reported in the literature for similar catalysts. The transformations occurring at the surface of the catalyst during the oxygen evolution reaction have been studied *operando* by NEXAFS thanks to synchrotron radiation. This technique allowed the study the evolution of the metal cation oxidation state and evidenced a synergy between the Fe (II) in the core and the Co (II) in the shell during the OER. Moreover, transmission electron microscopy revealed that the core-shell structure was preserved during the OER and that it allows to prevent the formation of CoOOH in the potential range of the OER.

Keywords: Oxygen evolution reaction (OER): cobalt oxide; iron oxide; core-shell nanoparticles; operando near-edge absorption spectroscopy (NEXAFS).